UNIVERSITY OF LEICESTER

FREDERIQUE JOS VANHEUSDEN

INSIDE-OUT AGAINST OUTSIDE-IN INVERSE SOLUTIONS FOR ESTIMATING ATRIAL FIBRILLATION SOURCES

DEPARTMENT OF ENGINEERING
School Of Sciences And Engineering

PhD Thesis
Academic Year: 2014 - 2015

Supervisors: Dr Fernando S Schlindwein, Professor G André Ng
01/2015

“For better an approximate answer to the right question,

which is often vague,

than an exact answer to the wrong question,

which can always be made precise.”

John W Tukey, 1962.

INSIDE-OUT AGAINST OUTSIDE-IN INVERSE SOLUTIONS FOR ESTIMATING ATRIAL FIBRILLATION SOURCES

Frederique Jos Vanheusden

ABSTRACT

Atrial fibrillation (AF) is the most frequently occurring cardiac arrhythmia. Further understanding of the drivers and maintainers of AF is still necessary to improve treatment strategies and outcome. This thesis focussed on identifying AF sources using body-surface mapping and non-contact endocardial mapping (NCM, inside-out inverse solution) data. Analysis was focussed on dominant frequency (DF) and highest dominant frequency (HDF) behaviour. Atrial sources on the atrial muscle were estimated from body surface mapping (BSM) using a heterogeneous torso model (outside-in inverse solution).

The current work has shown that a significant difference exists between the DF and HDF behaviour on the BSM and NCM data. This shows the effect of the torso volume conductor on BSM data as previously suggested in simulation studies. This effect should be taken into account when analysing BSM data for diagnosing AF.

In this work, a new inside-out inverse solution was developed based on equivalent double layer cardiac sources. This was compared to commercially available software (EnSite, St Jude Medical), which was considered the gold standard. This system is based on a potential-based transfer, and therefore only provides a “closer look” at the pericardial potentials, but does not estimate sources. Due to this variation in source model, significant differences could be found between the inverse solutions, leading to high regularisation parameters to force the home-made inverse solution to be as equal as possible to the gold standard. This also meant that high-frequency components could not be reproduced accurately with the home-made algorithm, leading to significant variation in DF and HDF behaviour between both inside-out inverse solutions.

Lastly a double-layer based outside-in inverse solution was developed and compared to the gold standard inside-out inverse solution. Although both solutions originate from a different source model, it was possible to reconstruct simple AF behaviour based on the HDF behaviour.

ACKNOWLEDGEMENTS

Throughout the three and a half years of this PhD, I have had a chance to develop insights in a field that was very new to me. As a student who received his university degrees in biomedical sciences, the step from a niche in which mathematics are almost considered as “things to be avoided” to the current project in engineering was challenging. I am therefore very thankful to my supervisors, Dr Fernando Schlindwein and Professor André Ng for guiding me through this project. With their experience and dedication to science, I had the ability to develop as a researcher, discuss possible routes during the project, as well as receive objective advice and help throughout the PhD. I would also like to thank them for setting up this strong collaboration between the Engineering Department and the Cardiovascular Sciences Department. Through this, the group was able to implement new engineering development directly into clinic, as well as obtaining additional data to develop new technological ideas. I thoroughly enjoyed this collaboration, and it has given me an experience that will help me significantly in my future career.

I would like to thank Professor Adriaan van Oosterom (Radboud University Nijmegen) for all his advice during our collaboration. As the University of Leicester was not experienced with the inverse problem, the possibility to collaborate with one of the leaders in the field has had a significant impact on the development of this project. I would like to thank him for the time and effort he has put into helping constructing the inverse algorithm and the insight he has given me on the complicated theories behind the inverse problem and the numerical implementation of them.

A PhD can be a lonely experience and a mental struggle. I would therefore like to thank all my present and past colleagues of the Bio-Engineering Research Group and the Cardiovascular Department for helping me setting up the project, discussing results and sharing new ideas throughout the project. Besides this, I would also like to thank them for the fun moments in which we had some time to let go of the struggles of the PhD and enjoy the (student) life, and to always be there to talk about issues and trying to help in sorting them out.

I wish to express my gratitude to my parents, who have given me the chance to continue my studies in the UK. They have been ready to give me support and advice throughout the PhD and have always shown enthusiasm and interest in the projects I was working on.

Lastly, I would like to thank my girlfriend, Amee Kim, who has recently finished her PhD at the University, for all her support as well as her parents, Gong Sun-ja and Kim Young-ho for being very hospitable and their advice. Amee understood exactly the position I was in, and I was very happy to be able to openly discuss all the positive and negative sides of my project and life of a PhD student with her. She was able to show me the right way to go ahead and to keep me motivated. She has been an enormous inspiration, and we have been able to share many beautiful moments during our time in Leicester. I would like to say to her: 사랑하는 공주, 든든한 모든 지원과 늘 함께해서 정말 고마워요!

Regarding the materials used in this project, the author would like to thank his supervisors for providing the additional funding where needed throughout the project. I would also like to thank Professor Adriaan van Oosterom for providing the spherical 3D models as well as the analytical solution for the dipoles related to these models and algorithms for performing the inverse solution.

This project is funded by the Leicester Cardiovascular Biomedical Research Unit (BRU). The BRU at the University Hospitals of Leicester NHS Trust and the University of Leicester is funded by the National Institute for Health Research.

TABLE OF CONTENTS

LIST OF FIGURES

LIST OF TABLES

LIST OF EQUATIONS

LIST OF ABBREVIATIONS

AF	Atrial Fibrillation
AFFIRM	Atrial Fibrillation Follow up Investigation of Rhythm Management
ANOVA	Analysis of Variance
AP	Action Potential
APD	Action Potential Duration
AV	Atrio-Ventricular
BEM	Boundary Element Method
BS	Body Surface
BSM	Body Surface Map(ping)
BSP	Body Surface Potential
Ca^{2+}	Calcium
CFAE	Complex Fractionated Atrial Electrograms
Cl^{-}	Chloride
CO_2	Carbon dioxide
CoG	Centre of Gravity
CRESO	Composite Residual and Smoothing Operator
CS	Coronary Sinus
CS OS	Coronary Sinus Ostium
CT	Computed Tomography
CV	Cardioversion
dB	Decibel
DCCV	Direct Current Cardioversion
DFIQR	Dominant Frequency Interquartile range (temporal)
DFM	Dominant Frequency Median (temporal)
DFT	Discrete Fourier Transform
DICOM	Digital Images and Communication in Medicine
ECC	Excitation-Contraction Coupling
ECG	Electrocardiogram
ECGI	Electrocardiographic Imaging
EDL	Equivalent Double Layer
E_{eq}	Membrane/equilibrium/resting Potential
EED	Endo-Epicardial Decoupling
E_{in}	Intracellular Potential
EnS	EnSite Inside-out inverse solution
E_{out}	Extracellular Potential
EPS	Electrophysiological Study

F	French
FFT	Fast Fourier Transform
FIR	Finite Impulse Response
GMRes	Generalised Minimum Residual
HASTE	Half Fourier Acquisition Single Shot Turbo Spin Echo
HDF	High/Highest Dominant Frequency
IC	Information Criterion
I_{Ca}	Calcium current
IQR	Interquartile Range
IVC	Inferior Vena Cava
K^+	Potassium
LA	Left Atrium/Left Atrial
LAA	Left Atrial Appendage
LGE-MRI	Late Gadolineum Enhanced-Magnetic Resonance Imaging
LLPV	Left Lower Pulmonary Vein
LSSA	Lomb-Scargle Spectral Analysis
LUPV	Left Upper Pulmonary Vein
LV	Left Ventricle/Left Ventricular
MAPK	Mitogen-activated-protein kinase
MDL	Minimum Descriptive Length
MEA	Multi-Electrode Array
mRNA	Messenger Ribonucleic Acid
mV	Millivolt
MV	Mitral Valve
Na^+	Sodium
NCM	Non-Contact Mapping
O_2	(Molecular) Oxygen
OI	Outside-In (inverse solution)
pAF	Paroxysmal Atrial Fibrillation
PCA	Principal Component Analysis
persAF	Persistent Atrial Fibrillation
PM	Pacemaker
PV	Pulmonary Vein
PVC	Premature Ventricular Contractions
PVI	Pulmonary Vein Isolation
PVO	Pulmonary Vein Ostium/Ostia
RA	Right Atrium/Right Atrial

RAA	Right Atrial Appendage
RE	Relative Error
RLPV	Right Lower Pulmonary Vein
RUPV	Right Upper Pulmonary Vein
RV	Right Ventricle/Right Ventricular
SA	Sino-Atrial
SR	Sinus Rhythm
SSIM	Structural Similarity Index
SVC	Superior Vena Cava
TSVD	Truncated Singular Value Decomposition
TV	Tricuspid Valve
UDL	Uniform Double Layer
uint16	16-bit unsigned integer
UoL	University of Leicester (Inside-out inverse solution)
VCG	Vectorcardiogram
WCT	Wilson Central Terminal

LIST OF PUBLICATIONS

Peer-reviewed Journals

SALINET Jr, J. L., OLIVEIRA, G. N., VANHEUSDEN, F. J., COMBA, J. L. D., NG, G. A. & SCHLINDWEIN, F. S. 2013. Visualizing intracardiac atrial fibrillation electrograms using spectral analysis. Computing in Science and Engineering, 15, 79-87.

Conference Papers

VANHEUSDEN, F. J., LI, X., CHU, G. S., ALMEIDA, T. P., NG, G. A. & SCHLINDWEIN, F. S. Analysis of spatial variability for the development of reduced lead body surface maps. 40th Computing in Cardiology Conference, CinC 2013, 2013 Zaragoza. 535-538.

VANHEUSDEN, F., SALINET Jr, J.L., NICOLSON, W. B., MCCANN, G. P., NG, G. A. & SCHLINDWEIN, F. S. Patient-specific three-dimensional torso models for analysing cardiac activity. 39th Computing in Cardiology Conference, CinC 2012, 2012 Krakow. 973-976.

DASTAGIR, N., SALINET, J., VANHEUSDEN, F. J., ALMEIDA, T. P., LI, X., CHU, G. S., NG, G. A. & SCHLINDWEIN, F. S. 2014b. Spatiotemporal Behaviour of High Dominant Frequency during Persistent Atrial Fibrillation. 41st Computing In Cardiology Conference, CinC 2014, 2014 Boston, USA.

LI, X., SALINET, J. L., ALMEIDA, T. P., VANHEUSDEN, F. J., CHU, G. S., NG, G. A. & SCHLINDWEIN, F. S. 2014. A Platform to guide Catheter Ablation of Persistent Atrial Fibrillation using Dominant Frequency Mapping. 41st Computing In Cardiology Conference, CinC 2014, 2014 Boston, USA.

BIALA, T. A., VANHEUSDEN, F. J., SCHLINDWEIN, F. S. & WAILOO, M. QT analysis of intrauterine growth retarded and normal children at 10 years old. 39th Computing in Cardiology Conference, CinC 2012, 2012 Krakow. 433-436.

Conference Proceedings

VANHEUSDEN, F. J., LI, X., CHU, G. S., ALMEIDA, T., SCHLINDWEIN, F. S. & NG, G. A. Development of Reduced-Lead Body Surface Mapping Systems using Spatial Frequency Analysis. Heart Rhythm Congress 2013, 2013 Birmingham.

VANHEUSDEN, F. J., SALINET Jr, J. L., NICOLSON, W. B., MCCANN, G. P., NG, G. A. & SCHLINDWEIN, F. S. Structured 3D Finite Element Torso Models for Cardiac Activity Analysis. BioEngineering12, 2012 Oxford.

ALMEIDA, T., CHU, G., VANHEUSDEN, F., LI, X., SALINET, J., TUAN, J., STAFFORD, P., SCHLINDWEIN, F. & NG, G. 2014. Investigating differences in complex fractionated atrial electrogram discrimination as performed by CARTO and NavX algorithms. EP Europace, 16, iii25-iii25.

DASTAGIR, N., CHU, G., VANHEUSDEN, F., SALINET, J., ALMEIDA, T., LI, X., STAFFORD, P., SANDILANDS, A., SCHLINDWEIN, F. & NG, G. 2014a. Ablation for persistent atrial fibrillation shrinks left atrial high dominant frequency areas. EP Europace, 16, iii28-iii28.

Other Conferences and Local Events

VANHEUSDEN, F. J., SCHLINDWEIN, F. S. & NG, G. A. Combining MRI Images and Body Surface Signals To Reveal the Heart's Secrets. Festival of Postgraduate Research 2012, 2012 Leicester.
Winner of the Leicestershire Asian Business Association Prize for Best Poster (College of Science and Engineering).

VANHEUSDEN, F. J., SALINET Jr, J.L., NICOLSON, W. B., MCCANN, G. P., NG, G. A. & SCHLINDWEIN, F. S. Patient-Specific Three-Dimensional Torso Models for Analysing Cardiac Activity, BRU Training Camp 2012, 2012 Ashridge.

1 Cardiac Electrophysiology and Atrial Fibrillation

1.1 Introduction

The main function of heart is to circulate blood through the body. The blood is circulated by well-organised rhythmic contractions. This rhythm is governed by electrical signals which are generated in and sent through the heart following specific conduction pathways. In cases where these pathways do not follow the normal conduction routes, or where the heart beats at an abnormal rate or rhythm, disturbances occur which are defined as cardiac arrhythmias.

The most common form of cardiac arrhythmia is atrial fibrillation (AF). In AF, regions of the upper chambers of the heart (the atria) deviate from the normal heart rate (Nattel, 2002). AF is estimated to affect almost 1% of the population in the world (Kannel *et al.*, 1998). From the 2007 Department of Health figures, more than 600,000 people in the UK are affected by AF (AFA, 2011). As its prevalence is highly related with age, the number of AF patients is likely to strongly increase over the next decades (Hobbs *et al.*, 2005). Much effort has been focussed on better understanding AF in order to improve prevention, diagnosis and treatment of the disease.

This project attempts to provide additional understanding of AF by combining Body Surface Mapping (BSM) and Magnetic Resonance Imaging (MRI). Body surface mapping (BSM) can be described as measuring the cardiac electrical signals with many (32 or more) electrodes on the torso surface (van der Graaf *et al.*, 2014). MRI is a form of medical imaging which can be used to develop models of the torso geometry. These models can then be used to calculate the effect of the torso volume conductor on the estimation of body surface signals from cardiac signals. This estimation is known as the forward problem of electrocardiology. Once this is understood, attempts can be made to estimate cardiac signals from body surface maps. This analysis is known as the inverse problem of electrocardiology, which can be defined as the reconstruction of cardiac signals from measurements remote of the heart (Barr *et al.*, 1966, Pullan *et al.*, 2003). The inverse problem from the BSM will be referred to as the outside-in inverse problem in this thesis. It will be compared to inside-out

inverse problems collected from non-contact balloon catheters in the atrial cavities.

To better understand the concepts behind AF, a well-founded knowledge of cardiac electrophysiology is needed. The next sections give an overview of the normal cardiac electrophysiology. This will be followed by a discussion of the current knowledge regarding AF (section 1.3). As mentioned previously, this project includes investigations of the possibility to enhance AF management by improving the signal's spatial resolution using BSMs. An overview of the current knowledge in atrial BS mapping will be given in section 1.4. Lastly, an attempt is made to estimate the cardiac AF sources from BSMs as well as invasive non-contact mapping (NCM), which would solve the inverse problem from an inside-out (balloon to endocardium) as well as outside-in (torso to epicardium) perspective. The theory behind the inverse solution will be detailed in section 1.5, and an overview of current studies on the AF inverse solution will be given in section 1.6.

1.2 Normal Cardiac Electrophysiology

1.2.1 Cardiac Anatomy

The heart is positioned in the chest between the lungs and above the diaphragm. The heart consists of two "pumps" (Figure 1-1). Both pumps (left and right) have an atrium collecting blood from the rest of the body and a ventricle sending blood out to the body. The muscular wall of the heart consists of an outer layer (epicardium) and an inner layer covering the chamber surfaces (endocardium). The muscular tissue between these surfaces is called the myocardium. The heart is protected by an adipose tissue layer called the pericardium (Agur and Dalley, 2005).

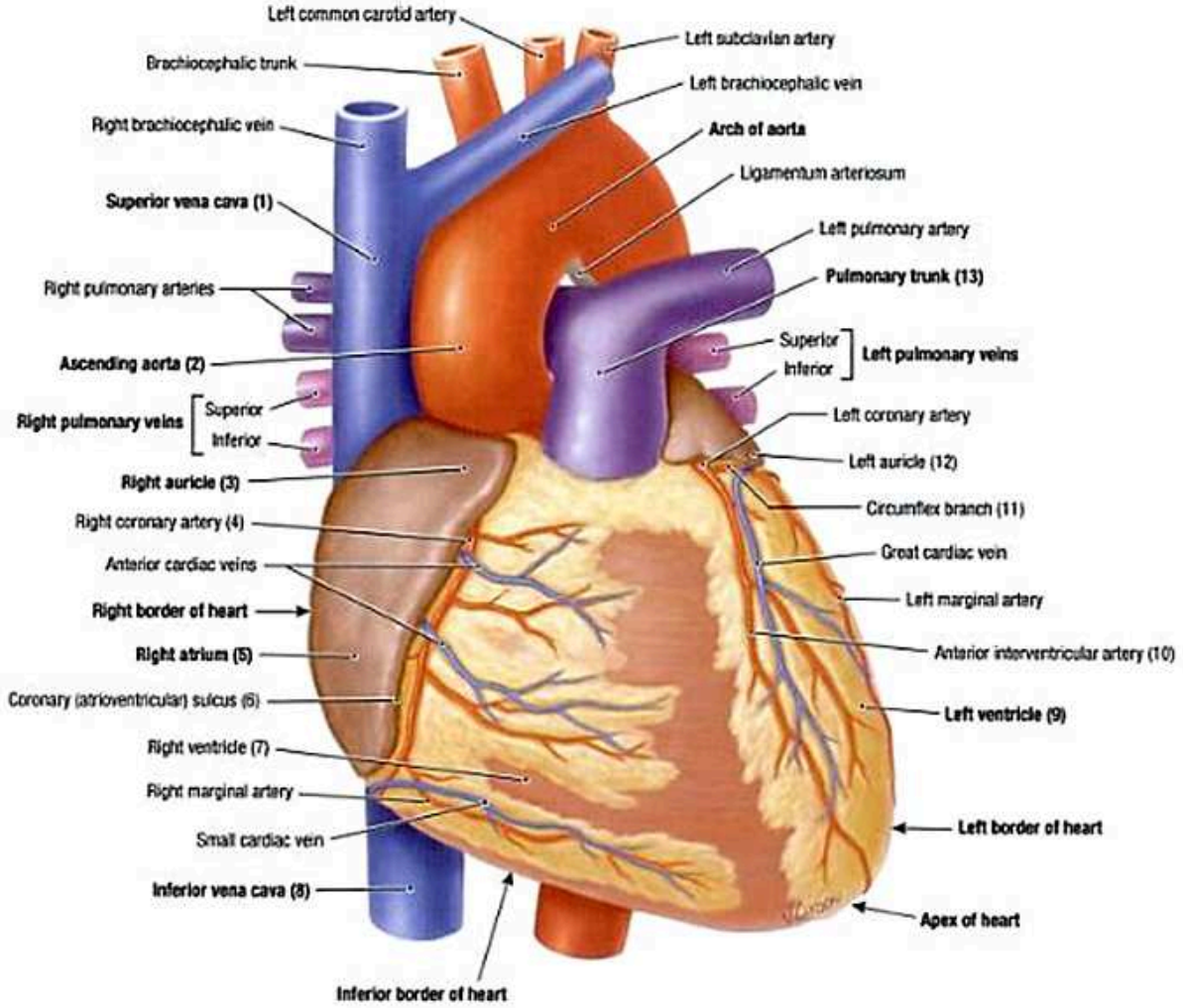

Figure 1-1: Overview of the heart anatomy (Agur and Dalley, 2005) (Reproduced with permission from the publisher).

The main cardiac function is to collect blood from and return it to the body. For this purpose a cyclic process occurs as follows. Blood full of waste products and CO_2 returns from the body to the right atrium (RA). The RA pumps the blood to the right ventricle (RV) and the RV sends the blood to the lungs, where CO_2 is exchanged for O_2 (Shoucri, 1991, Shoucri, 1993). The blood rich in oxygen returns to the heart and is spread through the body via the left atrium (LA) and ventricle (LV).

The cardiac cycle is induced by action potentials (APs) which activate the muscle cells. Action potentials originate spontaneously in the sino-atrial (SA) node located in the right atrium. These action potentials (APs) are directed throughout the heart to induce contraction in a highly regulated manner (Benarroch, 1993, Cranefield, 1977). The cycle frequency is set between 60 and 90 beats per minute for a person in rest. This rate can be increased or decreased by the sympathetic or parasympathetic branches of the autonomic nervous system (Benarroch, 1993) and humoral inputs (Kallergis *et al.*, 2010, Shor *et al.*, 2008). An overview of both mechanical and electrical functioning of the heart will be discussed in the next sections.

1.2.2 Mechanical Function of the Heart

The heart is a syncytium of two pumps (left and right) that distributes blood throughout the body (Seifter *et al.*, 2005). During one cardiac beat, each pump goes through phases linked to ventricular contraction (systole) and relaxation (diastole). Systole begins with the start of ventricular contraction. Since blood is in the ventricular cavity, a high pressure is developed within the chamber leading the valve between the atrium and ventricle to shut. When the valve is shut, a period arises where the contraction of the ventricles further increases the pressure in the ventricular chamber without the expulsion of blood, known as the isovolumic contraction. When the pressure exceeds the pressure within the outflow tract, the valve linking the ventricle to the circulatory system opens and blood flows rapidly out of the ventricle (fast ejection phase). Initially, this leads to a further increase in the ventricular pressure, but as the blood volume gets displaced throughout the circulatory system and the force of contraction decreases, the pressure drops and less blood is expulsed (slow ejection

phase). The ventricular pressure then falls below the threshold to keep the valves between the left ventricle and aorta - as well as the valves between the right ventricle and pulmonary arteries - open. The closure of the valves ends the systolic period (Brutsaert, 2003, Shoucri, 1991).

During diastole, the pressure in the ventricles keeps decreasing; however, no blood is injected from the atria (isovolumic relaxation). In the meantime, the atria are filled with blood. The atrio-ventricular valves open when ventricular pressure falls below atrial pressure. Blood flows rapidly from the atria into the ventricles (rapid filling phase). The atrial pressure drops, leading to a period of minimal ventricular filling (diastasis). In the last part of diastole, atrial contraction takes place to push an additional volume of blood into the ventricles, allowing ventricular pressure to be built up and therefore closure of the valves (Brutsaert, 2003, Shoucri, 1991). The process then restarts with another systolic phase. A schematic overview of the variation in pressure and volume in the left ventricle during the various parts of the pump action is given in Figure 1-2.

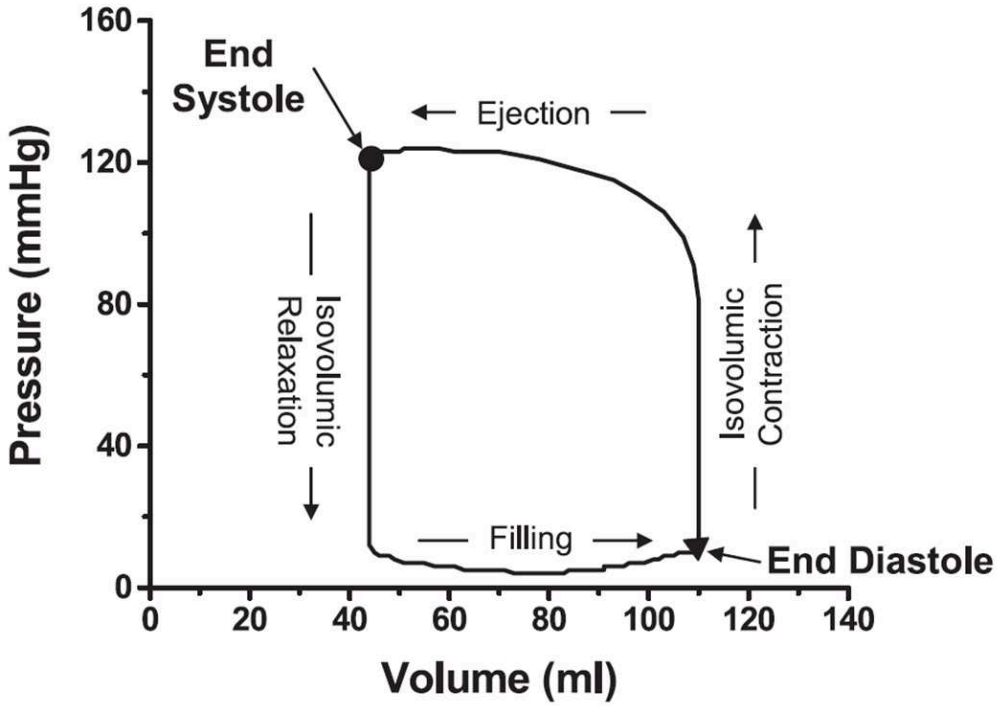

Figure 1-2: Overview of the mechanical function of the LV (pressure-volume loop) (Burkhoff *et al.*, 2005) (Reproduced with permission from the publisher).

1.2.3 Electrical Function of the Heart

The mechanical functioning of the heart is directly dependent on proper electrical function, and *vice versa* (Fozzard *et al.*, 1995). This electrophysiological function can be attributed to the generation of an appropriate stimulus at the SA node, which generates an action potential and activates the cells for contraction. This activation signal is propagated through the cells using electrical coupling (gap junctions) between the cells, allowing the heart to contract in a synchronous manner (Nerbonne and Kass, 2005).

1.2.3.1 Stimulation and Activation of a Single Cell

Cells reside in an electrochemically inhomogeneous environment. It can be divided in an extracellular region (outside the cell) and an intracellular region (inside the cell). These regions are separated by the cell membrane. One particular inhomogeneity is the different concentrations of ions present in the extracellular compared to the intracellular compartment (Fry and Jabr, 2010). For cells which can be stimulated electrically, the ions of major importance are sodium (Na^+), potassium (K^+), calcium (Ca^{2+}) and chloride (Cl^-). High concentrations of Na^+; Ca^{2+} and Cl^- exist in extracellular space, whereas K^+ is more concentrated intracellularly. The cell membrane is semipermeable to these ions. Depending on chemical and electrical gradients established between the intracellular and extracellular space at a specific moment, specific ions will be allowed to flow into or out of the cell, whereas the flow of others is restricted. If no stimulus is present, the cell is considered to be at rest, and the flow of ions is regulated such that an equilibrium potential difference between the cellular space and its environment is maintained. This equilibrium (or membrane) potential (E_{eq}) is by agreement measured as the subtraction of the intracellular potential (E_{in}) and extracellular potential (E_{out}).

$$E_{eq} = E_{in} - E_{out} \tag{1-1}$$

Due to the higher concentration of positive ions outside the cell, E_{eq} is negative (between -60 and -80 mV) (Seifter *et al.*, 2005).

When a stimulus reaches the excitable cell, a change in the resting potential will occur, and the cell depolarises. Only if this stimulus is sufficiently strong to

depolarise the cell to a threshold potential, it will trigger a cascade of changes in ion permeability in the cell's membrane and induce an action potential (Nerbonne and Kass, 2005).

The action potential of a cardiomyocyte differs from action potentials of other excitable cells, in that they are spread over a longer time interval (Keating and Sanguinetti, 2001). Depending on the heart region, variations in the shape of the action potential exist, which help coordinate propagation direction (Nerbonne and Kass, 2005). In essence, however, the cardiac action potential is separated into 5 phases. These will be explained based on the general action potential of atrial muscle cells, developed according to the Courtemanche model (CRM, Figure 1-3) (Courtemanche *et al.*, 1998).

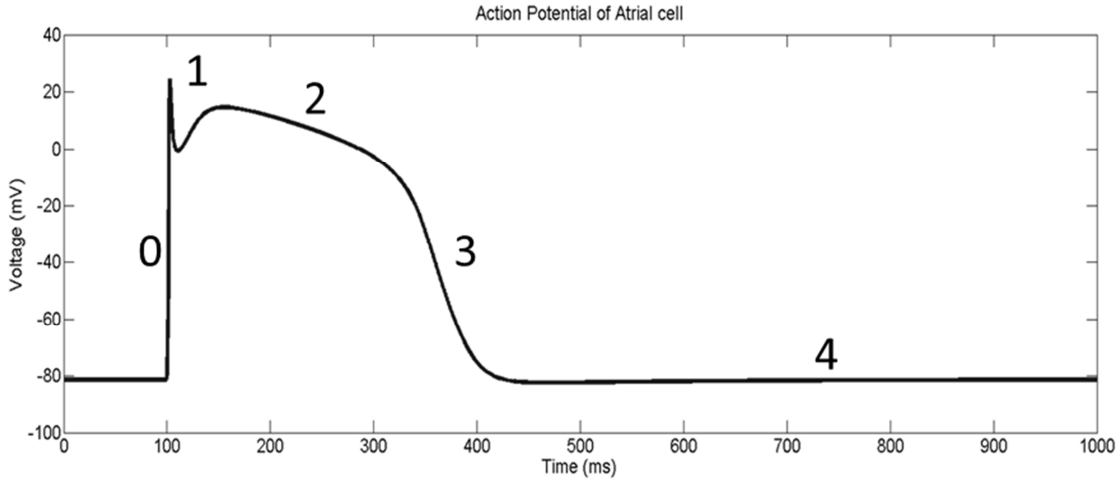

Figure 1-3: Atrial cell action potential according to the Courtemanche model. Numbers indicate phases of action potential as described in the text.

The depolarisation phase (Phase 0) shows a steep upstroke in the membrane potential from the resting potential to about 30 mV. This is mainly due to the rapid activation (opening) of voltage-gated Na^+ channels in the cell membrane (Keating and Sanguinetti, 2001). Besides this, Ca^{2+} is allowed to enter the cell from the extracellular space as well as the intracellular storages within the sarcoplasmatic reticulum (Seifter *et al.*, 2005). A high concentration of Na^+ ions is allowed to enter the cell, making the intracellular environment positive compared to the extracellular region. A partial, fast repolarisation phase (Phase 1) follows due to the inactivation of Na^+ channels and the activation of a transient outward K^+ current (Keating and Sanguinetti, 2001). After this, the

inward Ca^{2+} current slowly decreases and the outward K^+ current get activated, leading to a plateau phase (Phase 2) in the action potential. The repolarisation phase (Phase 3) is mainly governed by outward K^+ currents and leads immediately to a return to the resting membrane potential (Phase 4) (Keating and Sanguinetti, 2001). During Phase 1 to 3, the cell is insensitive for new stimuli. This period is called the refractory period of the cell and it is especially due to the inactivation of Na^+ channels (Seifter *et al.*, 2005). In SA and AV nodal cells, Phase 0 is less steep, leading to a slower activation of these cells, which helps in regulating propagation. Ventricular muscle cells show a longer plateau phase than atrial muscle cells (Zaza *et al.*, 2012).

1.2.3.2 The Electrical Stimulus and Cell Contraction

Cell membrane depolarisation induces cell contraction, known as excitation-contraction coupling (ECC). A main factor in governing ECC is Ca^{2+} (Gordon *et al.*, 2000). During the depolarisation wave, L-type Ca^{2+} channels are activated and allow Ca^{2+} to enter into the cells. This influx allows Ca^{2+} to bind to the ryanodine receptors located at the sarcoplasmatic reticulum. The activation of these receptors allows the Ca^{2+} stored inside the sarcoplasmatic reticulum to enter the cell plasma. This mechanism is known as Ca^{2+}-induced Ca^{2+} release (Schotten *et al.*, 2011).

The released Ca^{2+} will then bind to the troponin complex of the cell's actin-myosin filaments. This allows the cell to contract. During repolarisation, intracellular Ca^{2+} concentrations are reduced again by efflux and resequestration into the sarcoplasmic reticulum (Ebashi, 1991, Gordon *et al.*, 2000). A proper electrical function is thus necessary to allow the heart to perform its main mechanical function.

1.2.3.3 Electrical Stimulus Conduction in Healthy Hearts

Contraction of the heart follows a well-organised pattern related to the pathway of electrical activation which starts at the sino-atrial SA node located in the RA close to the right border of the superior vena cava. Following these impulses, activation is almost concentrically spread through the atria, with the latest activation at the left atrial appendage. Ventricular activation is moderated by the atrio-ventricular (AV) node, which is the unique direct electrical connection

between atria and ventricles. The left side of the septum separating the ventricles is activated first. Left ventricular activation then occurs via the left bundle branch and Purkinje fibre system, which finally reaches the postero-basal part of the left ventricle. Right ventricular activation is shortly delayed compared to LV activation, but follows a similar route. For both ventricles, activation along the endocardium is faster than from endocardium to epicardium (Durrer *et al.*, 1970). This anisotropic behaviour is due to a higher density of cell-cell connections (gap junctions) in parallel with compared to perpendicular to the fibres' direction (Jongsma and Wilders, 2000). A schematic overview of the electrical propagation is given in Figure 1-4.

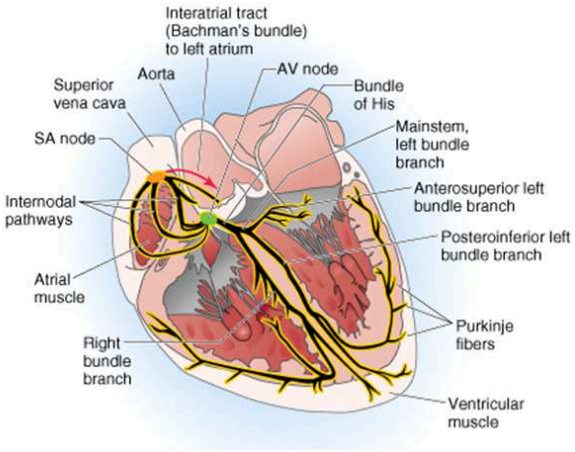

Figure 1-4: Schematic overview of the main electrical propagation pathway in the heart (Boron and Boulpaep, 2012) (Reproduced with permission from the publisher).

In AF, alterations of the atrial activation and conduction pathway occur, leading to inappropriate contraction or even quivering of the atria (Nattel, 2002). Several mechanisms have been suggested underlying these phenomena. The following section will briefly discuss the main principles thought to be responsible for AF.

1.3 Atrial Fibrillation Pathophysiology

Although AF is a frequently occurring arrhythmia, its complex behaviour has not led to straightforward diagnostic and therapeutic strategies. This cumbersome

behaviour already becomes clear in the classification of AF, which appears based on the general presentation and duration of AF.

AF can be classified in 5 types (Camm *et al.*, 2010). Patients who are diagnosed for the first time with AF is classified as a first-diagnosed AF patient. Paroxysmal AF (pAF) is defined as patients presented with self-terminating AF cycles that last for 48 hours up to 7 days. The 48 hour threshold is based on the loss of likelihood that a patient will cardiovert spontaneously to sinus rhythm after suffering AF for longer time periods, as well as the need to provide anticoagulation therapy from this point onwards. Persistent AF (persAF) occurs when AF remains over periods longer than 7 days or when cardioversion is necessary to restore sinus rhythm. Long-standing persAF can be considered AF the remains for more than 1 year. Patients are classified under permanent AF when consistent AF manifestation is accepted by both patient and physician and no rhythm control intervention is pursued any longer,

The electrophysiological evolution between the different types of AF is unclear, as multiple triggers and maintainers of AF can be considered to worsen the AF or maintain AF at a stable state. An overview of these triggers and maintainers is given in the following paragraphs.

1.3.1 Triggers of AF

As was shown in the classical study of Wijffels *et al.* (Wijffels *et al.*, 1995), repetitive pacing and maintenance of AF led to a higher AF susceptibility in goats, introducing the concept of *"*AF begets AF". In many (human) patients, AF behaves as a progressive disease as well, starting with asymptomatic & self-terminating events (Israel *et al.*, 2004) that progress into persistent AF (persAF) and permanent AF over decades (Kerr *et al.*, 2005). Several mechanisms have been suggested to play a role in AF triggering. The variation in which (combinations) of these mechanisms occur leads to the various patterns of AF which can be seen in different patients, and to the complexity in finding appropriate ways of treating this disease. In the following, the possible AF triggers are separated into very local (cellular) alterations and more regional re-entry mechanisms. These are schematically represented in Figure 1-5.

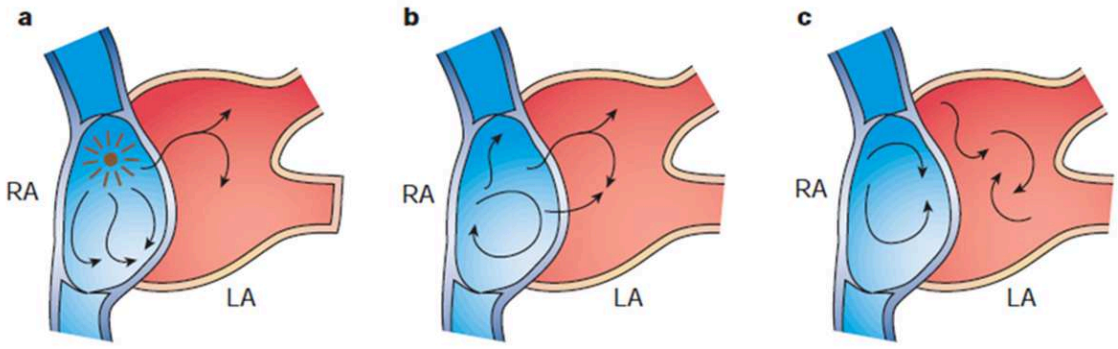

Figure 1-5: Schematic overview of three main mechanisms suggested to trigger AF: Left: ectopic focus, Middle: single re-entry circuit, Right: multiple re-entry circuits (Nattel, 2002) (Reproduced with permission from the publisher).

1.3.1.1 Cellular Pro-Arrhythmic Dysfunctions

Triggers of AF can arise locally by alterations in the function of a group of myocytes. One such alteration is enhanced automaticity, in which pacemaker cells increase their rate of spontaneous discharge. This can be due to a reduced threshold for the AP upstroke, a reduced maximum negative diastolic potential, or an increase in the slope of diastolic depolarisation (Schotten *et al.*, 2011).

Another local effect is abnormal automaticity, in which cells are depolarized by ion currents, which lead to spontaneous discharge at high frequencies (Schotten *et al.*, 2011).

Another suggested AF initiator is triggered activity. Due to oscillations in the cell membrane during the action potential, strong re-depolarisations can arise. If these occur after the cell's refractory period and have sufficient strength, a new AP may be induced. Experiments have shown that strong depolarisations can occur after the repolarisation phase (delayed afterdepolarisations) or during the plateau or repolarisation phase of the AP (early afterdepolarisations) (Cranefield, 1977).

1.3.1.2 Re-Entry Mechanisms

Generally, re-entry mechanism can be described as cases where the cardiac activation wavefront finds a route to re-excite areas of the heart from which the front originated (Nattel, 2002). The re-entry concept was first introduced by

Mines in 1913. He suggested that activation fronts travel around an unexcitable anatomical structure (e.g. fibrotic tissue) and as such could re-excite tissue where the activation wave was initiated. This re-entry mechanism can only persist if the time for the activation wave to return to its site of origin is longer than the refractory period of tissue (Mines, 1913).

In 1924, Garrey issued that no anatomical structure was needed to induce re-entry. In his leading circle concept, he suggested that rotating waves could travel around a non-excitable area throughout the atria (Garrey, 1924). The non-excitability of the area would be induced by electrotomic depolarisation (Schotten *et al.*, 2011). The rotating waves would follow the smallest loop in which they could propagate, leading to an unstable form of conduction.

The idea of a single re-entry wave was dismissed after Moe and colleagues developed computer simulations to analyse AF (Moe *et al.*, 1964). These simulations suggested a constant interaction of wavefronts and wavetails between multiple wavelets, which leads to a disorganised combination of propagation, wave break and wave generation. As long as there are sufficient wavelets present, atrial fibrillation can be maintained (Moe *et al.*, 1964). Allessie and co-workers experimentally observed the occurrence of multiple wavelets, strengthening Moe's hypothesis (Allessie, 1985, Allessie *et al.*, 1977, Konings *et al.*, 1994).

Other computer simulations showed the possibility of spiral wave re-entry mechanisms (Panfilov and Hogeweg, 1993). Spiral waves could occur as convex or concave wave forms. With convex waveforms, a small region of depolarized cells (sources) has to propagate the activation wave front to a large area of cells still at rest (sinks). This leads to a slow propagation. In concave waveforms, a large source area has to excite a small sink, leading to high conduction velocity. To induce spiral wave re-entry, one wavefront would collide with the wavetail of another wave. If the tissue behind the wavetail is excitable, the wavefront will re-excite this tissue and turn towards newly recovered tissue, suggesting the appearance of a rotor around a non-excited core (Comtois *et al.*, 2005). Recently, spiral wave re-entry mechanisms have been observed after phase analysis of body surface maps and electrograms

recently (Gray *et al.*, 1998, Rodrigo *et al.*, 2013). More experiments have to be conducted however to strengthen the spiral wave concept.

1.3.2 Maintenance of AF

Many other factors play a role in triggering or maintaining AF however, and in some cases this leads to the spontaneous development of permanent AF, or prevents stabilization of AF, leading to continuously recurring episodes of paroxysmal (short-term) AF (pAF) (Schotten *et al.*, 2011). One major factor is hypertension, which occurs in about 60% of AF patients, causes AF progression and was found to be an independent predictor of AF (Nabauer *et al.*, 2009). Besides this, co-incidence of other heart or vascular diseases, such as coronary artery disease and heart failure occur in about 30% of AF population (Cleland *et al.*, 2003, Nieuwlaat *et al.*, 2005). A schematic overview of how these diseases can be an effective trigger or substrate of AF is presented in Figure 1-6 (Aliot and Ruskin, 2008, Nattel, 2002). Briefly, cardiac dysfunction, induced by AF, atrial remodelling or ventricular remodelling, will decrease cardiac output, which in many cases leads to hypertension and tachycardia. Hypertension leads to an increased angiotensin II release from the kidneys. This triggers the Mitogen-Activated-Protein Kinase (MAPK) pathway, which can lead to (atrial) tissue fibrosis and therefore atrial remodelling (Boron and Boulpaep, 2012). The regions of fibrosis could induce sources of ectopic activity, wavelet breakdown or re-entry mechanisms stimulating fibrillation.

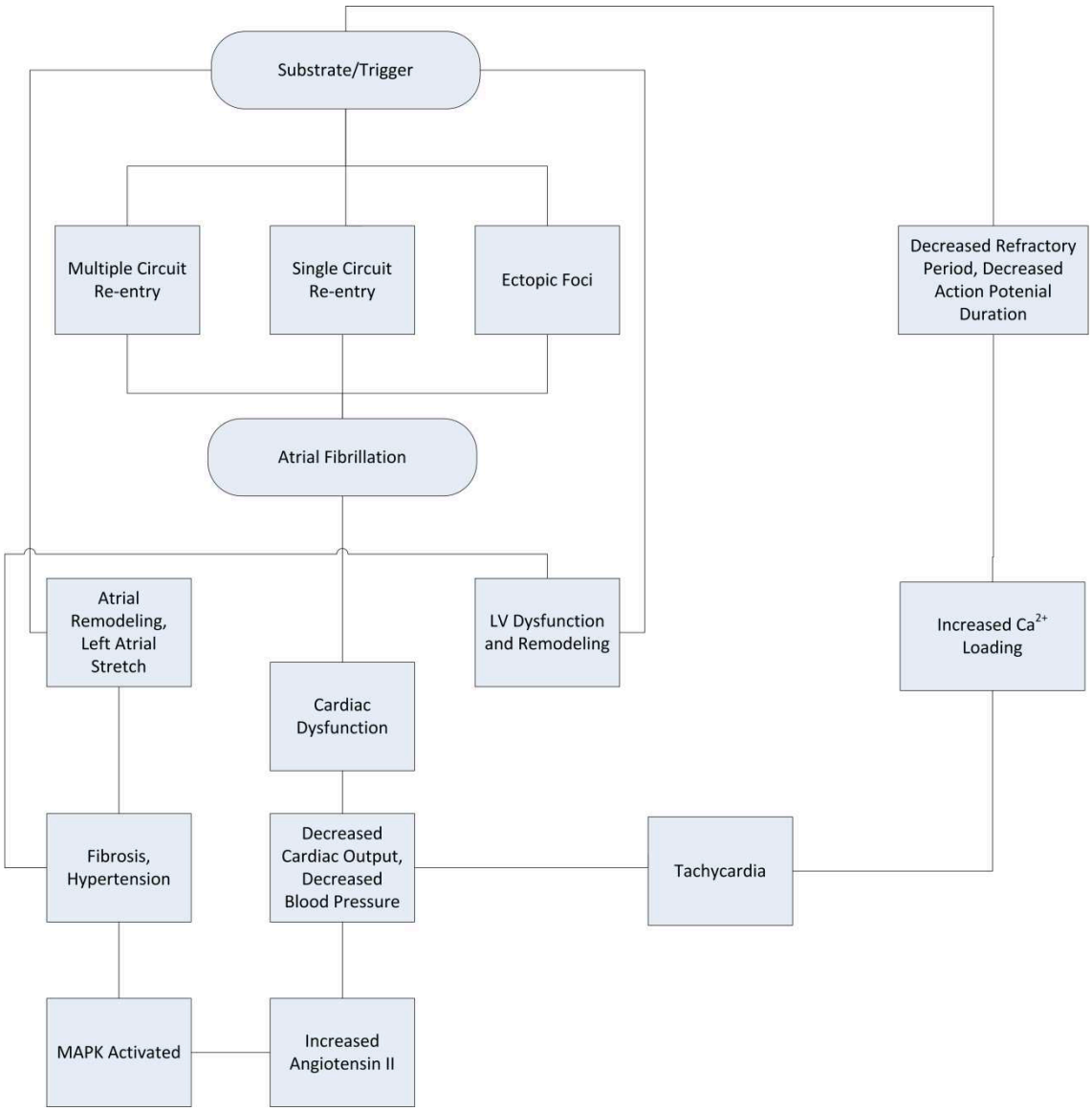

Figure 1-6: Overview of most important triggers and substrates of AF (Schotten *et al.*, 2011).

If tachycardia occurs, the Ca^{2+} homeostasis malfunctions, and an increased cellular Ca^{2+} loading occurs (Nattel, 2002). As can be seen in Figure 1-7, this inactivates the Ca^{2+} current (ICa) and decreases the production of Ca^{2+} messenger ribonucleic acid (mRNA). Therefore, the presence of Ca^{2+} channels decreases, which reduces the Ca^{2+} loading, but also decreases the action potential duration (APD) and refractory period of atrial cells. This reduction in refractory period could allow the development of re-entry circuits, leading to (the progression of) AF.

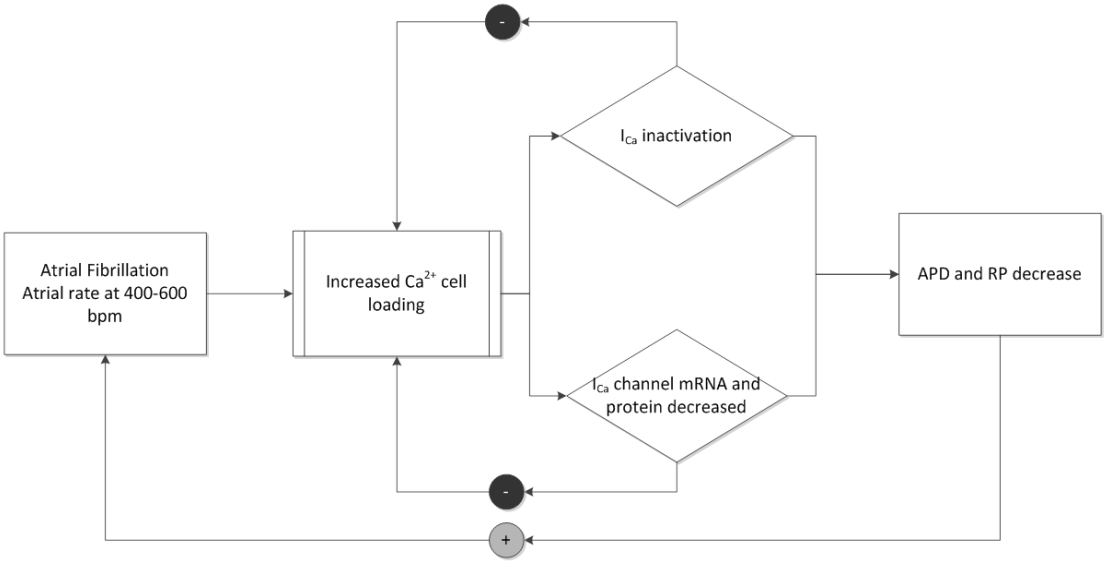

Figure 1-7: Link between changes in cellular Ca^{2+} homeostasis and AF (Nattel, 2002).

1.3.3 Symptoms and Diagnosis of AF

The first onsets of AF are mostly asymptomatic (Schotten *et al.*, 2011). The earliest signs for patients are palpitations and chest pain. Besides this, many patients complain about light-headedness, fatigue and suffer from exercise intolerance. AF can only be diagnosed based on the patient's history and a proven occurrence of AF seen on the electrocardiogram (ECG).

A problem with ECG systems is the low number of measurement spots on the torso, which do not allow for a full appreciation of the source location of AF nor possible mechanisms behind it (van Oosterom *et al.*, 2007). Body surface mapping (BSM), which can be described as measuring the cardiac activity with many (32 or more) electrodes on the torso (van der Graaf *et al.*, 2014), has proven to be a good alternative to better understand the electrophysiological aspects of heart disease from torso measurements (Taccardi *et al.*, 1998). However, the increased time consumption to set up BSMs, as well as the complexity of handling, analysing and understanding BSM data has so far prevented routine clinical use of BSMs (Hoekema *et al.*, 1999, Punske, 2003).

Further evidence for AF is routinely gained from echocardiograms -to identify abnormal size of the atria-, Holter (24 hour ECG) monitoring, exercise tests or electrophysiological studies (EPS) (Fuster *et al.*, 2006).

1.3.4 Consequences of AF

Although AF by itself is not lethal, it increases the risk of death and other diseases. According to the AFFIRM trial, AF doubles death rates, independent of co-existing cardiovascular conditions (Epstein, 2004). A portion of these deaths are caused by strokes. It has been found that AF is the cause of 20-25% of all strokes, and there is a tendency that strokes caused by AF are more severe than other strokes (Miyasaka *et al.*, 2005). Some studies also showed a reduced LV function in AF patients, which could induce other, more severe, heart diseases (Hsu *et al.*, 2004). To avoid these consequences, and to improve the quality of life of AF patients, different methods for treating AF have been developed and improved during the previous decades.

1.3.5 Alternatives for AF Treatment

Generally, AF treatment comprises three objectives: rate or rhythm control, the prevention of blood clotting, and restoration of sinus rhythm. The strategy for obtaining these objectives in a specific patient depends on several aspects, including the duration of AF prior to treatment, the severity and type of symptoms, patient age and other medical conditions from which the patient is suffering (Fuster *et al.*, 2006). Primary treatment consists of a combination of drugs to restore rhythm or heart rate. It has been shown that death rates reduce in patients treated with ion-channel blocking drugs or beta-blockers for rate control (Epstein, 2004). Drugs such as flecainide can also be used for cardioverting the atria back to sinus rhythm (Fuster *et al.*, 2006). When sufficient evidence is present for high risk of thrombo-embolism, patients will also receive anticoagulation drugs, e.g. warfarin (Connolly *et al.*, 2009). Drug treatment can however induce side effects, albeit in a small subgroup of patients. Anti-arrhythmic drugs are generally not specific to the atria, and can therefore induce ventricular arrhythmias or heart failure. Inappropriate use of antithrombotic agents can also induce bleeding. Drugs used for cardioversion can also induce ventricular arrhythmias (Camm *et al.*, 2010, Fuster *et al.*, 2006).

When patients do not respond to drugs, or if the negative effect of drugs might worsen other medical conditions, clinicians might opt to restore sinus rhythm

with electric direct current cardioversion (DCCV). DCCV has shown to be more effective than pharmacological cardioversion, but requires sedation or anaesthesia and therefore complicates the procedure. DCCV can also induce arrhythmia or thromboembolism (Fuster *et al.*, 2006).

Alternatively, AF sources can be isolated from the rest of the atria by catheter ablation. Catheter ablation introduces scars in the atrial endocardium by applying radiofrequency signals (Fuster *et al.*, 2006) or by freezing endocardial regions (cryo-ablation) (Neumann *et al.*, 2008). This procedure is currently considered secondary, and will only be used to treat patients who are non-responsive to drug treatment or DCCV (Fuster *et al.*, 2006). Catheter ablation gained much interest after studies proved the effectiveness of this method to isolate AF sources arising near the pulmonary vein ostia (PVO) (Haïssaguerre *et al.*, 1998). Other regions of interest for ablation have been suggested since then (Lin *et al.*, 2003). A review by Cappato *et al.* showed that the current success rates of AF ablation are approximately 90% for paroxysmal AF and 80% for persistent AF (Cappato *et al.*, 2005). Complications do exist, however, and may arise as PV stenosis, thromboembolism and embolic stroke, atrial flutter or cardiac tamponade (Camm *et al.*, 2010, Fuster *et al.*, 2006).

In very specific circumstances, especially when additional cardiac disorders need to be treated, clinicians can opt to treat AF by surgery or pacemaker implantation. Surgical AF treatment is only performed if patients are simultaneously undergoing cardiac surgery, due to the high risk and need for cardiopulmonary bypass (Fuster *et al.*, 2006). The most used procedure is the isolation of regions prone to sustain AF by incision, creating a geometrical maze on the heart (Cox *et al.*, 1989, Cox *et al.*, 1991). In case of patients needing a pacemaker to treat ventricular problems, an additional pacemaker lead can be placed in the atrium after AV node ablation. The pacemaker would then control cardiac rhythm. This approach makes the patient lifelong dependent on the pacemaker and does not necessarily avoid the need for drug treatment (Fuster *et al.*, 2006).

Further optimisation of diagnosis, treatment and prevention of AF is still required and is intensively researched. Interesting new ideas arise from

medical image analysis (Oakes *et al.*, 2009) and estimation of AF sources using BSMs (Cuculich *et al.*, 2010). The next sections will give an overview of the current knowledge regarding these techniques.

1.4 The Analysis of Atrial Signals Using Body Surface Maps

Although the first BSM measurement on animals and humans were performed by Waller at the end of the 19th century (Waller, 1888), BSM has only been used more frequently since the 1960s. Since then, BSM was performed for the diagnosis of various types of cardiac diseases (Taccardi, 1963). In the next paragraph, different ways to represent BSMs in time-series analysis will be described. Furthermore, recent interest has focussed on relating BSM maps to invasive studies, especially regarding dominant frequency (DF) analysis (Guillem *et al.*, 2013). A short description of DF will be given, as this project partly focussed on further determining possible relationships between BSMs and invasive studies based on frequency analysis.

1.4.1 Body Surface Mapping Techniques

The analysis of data measured from BSM can be performed in different ways (Medvegy *et al.*, 2002). Mostly, isopotential maps are created (Figure 1-8). Here, contour maps of body surface sites which have equal potentials at a specific moment during cardiac activation are indicated. In most cases, the maximum, minimum and zero potential are highlighted. Although BSMs are independent of the reference site (Horan *et al.*, 1964, Taccardi, 1963), except for a constant, the Wilson's Central Terminal (WCT) is considered as reference in most studies. Some research groups have suggested using the average value over all electrodes as a reference (Hoekema *et al.*, 1999).

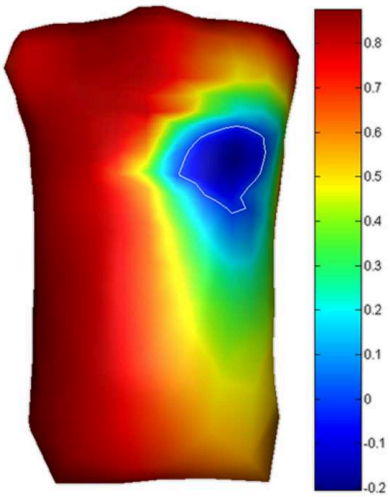

Figure 1-8: Example of an isopotential map during the QRS interval. Colour bar values are in mV.

Alternatively, BSMs are created by linking sites that are activated at the same time during the cardiac cycle. In other words, this type of mapping shows the progression of the depolarisation or repolarisation wavefront. These maps are called isochronous maps (Hoekema *et al.*, 1999).

Less frequently, iso-area maps are calculated based on the distribution of the time-integral of the potential during a time interval (Medvegy *et al.*, 2002). Lastly, in large studies especially based on myocardial infarct (MI) analysis, BSM data from large patient groups were averaged and compared to an average healthy BSM. Regions of patient-maps that significantly differed from the healthy map were indicated only. These maps were termed departure or difference maps (Kornreich *et al.*, 1986, Kornreich *et al.*, 1985).

The analysis of BSM data has generally focussed on specific aspects of the generated maps. Much interest has been given to the progression of positivity and negativity on maps. Positivity can indicate that the heart region under the electrode is activated (isochronous map), or that the activation wave front is moving towards an electrode (isopotential map). Negativity, oppositely, can indicate the end of depolarisation or an activation wave front moving away from the electrode (Medvegy *et al.*, 2002). Besides this, the spatio-temporal wandering of maxima and minima, as well as the ratio of maximal potential over minimal potential, can indicate various types of disease. Differences between

healthy and diseased BSM have been described by Medvegy and co-workers (Medvegy *et al.*, 2002).

Lately, due to the increased amount of analytical tools from invasive studies, BSM representation is shifting towards time-frequency analysis. This has especially been the case for the analysis of atrial fibrillation (AF).

Generally, mechanisms triggering and sustaining AF are believed to induce regional pacing rates which are much higher than the normal SA pacing rate (Nattel, 2002). It has been possible to identify these sites in atria using DF analysis on data from invasive studies (Salinet Jr *et al.*, 2010). In most papers discussing DF analysis (Figure 1-9), the power spectral density of an electrogram is calculated from the Fast Fourier Transform (FFT) by squaring the FFT amplitude spectrum (Salinet Jr *et al.*, 2010) of applying the Welch method (Guillem *et al.*, 2013). The dominant frequency is defined as the frequency with the highest power in a frequency range up to 20 Hz (Guillem *et al.*, 2013). Analysis is performed on windowed data, with a suggested window length of 4 seconds (Salinet Jr *et al.*, 2010).

The possibility for non-invasive DF analysis was first developed for ventricular fibrillation (VF) (Langley *et al.*, 2009). In AF, the possibility to use maximal frequency sites from BSMs to guide ablation was first indicated by Guillem and co-workers (Guillem *et al.*, 2013). The close correlation of body surface DFs and intracardiac DF recordings was further indicated by Bojarnejad *et al.* (Bojarnejad *et al.*, 2013).

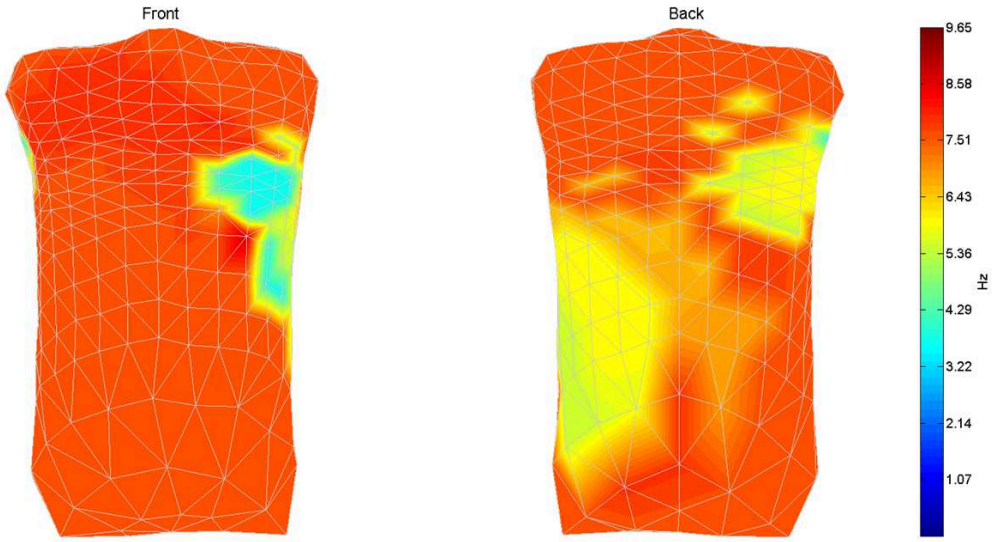

Figure 1-9: Example of a dominant frequency body surface map (4 second window).

For the above studies, different setups for BSMs have been used, which makes a comparison between the studies challenging (Hoekema *et al.*, 1998). An optimal solution would be to provide a standard setup for BSMs, probably with as few electrodes as possible. Various studies have investigated reduced-lead BSM analysis with success (Barr *et al.*, 1971, Finlay *et al.*, 2006, Lux *et al.*, 1978). Besides this, online tools for BSM analysis have been provided (Bond *et al.*, 2010b, Bond *et al.*, 2010a).

The above steps have however not led to any standardisation. This lack of standardisation together with the complexity of applying BSM systems to the patient and the high amount of data to be stored and analysed, have hampered the routine application of BSM in clinic (Punske, 2003). This might change in the near future, as much progress is made towards using non-invasive signals for predicting sources of cardiac disease on the heart surface. This estimation problem is generally known as the inverse problem of electrocardiology (van Oosterom, 2012c).

1.5 The Inverse Problem: Theoretical Background

From a general perspective, one could consider a problem where a source below the surface generates electrical signals which can be measured on the surface through a conducting medium (Hansen, 2010). Assuming that the

medium can be described accordingly, if one knows the data at the source, the signals arising from these source data at the surface can be determined. This type of problems is called forward problem. On the other hand, if one knows the signals at the surface, the data at the source could be calculated. These problems are inverse problems**.**

Most inverse problems can be stated mathematically as a Fredholm integral of the first kind. A generic form of this integral reads as:

$$g(x) = \int_0^1 K(x, x')f(x')dx' \tag{1-2}$$

Here, the relationship between the source $f(x')$ and surface data $g(x)$ is described by kernel $K(x, x')$. In the case of the inverse problem, both $g(x)$ and $K(x, x')$ are assumed known, albeit with errors (e.g. signal noise) in realistic environments (Hansen, 2010).

Inverse problems are part of the class of ill-posed problems. In 1902, Hadamard suggested that well-defined problems should have three requirements (Hadamard, 1902):

1. Existence: a solution for the problem must exist,
2. Uniqueness: the solution should be unique, and
3. Stability: the solution should be continuously dependent on the data.

Any problem not covering all three requirements is an ill-posed problem.

For the inverse problem in electrocardiology, the source is considered to be the active source on the heart that generates torso signals. The system is the torso geometry and electrical conduction properties of the tissues within the torso. The surface is the torso surface. The inverse problem is ill-posed as for requirements 2 and 3. The uniqueness of the electrocardiological inverse problem is an issue as the source on the heart surface is not known (Nash and Pullan, 2005). Cardiac sources can however be estimated, as will be described in sections 1.5.4 and 1.5.5. Previous research has provided elegant strategies for accurate source estimations, and the lack of uniqueness is therefore no longer considered an issue (Cheng *et al.*, 2003a, van Oosterom, 2012c).

The instability of inverse solutions is inherent to integral equation features. According to the Riemann-Lebesque lemma, as the signals are calculated from the source, higher frequencies in the source signal are damped more than lower frequencies. From this, the surface signals will behave more smoothly than the source signals (Hansen, 2010). The opposite happens in the inverse problem, meaning that high frequencies in the surface signals will be amplified more than lower frequencies. Noise will therefore be amplified on the cardiac signals, and a correct analysis of the sources will be challenging (Cheng *et al.*, 2003b, Colli-Franzone *et al.*, 1985b). This problem can be partly solved by regularisation (Cheng *et al.*, 2003a), in which a smoothing function is added to the inverse problem equation.

The following paragraphs will discuss in more detail ways to set up inverse solutions in electrocardiography. Different source types, volume conductor equations and regularisation techniques will be described. First, an overview will be given about the physical properties of electric volume conduction.

1.5.1 The Laplace and Poisson Equations as Starting Points for the Inverse Problem

To determine the principal mathematical equations behind the inverse problem, physical properties of sources in a volume conductor will be explained based on the image shown in Figure 1-10. Here, the source is considered a point source at $\vec{x}$. It is desired to know the potential generated by this source at field point $\overrightarrow{x'}$, assuming a homogeneous volume conductor (conductivity σ). The conductor is bounded by surface S (Geselowitz, 1989).

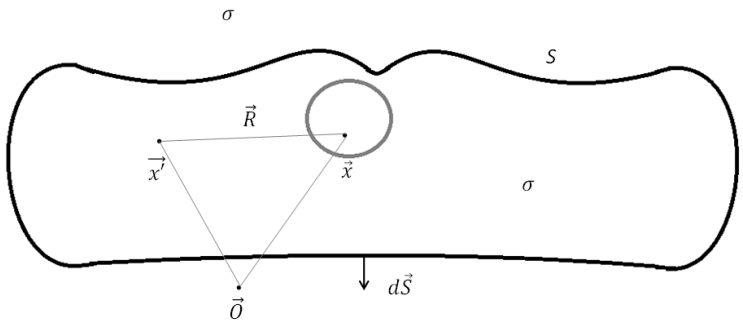

Figure 1-10: Schematic representation of an electrical source $\vec{x}$ in a medium of homogeneous conductivity (σ), bounded by the surface S (Barr *et al.*, 1966).

The point source can generate an electric field $\overrightarrow{E_x}$ in the volume conductor. In a homogeneous volume conductor, the current density $\overrightarrow{J_x}$ can be calculated according to the third dimensional extension of Ohm's law:

$$\overrightarrow{J_x} = \sigma \overrightarrow{E_x} \tag{1-3}$$

Here, σ is constant. In cases where (parts of) the volume conductor is anisotropic, σ becomes a $3x3$ tensor (Plonsey and Barr, 2007).

The volume conductor is considered passive. This means that all the electrical variables considered are assumed to arise only from the source $\vec{x}$, and no charge is accumulated within the volume conductor. As the source can be specified for each time instant independently, the electrical variables can be estimated for each instant. This is known as the quasi-static approximation (Colli-Franzone *et al.*, 1982).

For the passive medium, this means that the following equation holds:

$$\nabla \cdot \vec{J} = 0 \tag{1-4}$$

Besides this, the electrical potential Φ can be defined as follows:

$$-\nabla \Phi \triangleq \vec{E} \tag{1-5}$$

Inserting (1-5) into (1-3), and following (1-4), this leads to:

$$\nabla \cdot \sigma \nabla \Phi = \sigma \nabla^2 \Phi = 0 \tag{1-6}$$

This is known as the Laplace equation. It holds when considering the potential distribution in passive media (Plonsey and van Oosterom, 2012).

As the part of the volume conductor indicated in grey on Figure 1-10 contains an active source that contributes current to the volume conductor, the starting point is (van Oosterom, 2014b):

$$\nabla \cdot \overrightarrow{J_x} = -i_v \tag{1-7}$$

Here, i_v describes the current provided by the source $\vec{x}$. For internal sources, the current in described by an impressed current density (van Oosterom, 2014b). Accordingly, as in equation (1-6):

$$\nabla \cdot \sigma \nabla \Phi_x = -i_v \tag{1-8}$$

This is the Poisson equation which holds for the active region in the volume conductor.

In realistic models, the region of active cardiac sources is embedded in a heterogeneous volume conductor consisting of various isotropic or anisotropic passive regions (Geselowitz, 1989). Accurate forward and inverse solutions therefore require an appropriate integration of both Poisson and Laplace equations into the mathematical model. As this implementation can be cumbersome, a mostly chosen starting point is to determine the infinite medium potential $\Phi_\infty(\overrightarrow{x'})$ at a point of interest. The infinite medium potential is calculated assuming an infinitely large, homogeneous volume conductor with the potential at infinity equal to zero (d' Alché *et al.*, 1974, Messinger-Rapport and Rudy, 1985). The calculation of this potential for various source models will be discussed next.

1.5.2 The Infinite Medium Potential

Assuming only one current density point source I at location $\vec{x}$ in the infinite volume conductor, the current density strength at a point $\overrightarrow{x'}$ inside the volume conductor can be calculated as (van Oosterom, 2014b):

$$J\left(\overrightarrow{x'}\right) = \frac{I}{4\pi R} \tag{1-9}$$

Here, R is the distance between the source point and observation point. From (1-3), it follows that

$$E\left(\overrightarrow{x'}\right) = \frac{I}{4\pi\sigma R} \tag{1-10}$$

The infinite medium potential can then be found according to (1-5). For this, an integration equation has to be solved:

$$\Phi_\infty(\overrightarrow{x'}) = \frac{-I}{4\pi\sigma}\int_\infty^{x'} \frac{1}{\rho^2}\, d\rho \tag{1-11}$$

In this form, ρ is a scalar integration variable along $\vec{R}$ (Plonsey and van Oosterom, 2012).

In case the current densities are spread throughout the volume conductor, I would be replaced by $i_v dv$ and the integration would be

$$\Phi_\infty(\overrightarrow{x'}) = \frac{1}{4\pi\sigma}\int_{vol} \frac{i_v(\vec{x})}{R(\overrightarrow{x'}, \vec{x})}\, dv(\vec{x}) \tag{1-12}$$

Here, $i_v(\vec{x})$ is the current source volume density at $\vec{x}$.

The infinite medium potential is of high importance in the calculation of potential fields in a finite, heterogeneous volume conductor, as will be described next (Geselowitz, 1989).

1.5.3 The Potential Field in Bounded Media

Focussing back on Figure 1-10, the volume conductor can be considered as a bounded medium in which there resides a small area containing all the primary sources of electricity. If the potential at $\overrightarrow{x'}$ due to sources at point $\vec{x}$ is to be known, one could apply Green's second theorem to the bounded medium (Barr *et al.*, 1966):

$$\int (\varphi\nabla^2\vartheta - \vartheta\nabla^2\varphi)dv = \int (\varphi\nabla\vartheta - \vartheta\nabla\varphi)\cdot d\vec{S} \tag{1-13}$$

The integral on the left is a volume integral, whereas the right integral is a surface integral. The integrand $d\vec{S}$ points along the outward normal of the surface.

This expression means in essence that the potential field within the volume conductor can be described by the variations in potential at the surface of homogeneous regions within the volume conductor. Both ϑ and φ are scalar functions of position. Applying the theorem to Figure 1-10, making φ equal to Φ and ϑ equal to $\frac{1}{R}$, and splitting both integrals, one gets (Barr *et al.*, 1966):

$$\int \Phi \nabla^2 \left(\frac{1}{R}\right) dv - \int \frac{1}{R} \nabla^2 \Phi dv = \int \Phi \nabla \left(\frac{1}{R}\right) \cdot d\vec{S} - \int \frac{1}{R} \nabla \Phi \cdot d\vec{S} \quad (1\text{-}14)$$

These integrals can be worked out (Plonsey and van Oosterom, 2012), resulting in the fundamental expression:

$$\Phi(\overrightarrow{x'}) = \Phi_\infty(\overrightarrow{x'}) - \frac{1}{4\pi} \int \Phi(\vec{x}) d\omega(\overrightarrow{x'}, \vec{x}) - \frac{1}{4\pi\sigma} \int \frac{J_n}{R} dS \quad (1\text{-}15)$$

In this equation, $d\omega(\overrightarrow{x'}, \vec{x})$ is the solid angle subtended by surface element $dS(\vec{x})$ at $\overrightarrow{x'}$, and J_n is the normal component of current density across surface S.

From equation (1-15), it can be seen that the potential at a point in a bounded medium is the sum of its infinite medium potential, a weighted integral of the potential at the boundary and a weighted potential of the current densities at the boundary on the surface(s) surrounding the (primary or secondary) sources. The first integral can be seen as a virtual double layer at S, the second as a virtual monolayer at S (Plonsey and van Oosterom, 2012).

The method for calculation of the infinite medium potential depends on the source distribution that is assumed to arise on the heart. Earliest ideas focussed on monopole or dipole sources (Frank, 1956, Gabor and Nelson, 1954, Geselowitz, 1964). Besides this, moving dipoles and multipole extensions received some attention (Arthur *et al.*, 1972, Geselowitz, 1965, Trost *et al.*, 1977). As this work focussed on monolayer and double layer source distributions, which are also necessary for solving the integrals of equation (1-15), only the calculations for these sources will be given.

1.5.4 Current Layer-Based Source Models

As from above, Green's theorem can be applied to describe the behaviour of a (current density) vector field inside a volume using only measurements at the surface of this volume. Here, the surfaces will be the boundary around the volume containing primary sources in the torso.

In case this surface is considered to be feeding a current density J_x into the torso volume conductor, the infinite medium potential at a point $\overrightarrow{x'}$ inside the

volume conductor can be found by integrating the contribution of elementary dipoles $j_x dS$ positioned along the surface. Therefore:

$$\Phi_\infty(\overrightarrow{x'}) = \frac{1}{4\pi\sigma}\int_S \frac{j_x}{R} dS \tag{1-16}$$

As seen from equations (1-15) and (1-16), the monopole layer has an important role in describing both primary and secondary (or virtual) sources. Monolayers were already suggested in the early work of Gelernter and Swihart (Gelernter and Swihart, 1964) as secondary sources. As virtual sources, monolayers are used to describe differences in conductivities at boundaries in the volume conductor. In case j_x is constant, analytical expressions are known for simple surfaces. Torso volume conductors are therefore discretised in many small simple surfaces to which the analytical expressions can then be applied (Geselowitz and Miller III, 1983).

A more frequently used two-dimensional source model is the dipole layer or double layer (De Munck, 1990). Each elementary unit of the double layer is considered to carry a dipole of strength $p(\vec{x})dS$ with $p(\vec{x})$ the local dipole moment. The infinite medium potential for any point inside the volume conductor can then be calculated as:

$$\Phi_\infty(\overrightarrow{x'}) = \frac{1}{4\pi\sigma}\int_S \frac{\vec{R}\cdot p(\vec{x})}{R^3} d\vec{S} \tag{1-17}$$

Besides this, it can be shown that (Plonsey and Barr, 2007):

$$\frac{\vec{R}\cdot d\vec{S}}{R^3} = \frac{dS_n}{R^2} = d\omega \tag{1-18}$$

Here, S_n is the normal component of the surface element dS and $d\omega$ is the solid angle subtended by this element at $\overrightarrow{x'}$. This leads to the following expression

$$\Phi_\infty(\overrightarrow{x'}) = \frac{1}{4\pi\sigma}\int_S p(\vec{x})d\omega(\vec{x}) \tag{1-19}$$

As with the monolayer, the double layer model is important both for describing primary and secondary sources. The transfer matrices described in the current

thesis will be based on double layer models, with the inclusion of monolayer-based sources, as represented by equations (1-17) and (1-19).

1.5.4.1 Applications of Current-layer Source Models

In case the double layer strength is constant over the surface, the double layer is called the uniform double layer (UDL). This source configuration was first introduced by Wilson (Wilson *et al.*, 1933) and is considered to be the classical source model of the depolarisation wave fronts progressing through the myocardium. This model showed a better correlation with the electrocardiogram than multipole expansions, and has served well to describe the ECG features qualitatively (Holland and Arnsdorf, 1977).

The major weakness of the UDL model is its inappropriateness for describing repolarisation (van Oosterom, 2012b), as well as possible issues when dealing with anisotropy (Clerc, 1976, Corbin II and Scher, 1977). To overcome these issues, an equivalent double layer (EDL) model was suggested. This model includes a Heaviside function which is zero for time samples earlier than the local depolarisation time in cardiac tissue and one otherwise. This allows the inclusion of temporal behaviour of the source model into the calculations. A first attempt to provide this type of models was suggested by Barr *et al.* (Barr *et al.*, 1970). A more complete implementation was obtained by Salu (Salu, 1978) and Cuppen (Cuppen and van Oosterom, 1984).

A priori knowledge about the propagation (or timing) of the depolarisation wave front is needed for the correct implementation of this model. Depending on the desired complexity, different propagation models can be used to obtain accurate estimates of the cardiac activation times. The simplest form of propagation can be calculated using the Shortest Path Algorithm, which only provides routes of excitation (van Dam and van Oosterom, 2003). Alternatively, eikonal (i.e. non-linear partial derivatives of wave propagation) approaches can be used which allow for the inclusion of anisotropy and a limited number of electrophysiological states (Dierckx *et al.*, 2011). Cellular automata also allow incorporation of electrophysiological states and anisotropy, as well as wave front curvature (Correa de Sa *et al.*, 2011) or action potential duration rate adaptations (Reumann *et al.*, 2008). The most complex models include ionic

current propagation between neighbouring cells (Henriquez, 1993). The bi-domain model takes into account current in intracellular and extracellular space as well as throughout cells via gap junctions (Geselowitz, 1989, Geselowitz, 1992). In case the extracellular and intracellular spaces are considered to have equal anisotropy ratios, the mono-domain model can be used (Dössel *et al.*, 2012).

As the EDL model focusses on determining the time of depolarisation and repolarisation, it is generally known as activation time imaging (Modre *et al.*, 2002, Tilg *et al.*, 2003). It has especially shown efficiency in ventricular repolarisation estimation (van Oosterom, 2001), but also can be used to estimate atrial activity (van Dam and van Oosterom, 2005).

1.5.5 Potential-Based Source Models

Besides current-based sources, voltage source models have been used frequently in inverse problems of electrocardiology. These models assume the cardiac source can be expressed as a surface of electrical potentials encompassing the epicardium (Colli-Franzone *et al.*, 1985b). This idea was first suggested by Zablow (Zablow, 1966) and later on mathematically described by Martin (Martin and Pilkington, 1972). Originally the cardiac source models were named pericardial potentials due to their similarity in encompassing the epicardium (Martin and Pilkington, 1972). Currently, they are mostly known as epicardial potential sources (Ramanathan *et al.*, 2004, Rudy and Burnes, 1999). This type of source is based on the theoretical one-to-one relationship between voltages on a surface bounding the volume conductor and a closed surface around the primary sources (Rudy and Messinger-Rapport, 1988). Furthermore, for correct application of this theory, one has to assume modelling and measurement errors can be neglected (Barr *et al.*, 1977). It allows for a ‘closer look’ at the cardiac sources without assuming any a priori knowledge about these sources except for their location. The major drawback of these models is the lack of a well-established relationship with cardiac electrophysiology (van Oosterom, 2012c). The advantage is that the potentials can be more easily verified by experimental measurements than current density equivalent sources (Barr *et al.*, 1977).

As the torso volume conductor has a complicated geometry, a direct analytical solution is impossible. After establishing the mathematical basics of the inverse problem and choosing the appropriate source for a particular application, a numerical solution has to be developed. This solution generally includes the discretisation of the torso into small, simple shapes for which analytical expressions are known, and then estimation of the sources by calculating the contribution of each small area to the source. For this project, the boundary element method (BEM) will be used for numerical analysis. This is further detailed in the next paragraph.

1.5.6 Boundary Element Methods in the Inverse Problem

The boundary element method has been used frequently for solving the inverse problem in electrocardiology (van der Graaf *et al.*, 2014). For the BEM, the volume conductor is considered having regional homogeneous conductivity, which allows for a direct application of Green's theorem. This is in contrast with techniques such as Finite Element Method and Finite Difference Method, which attempt to take into account effects within the entire volume (Colli-Franzone *et al.*, 1985a, Meng *et al.*, 2012). These methods have the advantage of being able to incorporate tissue anisotropy (Dössel *et al.*, 2012). However, as much debate is still going on about tissue anisotropy, it is difficult to apply volumetric methods directly (Gabriel *et al.*, 1996). Another disadvantage is the need to calculate potentials at a high number of locations, leading to high computational costs.

As a starting point for BEM application, the surfaces of regions with different conductivity are discretised in small triangles (Figure 1-11). From there, two methods can be followed. The oldest technique is to calculate potentials at the centroid of the triangles (Gelernter and Swihart, 1964, Lynn and Timlake, 1968b). More current calculations use the nodes at the vertices of the triangles, as was introduced by Barr (Barr *et al.*, 1966, Barr *et al.*, 1977, van Dam *et al.*, 2009).

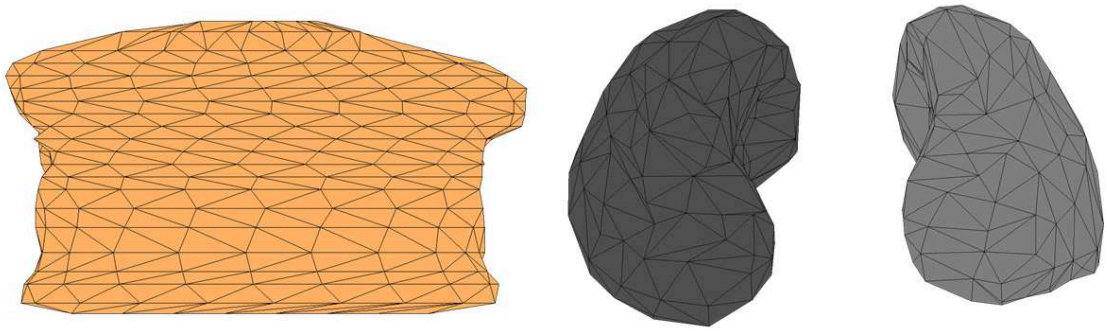

Figure 1-11: Example of torso (left) and lung discretisation (middle and right) into triangles.

For this latter approach, if there are N nodes ($i = 1, \dots, N$) on the triangulated surface of interest, the potentials at a given moment in time constitute the vector φ. The potential is calculated from the infinite medium potential, taking into account the effects of the virtual monolayer and double layer at the surface (equation (1-15)). The infinite medium potential depends on the chosen source configuration.

For simplicity, one could standardise equation (1-15) to:

$$\Phi(\overrightarrow{x'}) = \Phi_{\infty}(\overrightarrow{x'}) - \frac{1}{4\pi}\int \Phi(\vec{x})d\omega \tag{1-20}$$

stating that the potential at a point inside the bounded medium is the addition of the infinite potential at that point and a weighted sum of boundary potentials.

For numerical handling of this equation, the volume conductor is segmented into small triangles. For each node, the final potential is the summation of the contribution of all these triangles Q (j triangles, with $j = 1, \dots Q$):

$$\int_S \Phi(\vec{x})d\omega = \sum_{j=1}^{Q}\int_{\Delta_j} \Phi(\vec{x})\frac{\overrightarrow{R_i}\cdot d\overrightarrow{S_j}}{R_i^3} \tag{1-21}$$

The complication is in calculating the integral at the right hand side (van Oosterom, 2014b). This can be approximated by calculating the mean potential over the triangle (φ_j) and multiplying this by the solid angle of the triangle subtended at the node i ($\omega_{i,j}$).

$$\int_{\Delta_j} \Phi(\vec{x}) \frac{\overrightarrow{R_i} \cdot d\overrightarrow{S_j}}{R_i^3} \approx \overline{\varphi_j} \omega_{i,j} \tag{1-22}$$

Following the notations of equation (1-15), this can be rewritten as:

$$\varphi_i = \varphi_{i,\infty} - \frac{1}{4\pi} \sum_{n=1}^{N} \overline{\varphi_n} \omega_{i,n} \tag{1-23}$$

This equation can then be solved for all N nodes on the surface (van Oosterom, 2014b).

A major complication in this equation is the auto solid angle, i.e. the appropriate value for $\omega_{i,j}$ when the field point approaches node i from the interior (Meijs *et al.*, 1989). As the solid angle is continuous inside the volume and total solid angle subtended by the surface at any anterior point is -4π, (or 4π depending on the orientation) the auto solid angle $\omega_{i,i}$ can be found as:

$$\widehat{\omega_{i,i}} = -4\pi - \sum_{\substack{n=1 \\ n \neq i}}^{N} \widehat{\omega_{i,n}} \tag{1-24}$$

Here, $\widehat{\omega_{i,n}}$ is the solid angle subtended at all points $n \neq i$. The result is approximately -2π at places where the surface is planar. The auto solid angle is generally isolated from equation (1-23), leading to (Meijs et al., 1989, van Oosterom, 2014b):

$$\varphi_i = \varphi_{i,\infty} - \frac{1}{4\pi} \sum_{n=1}^{N} \overline{\varphi_n} \widehat{\omega_{i,n}} - \frac{-2\pi}{4\pi} \varphi_i \tag{1-25}$$

This isolation can then be brought to the left-hand side of the equation, ultimately leading to:

$$\varphi_i = 2\varphi_{i,\infty} - \frac{1}{2\pi} \sum_{n=1}^{N} \overline{\varphi_n} \widehat{\omega_{i,n}} \tag{1-26}$$

Both terms of the subtraction can then be rewritten, e.g. as:

$$a_{i,n} = -\frac{1}{2\pi}\widehat{\omega_{i,n}} \tag{1-27}$$

and:

$$\psi_i = 2\varphi_{i,\infty} \tag{1-28}$$

as vectors for the contribution of individual nodes. This can be written as a complete matrix of linear equations:

$$\Phi = \Psi + A\boldsymbol{\varphi} \tag{1-29}$$

A second complication is that the solution is only unique up to a constant, due to the nature of integral equations. One way of solving this issue is to set the mean potential over all nodes to zero, which can be mathematically incorporated as one additional linear equation, making the equation over-determined ($N + 1$ equations for N unknowns). This method is known as the deflation and was first implemented by Lynn and Timlake (Lynn and Timlake, 1968a).

Equation (1-29) can be used for solving forward problems in electrocardiology. The ways to establish ECG signals from known source models can be roughly separated into two alternatives. Indirect methods can be used in which an initial estimate of the solution for $\Phi = \Psi$ is refined until convergence. Nowadays, direct methods are preferred as computing memory has increased. Direct methods are also not dependent on the quality of an initial solution (Lawson and Hanson, 1974).

For direct analysis, equation (1-29) is rewritten as:

$$C\Phi = (I - B)\boldsymbol{\varphi} = \boldsymbol{\Psi} \tag{1-30}$$

Direct solutions are also advantageous when multiple source configurations Ψ are desired to be linked to the same volume conductor configuration. For this, the (inverse of) C can be calculated beforehand and stored, which has proven to be very useful in parameter estimation problems (Oostendorp and van Oosterom, 1989).

By inverting C, the effect of bounding the volume conductor can be expressed as a combination of linear systems W acting on the source Ψ, which depends linearly on the individual source components Ls. Therefore:

$$\Phi = W\Psi = WLs = Ts \quad (T \triangleq WL) \tag{1-31}$$

which is the final formulation for forward solutions (van Oosterom, 2012c).

1.5.7 Towards Inverse Solutions

In cardiac electrophysiology, there is high interest in estimating sources from surface signals. The problem with most inverse problems, as discussed before, is that they cannot be solved, as true bio-electrical sources cannot be estimated (Helmholtz, 1853). One has to be content with solving inverse problems towards source models which are postulated *a priori*. The parameters of this source model are then estimated from distant measurements.

One rare occasion in which sources can be found from surface signals is in case the source is considered a dipole inside a homogeneous volume conductor. This was first postulated by Gabor and Nelson (Gabor and Nelson, 1954) and has been used in deriving sources from vectorcardiography (van Oosterom *et al.*, 2007). However, in most literature the cardiac source is assumed to be more complicated. In case the volume conductor parameters are set up *a priori* and kept constant, only source parameters can be varied. From a forward solution, the parameters can be varied until the simulated signals resemble real, measured data. The inverse problem then becomes a parameter estimation problem, for which different solution methods have been developed (Beck and Arnold, 1977). In most cases, the best inverse solution is found by minimising the least square error (R) between observed and simulated data (Hansen, 2010)**:**

$$R = \min\|\Phi - Ts\|^2 \tag{1-32}$$

The appropriate method of determining the minimal least square error depends if one assumes that the source characteristics and measured potentials are linearly dependent or non-linearly dependent (van Oosterom, 2014b). Linear dependency is assumed if the source is modelled as a fixed point source or a

distributed voltage or current source. In this case, a linear least squares solution can be formulated, for which different solution methods are available (Lawson and Hanson, 1974). In many cases, an inversion of matrix $T'T$ is performed, where T' is the transpose of T:

$$S = (T'T)^{-1}T'\Phi \tag{1-33}$$

Alternatively, matrix T can be inverted by truncated singular value decomposition (TSVD) (Varah, 1979). Here, the matrix is first decomposed into two orthogonal matrices (U, V) and a diagonal matrix containing the singular values (Σ):

$$T = U\Sigma V^t \tag{1-34}$$

The singular values are ranked on the diagonal such that $\sigma_{1,1} > \sigma_{2,2} > \cdots > \sigma_{t,t} > 0$. A threshold for singular values can be applied to remove the smaller values which do not contain real signal information. Noise can therefore be efficiently reduced, which results in accurate source estimations (Damen and Van der Kam, 1982).

Non-linear least squares estimation have to be applied on the EDL and if the source is assumed to be a moving dipole. On frequently used non-linear least squares algorithm is the Marquardt algorithm (Marquardt, 1963). As mentioned previously, non-linear methodologies are dependent on good initial estimates of the parameters to be determined (van Oosterom, 2014b).

Even though the source model is postulated *a priori* and volume conductor matrix inversion techniques are available, inverse solutions are still prone to error. It is well known that any error in the description of T, i.e. the volume conduction effects, can lead to significant errors in parameter estimations. This has to be taken into account especially when a large number of parameters has to be estimated. These errors can be reduced by applying penalty functions to the inverse solution, which is more generally known as regularisation (van Oosterom and Huiskamp, 1992).

1.5.8 Regularisation of Inverse Problems

Different methodologies for inverse problem regularisation have been used in literature. These additional solution constraints can be of spatial, temporal or spatio-temporal nature. A general way of representing regularisation is as follows:

$$O = \|\Phi - Ts\|^2 + \lambda^2 \|D(s) - q\|^2 \quad (1\text{-}35)$$

Here, $D(s)$ and q are the additional regularisations and λ is the regularisation parameter to determine the effect of the regularisation function onto the final inverse solution. Higher values for λ will lead to smoother inverse solutions (Hansen, 2010).

A very frequently used type of regularisation is Tikhonov regularisation (Messinger-Rapport and Rudy, 1988). Three different smoothing functions have been used as a Tikhonov smoothing function: an identity matrix (zero-order Tikhonov), a surface gradient operator (first order) and a Laplacian (second order) operator (Cheng *et al.*, 2003a). The use of a specific order changes how the regularisation affects the inverse solution. A zero-order Tikhonov will affect the signal amplitude, whereas the first and second Tikhonov orders constrain the spatial domain of the solution (Oster and Rudy, 1992). Another frequently used regularisation technique is TSVD, as discussed previously.

The major limitation of the classical regularisation techniques is their lack of the incorporation of time-dependent effects on the data, leading to limited success in inverse solutions (Brooks and Ahmad, 1999, Greensite, 1994). One solution would be to improve the standard regularisation by additionally including temporal effects with the Twomey algorithm (Twomey, 1965). However, this technique requires an appropriate initial solution and the final solution will always be biased towards this solution (Cheng *et al.*, 2003a). Greensite suggested an alternative technique in which BSM data were considered as a family of solutions. From this family, the integral equations of the principal components were regularised, which resulted in more accurate solutions compared to regularising integral equations for each time point (Cheng *et al.*, 2003a, Greensite and Huiskamp, 1998). Other techniques for including

temporal behaviour have included Kalman filtering (Aydin and Dogrusoz, 2011) and inclusion of multiple constraints (Brooks and Ahmad, 1999).

In a commercially available system for the calculation of the inverse problem using a voltage source, the original solution is regularised by an iterative generalised minimum residual (GMRes) method (Saad and Schultz, 1986). The GMRes method does not need to have any a priori constraint implemented (Ramanathan *et al.*, 2003) and has shown improved solutions for ill-posed inverse problems in image restoration and electrocardiographic imaging (Calvetti *et al.*, 2000, Ramanathan *et al.*, 2003). To calculate the inverse solution with GMRes, a square matrix has to be used (Saad and Schultz, 1986). This is generally not the case for the transfer matrix as the electrocardiograms are in most cases estimated for more nodes on the pericardial surface then the number of electrocardiogram locations (Ramanathan *et al.*, 2003). To induce square matrices, GMRes is calculated on the transfer matrix multiplied by its transpose. GMRes suffers from the need of a good initial estimate, as do other iterative methods.

Lastly, in case of activation time imaging, an appropriate regularisation technique for the initial estimate is based on the critical point theorem (Huiskamp and Greensite, 1997). This technique was developed from the observations that a *hole* is formed in the cardiac wave front where it intersects the endocardial or epicardial wall. The position where the hole appears can be seen as a critical point and the time of occurrence as the critical time (Cheng *et al.*, 2003a). If all these critical times would be determined, the activation sequence of the heart would theoretically be a well-posed problem (Greensite, 1994). The detection of the critical time is difficult under noisy circumstances. This can be partly solved by the application of a second-order Tikhonov regularisation (Huiskamp and Van Oosterom, 1988).

A last consideration is determining the amount of regularisation that is needed to obtain a smooth solution which is still physiologically relevant. This depends on the accurate estimation of the regularisation parameter value λ.

1.5.9 Accurate Selection of the Regularisation Parameter

To determine a good balance between the solution and regularisation norms as in equation (1-35), different *a posteriori* methods can be used to choose an appropriate regularisation parameter value (Cheng *et al.*, 2003a). The most ideal, yet unfeasible solution would be the optimal criterion. It would allow calculating the optimal regularisation parameter for each time point for Tikhonov or TSVD regularisation. However, the epicardial potential distribution should be known beforehand (Cheng *et al.*, 2003a).

A more realistic and highly used method to estimate regularisation parameters is the Composite REsidual and Smoothing Operator (CRESO) suggested by Colli-Franzone and co-workers (Colli-Franzone *et al.*, 1985a). This method can only be used with continuous regularisation parameters and therefore not the TSVD. This algorithm attempts to find the optimal parameter by maximising the difference between the derivatives of the residual and smoothing term (Cheng *et al.*, 2003a).

Another frequently used alternative is the L-curve as suggested by Hansen (Hansen, 1994). Here, a log-log plot is generated of the residual norm against the solution norm. This function generally has an L-curved shape. The optimal parameter value is then the value at the corner of the L-curve (Cheng *et al.*, 2003a). However, some research groups have suggested that the optimal value would be found just outside the L-curve corner (Hoekema *et al.*, 1996).

Having discussed the theoretical background of the inverse problem, it can be appreciated that there are various ways to estimate cardiac sources. The next section will give an overview of practical attempts of electrocardiographic inverse problem calculations, with specific attention to atrial inverse solutions.

1.6 Inverse Problems for Estimating Cardiac Sources

In clinic, two types of inverse solutions are of interest: the inside-out (invasive) inverse solution and outside-in (non-invasive) solution. The inside-out solution allows for estimation of endocardial signals, whereas the outside-in solution estimates epicardial potentials.

1.6.1 The Inside-Out Solution

The inside-out inverse solution has seen most clinical applications. Here, a non-contact balloon catheter is placed inside one of the heart chambers (Figure 1-12 and Figure 1-13). The potentials measured at the balloon electrodes are then used to estimate the endocardial activity. The first inside-out inverse solution for ventricular endocardial analysis was performed by Taccardi *et al.* (Taccardi *et al.*, 1987). Currently, the commercial tool that is mostly used for these purposes is the EnSite system (St. Jude Medical, St Paul, Minnesota, USA), which consists of a 64-electrode non-contact multi-electrode array (MEA) that measures electrograms at a sampling frequency of 1200 Hz (EnSite 3000 system) or 2034.5 Hz (EnSite Velocity System) (Rajappan and Schilling, 2009). These electrograms are measured against a reference electrode located on the shaft of the MEA catheter, where it is in contact with the blood pool to provide a zero potential reference (Schilling *et al.*, 1998).

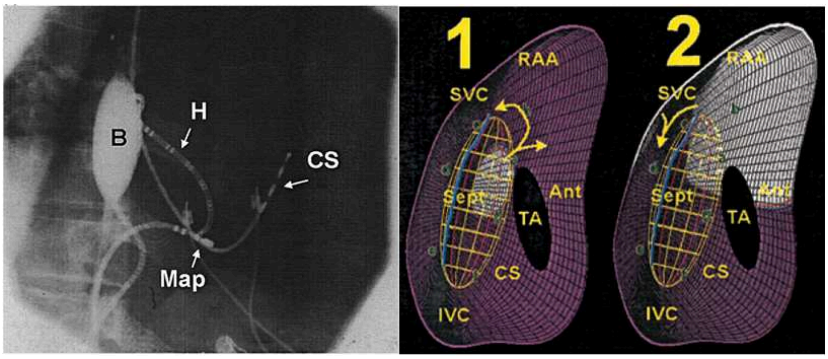

Figure 1-12: Left: Example of the EnSite balloon (B) positioned in the right atrium. H, halo catheter; CS, coronary sinus catheter; Map, mapping catheter. Middle and Right: Schematic representations of activation wave fronts from the EnSite system balloon (yellow mesh) in the right atrium. SVC; Superior vena cava; Sept, septum; IVC, inferior vena cava; RAA, right atrial appendage; Ant, Anterior side of the heart; TA, Tricuspid valve (Schilling *et al.*, 2000) (Reproduced with permission from the publisher).

The system is also provided with a locator signal situated between two balloon electrodes. This locator detects the position of various catheters, including a mapping catheter used to develop the 3D geometry of the cardiac chamber (Ben-Haim *et al.*, 1996). This is achieved by determining points on the endocardial wall with the mapping catheter and then applying a convex hull

algorithm for three-dimensional spatial interpolation. This algorithm calculates facets which link the individual points and combines these facets to a 3D geometry. Points which are interior to these facets are ignored (Kadish *et al.*, 1999).

The EnSite system solves the inverse solution for 64 points located on the endocardium. After this, the system uses a bi-cubic spline interpolation to interpolate potential values for up to 3360 locations on the geometry. This provides the clinicians with a detailed isopotential map along the entire endocardial wall of the cavity (Ben-Haim *et al.*, 1996). Major limitations of the system are the possible poor quality of the inverse solution for areas which are remote from the MEA centre. It has been reported that sites which are more than 4 cm away from the centre show this problem (Kadish *et al.*, 1999). Patient or balloon movement would also induce the need for recreating the cardiac geometry (Rajappan and Schilling, 2009). Other issues are the relative high cost of the system and the risks associated with invasive procedures.

Although the exact algorithm is patented, the EnSite inverse solution seems to show some similarities to the work of Khoury *et al* (Khoury *et al.*, 1995). Here a potential-based source model is set up for solving the inverse problem in a volume conductor discretised to be analysed with the BEM. In this work, the inverse solution was validated by analysing data from an isolated canine heart, with the balloon positioned inside the left ventricle. Data were also collected from electrodes located on intramural needles for comparison. From cardiac stimulation data, it could be observed that the inverse solution was able to estimate the location of the pacing site within a range of 10 mm of the actual site. The system was also able to distinguish multiple pacing sites with a distance between 10 and 20 mm from one another.

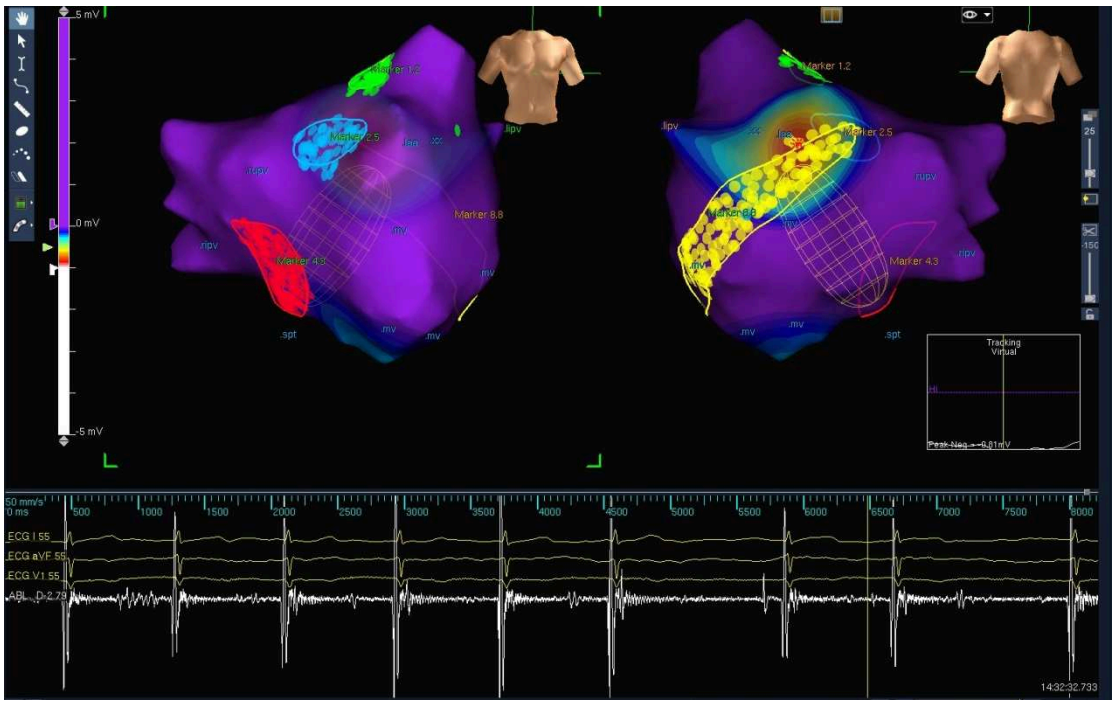

Figure 1-13: Example of a left atrial isopotential map from the EnSite Velocity system. The atrium is shown from a posterior (left image) and anterior (right) view. Coloured dots indicated ablation locations. The signals below show three ECG signals as well as a bipolar signal from the ablation catheter.

The commercially implemented system has been validated both for its accuracy in determining the geometry and the endocardial electrograms. In one study, Kadish *et al.* successfully validated the geometrical accuracy of EnSite system (Kadish *et al.*, 1999). Using 12 dogs, the accuracy was determined by analysing the ability of the EnSite system to determine the distance between electrodes from a multipolar catheter positioned at different places in the right atrium. The distance between these electrodes was determined a priori to be 5.5 mm. This study also showed a correlation coefficient of 0.81±0.18 (mean±SD) between estimated virtual electrograms from the EnSite system and electrograms measured by contact mapping in sinus rhythm, atrial flutter and atrial fibrillation. An early study on reconstruction of ventricular electrograms in humans showed similar correlations (0.87±0.12) (Schilling *et al.*, 1998).

The possibility of estimating full endocardial maps has extended various research regarding AF mechanisms into an additional dimension. One way of looking at AF which is of particular interest in this thesis is the dominant (or

fundamental) frequency (DF) determination of AF. In earlier data obtained from contact (point-by-point) mapping, Sanders *et al.* concluded that DF was spatiotemporally stable over 5 second windows (Sanders *et al.*, 2005). Dominant frequencies were defined as the highest amplitude frequency between 3 and 15 Hz with a regularity index >0.2. They were also able to determine the stability of DF over 30 seconds divided into 6 successive windows of 5 seconds, as well as after repeated mapping within 15 minute intervals. Their site of highest DF (HDF) showed also relative stability, providing ground to consider HDF sites as AF ablation targets. Here, HDF sites were considered sites where the DF gradient with neighbouring points was higher than 20% (Sanders *et al.*, 2005). This suggested an important role of HDF sites in representing drivers or maintainers of HDF. The work by Atienza *et al.* showed that addition of HDF ablation to standard pulmonary vein isolation improved AF ablation outcome by extending the time for which patients did not suffer AF relapse (Atienza *et al.*, 2009).

Later studies, performed with balloon catheters providing a global view of DF at each time point, rejected this HDF stability however. The work of Jarman *et al.* (Jarman *et al.*, 2012) especially showed no discrete HDF areas in subjects with persistent AF after analysing 6.8 second long windows of 256 QRS subtracted virtual electrograms (range 3-20 Hz). This work showed however 3 distinct patterns of HDF behaviour. In 33% of the cases, HDF would appear, disappear and reappear at a specific location. In another 31% of cases, the HDF site would migrate to a neighbouring area between successive windows. In 36% of cases, a random behaviour of HDF sites was found. This led to the conclusion that HDF sites would not be the sites of AF sources in patients, and an ablation strategy solely based on HDF site ablation would be ineffective, as was suggested by Verma *et al.* (Verma *et al.*, 2011). DF calculated from virtual electrograms as measured using the inverse solution was found to be significantly similar to the DF as determined from contact mapping signals (Jarman *et al.*, 2012).

Another advantage of non-contact, global AF mapping is the ability to determine bi-atrial electrical coupling from measurement close to the atrial activation source. Lemery and co-workers were the first to study the

electrophysiological aspects of atrial activation in sinus rhythm and after stimulation in persistent and paroxysmal AF (Lemery *et al.*, 2004). They used two EnSite 3000 systems to simultaneously analyse both atria. After geometrical mapping, atria were aligned along the septum (fossa ovalis) and activation maps were acquired. They showed that, in sinus rhythm, septal activation occurs earlier at the RA side than the LA side. LA activation occurred over the Bachman bundle, which was activated earlier than the RA septum. Under inferior RA pacing, septal activation was delayed significantly. With LA appendage pacing, atrial activation was perceived as opposite to normal sinus activation. The study's main contributions were however the clarification of the partial isolation of both atria at the septal region, as well as the unique feature of the Bachman bundle in fast activation of the LA.

In canine and simulation studies, it has also been shown that non-contact mapping can give information regarding atrial repolarisation waves (Sabouri *et al.*, 2014). However, limitations were found in case of inappropriate geometrical modelling, enhancing the hypothesis that the need of accurate geometric models for inverse solutions is necessary (Klepfer *et al.*, 1997). This is a general limitation for the non-contact mapping systems, as mapping of e.g. the appendage regions is cumbersome (Sabouri *et al.*, 2014). One also has to take into account possible effects of sedation, as well as the limited resolution of the inverse solution from 64 measurement locations. Besides this, mapping over long time intervals is not practical (Cuculich *et al.*, 2010). Other major limitations are the continued need for invasive procedures carrying risks for the patient and high costs. Outside-in inverse solutions attempt to overcome these drawbacks.

1.6.2 The Outside-In Inverse Solution

The use of BSM for non-invasive estimation of epicardial (or pericardial) potential has recently received more clinical interest. This is mainly due to the commercialisation of the electrocardiographic imaging (ECGI, Figure 1-14) system, developed mainly by Rudy and co-workers (Rudy and Burnes, 1999). This system applies an inverse solution based on voltage sources, with a volume conductor discretised according to the BEM (van der Graaf *et al.*,

2014). The current system (ecVUE, CardioInsight, Cleveland, OH, USA) estimates cardiac potentials from 252 body surface electrodes (Haïssaguerre *et al.*, 2013). The torso geometry is obtained from computed tomography (CT) images and consists generally of a heart and torso surface segmentation, although more inhomogeneities can be included (Rudy and Burnes, 1999). The software consists of 4 modules (Ramanathan *et al.*, 2004). First, the acquired body surface potentials (BSPs) are filtered and baseline corrected (preprocessing module). Bad contact electrodes are discarded and signals interpolated. The geometry module allows a segmentation of the heart and torso from CT as well as a triangular meshing of these segmented areas. The transfer matrix for projecting BSP signals to the cardiac surface using this segmentation is calculated by the numerical module. It also calculates and regularises the inverse solution using Tikhonov and GMRes algorithms. The postprocessing module allows visualisation of the results from the inverse solution as epicardial maps, reconstructed electrograms, activation maps with the local activation time taken as the maximum negative derivative of the QRS complex, and recovery maps with recovery time taken to be the maximum positive derivative of the T wave.

After validation of this system on torso tank models (Oster *et al.*, 1997), where the possibility to determine epicardial and intramural activation patterns was demonstrated (Oster *et al.*, 1998, Oster *et al.*, 1997), the first test in volunteers showed accurate estimation of pacing spikes as well as activation pattern similar to those found in animal studies and isolated heart analysis (Ramanathan *et al.*, 2004, Rudy and Burnes, 1999). A first major analysis of AF using ECGI was presented by Cuculich and co-workers (Cuculich *et al.*, 2010). This study comprised both patients in paroxysmal AF (pAF, 11 of 36 patients), persAF (19) and permanent (6) AF. In a testing phase, the estimation of atrial pacing spike locations from BSMs was verified, showing an accuracy of 6.3±3.9 mm (mean±SD). During the study phase, the AF behaviour was analysed based on the number of wavelets, rotors and focal activation sites found for each subject. An index of complexity was determined as the sum of these three AF activation patterns. Results showed that patients with pAF had significantly fewer wavelets and ectopic foci than patients with persAF and permanent AF.

From this, it could be derived that the complexity index in pAF was significantly lower than in other patients. No significant difference was observed between persAF and permanent AF.

It was also observed that the location of “AF sources” in pAF was mostly around areas which are routinely ablated. This phenomenon was not as clearly observed in persAF and permanent AF subjects, indicating a possible reason of reduced success rates of AF ablation in these patents. The work also showed the limitations of ECGI, as it is not possible to determine endocardial activity (which could vary from epicardial activity) nor to differentiate between micro-reentry and focal activity. As the atrial signal is weak on the body surface, the distinction between true signal and artefact is also difficult to establish.

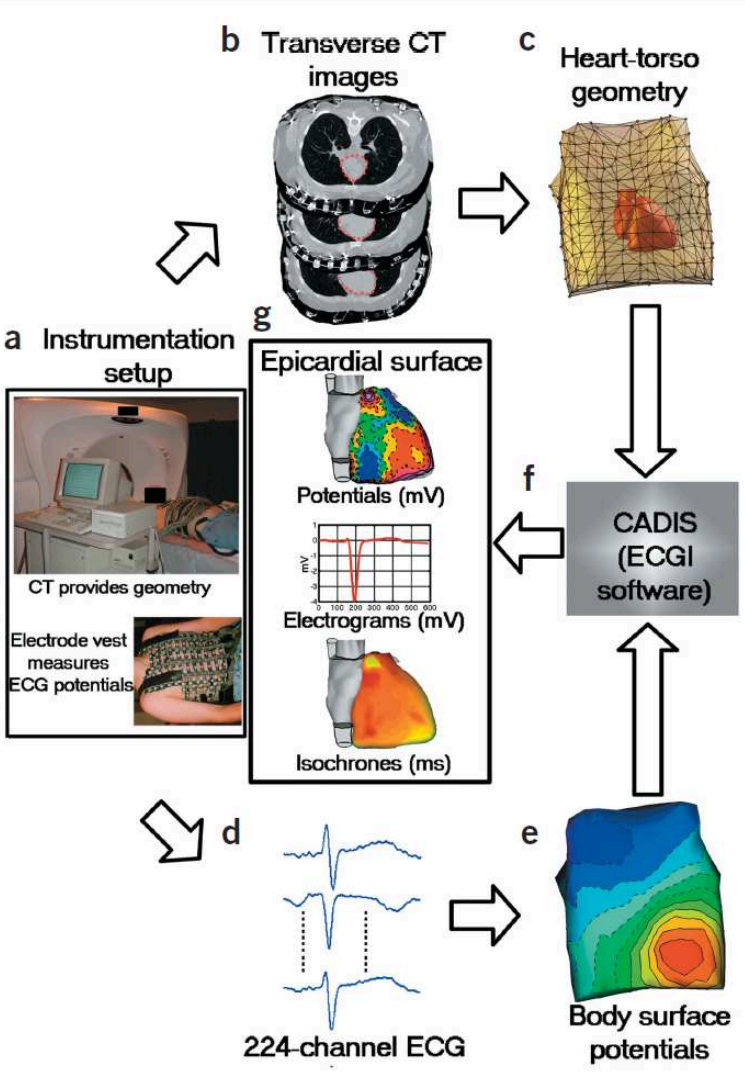

Figure 1-14: Overview of the ECGI system (Ramanathan *et al.*, 2004) (Reproduced with permission from the publisher).

Reports have, however, shown that it is feasible to perform AF ablation based on the ECGI source estimation with successful results (Haïssaguerre *et al.*, 2013). Here, further processing was performed on the estimated electrograms to allow for phase analysis. This technique has received increased attention lately as it might provide means to determine rotational behaviour related to AF sources (Narayan *et al.*, 2012). Mathematical models confirmed the possibility of estimating rotors from BSPs (Rodrigo *et al.*, 2013). The same group has also suggested a good correlation between the location of dominant frequencies (DF) on the torso and the endocardium in cases of high DF gradients (Guillem *et al.*, 2013). In this study, however, DF sites were determined with point-by-point catheter mapping, which does not allow analysing global DF behaviour.

No inverse solution was attempted either to confirm a direct relate high DF torso sites with high DF endocardial sites.

There are some major limitations and concerns related to the voltage-source based inverse solution, as already pointed out in section 1.5.5. Other source models have been used to determine atrial activation time with satisfactory results (Modre *et al.*, 2003), but were only applied in a limited number of subjects.

Both inside-out and outside-in inverse solutions thus still have some major limitations. Commercially available tools are based only on voltage-source models. Direct comparisons between different solutions have been exploited in simulation studies (Cheng *et al.*, 2003a), but not in clinical environments. Besides this, AF studies analysing inside-out solution with outside-in solutions simultaneously are, as per the author's knowledge, unavailable. These would be of major clinical importance, not only to further understand AF electrophysiology but also to validate the possibility of analysing diagnostic tools such as phase and DF from body surface maps.

This project can be considered a start-up of a multi-year project for further validation of inverse solutions, both in the inside-out as the outside-in inverse solution, by applying different (current density based) source models. In a first instance, a current-based inverse solution (van Oosterom, 2012a) was set up in a spherical model for estimating a dipole location. After verification, this inverse solution was used for patient-specific analysis of AF behaviour in persAF patients. An inside-out inverse solution was calculated and compared to data obtained from EnSite Velocity or EnSite 3000 virtual electrograms. For the outside-in inverse solution, patient-specific torso geometries were developed an the inverse solution was calculated with the current-based model (van Oosterom and Oostendorp, 2004, van Oosterom *et al.*, 2011). The reconstruction of DF maps from the current-based outside-in solution was compared to the inside-out solutions. A first attempt was also given towards reducing the number of BSM leads necessary for outside-in inverse solutions.

1.7 Project Aim and Objectives

The aim of this project was to establish means of comparing data obtained from outside-in inverse solutions with inside-out inverse solutions for the further understanding of atrial fibrillation. To reach this aim, several objectives had to be met:

1. Determine how atrial signals are represented on the body surface maps by comparing body surface signals with endocardial electrograms. The endocardial electrograms were estimated with a commercial inverse solution (EnSite 3000 or Velocity system). A comparison of the body surface signals and virtual electrograms was made based on time and frequency aspects of the signal.
2. Provide an understanding of the inside-out and outside-in inverse solution using model simulations.
3. Determine an outside-in inverse solution method based on a current-based cardiac source model.
4. Re-establish the inside-out inverse solution provided by the EnSite systems (voltage-based model) according with a current-based source model to allow for direct comparison between the inside-out and outside-in inverse solution.
5. Improve clinical applicability of outside-in inverse problem analysis by studying the effect of including tissue inhomogeneity and BSM lead reduction on the inverse solution and BSM signal quality.

1.8 Thesis Overview

Prior to starting the inverse problem analysis, further understanding of the immediate relation between the signal collected from the torso and from the atria was desired. This relationship was investigated in chapter 2. The analysis focussed heavily on the behaviour of the atrial dominant frequency. A comparison between BSMs and data from virtual electrograms simultaneously collected for both right and left atrium was made.

An introduction to reduced-lead BSM and the analysis of spatial information using Lomb spectral analysis will be given in chapter 3. Although this spectral

analysis does not allow by itself to develop reduced-lead body surface mapping systems, it can provide further understanding of the areas on the body surface from which most information of the cardiac signal can be obtained, and how this could influence the use of reduced-lead BSMs in providing inverse solutions.

Chapter 4 will discuss the application of the monolayer/double layer current-source used in this project for analysing the inverse problem. An intuition in the advantages and drawbacks of this method will be presented based on spherical models of the torso, a non-contact balloon catheter and the atrial surface.

Chapter 5 will provide an implementation of this cardiac source description into patient-specific models of inside-out inverse solutions. For this, balloon data collected from the EnSite Velocity system were used to recreate an inverse solution to the left atrial endocardium. Results were then compared using time and frequency analysis with the inverse solution calculated directly by the EnSite system (voltage-based source model).

An outside-in solution based on the monolayer/double layer current source model will be discussed in Chapter 6. Here, body surface maps generated at the same time as the balloon data from Chapter 5 were used to estimate epicardial signals on the atria. A heterogeneous torso model including the torso, lungs and atrial muscular wall was generated from magnetic resonance images for the volume conductor model. Results of the inverse solution were compared with data generated in Chapters 2 and 5 to determine if the relationship between body surface data and endocardial data could be regenerated.

The last chapter will provide a general summary. As this project was the first project at the University of Leicester Bio-Engineering Research Group to focus on the inverse problem, many aspects of this complex analysis could not be fully investigated. Future steps will therefore be discussed which could provide a better understanding and implementation of the inverse problem in clinical situations.

2 Comparisons of AF Behaviour on BSM and Non-Contact Mapping Data: a Frequency–Based Perspective

2.1 Introduction

The correct identification of atrial fibrillation (AF) sources from non-invasively obtained signals would provide a desirable alternative for current invasive studies. Current investigations are ongoing in which the EcVue system is used for AF driver identification according to a voltage-source based inverse solution (Cuculich *et al.*, 2010, Haïssaguerre *et al.*, 2013). These studies have focussed analyses on small-sized groups, and are affected by several limitations of the inverse problem procedure (Haïssaguerre *et al.*, 2013, van Oosterom, 2012c). Interesting results could however possibly be obtained from an immediate (direct) comparison of body surface signals with signals obtained invasively.

2.1.1 Investigations of Atrial Signal Representations on BSMs

Dedicated research in body surface mapping for atrial activity has only started about 20 year ago. Early research was based on isopotential and isochronal mapping. Lately, BSM analysis of atrial activity has focussed on the implementation of metrics used for invasive analysis of AF.

A first elaborate analysis of atrial activation on body surface maps was presented by SippensGroenewegen and colleagues (SippensGroenewegen *et al.*, 1998). This study investigated the possibility of distinguishing ectopic pacing stimulations from 9 different areas in the right atrium on body surface maps. Nine volunteers with structurally normal atria undergoing RA pace mapping prior to intervention of their arrhythmia were involved in this study. Body surface maps were taken from 62 positions during bipolar RA pacing. The location of the pacing catheter was verified by fluoroscopy. Signals were manually assessed and removed in case of extensive baseline wandering. After baseline correction, P wave onsets and offsets were identified and a P wave integral map was calculated. P wave integral maps were defined as standard if at least 3 consecutive P-waves generated similar patterns. A total of 86 P-wave integral maps were then visually inspected and grouped according

to the location of extreme voltage values and zero-line. Intragroup pattern uniformity was analysed using a jackknife procedure. Intergroup variability was assessed from correlation coefficients obtained after comparing mean P-wave integral maps from all groups. A total of 17 groups of P-wave integral maps could be identified, indicating that BSM has sufficient resolution to reveal distinct patterns with different stimulus locations. A specific average P-wave integral map could not be identified for individual pacing locations, however. This could be due to variations in the location of the pacing catheter as well as in volume conductor effects (Klepfer *et al.*, 1997).

In a following study, SippensGroenewegen *et al.* attempted to determine body surface patterns in the analysis of clockwise and counter-clockwise typical, as well as atypical atrial flutter (AFlut) (SippensGroenewegen *et al.*, 2000). Clockwise AFlut was defined as a right atrial arrhythmia with clockwise wave front propagation around the tricuspid annulus. Counter-clockwise AFlut would propagate in counter-clockwise direction. Atypical AFlut was defined as any propagation which did not have specific wave front propagations. A similar BSM setup was used as in the previous study. The patient database consisted of 20 volunteers with atrial flutter undergoing first-time catheter ablation. AFlut was stimulated with pacing in case no AFlut was presented during the BSM recordings. After processing BSM maps, flutter wave onsets and offsets were indicated manually and integral maps were calculated. These maps were then allocated to one type of AFlut. The intra-group uniformity and intergroup variability were assessed as in the previous study. Results were sufficiently significant to conclude that clockwise and counter-clockwise AFlut could be distinguished on body surface integral maps of fibrillation waves (f waves).

Analysis of persistent AF (persAF) with body surface mapping was first performed by Guillem and co-workers (Guillem *et al.*, 2009). Here, 14 patients with persAF had body surface mapping performed for at least 2 minutes. The BSM electrode configuration consisted of 40 electrodes placed anteriorly and 16 placed posteriorly. The WCT was used as reference. No QRST cancellation was applied in this study. Instead, after a first baseline subtraction, RR intervals longer than 950 ms were selected and their respective TQ (atrial activation) segments were defined as starting 300 ms after the first QRS complex and

ending 150 ms before the successive QRS complex. After another baseline subtraction, the atrial signals were low-pass filtered at 20 Hz. These signals were then plotted as isopotential and isochronal maps on a 2D grid representative of the torso model. From the isochronal maps, 3 AF patterns were defined as: 1) propagation of a single wave front, 2) propagation of a single wave front that becomes blocked or splits over time and 3) unclear or multiple wave fronts. Results showed that all three patterns could be visualised on the body surface maps using isochronal mapping. Reproducibility was proven by analysing the isochronal maps of different time intervals per patient separately.

2.1.2 Frequency Analysis of AF on BSM and EGM data

In a following study, Guillem and co-workers compared the frequency behaviour of AF on body surface maps with data obtained from contact mapping catheters (Guillem *et al.*, 2013). Frequency analysis can summarise AF behaviour over short time segments and provide further understanding about AF drivers. In this work, 14 patients with drug-refractory AF underwent an electrophysiological study under general anaesthesia. AF was induced in case subjects were in sinus rhythm at the start of the procedure. After obtaining 3D models of both atria, the intracardiac site with highest dominant frequency was identified using a commercial point-by-point contact mapping system. A navigation catheter was placed at this site for collection of EGM signals for 5 minutes after adenosine injection. Simultaneously, EGMs were obtained with a lasso catheter at the contralateral pulmonary vein junction, and ECGs were obtained with a 67-lead BSM system. A 4 second segment including the highest RR interval was used for DF analysis on 2 second windows with 50% overlap. In most patients, this 4 second window was free of ventricular activity due to the adenosine influence. For cases that were exposed to ventricular activity, a QRST cancellation was performed based on principal component analysis (PCA) (Castells *et al.*, 2005). Both EGMs and ECGs underwent baseline correction and filtering procedures to solely show physiological aspects of the atrial signal. Body surface ECGs were then plotted on a 2D rectangle with nodes representative of the 3D electrode positions. Interpolation was performed to complete the 2D BSM. DF maps were created for

comparison to the intracardiac DF values. Other 2D maps identifying the differences in body surface DF with the DF of most closely positioned EGM were also created. Results showed that body surface DF correlated mostly with the activation rate of nearest atrial tissue. No direct comparison could be made as it was only possible to measure one point on the endocardium at a time. Besides this, the effect of adenosine could hamper direct comparisons (Guillem *et al.*, 2013). These limitations could partly be solved by using non-contact mapping balloon catheter capturing virtual electrograms from up to 2048 points (Salinet Jr *et al.*, 2010) and application of QRST subtraction techniques to avoid the need of adenosine.

A last interesting point of the previous work was the variation in DF value between body surface maps and electrograms. This observation was not fully explained, but could be due to (non-)linear volume conductor effects. Especially, it has been shown that the torso volume conductor has a spatio-temporal low-pass filtering effect on the electrophysiological signals in simulation studies (Nowak *et al.*, 2008, Stinstra and Peters, 1998). The effect of the volume conductor on the DF difference between body surface and endocardial data could therefore be further investigated.

2.1.3 Research Aims and Objectives

This research aims to provide additional information of AF behaviour on BSM signals by analysing the behaviour of the dominant frequency and comparing this to the DF behaviour on the atrial endocardium (Salinet *et al.*, 2014). This work especially investigated the spatiotemporal behaviour of highest DF (HDF) areas. The analysis was performed with at 128-lead BSM system recording data simultaneously with bi-atrial non-contact mapping as performed by Lemery and colleagues (Lemery *et al.*, 2004). It was expected that this comparison would give an indication of the effect of the torso volume conductor on the propagation of cardiac signals to the torso, which is essential for appropriately correlating these signals. As the main objective was to obtain further insight, the current work only focusses on a small group of subjects. Further research on a larger population of patients is ongoing in our research group.

2.2 Methodology

The methodology described below includes a complete overview of the BSM setup, invasive non-contact mapping setup and volunteer database. The segmentation of atrial signals from BSMs and (virtual) EGMs will be discussed. After this, the methodology focused on the analysis of AF dominant frequencies.

2.2.1 Database

A cohort of 9 volunteers undergoing first time ablation for drug-refractory persAF was involved in this study. Prior to ablation, all anti-arrhythmic drugs were stopped for at least 5 half-lives, except for amiodarone. Ethical approval was obtained from the local ethics committee. Volunteers were informed regarding the aspects of the study in writing and written informed consent was obtained. Clinically relevant information of the cohort is given in Table 2-1.

Table 2-1: Overview of the database.

Number of volunteers (male)	9 (9)
Age (mean ± SD)	58 ± 13
Height in cm (mean ± SD)	178.07 ± 5.57
Weight in kg (mean ± SD)	99.83 ± 20.12
Smokers	
Current (%)	1 (11%)
Never (%)	2 (22%)
Ex (%)	6 (67%)
Subjects on Warfarin (%)	9 (100%)
Ablation Procedure	
Radiation Time in min (mean ± SD)	77.72 ± 22.01
Radiation Dose in µGy (mean ± SD)	7451.7 ± 3484.4

2.2.2 BSM Setup

The system used for body surface mapping is a commercially available 128-electrode system (ActiveTwo, BioSemi, Amsterdam, Netherlands). These 128 channels are setup in 4 panels (A, B, C, D) of 4 strips containing 8 electrodes (labelled 1-32). The electrodes consist of an Ag/AgCl pellet and are considered active in that a signal pre-amplifier is located near the electrode.

Additionally, 3 individual electrodes are positioned at the left and right shoulder and left hip, providing the WCT reference. Lastly, a Common Mode Sense (CMS) active electrode and Driven Right Leg (DRL) passive electrode form a feedback loop to ensure subject safety, as well as to set up a zero-reference feedback loop. This zero-reference loop ensures that the Common Mode voltage is as close as possible to the reference voltage of an ActiveTwo Analogue to Digital (AD)-box (BioSemi, Amsterdam, Netherlands). The AD box is connected to a USB receiver via a fibre optic cable. The USB receiver can be connected to any laptop/desktop which runs the ActiveTwo LabView-based software package. Raw signals can be saved as '.bdf' files.

As the project focussed stronger on the analysis of atrial signals, a horizontal BSM setup was developed to keep the electrode density high around the atrial regions (Figure 2-1). Here, 8 strips were positioned both on the front and the back. This setup also included the electrode position suggested by Ihara and colleagues as the optimal positions for atrial vectorcardiography (Ihara *et al.*, 2007).

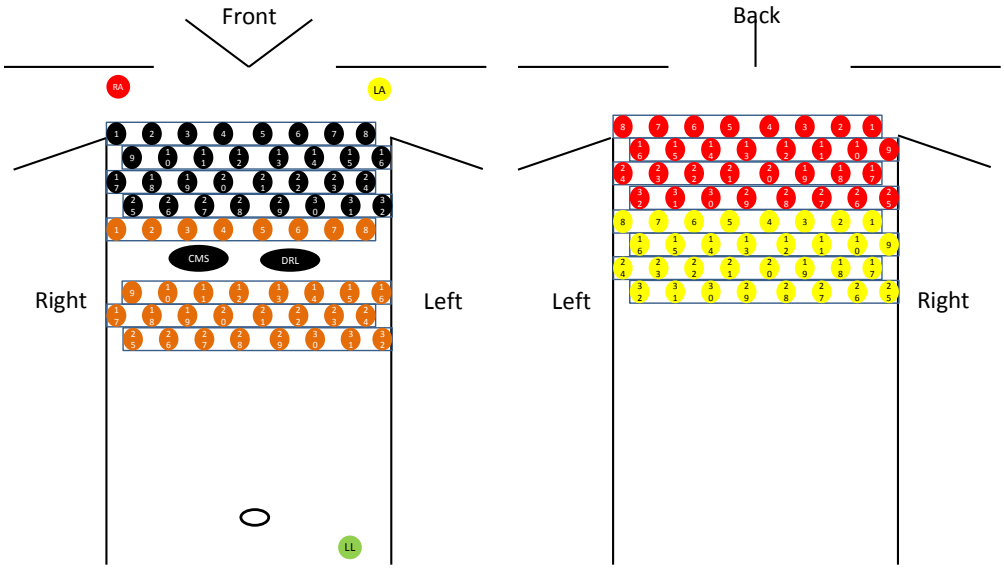

Figure 2-1: Horizontal BSM setup for the analysis of atrial activity. Strips are indicated by blue rectangles, electrodes by filled circles. The WCT electrodes on the left arm, left leg and right arm are indicated by individual yellow, green and red filled circles, respectively. The elliptical electrodes represent the CMS and DRL electrodes.

During the measurement, BSMs were recorded at a rate of 2048 Hz for all subjects. Subjects were in supine position during the recordings. A band-pass filter between 0.16 Hz and 50 Hz was active to allow appropriate visualisation of the signal and determine signal quality. Signals with an absolute offset higher than 40 mV were documented as bad-contact electrodes.

2.2.3 Invasive Non-Contact Mapping Setup

For bi-atrial recordings, a 9 French (F) EnSite Array balloon catheter was guided trans-septally into the right atrium from the left femoral vein. Once deployed, the catheter was anchored in the superior vena cava (SVC). In a similar fashion, another Array balloon was deployed in the left atrium via the right femoral vein. This balloon catheter was anchored in the left upper pulmonary vein (LUPV). Further to this, a 7F coronary sinus (CS) catheter (Inquiry, St Jude Medical) was deployed from the left femoral vein to support pacing protocols (Figure 2-2).

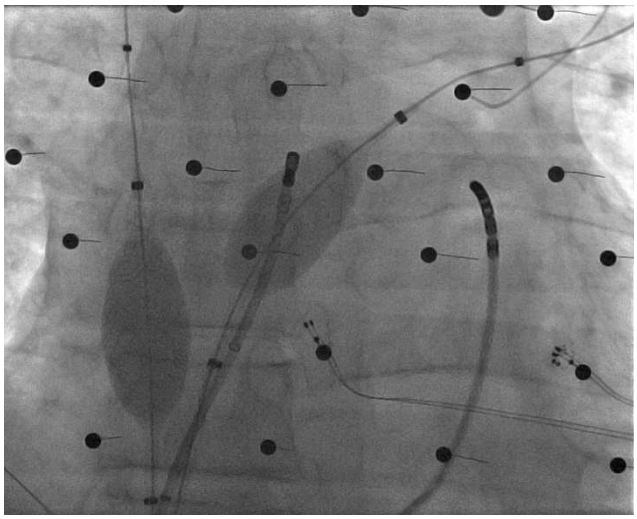

Figure 2-2: Fluoroscopic image of both balloon Array systems (dark grey ellipses) positioned in the left (right on image) and right (left on image) atrium: The black dots indicate the BSM electrodes.

A 7F ablation catheter (St Jude Medical) was deployed from the right femoral vein. This catheter was used for creating both right atrial and left atrial 3D geometries, as well as to identify atrial regions of interest. These areas included the superior and inferior vena cava, the four pulmonary veins, the mitral and tricuspid valve, the atrial septum and the coronary sinus ostium.

Identification of these areas was necessary for orientation purposes. During the ablation procedure, the catheter was also used to indicate areas were ablation was performed. Besides this, the ablation catheter has 4 electrodes with which unipolar contact electrograms could be obtained.

Lastly, Unipolar and Bipolar limb ECG data (lead I, II, III, aVL, aVR and aVF) were collected with the EnSite system for QRST segmentation. These electrodes were linked to both EnSite systems using an ECG splitter.

For data collection, the right Array catheter was linked to an EnSite 3000 system (sampling rate at 1200Hz). The left atrial Array was linked to an EnSite Velocity system (sampling rate at 2034.5Hz).

2.2.4 Ablation Procedure

Ablation was performed under general anaesthesia, with heparin boluses applied throughout the procedure to keep the activated clotting time between 300 and 350 seconds. The ablation would first target the centre of gravity (CoG) of areas in the left atrium where high dominant frequencies occurred. Dominant frequency (DF) areas were defined as regions which had the highest strength in the power spectrum in an AF physiological range of 4-10 Hz within a 4 second window. The HDF was defined as the maximal DF value found in the window over all electrodes. An overlap of 50% between successive windows was considered (Salinet *et al.*, 2014).

The determination of HDF areas was performed on 30 second data collected from the 2048 left atrial virtual electrograms. Data were analysed offline prior to the ablation procedure in Matlab (version R2013b, The Mathworks Inc. Natick, Massachusetts, USA) using an in-house developed graphical user interface. The HDF determination will be further detailed in sections 1.1.1 and 2.2.7. The HDF area was plotted on a 2D mesh representative for the left atrium. The CoG was defined as the central point of a bounding rectangle delineated by the extreme points of the HDF area (Figure 2-3).

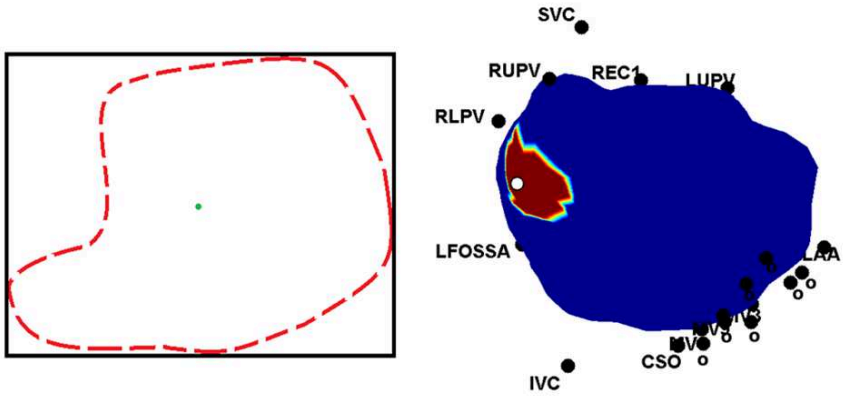

Figure 2-3: Left: An illustration of the centre of gravity (CoG, green dot) detection for a high dominant frequency (HDF) area (red dashed line). A bounding rectangle (black) is drawn around the extremities of the HDF area and the centre point (green dot) of this rectangle is considered the CoG. Right: Image of a CoG (white dot) location on a heart mesh exported from an EnSite Velocity system. The red area indicates the cloud of highest DF sites.

After this, both EnSite systems were removed and standard left atrial pulmonary vein isolation (PVI) was performed. If the subject was still in AF after PVI, internal cardioversion was performed with flecainide or internal direct current cardioversion.

2.2.5 BSM and NCM Data Collection and Extraction

Data were collected for 3-8 minutes before and after DF ablation. All volunteers were in AF during the measurements before ablation. Subject 4 converted after DF ablation to atrial flutter. All other volunteers were still in AF for the post-ablation measurements. Data were simultaneously obtained for both atria and body surface mapping electrodes. Besides this, the EnSite ECGs were collected during these measurements. Lastly, the ablation catheter was anchored at a position in the left atrium for collection of unipolar contact electrograms. To allow appropriate alignment of the different signals, a series of pacing spikes was invoked at the beginning of each segment.

Data were extracted from the different systems after ablation as follows. Raw BSM data were collected from the BSM system as '.bdf' files. For both EnSite systems, raw and filtered ECG and virtual EGM data were extracted. For filtered data, ECGs were band-pass filtered between 0.5 and 50 Hz, whereas

EGM data were filtered between 1 and 100 Hz with EnSite's built-in filter functions. No spatial filtering was applied to the EGM data. Furthermore, to develop 3D geometries of the atria, geometrical labels and ablation lesions were collected together with a 3D grid of the atria representing the position of the 2048 virtual electrograms.

Raw and filtered Array data as well as unipolar contact EGMs could only be obtained for the left atrium. Both were filtered between 1 and 100 Hz using the EnSite filter functions. An overview of the data collected for each measurement can be found in Table 2-2.

Table 2-2: Overview of the data collected per measurement for all volunteers.

Data Location	Data collection system (sampling rate)	Signals (number of points or electrodes)	Geometry
Left Atrium	EnSite Velocity (2034.5 Hz)	Virtual non-contact EGM (2048)	Virtual grid of 2048 locations
		Unipolar contact EGM (4)	Geometry labels for orientation
		Balloon data (64)	Label for catheter tip location
		ECG (6)	Balloon grid of 64 electrodes
			Lesions of ablation sites
Right Atrium	EnSite 3000 (1200 Hz)	Virtual non-contact EGM (2048)	Virtual grid of 2048 locations
		ECG (6)	Geometry labels for orientation
Torso	ActiveTwo (2048 Hz)	Body surface ECG (128 electrodes + 3 WCT channels)	

2.2.6 Atrial Signal Segmentation

To allow accurate AF analysis, the effect of ventricular activity was removed from the body surface signals, electrocardiograms, contact and non-contact mapping data as described below. To obtain optimal segmentation, raw BSM data had to be pre-processed and filtered. Only filtered virtual EGM data were used for atrial signal analysis. Besides this, data taken from the various systems had to be aligned.

2.2.6.1 BSM Pre-Processing

BSM data were read into Matlab using EEGLAB (Delorme and Makeig, 2004). After this, signals were zero-referenced by subtracting the mean value of all electrodes for each individual sample. To avoid baseline wandering and noise interference, signals were band-pass filtered between 2 Hz and 50 Hz using a moving average filter prior to further processing (Ihara *et al.*, 2007). Filter effectiveness was analysed using a FFT algorithm. If the power at 50 Hz was higher than 0.5% of the total area under the curve for the power spectrum of that particular electrode, signals from this electrode were discarded (Guillem *et al.*, 2013). Afterwards, other electrodes were visually inspected and removed when necessary (e.g. in case of excessive baseline wandering or signs of bad contact with the torso).

Interpolation of noisy electrodes was performed by plotting signals on an unstructured triangular mesh representing a general torso model (375 nodes, 131 nodes positioned to coincide with electrode positions). Interpolation was performed using the Surface Laplacian algorithm developed by Oostendorp and co-workers (Oostendorp *et al.*, 1989). Signals were then visualised as 3D isopotential maps.

2.2.6.2 Alignment of NCM, ECG and BSM Data

For aligning the EnSite ECGs, virtual EGMs, unipolar contact EGMs and balloon data with the body surface maps, a pacing stimulus series was setup from the CS catheter at the beginning of each dataset. It was decided to align every dataset after the fifth QRST complex following the last pacing spike. This

would avoid possible issues with QRST morphology immediately after the pacing stimulus, which could hamper QRST cancellation.

Prior to alignment, however, data had to be resampled, as the sampling rate for the RA (1200 Hz), LA (2034.5 Hz) and BSM (2048 Hz) were different. It was opted to down-sample each dataset to 512 Hz, as this would still allow correct analysis within the physiological range of AF while reducing memory allocation and processing time. Resampled data were stored prior to further processing.

For alignment, the reference point was manually indicated on Lead II of the resampled left atrial ECG data. The reference point of the other resampled datasets was estimated taking into account the variation of sample numbers between each dataset and the left atrial ECG data. These reference points were then manually checked and adapted were needed. After complete alignment of the starting points, the end points were equalised by removing samples at the end of data signals longer than the left atrial ECG data. These aligned datasets were then stored for further processing.

2.2.6.3 Extraction of Atrial Activity on BSMs and NCM Data

To allow analysis of long segments of atrial activity, a QRST cancellation technique was used that was developed previously in our research lab (Madeiro *et al.*, 2012, Salinet Jr *et al.*, 2013, Schlindwein *et al.*, 2006). For each dataset collected, the QRST subtraction was performed simultaneously on resampled LA balloon data (64 signals), LA and RA virtual EGMs (twice 2048 signals), contact catheter data (4 signals) and BSM signals (131), giving a total of 4295 signals undergoing segmentation. Segmentation of the QRST complex was performed by first detecting QRS peaks. From there, QRS onset and T end were indicated in a similar fashion as used in average beat subtraction algorithms (Slocum *et al.*, 1985) (Figure 2-4).

A pre-processing step was set up for detection of QRS peaks. Lead II ECG signals were first band-pass filtered between 14 and 24 Hz using a symmetrical finite impulse response (FIR) second order Butterworth filter to impose flat group delay. These filter settings have been considered optimal for emphasising QRS peaks during arrhythmia (Schlindwein *et al.*, 2006). After

this, a low-pass second order Butterworth filter with cut-off at 10 Hz was applied for QRS peak detection. An adaptive voltage threshold was used for detection of QRS-peaks. A refractory period of 210 ms was set after finding a QRS peak before continuing the search for the successive peak.

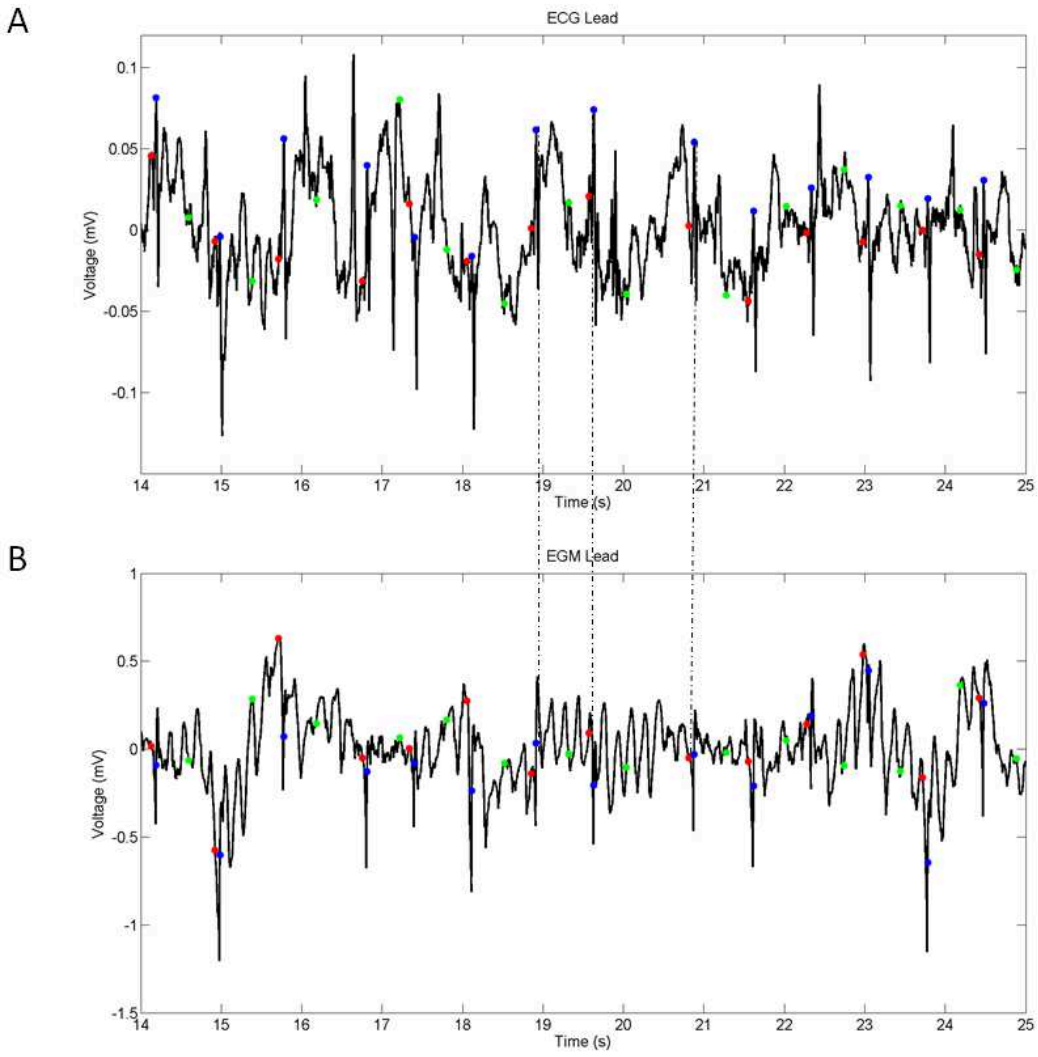

Figure 2-4: Example of QRS-T segmentation. A: QRS onset, QRS peak and T end are detected on a standard ECG lead. B: The time points of QRS onsets, peaks and T ends are projected to the EGM and BSM signals under investigation. The dotted lines show the relation between 3 QRS peaks on the ECG and an EGM from the left atrium.

For detection of the QRS onset and T end, all RR intervals were calculated. The QRS onset threshold was set at 12% of the minimum RR interval length, whereas the T end threshold was set at 78% of this length. These time

thresholds were then used to provide an interval from the QRS onset to T end for each beat (Salinet Jr *et al.*, 2013).

For QRST cancellation, a signal-by-signal adaptive QRST template was calculated (Figure 2-5). A first template was determined for all beats falling within the first 7 seconds after the start of the signal. The median duration τ_{med} of each beat n within this window was calculated. After this, a $Mx\tau_{med}$ $(M = 1, \dots, n)$ zero-matrix was set up. Each beat within the segment was then positioned in this matrix such that the fiducial points aligned. Alignment was performed via cross-correlation. In case the beat was longer than the median time, the extreme samples were neglected. In case the beat was shorter, the extreme values of the matrix in that row remained zero. The median of each column of the matrix was then calculated to obtain a $1x\tau_{med}$ matrix corresponding to the QRST template. This template was subtracted from the first beat after aligning the template fiducial points with the specified beat using cross-correlation. After this, the 7 second segment was moved by 1 QRST complex (sliding window) and the process repeated, thereby updating the template QRST interval for segmentation (Salinet Jr *et al.*, 2013).

2.2.7 Dominant Frequency Analysis

After QRST cancellation, attention was given to the frequency analysis of the atrial signals. Atrial frequency spectra were generated for each signal over 4 seconds windows (Hamming window (Harris, 1978), 50% overlap). To smooth the spectra, a zero padding factor of 5 was implemented. Frequency spectra were generated for all signals simultaneously. The number of windows analysed per subject is given in Table 2-3.

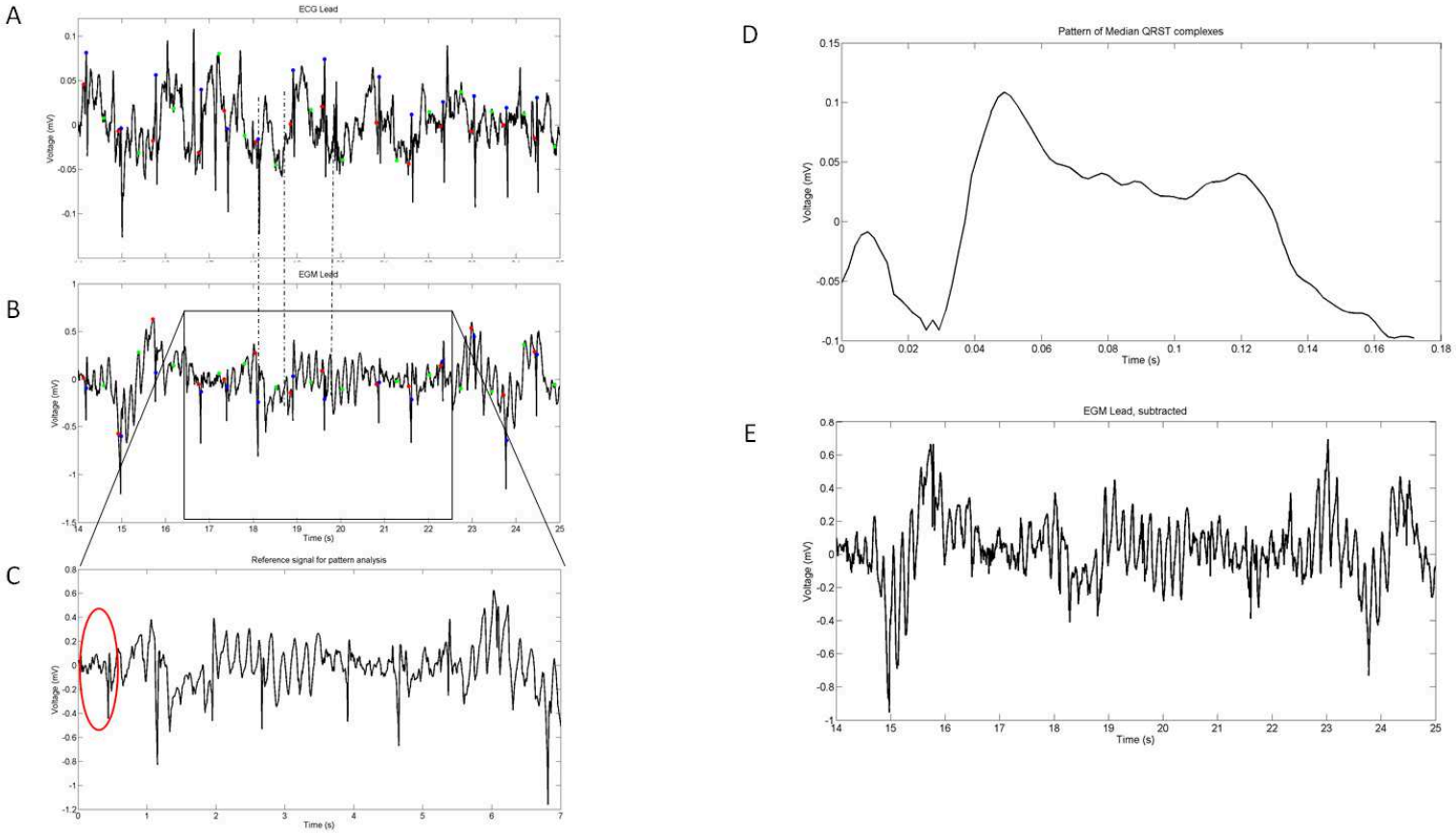

Figure 2-5: Overview of QRST subtraction. After identifying the fiducial points on the ECG (A) and EGM or BSM (B), a 7 second window is selected from the EGM/BSM signal under investigation (C). QRST segments are concatenated for this window and a median QRST is calculated (D). This pattern is used for subtracting the first QRST interval in the 7 second window (circle in C). This process is reiterated until all QRST intervals have undergone subtraction (E).

For each individual signal and each window, the DF was determined as the frequency with highest power between 4 and 10 Hz. This range was defined as it considers the expected physiologically range of AF (240-600 beats per minute) (Nattel, 2002). Further analysis was performed on the spatial and temporal behaviour of the DF. This analysis only focussed on providing additional information to interpret BSMs. Current projects in the research group will provide deeper analysis of time and frequency behaviour of AF signals based on non-contact invasive mapping and body surface mapping.

DF analysis focussed on the data obtained before DF ablation and after DF ablation. Post-ablation data from subject 4 were omitted from the analysis as this subject was no longer in AF.

Table 2-3: Overview of number of 4 s windows analysed per volunteer. N/A: not applicable; DF: Dominant Frequency.

Subject	*Number of 4 second windows analysed*		
	Before DF Ablation	**After DF Ablation**	**TOTAL**
1	142	155	297
2	155	164	319
3	148	157	305
4	131	*N/A*	131
5	158	154	312
6	144	148	292
7	146	148	294
8	148	134	282
9	150	152	302
TOTAL	1322	1212	2534

In first instance, the overall distribution of dominant frequencies before and after ablation was analysed on both the EGM and BSM data for individual volunteers. The median and 25^{th}–75^{th} percentile interquartile range (IQR), maximum and minimum DF value were chosen to describe the distribution as it was shown by a Shapiro-Wilk test that the DF distribution did not follow a Gaussian behaviour.

An interesting way to analyse possible volume conductor effects is to focus on the DF analysis between atrial and body surface data. In first instance, a better description for the temporal aspects of the dominant frequency at a specific location was desired.

2.2.7.1 Temporal DF Distribution

It has been shown previously that sites of high dominant frequency are spatiotemporally unstable (Salinet *et al.*, 2014). One reason for this could be the variation of the DF at individual measurement locations. To assess this temporal variation, the distribution of DF values over all windows was analysed on the EGM and BSM signals.

For all data, DF temporal behaviour for each electrode was assessed from its DF median (DFM) and interquartile range (DFIQR). A comparison between the temporal DF distribution before and after DF ablation was made.

2.2.7.2 Highest Dominant Frequency Site

More specific spatiotemporal information regarding the DF behaviour was sought by analysing the behaviour of the highest dominant frequency (HDF). For each time window assessed, the highest dominant frequency was determined for the body surface signals. This was achieved by first finding the maximum DF in a specific window over all nodes. All nodes which had a dominant frequency within a 0.5 Hz interval around this maximum value where then considered hosting the highest dominant frequency. After this, the HDF analysis was performed simultaneously on the RA and LA virtual electrograms. The HDF value was compared between the endocardium and the body surface.

Besides this, to understand the behaviour of the HDF value on the BSMs in comparison to the cardiac data, HDF values on the EGMs for all volunteers were sorted and binned in groups of 0.5 Hz. The difference between the body surface HDF and EGM HDF was then evaluated for each sample per bin. A correlation between this difference and the corresponding EGM HDF value was sought. A schematic overview of the procedure is given in Figure 2-6.

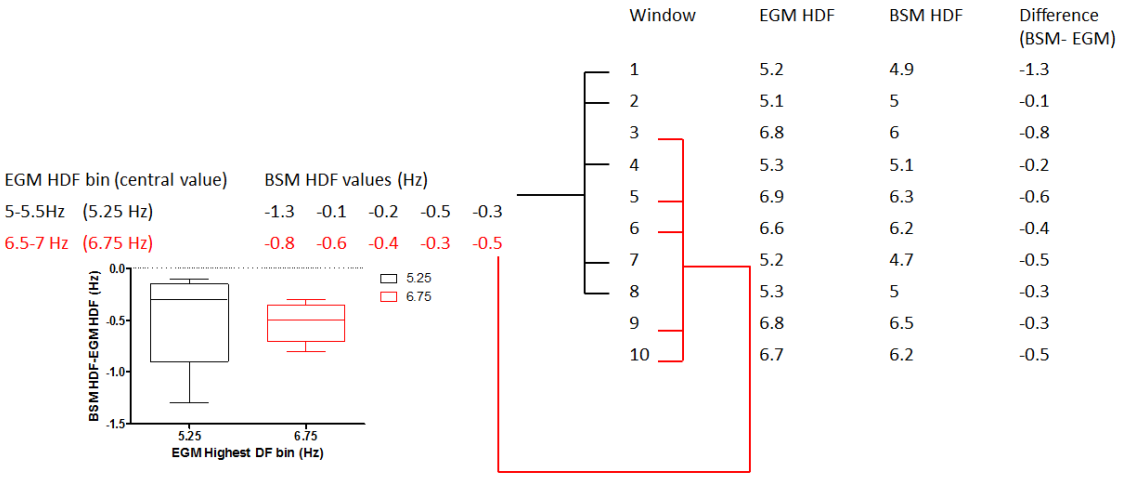

Figure 2-6: Example of Highest DF (HDF) binning. For each window, the HDF for the electrograms is found. EGM HDF values within a 0.5Hz range are combined into a single HDF bin. The difference in HDF values between the BSM and EGM data for all windows within one HDF bin are then collected and their distribution is represented as a boxplot. The median values of these boxplots were used to determine a correlation between EGM HDFs and BSM HDFs.

2.2.7.3 Statistical Analysis

Statistical analysis was performed with Prism 5.03 (GraphPad Software, Inc , La Jolla, California, USA). As DF data were not normally distributed and no consistent behaviour was found between the datasets before and after ablation (Figure 2-7), non-parametric tests were used for analysis. All statistical comparisons were considered significant at an alpha level of 0.05.

The overall distribution of DF values on the body surface before and after ablation per subject was analysed using a Wilcoxon matched-pairs signed-rank test. This test was also performed on the EGM DF distributions before and after ablation. Besides this, a Mann-Whitney test was used to determine if there

existed a significant variation in DF distribution on BSMs and EGMs within a patient. The test was performed on data before and after ablation, individually.

For temporal DF analysis, the DF distribution was compared before and after DF ablation for each subject. A Wilcoxon matched-pairs signed-rank test was used to determine the DF distribution variation for each individual node on the endocardium as well as for each BSM electrode. The null hypothesis was that for each electrode or node, the DF distribution would be the same before and after DF ablation.

Furthermore, HDF values were compared between EGM and BSM data for each subject before and after DF ablation. A Wilcoxon matched-pairs signed-rank test was used to compare the HDF distribution over EGM and BSM data. After this, for each subject, the number of windows in which the HDF value of the EGMs was higher than on the BSM was counted. The behaviour of these proportions was compared between subjects using a 2-by-9 contingency table before ablation and a 2-by-8 table for data after ablation. To test if similar proportionality existed between volunteers, a chi-squared test was performed over all volunteers. This test determines if a proportion p_0 out of N proportions is significantly different from an expected proportion p_e (Levine *et al.*, 2005):

$$\chi^2 = \sum_{i=1}^{n} \frac{(p_{o,n} - p_{e,n})^2}{p_{e,n}} \qquad n = 1,2, \dots N \tag{2-1}$$

The expected proportion is that proportion which would occur if the proportion of all individual cases were identical, and can be calculated as:

$$p_e = \sum_{j=1}^{n} \frac{X_n}{T_n} \qquad n = 1,2, \dots N \tag{2-2}$$

For this case, X_n is the number of windows where the HDF value is higher on the EGMs than on the BSM for subject n, and T_n is the total number of windows considered for all subjects. The null hypothesis stating that all subjects have a similar HDF behaviour would be rejected if the result for equation (2-1) is higher than the χ^2 statistic at an alpha level of 0.05 for 8 (before ablation) or 7 (after ablation) degrees of freedom.

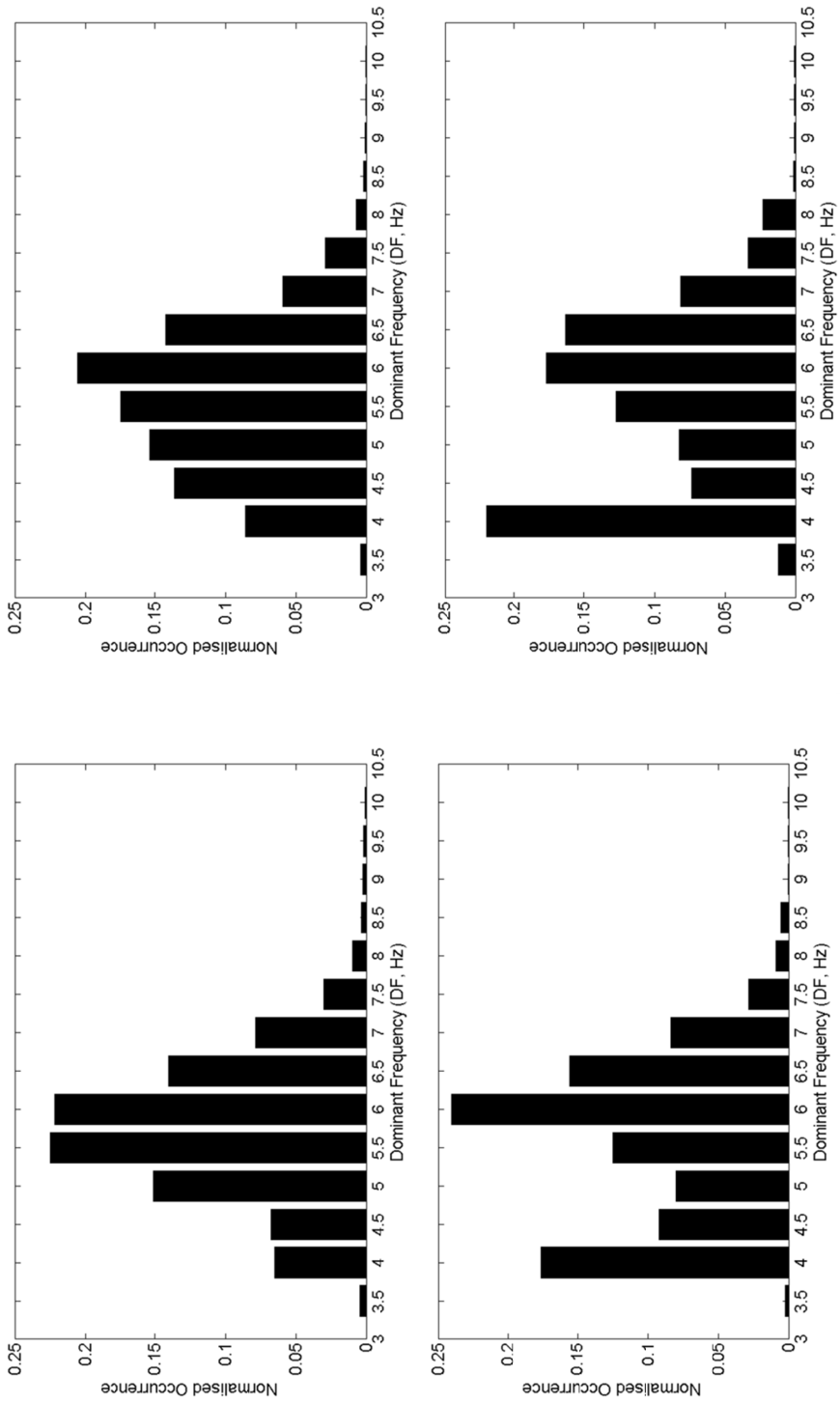

Figure 2-7: Normalised DF distribution for all volunteers on the body surface before (left upper) and after (left lower) ablation. The figures on the right show the DF distribution for EGM data before (right upper) and after (right lower) ablation. Normalisation was performed by dividing the number of samples within a 0.5 Hz bin by the total number of samples.

In case variation could be observed in the proportions, it was analysed if volunteers could be grouped based on these BSM against EGM HDF proportions. For this, a Marascuilo procedure was set up (Marascuilo, 1966). Here, a χ^2 statistic critical value is determined and compared to the absolute difference in proportion between individual subjects. The critical value is calculated as follows (Levine *et al.*, 2005):

$$c = \sqrt{\chi_\alpha^2} \times \sqrt{\frac{p_{o,n}(1-p_{o,n})}{T_n} \times \frac{p_{o,m}(1-p_{o,m})}{T_m}} \tag{2-3}$$

$$n = 1,2,\dots,N; m = 1,2,\dots,N; n \neq m$$

Here, χ_α^2 is the chi-squared statistical value at $\alpha = 0.05$ for the appropriate degree of freedom. The result is compared with:

$$A = \left|p_{o,n} - p_{o,m}\right| \tag{2-4}$$

If the absolute difference A is smaller than the critical value, the proportions for subject n and m are considered identical at the alpha level of 0.05. The chi-square results were compared to the results from a Fisher Exact test, which performs better if numbers of occurrence smaller than 5 exist (Rosner, 2010). Due to the complexity of implementing a 2-by-n Fisher Exact test, multiple comparisons of proportions were performed using SPSS 23 (IBM, New York, US). Significance levels were corrected with a Bonferroni approach, leaving a significance level of 0.0013 for data before and 0.0018 for data after ablation, respectively. The null hypothesis was that the proportion of 2 patients was identical.

2.3 Results

All volunteers could be converted to sinus rhythm after ablation and cardioversion. Three subjects (4, 5 and 7) converted without the need for cardioversion.

2.3.1 Isopotential Maps

Body surface potential maps are shown for a particular QRS peak and an f-wave peak in Figure 2-8. The BSM during QRS was characterised by an

activation wave front moving from the central chest area (ECG lead V2 region) towards the left (V6 region). This behaviour was not affected by atrial fibrillation. No distinct pattern could be observed describing atrial fibrillation activity on isopotential maps.

Further analysis was performed on AF signals only. In order to investigate the atrial signals further and over longer periods, a previously developed and implemented QRST segmentation and subtraction technique was used.

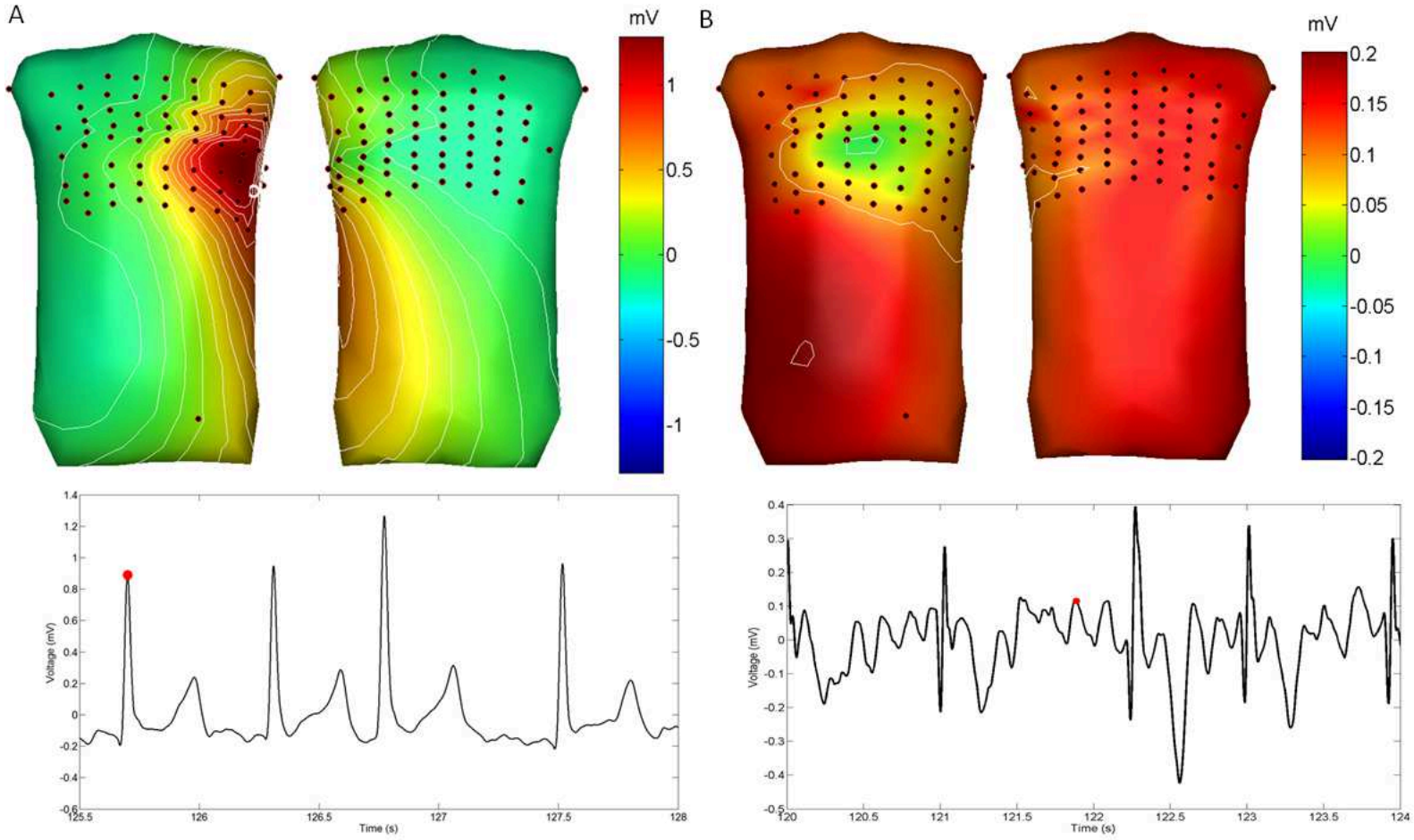

Figure 2-8: Body surface isopotential maps obtained during QRS peak (A) and a particular AF fibrillation wave peak (B). A standard torso model was used for representation. Red dots on the ECG indicate the time of the isopotential map.

2.3.2 Dominant Frequency (DF) Distribution

An example of a DF map for both atria and body surface is presented in Figure 2-9. For both atria, a virtual electrogram was available for each node. The position of the electrodes on the body surface is indicated by black dots. Further interpolation towards other locations was performed using the surface Laplacian.

An overall distribution of dominant frequency values on the BSM and EGM data is presented in Figure 2-10. For most subjects, a significant change in BSM DF and EGM DF distribution occurred after ablation. No specific direction in this change could be observed, however.

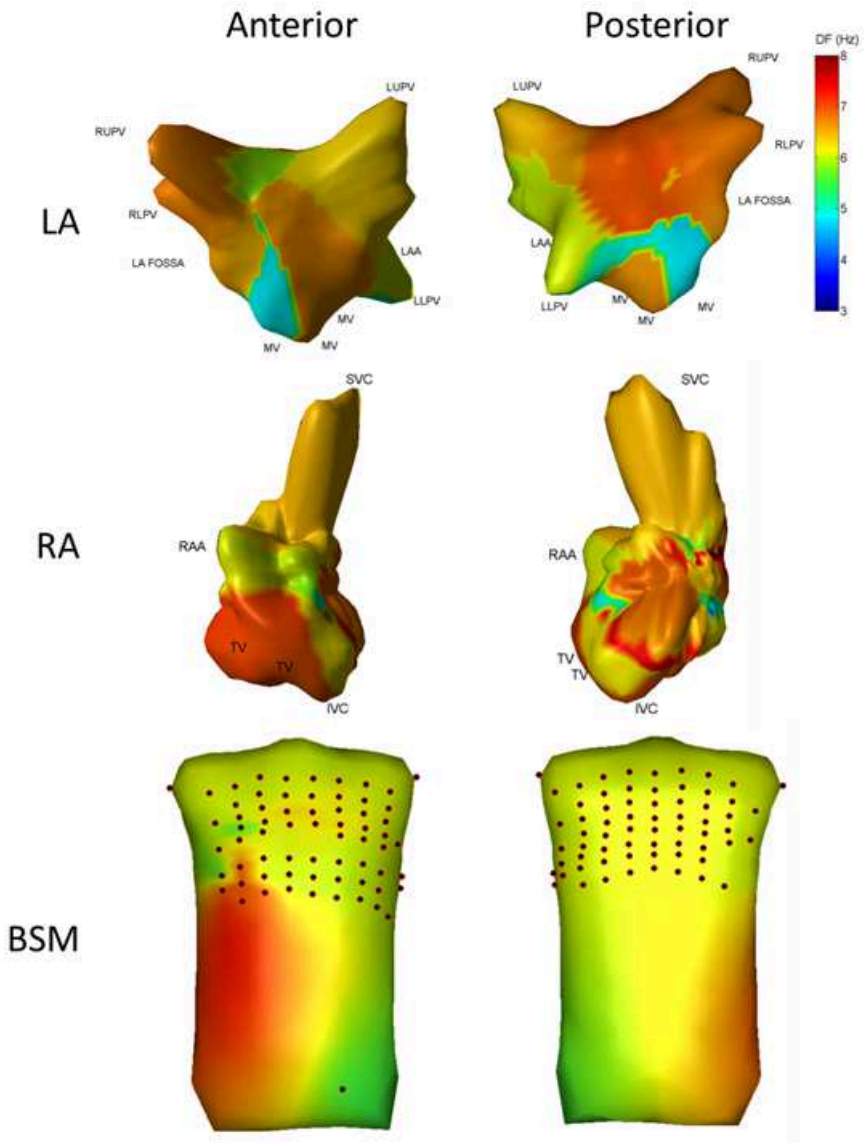

Figure 2-9: Example of the DF distribution during one 4s window. Black dots indicate the position of electrodes on the body surface map. LA: Left Atrium; RA: Right Atrium; BSM: Body Surface Map. RUPV: Right Upper Pulmonary Vein; LUPV: Left Upper Pulmonary Vein; RLPV: Right Lower Pulmonary Vein; LLPV: Left Lower Pulmonary Vein; LAA: Left Atrial Appendage; RAA: Right Atrial Appendage; TV: Triscuspid Valve; MV: Mitral Valve; IVC; Inferior Vena Cava; SVC: Superior Vena Cava.

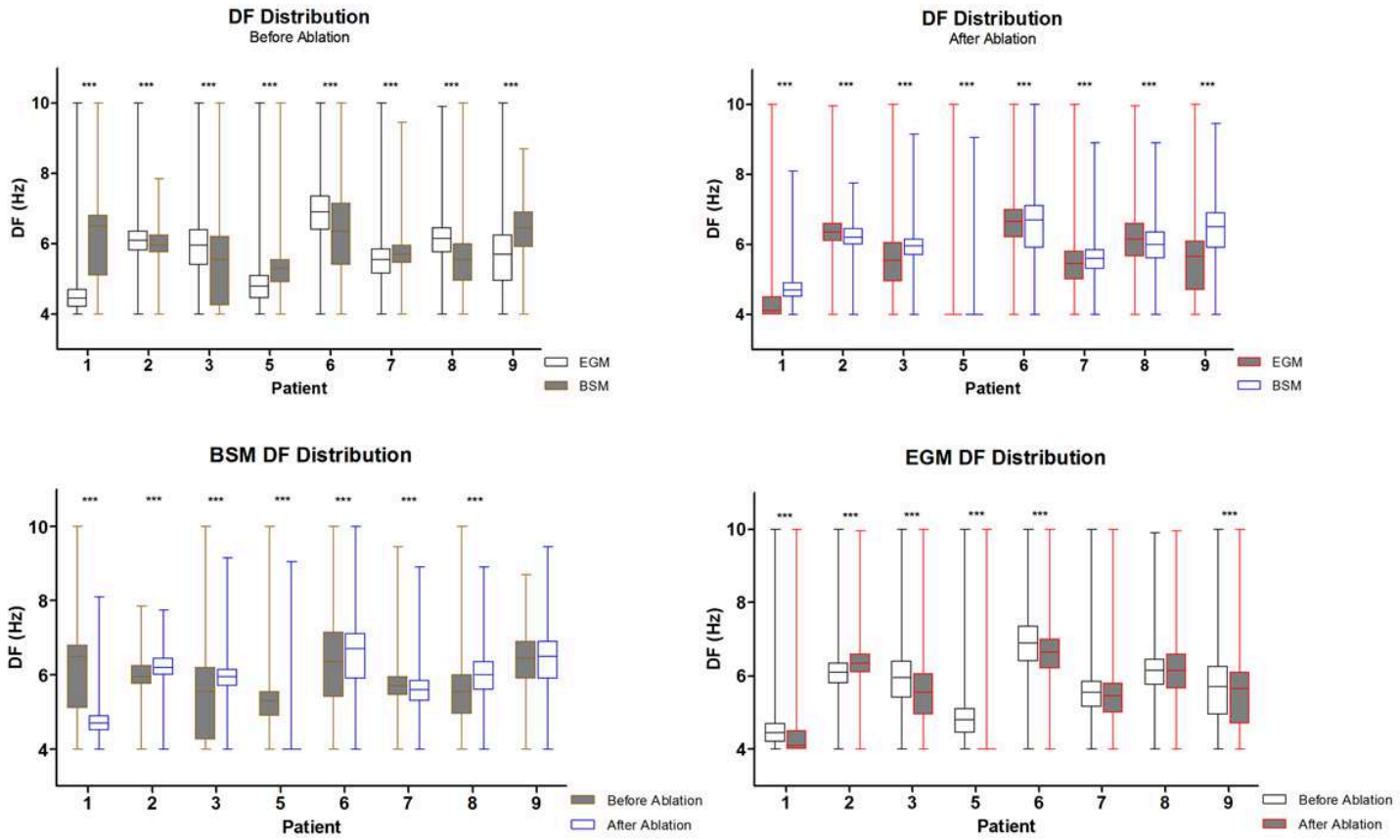

Figure 2-10: The distribution of DF values over all subjects. The upper graphs show a comparison of EGM and BSM DF distribution before (left upper) and after ablation (right upper) (window-by-window paired comparison). The lower graphs compare the BSM DF distributions (left lower) and EGM DF distributions (right lower) (unpaired comparison). Asterisks indicate statistical significance at *p* values equal to 0.05 (*), 0.01 (**) and 0.001(***).

2.3.3 Temporal Dominant Frequency Median Analysis

To determine if DF values showed temporal stability, the distribution of the DF over time was represented for each node on the atria and each electrode on the body surface. This distribution could then be represented with its median value. An example of the DF median on the atria and body surface is shown in Figure 2-11.

Figure 2-12 gives an overview of the behaviour of the DF median for all subjects on the atrial endocardium and body surface. As for the overall DF, DF median values were significantly different before and after ablation on both EGM and BSM in most subjects.

As for the temporal stability of the median, Figure 2-13 and Figure 2-14 show the behaviour of the DF median over all subjects for the body surface electrodes. Similar patterns could be observed on the electrograms. It appears that the temporal DF median is strongly varying, further indicating the instability of DF, and the possible movements of areas with highest DF. The data after ablation saw a similar pattern, with AF dominant frequencies being unstable over time.

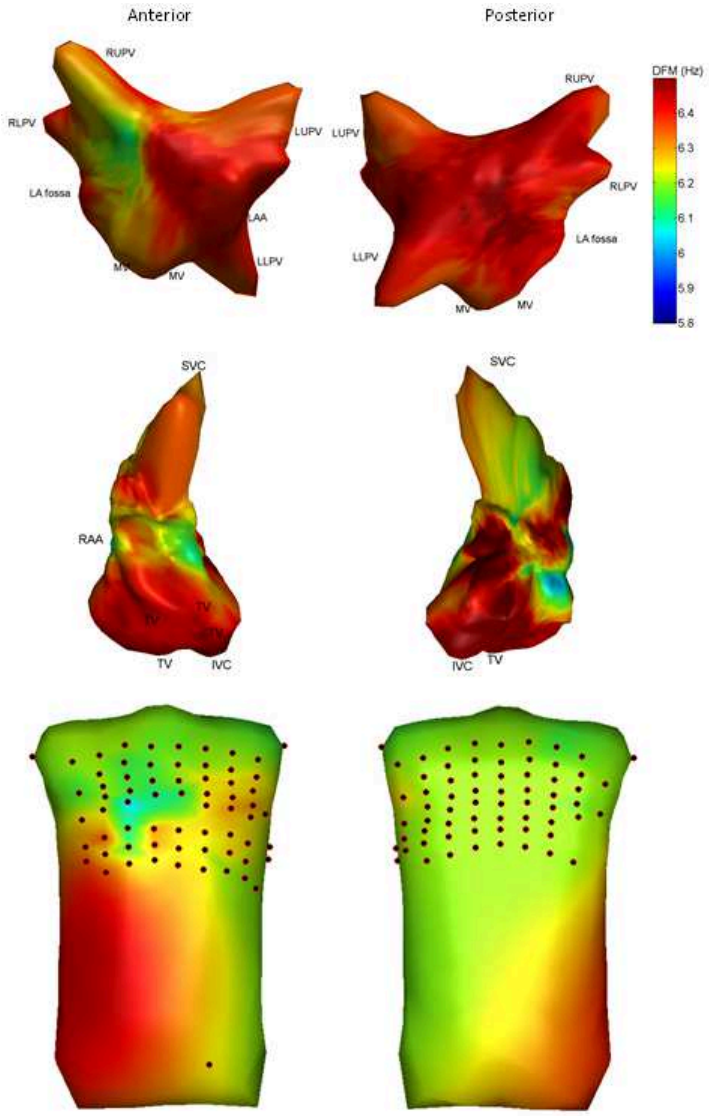

Figure 2-11: Example of temporal DF median maps for the left atrium (top), right atrium (middle) and body surface maps.

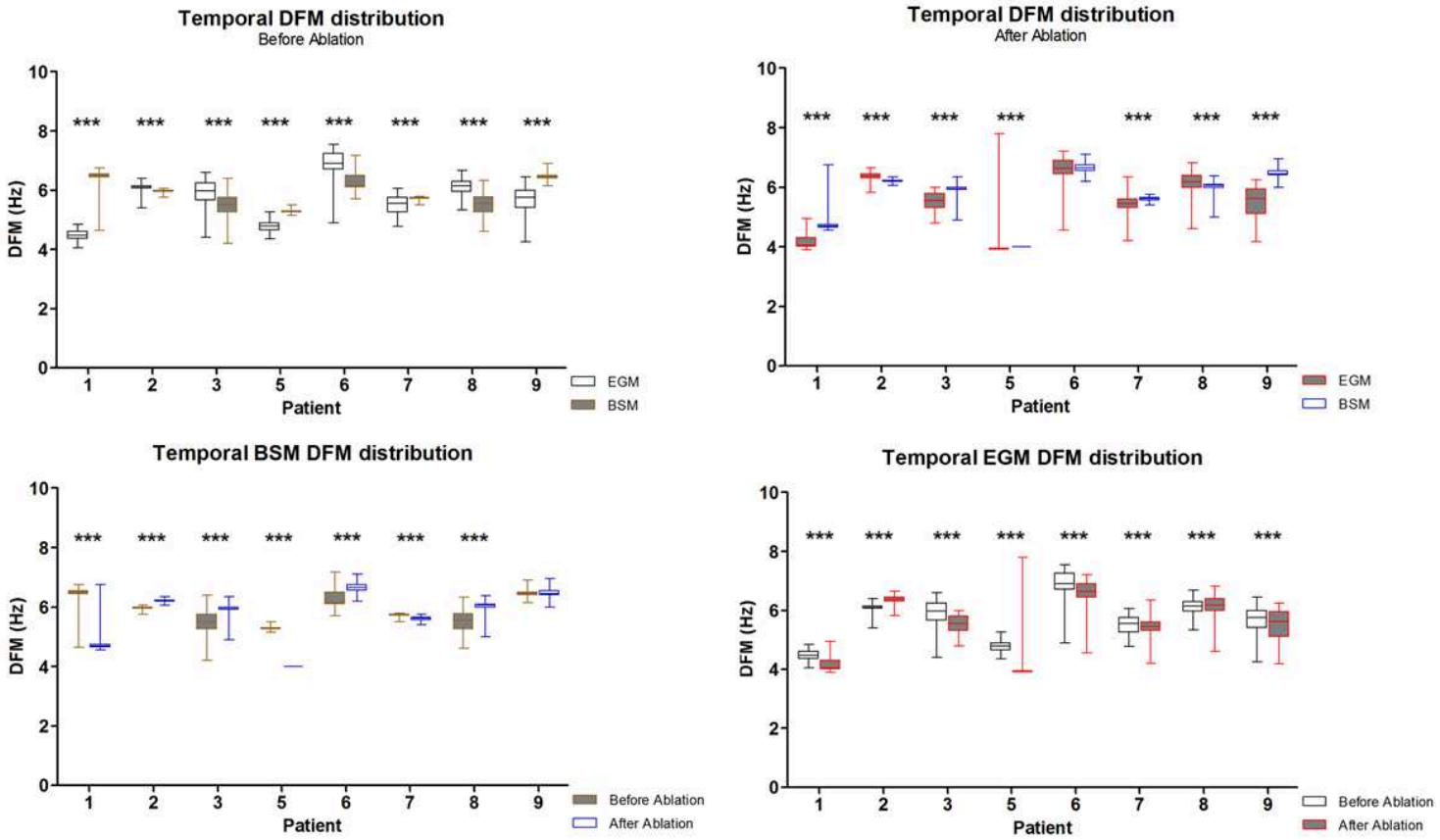

Figure 2-12: Overview of the temporal DF median distribution over all subjects. The upper graphs show a comparison of EGM and BSM DFM distribution before (left upper) and after ablation (right upper). The lower graphs compare the BSM DFM distributions (left lower) and EGM DFM distributions (right lower). Asterisks indicate statistical significance at *p* values equal to 0.05 (*), 0.01 (**) and 0.001(***).

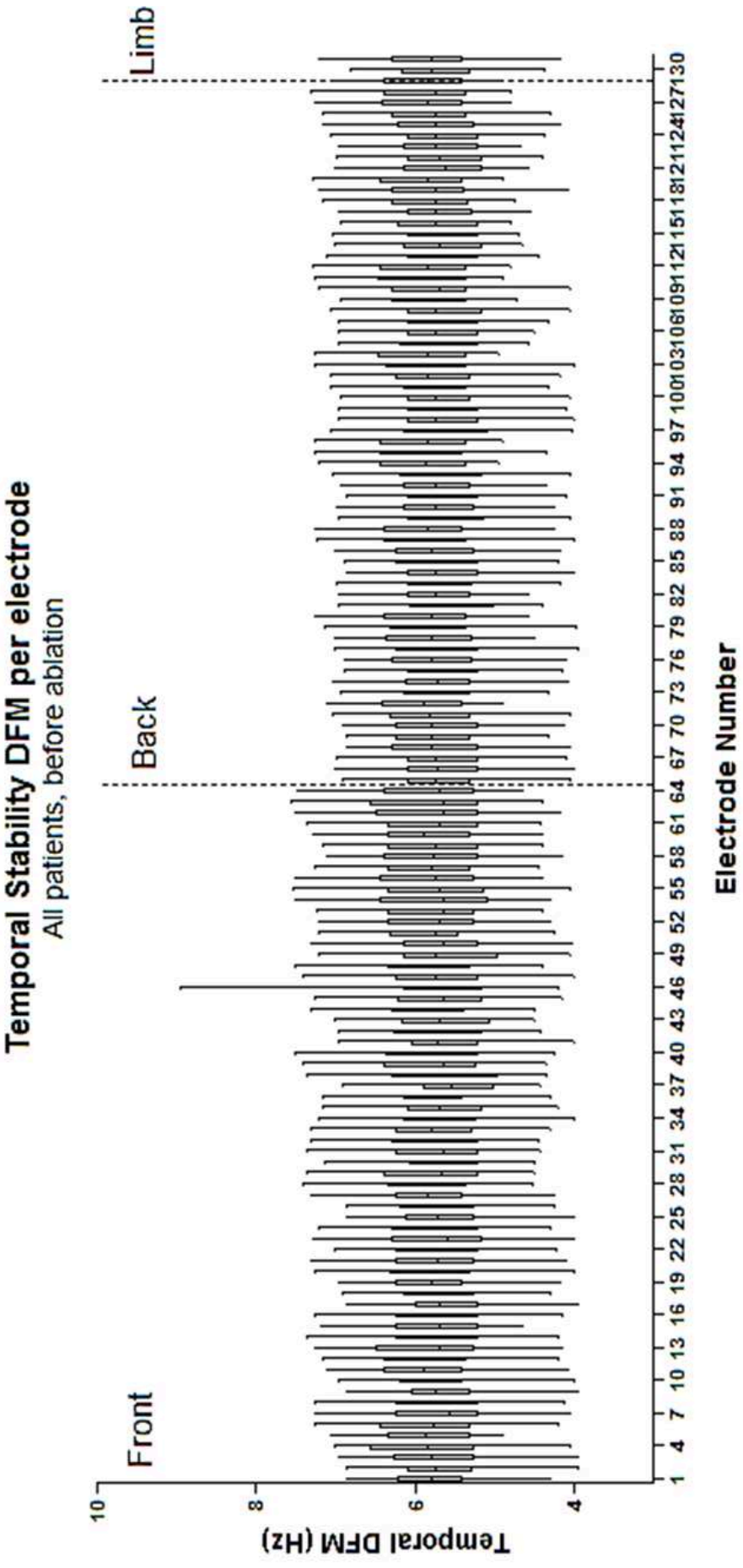

Figure 2-13: Temporal stability of DF median per electrode for all subjects before ablation.

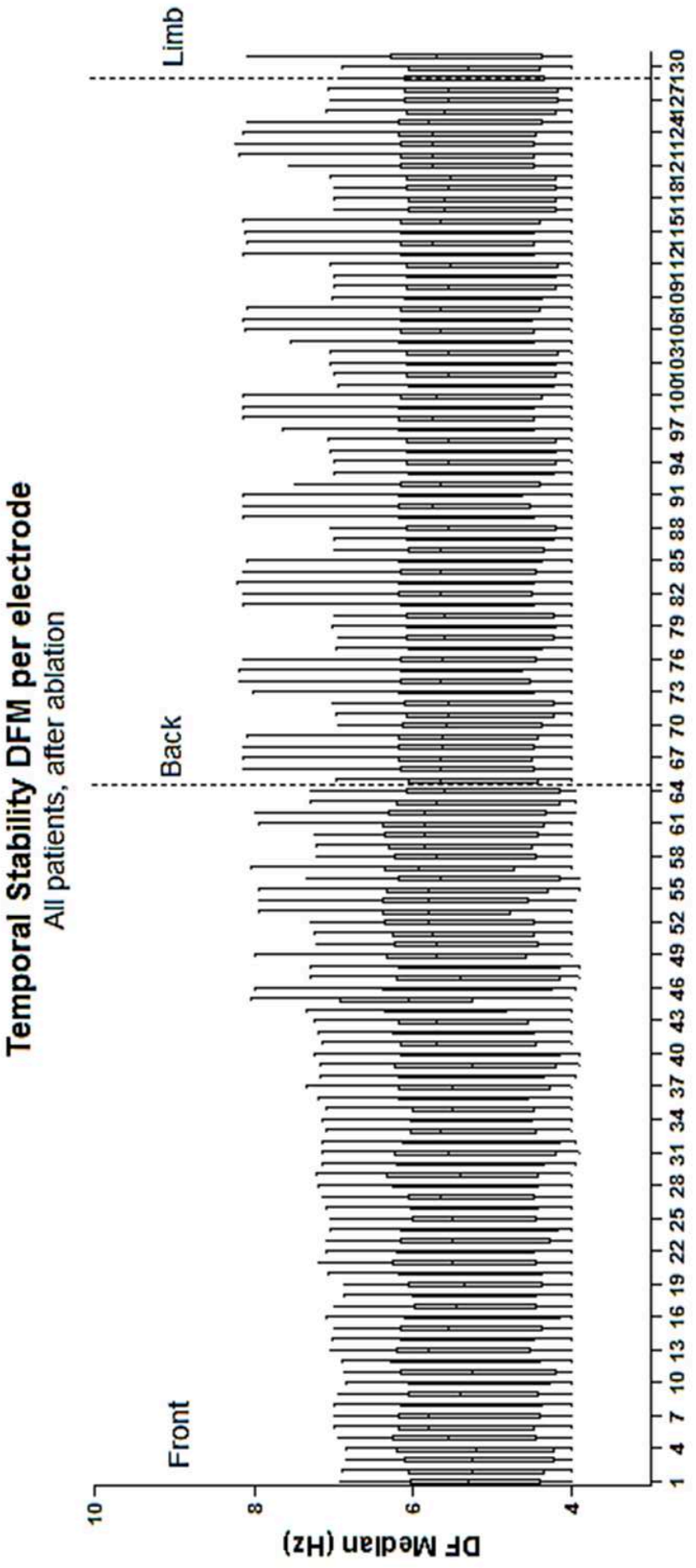

Figure 2-14: Temporal stability of DF median per electrode for all subjects after ablation.

2.3.4 Highest DF Analysis

The distribution of highest dominant frequency values (HDF) on the body surface map and atrial electrograms is compared for data before and after DF ablation in Figure 2-15. In both cases, the HDF value on the body surface is significantly different from the electrograms after a window-by-window comparison $(p < 0.001)$. Besides this, no linear correlation could be found between the HDF value on BSMs and EGM data (Figure 2-16). This linear correlation would be expected if BSM signals are a direct representative of the endocardial atrial data.

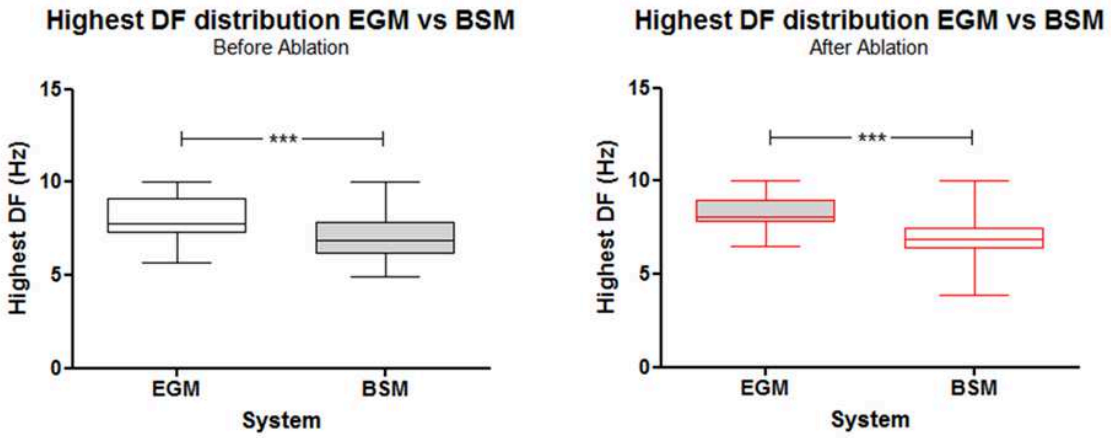

Figure 2-15: A comparison of the Highest DF (HDF) distribution between EGM and BSM data for all subjects. Overall, HDF distribution appears to reach lower values on the body surface before and after ablation (window-by-window paired comparison).

To fully investigate the latter, the number of windows in which the EGM HDF value was higher than the BSM HDF was calculated for each volunteer. Results for these calculations are shown in Figure 2-17 for data before and after ablation, respectively.

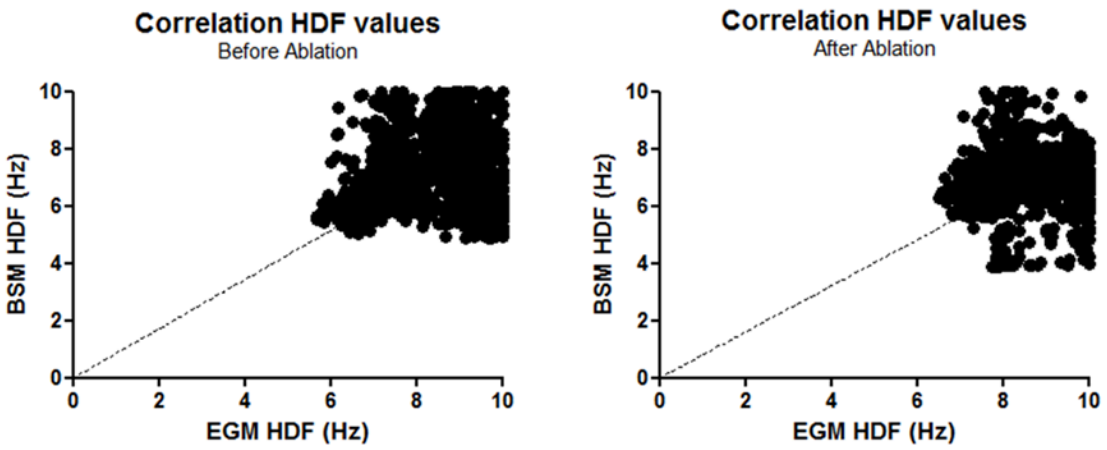

Figure 2-16: Correlation between Highest DF (HDF) values for all windows on the atrial virtual electrograms and BSM data. The dashed line indicated the expected correlation between BSM and EGM HDF values.

From the chi-squared test, it could be shown that there was a significant variation in the proportion of highest HDF windows in the EGM compared to BSM before ablation ($p < 0.001$). This can also be seen in Figure 2-17, where subjects 3, 6, 8 and 9 appear to have a different behaviour compared to the other subjects prior to ablation. After ablation, subjects 6, 8 and 9 seem to have a different proportion. To statistically enhance this, a Marascuilo procedure was used to determine which subjects showed identical proportion. All possible relationships between subjects were analysed. Proportions that are similar between different subjects are indicated above the bars on the figure. Results can be compared with the p-values for 2-by-2 Fisher exact tests on individual proportion comparisons as shown in Table 2-4 (before ablation) and Table 2-5 (after ablation).

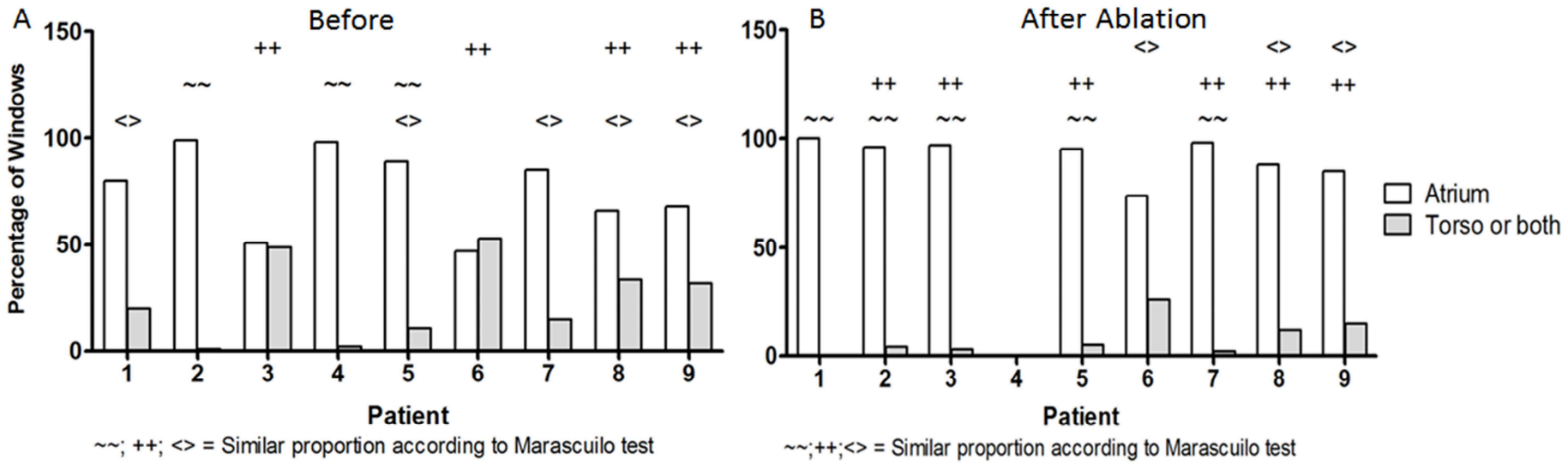

Figure 2-17: Proportion of Highest DF occurrence on atrial electrograms vs. body surface before (A) and after (B) DF ablation.

Table 2-4: Overview of p-values for the Fisher Exact tests before ablation. Data in red indicate comparisons in which the proportions differ significantly.

Patient	2	3	4	5	6	7	8	9
1	0.2	0	0.38	0	0	0	0	0
2		0.49	0.02	0.11	1	0.15	0.34	0.3
3			0.238	0	0	0	0	0
4				0.11	0.497	0.021	0.113	0.088
5					0.001	0	0	0
6						0	0	0
7							0	0
8								0

Table 2-5: Overview of p-values for the Fisher Exact tests after ablation. Data in red indicate comparisons in which the proportions differ significantly.

Patient	2	3	5	6	7	8	9
1	1	1	1	1	1	1	1
2		0	0	0.004	0.001	0	0
3			0	0.016	0.001	0.001	0.003
5				0.001	0.002	0	0
6					0.066	0	0
7						0.013	0.024
8							0

Lastly, Figure 2-18 shows the behaviour of the difference between EGM and BSM HDF values according to the EGM HDF value. Differences between the BSM and EGM HDF values appear to increase with an increasing HDF found on the EGM. As this difference appeared to behave exponentially, an exponential curve was fitted to the median difference between the BSM and EGM data. These curve showed a high goodness of fit with the data (R^2=0.90 before ablation; R^2=0.98 after ablation).

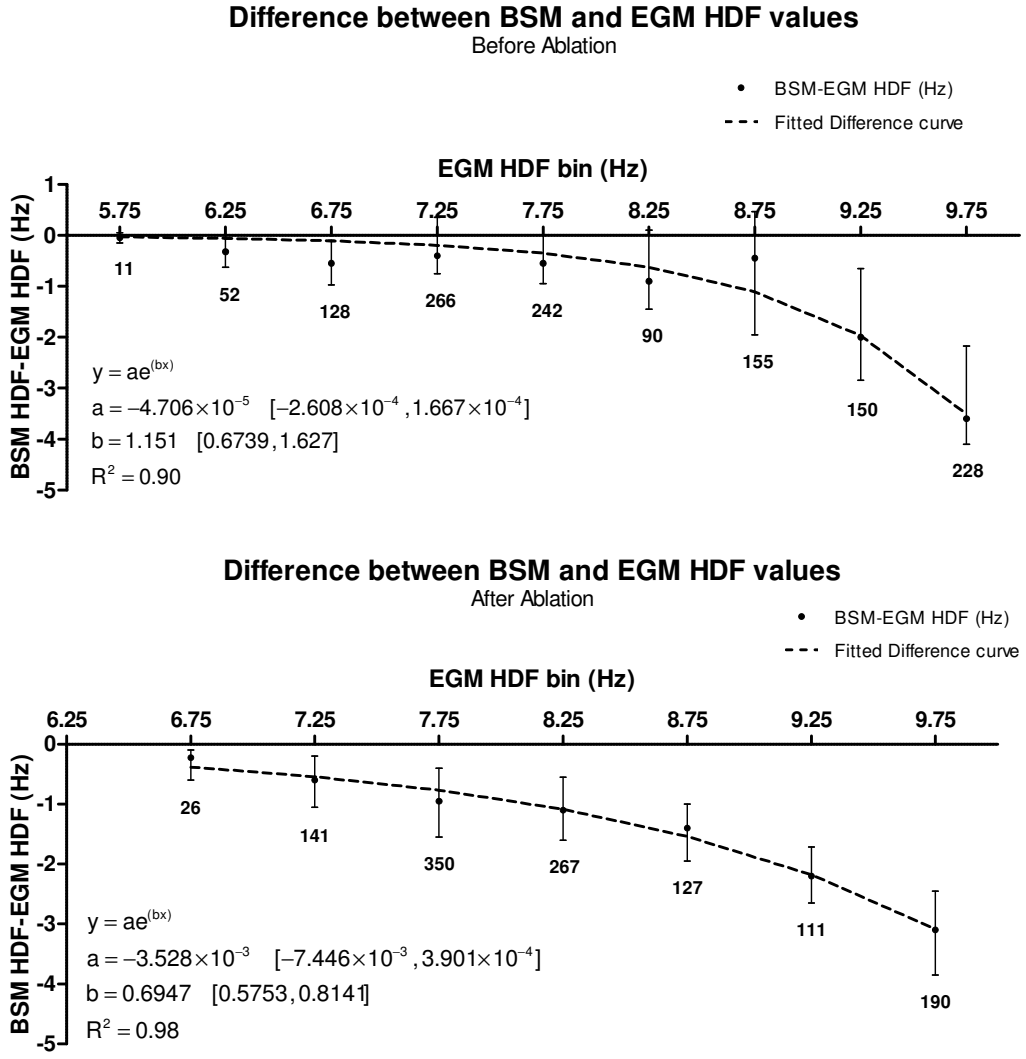

Figure 2-18: Comparison of the difference in HDF values on the body surface map and EGM according to the EGM HDF value. The BSM HDF value seems to differ stronger with increasing EGM HDF. An exponential curve has been fitted through the median difference points to indicate a possible correlation between BSM HDF and EGM HDF.

2.4 Discussion

2.4.1 Isopotential Maps

2.4.1.1 Interpolation Method

Interpolation had to be performed to complete the body surface (isopotential) maps. It was opted to use the surface Laplacian interpolation. Due to the irregular shape of the torso, the interpolation approximates the surface Laplacian in a least-square sense. For this, a relative contribution of neighbouring node potentials on a node under investigation is calculated (Huiskamp, 1991, Oostendorp *et al.*, 1989). This technique takes into account the distance as well as the angle between neighbouring nodes. The Surface Laplacian has also been used as a regularisation function for the inverse solution, and is more generally known as a second-order Tikhonov regularisation (Messinger-Rapport and Rudy, 1988, Oostendorp *et al.*, 1989).

One problem with this technique is the higher emphasis on neighbouring nodes. In case the values of these nodes themselves are a result of interpolation, significant distortions can be observed. One example in Figure 2-9 is the red coloured area on the lower right of the torso. This large area of apparently high DF is due to the transition of the DF from few electrodes – which are probably suffering from noise. The surface Laplacian is therefore only used for visualisation in this work. For analysis, only values observed at the electrode locations are considered.

2.4.1.2 Body Surface Mapping of AF

During the QRS interval, a standard observation as described previously in literature could be observed on the BSM (Medvegy *et al.*, 2002, Taccardi *et al.*, 1998). The QRS activation peak appears to move from the central torso region in a downward direction to the left of the torso. As the QRS is related to the ventricular depolarisation, its development on the body surface signals throughout the cardiac cycle remains unaffected.

From the isopotential maps during AF, no specific pattern could be obtained. This is due to the complexity of the disease, as well as to the lower strength of the atrial signal. Previous research on isochronal maps could distinguish

patterns of AF similar to those found on endocardial data (Guillem *et al.*, 2009). As all volunteers were in drug-refractory persAF, it could be argued that a multiple of sources of AF would lead to the complexity of the signal found on the body surface. Many different theories have been suggested regarding the sources and maintainers of AF, as discussed in Chapter 1. It is most likely that the subjects involved in this study suffered from a combination of co-existing ectopic foci, re-entry circuits and/or wavelets, as significant electrical, structural and mechanical remodelling will have occurred during their period in AF, as well as before the initiation of AF (Allessie *et al.*, 2002). Similar complexity can possibly be found during invasive atrial mapping, which makes guiding AF ablation based on isopotential maps challenging. Alternative strategies have been suggested. A first major improvement was made with the classical work of Haïssaguerre *et al.* in which ablation could be focussed towards pulmonary vein isolation (Haïssaguerre *et al.*, 1998). Later on, Nademanee and co-workers suggested targeting areas of complex fractionation for the successful treatment of AF (Nademanee *et al.*, 2004). Recent work by Narayan and collaborators has paid attention to ablation of electrical rotors and focal impulses for the treatment of AF (Narayan *et al.*, 2012). In this study, further focus was based on highest dominant frequency sites, which were suggested as interesting targets for AF treatment by Atienza *et al.* and Yoshida *et al.* in separate studies (Atienza *et al.*, 2009, Yoshida *et al.*, 2009). First, further understanding of general dominant frequency behaviour was sought. After this, attention was focussed on highest DF mapping.

2.4.2 Dominant Frequency (DF) and Highest DF Distribution

Only a small number of research groups have previously investigated DF ablation or attempted to link DF behaviour with AF ablation outcome. Atienza and co-workers showed that addition of HDF ablation to standard pulmonary vein isolation improved AF ablation outcome in subjects with persAF and paroxysmal AF (Atienza *et al.*, 2009). Other studies have demonstrated a reduction in DF on electrograms after AF ablation (Lemola *et al.*, 2006, Tuan *et al.*, 2011), which might be an indicator for improved outcome of ablation (Yoshida *et al.*, 2009).

The results shown in Figure 2-10 seem to contradict previously observed data, where the DF appeared to reduce after ablation (Kumagai *et al.*, 2013, Tuan *et al.*, 2011, Yoshida *et al.*, 2009). It has to be taken into account, however, that ablation in this project focussed on different targets for ablation in comparison to the previous studies. In these studies, ablation targeted pulmonary vein isolation (PVI) with roof line ablation (Tuan *et al.*, 2011), PVI followed by complex fractionated atrial electrogram (CFAE) ablation (Yoshida *et al.*, 2009) or PVI followed by HDF and CFAE ablation (Kumagai *et al.*, 2013). Furthermore, in these studies, DF was analysed by point-by-point mapping, which does not allow taking into account the temporal instability of HDF areas. This instability has been shown in previous studies on epicardial mapping (Schuessler *et al.*, 2006) as well as in non-contact endocardial mapping (Jarman *et al.*, 2012, Salinet *et al.*, 2014), Point-by-point contact mapping might therefore mask the true HDF behaviour.

Another interesting observation is the significant difference in DF behaviour between atrial and body surface data. In all subjects, the DF values seem to spread over the entire spectral range of 4-10 Hz for EGM data before and after ablation. On the body surface, the DF distribution appears more condensed after ablation. This could indicate an effect of the ablation of HDF areas on the sources of the cardiac signal. Previous studies have suggested possibilities to predict catheter ablation success based on ECG measurements (Meo *et al.*, 2013), as well as the occurrence of significant variations in ECG morphology after ablation (Di Marco *et al.*, 2014). In a first study, Meo *et al.* attempted to predict success of AF catheter ablation by exploiting the spatial diversity in a standard ECG setup. This diversity was analysed by calculating a normalised mean square error between successive TQ intervals and a rank-n PCA reconstruction of these intervals (Meo *et al.*, 2013). Results suggested that the parameters based on this normalised mean square error were able to distinguish catheter ablation outcome as AF termination and non-termination. Stronger evidence of changes in ECG measurements reflecting CA success came from a study by Di Marco and co-workers (Di Marco *et al.*, 2014). Here, it was shown that the frequency recurrence of specific patterns during the TQ

interval were indicative of AF freedom in subjects at 3 and 6 months after catheter ablation.

Another possible explanation for the more condensed HDF value on the BSM could be the spatiotemporal low-pass filtering effect of the volume conductor. Many studies have focussed on the effect of the volume conductor model in the propagation of cardiac signals. In a series of studies on spherical heart models taking into account torso inhomogeneities, Rudy and Plonsey showed that changes in conductivity of specific tissues and organs, as well as a repositioning of the heart could significantly alter body surface signals (Rudy and Plonsey, 1980, Rudy *et al.*, 1979, Rudy *et al.*, 1982).

The effect of torso inhomogeneities was further investigated by Gulrajani and Mailloux in a standard torso model (Gulrajani and Mailloux, 1983). They showed that, during QRS activation, a spatiotemporal filtering occurred after inclusion of lungs and muscle layers and blood masses. This filtering effect was visualised by a smoothing of notches and isopotential maps on the ECG. A following study by Bruder and co-workers further enhanced these findings (Bruder *et al.*, 1994). In a simulation study, the effect of lungs, skeletal muscle and blood masses on the BSM data for 2 Wolff Parkinson White patients showed that especially muscle anisotropy had a significant effect on body surface maps. In a simulation study on cubic models representing the heart and torso, Nowak and co-workers observed the impossibility of reproducing high frequency components induced by the heart on the torso after a forward solution (Nowak *et al.*, 2008). Besides this, specific regions with a particular dominant frequency value on the heart could not be distinguished on the torso. These results were obtained without the inclusion of torso inhomogeneities or mathematically induced low-pass filters. Focussing on P wave genesis, van Dam and van Oosterom concluded that the atrial blood masses (Brody effect) can significantly affect P wave morphology on near- and far-field ECG signals (van Dam and van Oosterom, 2005). The effects appeared to be non-uniform over the torso and varied with time. Atrial signals appeared to be more affected by this Brody effect than ventricular signals.

From the above, it can be considered that, due to the relatively large distance between the BSM electrodes and the AF sources, as well as inhomogeneities throughout the pathway the AF signal travels to the body surface, the strength of these signals can get diminished and blurred. This might mask the appearance of AF dominant frequencies on the body surface, especially if these DF amplitudes are of lower strength. This idea has been well documented in wireless communication networks, where determining the source of a signal can be estimated from the strength of the signal at different locations (Roos *et al*., 2002). Therefore, in case the DF occurs in very localised atrial regions, the blurring effect of the volume conductor might mask their expression on the body surface (van Dam and van Oosterom, 2005). One example of the latter is shown in Figure 2-19.

The low power of the dominant frequency could play an important role in the variation of the position of the highest dominant frequency, which was targeted during ablation. This could jeopardise the usefulness of DF as an ablation target. Low power DF could also decrease its significance as a representative of AF sources. To further investigate this, the DF was analysed for each node on the atria as well as on the body surface over time.

2.4.3 Temporal DF Median Analysis

Significant variation existed between EGM and BSM DFM taken at the same moment. This indication was in accordance with previous investigations regarding temporal stability of HDF sites (Salinet *et al*., 2014).

One particular case occurs for subject 5 after ablation. The variation in DFM could be clearly explained by the occurrence of harmonics. This volunteer appeared to have a highly consistent AF cycle length of about 255 ms after ablation, as obtained from ECG analysis by clinical experts. The volunteer could also be converted to sinus rhythm after PVI. For some electrodes, the DF median appeared at 7.8 Hz, and most electrodes had a DF median of 4 Hz. As this DF value was at the extremity of the frequency interval of interest, peculiar boxplots can be seen in Figure 2-10 and Figure 2-12 for this subject, consisting of a flat box with occasionally long tails towards 10 Hz. After visual inspection of the spectra between 0 and 20 Hz, a high amplitude frequency component

could be visualised at 3.9 Hz, which corresponds to the inverse of the AF cycle length (Figure 2-20). The effect of harmonics on determining the DF of atrial activation has been discussed previously (Lemay *et al.*, 2007, Ng and Goldberger, 2007). Harmonics should be taken into consideration as possible disturbances in interpreting the periodicity of AF activation (Ng and Goldberger, 2007). However, they could also help indicating complexity of multiple wavelet re-entries, as has been shown in simulation studies (Lemay *et al.*, 2007). In this case, the DF of 3.9 Hz became 4 Hz due to the cut-off used at this particular frequency, and the possibility of identifying the downslope in spectrum after the 3.9 Hz peak as the maximum.

Although striking in subject 5, the effect of harmonics could not be observed clearly in other volunteers. Besides this, no clear correlation existed between DF and AF cycle length in other volunteers. Previous work has emphasised on this poor correlation (Elvan *et al.*, 2009, Ng *et al.*, 2006).

Further reasons for temporal instability could be given based both on the mechanisms behind AF as on the methodology for finding the DF.

From a physiological point of view, the co-existence of various maintainers and sources of AF might provide an explanation for the complex behaviour of DF, and its variability over time. The prolonged exposure to AF for the volunteers under investigation will have had significant impact on remodelling processes within the cardiac muscle. Variation on the body surface could be partly explained by the effect of the volume conductor model. As suggested by Rudy (Rudy and Plonsey, 1980), fluctuations in conductivity of the lungs, which could occur by a mere change of inspiration rate (Gabriel *et al.*, 1996), would influence data shown on body surface maps. The Brody effect and possible alterations in blood mass and conductivity could influence electrical signals on the endocardial surface (Brody, 1956).

Methodologically, it has to be appreciated that the 2048 virtual electrograms obtained per atrial chamber are an interpolation from 64 direct measurement sites, for which the electrograms are estimated according to a potential-based inverse solution (Kadish *et al.*, 1999, Rajappan and Schilling, 2009, Schilling *et al.*, 2000). Although much validation has been performed on the applicability of

the inverse solution, the correlation between direct contact mapping data and the estimated electrograms was shown to be 0.7±0.15 (mean±SD) for 62 random locations (Jarman *et al.*, 2012). Many factors such as the movement of the heart and Array as well as volume conductor effects can only be accounted for to a certain extent (Budd *et al.*, 1996, Kagan *et al.*, 1994, Beatty *et al.*, 2010). The Array will therefore be prone to a consistent change in distance relative to the heart and environment. Not all of these sudden changes can be accounted for during data collection. Besides this, the effect of equipment noise can influence the accuracy of the electrograms (van Oosterom, 2012c). Systematic errors within the QRST segmentation algorithm could affect the accuracy of QRST subtraction, leaving artefacts of ventricular activity apparent in the body surface signals or EGM signals. These can affect frequency components within the signal. After manual checking, subjects 6 and 9 showed visible QRST residuals in data after ablation at some intervals in the analysis.

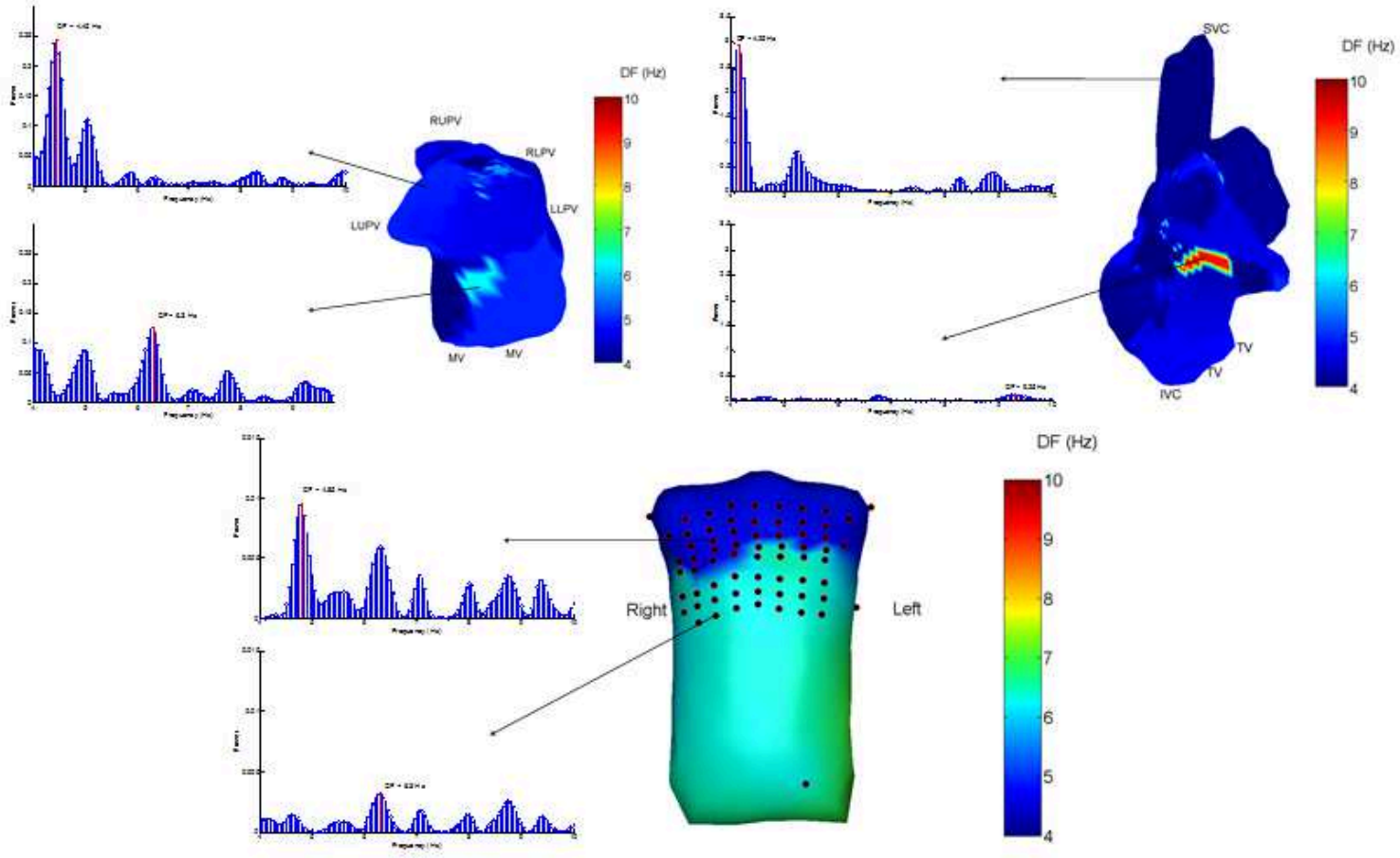

Figure 2-19: Examples of DF maps from subject 2, showing frequency spectra of a region with low (upper) and high (lower) DF. A localised high DF area on the right atrium could not be reproduced in the BSM signals, possibly due to its low power.

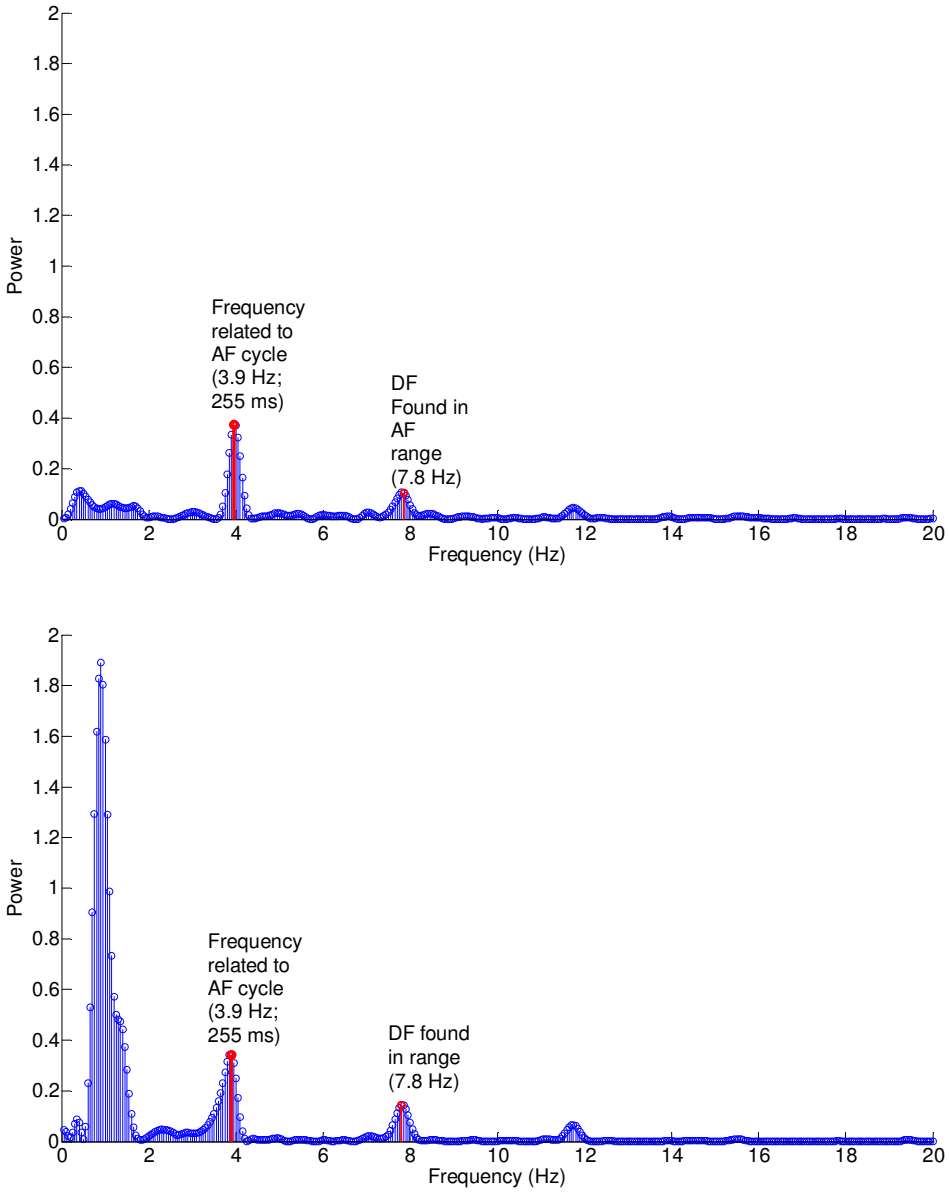

Figure 2-20: Example of 2 Spectra from 0-20 Hz of subject 5 after ablation. A highly organised AF was established after DF ablation with a cycle length of 255 ms. DF analysis in the chosen range (4-10 Hz) gave a consistent highest DF value of 7.8 Hz in the left atrium. This appeared to be a harmonic of a dominant frequency related to the AF cycle length (3.9 Hz).

2.4.4 Effect of Volume Conductor on Highest DF

HDF values appear to be lower on the BSM. These results seem to be in accordance with previous work (Guillem *et al.*, 2013) and seem to correspond

to the assumed spatio-temporal low-pass filtering effect of the volume conductor discussed previously (Nowak *et al.*, 2008).

The results in Figure 2-18 resemble strongly the results found from electromyographical simulations by Lindstrom and Magnusson (Lindstrom and Magnusson, 1977). In their work, various essential elements of understanding variations in frequency spectra from electromyography recordings where expressed in terms of filter functions. They found that the loss in power in the spectra according to frequency could be represented by second-kind Bessel functions. Furthermore, it could be shown that this function behaves as a low-pass filter. An increase in distance between the muscle fibre and measurement location augmented the effect of this low-pass filter. This behaviour was reproduced in the works of Stegeman (Stegeman *et al.*, 2000) and Farina (Farina and Merletti, 2001).

From Figure 2-21, retrieved from the work of Lindstrom, it can be shown that, based on the relative distance from the heart to the torso, a strong filtering could occur at frequencies of 5-10 Hz. As the endocardial HDF can suffer from low power, it can easily be understood why this low-power HDF cannot be visualised on the body surface. This effect has to be taken into consideration when relating body surface signals and derived analyses of these to their cardiac counterparts.

The volume conductor effect also explains the proportionality of HDF occurrence in Figure 2-17. After ablation, the HDF values seem to occur even more often on the endocardial data compared to pre-ablation results. This could indicate that DF ablation successfully reduces the power of high-frequency components in the AF signal. Variation in results can be observed when comparing this figure with the data from the Fisher Exact test. Reasons could be due to the improved handling of low-frequency variable by this latter test. The fact that individual 2-by-2 Fisher tests had to be conducted due to the complexity of handling 2-by-n tables with this test might have however induced error in the statistical analysis (Rosner, 2010). Overall, it can still be concluded that variation exists in the proportions of HDF values occurring on the BSM and electrograms between patients.

For some volunteers, a higher proportion of windows showed an equal or higher HDF value on the BSM compared to the EGM data before ablation. This could indicate variations in torso geometry and therefore the volume conductor, or the fact that HDF also exhibits high power in these volunteers.

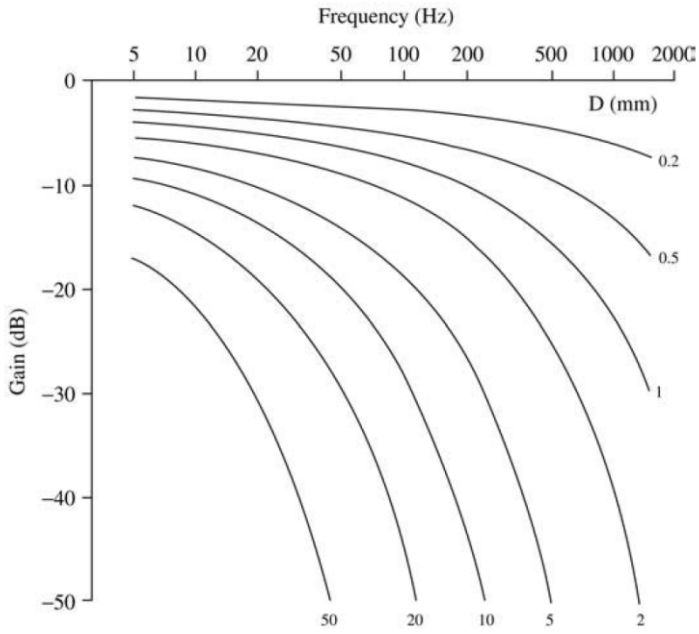

Figure 2-21: Gain loss for different frequencies at varying measurement distances in electromyography simulations. A low-pass filter effect occurs which has a stronger effect with further distance of measurement, which allows the volume conductor to have a stronger effect (Moore Jr and Maitland, 2013) (Reproduced with permission from the editor).

2.5 Study Limitations

The study focussed on persAF volunteers suitable for catheter ablation. As the ablation was performed with a new strategy targeting CoGs of HDF areas, only a small number of subjects was selected to participate. Future research on the HDF and volume conductor effects would need to include larger cohorts.

From the methodological point of view, it has to be appreciated that QRST cancellation on AF signals is not straightforward, and small errors might have occurred. The endocardial data are estimated from an inverse solution, and therefore might not always be an accurate representation of cardiac activity (e.g. contact mapping). Although indicated in the discussion, the definition of the (highest) dominant frequency did not take into account the occurrence of

harmonics, nor organisation (i.e. power) of this frequency component. This additional information could be of importance when considering ablation targeted on HDF areas.

2.6 Clinical Relevance of Findings

High dominant frequency areas have been considered a possible representative of AF drivers in various studies. Most of these studies have evaluated HDF using invasive tools (contact mapping and non-contact mapping). The current surge in non-invasive analysis of cardiac arrhythmias has induced a transfer of invasively investigated AF metrics such as DF and phase analysis to body surface signals (Guillem *et al.*, 2013, Rodrigo *et al.*, 2014).

The immediate application of these metrics might however be cumbersome, due to an incomplete understanding of the electrophysiological relevance of the metric and technical considerations that should be taken into account (Ng and Goldberger, 2007). Besides this, volume conductor effects could influence the representation of HDF (and phase metrics) on the body surface. These complexities could strongly affect the clinical interpretation of DF data.

This chapter has shown how DF values vary between endocardial virtual electrograms and body surface signals. It was shown that the HDF on the endocardium was generally higher than on the body surface. One possible explanation, besides effects of noise and other signal artefacts, could include the mostly local HDF phenomenon on the endocardium. As the volume conductor behaves as a low-pass filter, only a blurred version of cardiac data is represented on the body surface. Localised phenomena would therefore remain masked on the torso, which could make a detailed clinical assessment of AF from BSMs challenging.

These findings could however provide ideas for a rigorous discussion of what dominant frequency and highest dominant frequency (should) represent electrophysiologically, and how these metric could improve in clinical relevance. An interesting approach would be to compare how endocardial and body surface DF and HDF relate to a gold standard directly related to AF

behaviour (e.g. AF cycle length). One outcome could be that body surface HDF distribution reflects global information of the behaviour of the main AF driver (e.g. activation frequency of mother rotor), whereas endocardial data might provide information about maintainers or secondary AF drivers with local effects, including wavelets, spiral wave disintegrations, non- or low-conducting areas inducing wave collision or wave breaks and localised re-entry phenomena. Correct interpretation will of course be strongly dependent on the technical consideration regarding DF analysis (Ng and Goldberger, 2007). Once established, body surface DF analysis could become compatible with electrophysiological studies as a tool for primary DF assessment to help clinicians develop a treatment strategy prior to intervention.

2.7 Conclusion

This study focussed on the direct comparison of body surface signals and endocardial virtual electrograms from persAF subjects undergoing a DF-based catheter ablation. Data analysis was focussed on the frequency analysis of AF data after QRST subtraction. The dominant frequency was used as a representative for AF behaviour, and areas on the left atrium exposed to the highest DF value per 4 s window were targeted for ablation.

Data before and after ablation did not provide strong information about the appropriateness of HDF as a target site for ablation. This could be due to the temporal instability of DF. It could however be found that BSM DF values appeared lower than those measured with the virtual electrograms. This indicates with high possibility the effect of the volume conductor on the AF signals, as was previous shown in simulation studies. This effect is significant when comparing HDF values on the heart and body surface. Here, the low-pass filtering effect of the volume conductor could be well established. This effect should be taken into consideration when directly comparing frequency-based data from the torso and heart.

3 Effect of Lead Reduction on BSMs: A Spatial Frequency Perspective

3.1 Introduction

Reduced-lead BSMs have been developed roughly for two purposes. One is to find the electrode positions which give most contribution to the total signal, the other attempts to determine electrode locations which give the most significant variation for a disease compared to healthy standards are chosen.

3.1.1 Best Diagnosis BSMs

The first disease-specific systems were developed based on difference maps for the detection of myocardial infarction. These systems generally are an adapted version of the standard ECG, with the possibility of a small amount of additional electrodes (Gerstenfeld *et al.*, 2000, Kornreich *et al.*, 1986, SippensGroenewegen *et al.*, 1998).

In other studies, BSMs were developed for the optimal detection of AF. Guillem *et al* derived a 23-lead system for AF detection from a 64-electrode BSM covering the entire torso (Guillem *et al.*, 2009). This enabled locating the source of AF on the torso and follows its movement over successive cardiac cycles. To reduce the time for application, a 56-lead system was developed around the V_1 precordial lead.

An issue with disease-based systems is that they can only be applied if the disease type is known, or at least assumed to be known. Alternatively, BSMs have been developed which give a better overall view of cardiac activity, independent of disease.

3.1.2 Best Signal BSMs

Not considering the standard ECG and vectorcardiogram (VCG), a first elaborate study looking to reduce BSM systems was suggested by Barr *et al.* (Barr *et al.*, 1971). Starting from a 150-electrode BSM system which included the standard ECG and VCG positions, an attempt to reduce the amount of leads was developed based on the calculation of a “Generators” matrix and a coefficient matrix that relates these mathematical generators to surface

recording positions. The study was performed for QRS potential maps from 45 volunteers with various heart diseases. The matrices were calculated using Principal Component Analysis (PCA). Reconstructed reduced-lead BSMs were compared to the original maps both based on voltages and morphology to determine the correctness of the reduced map. It was suggested that by appropriately positioning 24 electrodes on the subject's torso, the original BSM could be reconstructed with an error smaller than 2%.

Monro *et al.* suggested a different approach based on Fourier interpolation (Monro *et al.*, 1974). In this work, interpolation of data obtained from 24 electrodes positioned uniformly around the torso was used to develop complete BSMs. The Discrete Fourier Transform (DFT) of 8 samples per strip was calculated and expanded to twice its length by insertion of zeroes. Using an inverse DFT, the original signal was reconstructed, sampled twice as often as the original measurements.

Next, in a series of studies, Lux and co-workers reduced a 192 –electrode system to 32 electrodes based on the correlation of one electrodes site with the other electrodes, taking into account signal variation (Lux *et al.*, 1978). This "information index" was then used to rank electrode in a similar way as PCA. Firstly, on a full 192 system, the information index of each electrode was calculated. The electrode with the highest index was then removed, and a new index was calculated from the remaining electrodes. This was repeated until a stopping criterion was reached. A similar process was used by Finlay and co-workers (Finlay *et al.*, 2006), but differed in that here, a bottom-up approach was used calculating how well a single electrode represented the 192-lead BSM, and adding electrodes until a criterion was reached. In this study, the reduced-lead system consisted of a similar amount of electrodes, but placed at different positions.

The determination of stopping criteria in both the works of Barr and Lux was criticised for its subjectivity, and alternative approaches were considered based on the Minimum Descriptive Length (MDL) (Uijen and van Oosterom, 1992). The MDL is a tool for the determination of the information criterion (IC) of a signal. To determine the IC for a signal with N samples, a model from a family

of probability models is selected which best fits the data, where the MDL is considered as a correlation factor. In this way, the IC is calculated using:

$$\mathrm{IC(k, MDL)} = -\log f(X|\theta_k) + v(k,p)MDL \tag{3-1}$$

Here, k represents the model dimension, f(…) the probability density of data X given model k, v(…) the number of free parameters and p the number of channels.

The MDL is calculated as:

$$\mathrm{MDL} = 0.5 * (\log(\mathrm{N})) \tag{3-2}$$

Using this algorithm, Hoekema *et al.* showed that the number of independent signals on BSMs taken with various lead systems consisting of 32-219 electrodes was about 10, with only a small increase in systems with many leads. They suggested BSM systems of 64 leads as sufficient for most applications (Hoekema *et al.*, 1999).

Although mathematical algorithms such as PCA and IC have shown robustness, one could argue that the relationship with the original measurements might be lost to an extent. It can also be considered difficult to position the electrode accurately, since the electrode locations are random. To more easily understand the number of electrodes needed, a more classical approach of spectral analysis, which is directly related to the BSM signals, can be used. Here, one would start from an oversampled, multi-lead BSM map, and determine the spatial sampling frequency needed to capture the important information of a BSM. Since in most cases the electrodes are positioned non-uniformly over the torso, direct DFT algorithms cannot be used. An alternative is using Lomb-Scargle periodogram analysis to determine the spatial frequency of interest.

3.1.3 Lomb-Scargle Periodogram

Lomb-Scargle spectral analysis (LSSA) can be considered an extended form of the DFT, in which the need for evenly sampled data is avoided (Press *et al.*, 2002). The analysis was developed by Lomb (Lomb, 1976) and elaborated by Scargle (Scargle, 1982), and consists of an evaluation of data on a per point

basis rather than a per (time) interval basis as is done by Fourier analysis. Lomb analysis provides a means to estimate the harmonic content of a signal at a given frequency ω=2πf by least-square fitting to the model:

$$h(t) = A\cos\omega t + B\sin\omega t \tag{3-3}$$

Supposing there are N data at point h_j, the periodogram can be calculated using:

$$P_N(\omega) = \frac{1}{2\sigma^2}\left\{\frac{\left[\sum_j (h_j - \bar{h})\cos\omega(t_j - \tau)\right]^2}{\sum_j cos^2\omega(t_j - \tau)} + \frac{\left[\sum_j \left(h_j - \bar{h}\right)\sin\omega(t_j - \tau)\right]^2}{\sum_j sin^2\omega(t_j - \tau)}\right\} \tag{3-4}$$

where

$$\bar{\mathrm{h}} = \frac{1}{N}\sum_j^N h_j \tag{3-5}$$

$$\sigma^2 = \frac{1}{N-1}\sum_j^N (h_j - \bar{h})^2 \tag{3-6}$$

are the mean and variance of the signal, respectively, and

$$\tan(2\omega\tau) = \frac{\sum_j \sin 2\omega t_j}{\sum_j \cos 2\omega t_j} \tag{3-7}$$

The offset τ is added to make the periodogram independent of shifting all time moments with a constant.

Based on these calculations, one can determine if any periodicity is present in the signal by calculating the significance of a peak within a spectrum (Press *et al.,* 2002). Most interest lies in finding the spatial frequency above which only very little signal energy (or information) can be observed.

3.2 Research Aims and Objectives

This chapter aims to develop a better understanding for BSM systems electrode positioning for the analysis of cardiac diseases. Lomb spectral analysis will allow understanding, in a mathematical way, the number of electrodes that could capture the cardiac signal appropriately. This technique

does not provide exact positions for these electrodes, as can be achieved with e.g. PCA. Previous studies with PCA have shown that different setups could give the same signal reproducibility, however, and therefore do not provide exactly one optimal torso coverage. The LSSA will give a more global idea of electrode numbers, which could be complementary to PCA-based reduced-lead systems.

3.3 Methods

3.3.1 Database

A group of 17 male healthy volunteers agreed to have a body surface map taken. For all volunteers, BSMs were taken twice for 1 minute in rest in supine position, with a resting interval of 5 minutes between measurements using the vertical setup as in Figure 3-1.

3.3.2 BSM Setup

BSM signals were collected with the vertical BSM setup (Figure 3-1). The electrodes strips were positioned on the subject's torso, with 9 strips on the front and 7 on the back. This setup resulted in an appropriate coverage of the torso to allow studying the effect of reduction in leads.

Data were processed and atrial activity was derived as described in chapter 2. Four subjects were discarded from the analysis, as more than 10% of the BSM electrodes were exposed to high noise distortions. Only the 128 body surface electrodes without the WCT were used for analysis. A zero-reference was applied to the body surface signals.

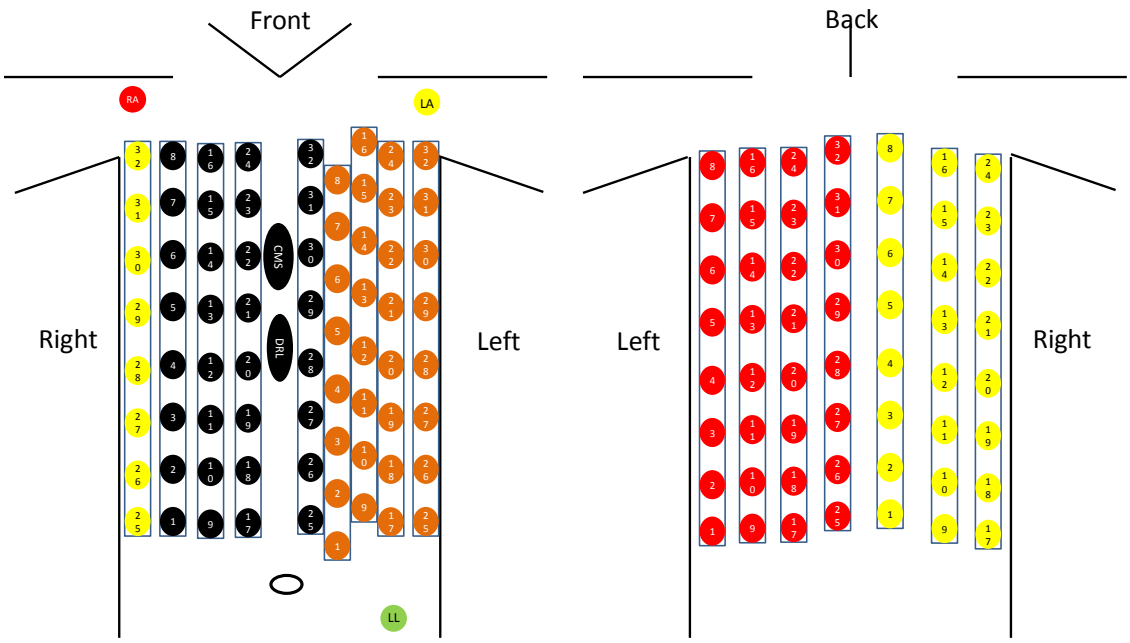

Figure 3-1: Vertical BSM setup for 128 leads. Electrodes are indicated as per Figure 2-1

3.3.3 BSM Spatial Frequency Analysis using Lomb-Scargle Spectral Analysis

For LSSA, a modified version of the algorithms suggested by Press *et al.* was developed in Matlab (Press *et al.*, 2002). LSSA was performed individually in horizontal (latitudinal) and vertical (longitudinal) direction, creating a 2D representation of electrode density (i.e. an $m \times n$ matrix with m the number of electrodes in horizontal and n the number of electrodes in vertical direction). To determine the spatial frequency, the voltage at a specific sample for all electrodes on the same latitude or longitude was selected and plotted over distance. For calculating this distance, the Euclidian distance between the xy-coordinates of two electrodes was determined, assuming that the electrode on the lower right chest was positioned at the origin (electrode D25). The spatial spectrum was then calculated using LSSA and the Fast Fourier Transform (FFT) for comparison. For each spectrum the Area Under the Curve (AUC) was calculated, taking into account a noise threshold of 6 dB smaller than the maximum power in the spectrum (Evans *et al.*, 1989, Keeton *et al.*, 1997). An overview of the methodology for QRS analysis is shown in Figure 3-2.

In a first instance, LSSA was performed on 3s windows with 25% overlap. The results of LSSA were compared with those obtained from Fast Fourier analysis on the same data. After this, attention was given on LSSA of the QRS segment and atrial activity. For this purpose, QRS peak detection and removal was performed as described above. The positions of the QRS peaks, and the QRST-removed ECG signal were stored individually. For QRS segment analysis, LSSA was performed on 200 ms windows in which a QRS peak was centralised. For atrial activity, a window size of 3 s with 25% overlap was used. In both cases, only every tenth sample in a window was considered to reduce processing time. The ratio of signal described by subsets of the total 128-lead BSM system and the 'total' signal were calculated based on the area under curve (AUC) of all spectra for each sample and each strip.

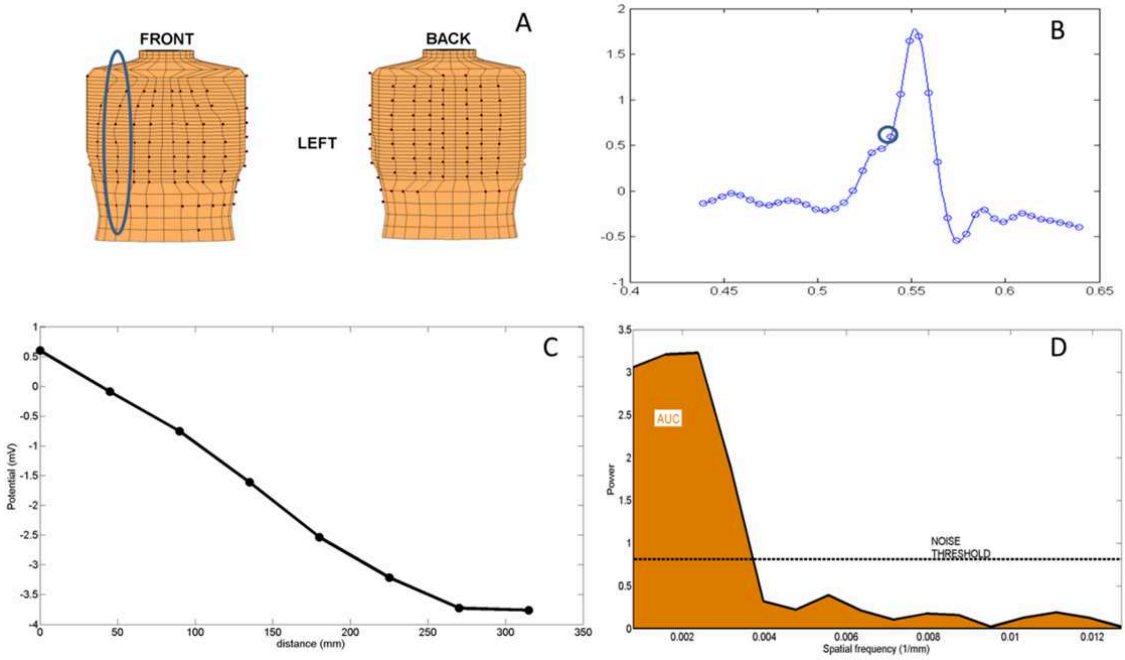

Figure 3-2: Example of LSSA analysis. For a vertical or horizontal line (A), an ECG time window of interest was selected as shown in B (QRS analysis). These ECG time windows were then down-sampled. For each individual electrode, the voltage at one of the selected samples was selected and plotted against distance with the right lower chest electrodes considered as being the origin (C). LSSA analysis was then performed and the area under the curve (AUC) was calculated considering a 6dB threshold (D).

To determine lead information in atrial activity, QRST-subtraction was performed as described in Chapter 2. After this, LSSA analysis was performed as for the QRS segment.

3.4 Results

3.4.1 Effect of BSM lead Reduction using Lomb Spectral Analysis

A comparison of the results between the FFT spectra and Lomb spectra for a 3 second window is shown in Figure 3-3. The ECGs of the windows were plotted for visualising their correlation with the spectra. The LSSA showed a remarkable high power of spatial frequencies at about 0.0065 mm^{-1}. This maximal power changed during QRS peak to 0.0035 mm^{-1}. The power value also increased, as is especially visible on the FFT spectrum.

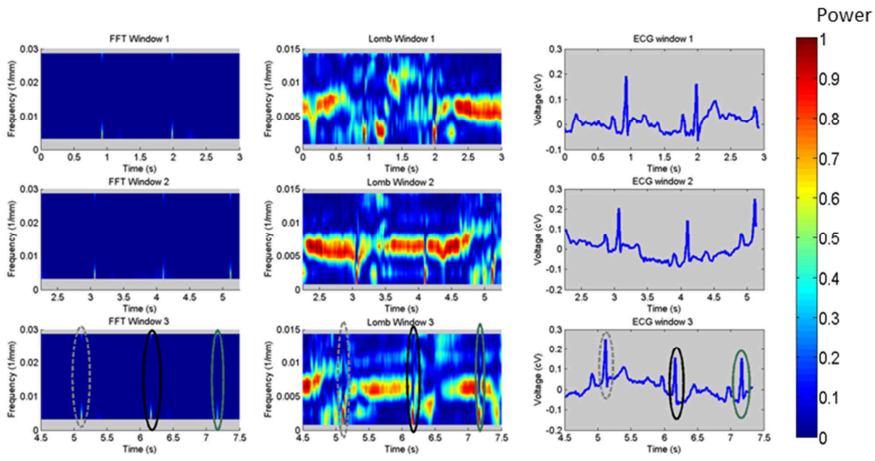

Figure 3-3: Comparison of 3 windows representing 3 seconds of the BSM signals. Left: the normalised Fourier power spectra show high-power spatial frequencies during the QRS interval (as indicated on the lower window). Middle: Normalised Lomb spectra show a dominant spatial frequency of about 0.0065 mm^{-1} during most of the BSM signal. This frequency lowers during QRS. Right: raw ECG signal from one of the BSM electrodes.

Since the QRS showed a remarkably distinct spectrum, a first analysis was focussed on 200 ms windows containing one QRS peak. The spectra for individual latitudinal and longitudinal strips consistently showed high power at low frequencies in the spectra, as e.g. shown in Figure 3-4.

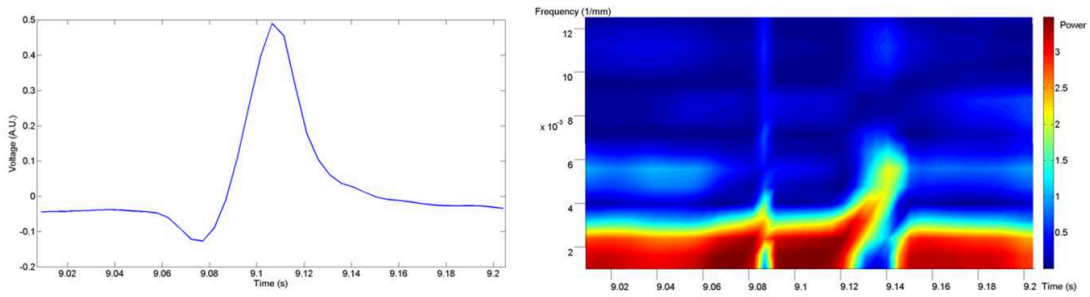

Figure 3-4: Lomb spectrum during one QRS interval. The spectrum shows the frequency power for each sample taken during the QRS complex. The spectrum of only one of the latitudinal electrode strips is shown.

For atrial activity measurements, spectra showed less consistency, with occasionally high power at high frequencies (Figure 3-5).

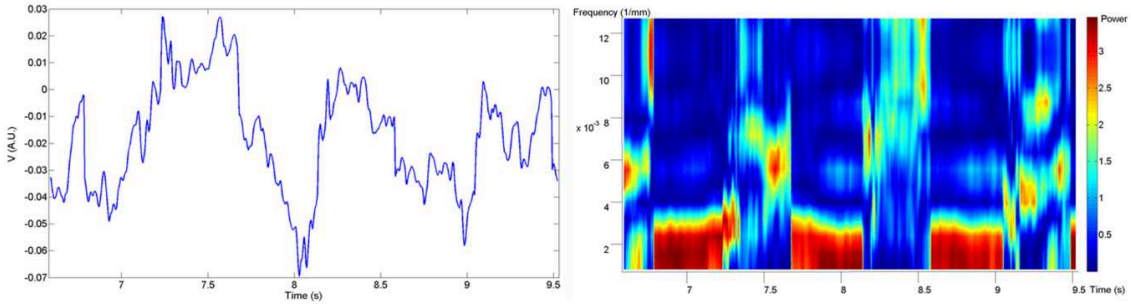

Figure 3-5: Lomb spectrum during atrial activity. The right figure shows the spatial frequency spectrum from each sample taken during the BSM interval shown left. The spectrum of only one of the latitudinal strips is shown.

The calculation of the AUC for each subject, over each sample considered, allowed for the estimation of how much of the total signal, generated by the 128-electrode system, could be reproduced with a reduced-lead system. The reproduction percentages for QRS intervals and atrial activity are shown in Figure 3-6 and Figure 3-7, respectively. For QRS complexes, a total of 6 electrodes in horizontal and vertical direction would allow the reproduction of 90% of the total BSM (36 electrodes in total). To reproduce the atrial activity with equal ratio, a total of 77 electrodes would be needed (11 horizontal by 7 vertical).

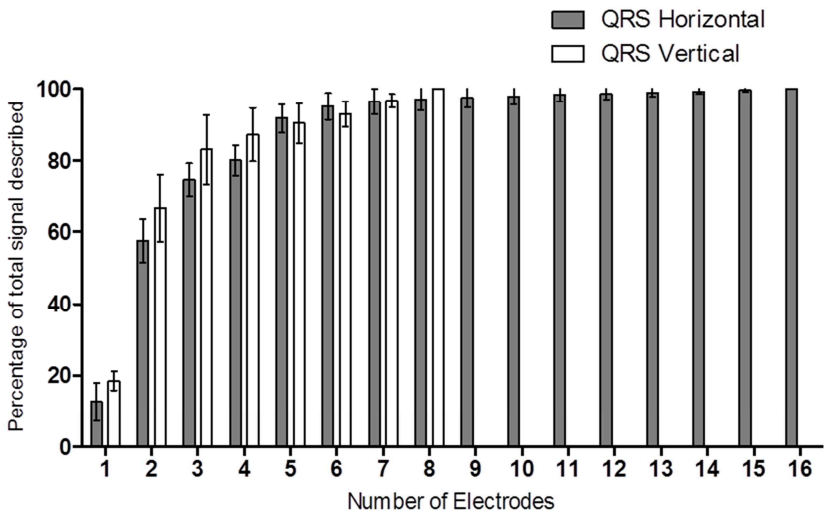

Figure 3-6: Average ratio of the signal reproduced by a subset of the total 128 electrodes for QRS intervals. Ratios are shown as a mean ± SD for all subjects over all strips.

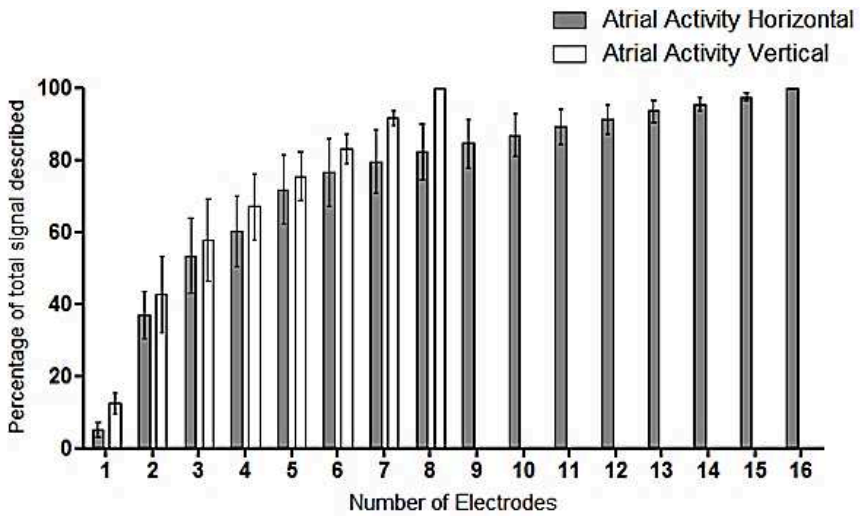

Figure 3-7: Average ratio of the signal reproduced by a subset of the total 128 electrodes for atrial activity. Ratios are shown as a mean ± SD for all subjects over all strips.

3.5 Discussion

A high increase in power could be observed in the Lomb and Fourier spectra during the QRS interval. This can be explained by the improved signal-to noise ratio during QRS. It also shows that the FFT, due to the assumption of uniform spacing, is unable to show possibly important spectral information. It was

therefore opted to use only Lomb-Scargle spectral measurements for more detailed analysis.

Since the QRS showed a remarkably distinct spectrum, a first analysis was performed on windows containing single QRS intervals. From these spectra, it could be observed that a low number of electrodes would be sufficient to reproduce almost complete information per electrode strip. High-frequency components of the signal could be attributed to measurement artefacts. For this purpose, a threshold was chosen for the calculation of the AUC of spectral functions (Evans *et al.*, 1989). From this, it could be estimated that most information acquired from the BSM could be reproduced by 36 equidistant electrodes, which is a similar number to the ones found in previous work (Barr *et al.*, 1971, Lux *et al.*, 1978).

During atrial activity, spectra showed less consistency. A higher number of 77 equidistant electrodes would be needed for atrial activity reconstruction. This would mainly be due to a reduced signal to noise ratio, although the effect of QRS removal on the BSM signal might also be a causing factor of high frequencies, albeit with low power. Reason for this is that, after the removal of the QRS complex, the atrial signal is interpolated over this interval, which occasionally leads to discontinuities in the signal. These discontinuities are interpreted as high-frequency components in spectral analysis. Further improvement in atrial activity interpolation is currently under investigation.

Different arguments have to be taken into account for a correct analysis of the graphs in Figure 3-6 and Figure 3-7. Firstly, the BSMs are estimated from 128 electrodes, which are assumed to provide the total body surface information. Since there is no gold standard for BSM recordings, the number of electrodes that were used in previous research varies from 20 to 400 electrodes (Taccardi *et al.*, 1998). Much information has been published regarding the number of electrodes is necessary to develop a ‘full’ BSM (Barr *et al.*, 1971, Finlay *et al.*, 2006, Hoekema *et al.*, 1999, Lux *et al.*, 1978). The previous ratios therefore have to be understood as a ratio with respect to the 128 electrode map, which is not necessarily identical to a full BSM map. However, the author argues that

128 measurement points should be sufficient for an appropriate analysis of cardiac activity.

Secondly, the position of the electrodes of the reduced-lead systems can be an argument. In essence, the Lomb spectrum provides a probability of the periodicities occurring within a signal (Lomb, 1976). Higher probabilities for a frequency are interpreted as a high chance that the main periodicity of the signal is the reciprocal of this frequency. This dominant frequency is therefore considered the Nyquist frequency, which determines the sampling frequency for a uniformly sampled system to reproduce the signal (Press *et al.*, 2002). Previous research has however shown that non-uniform electrode positioning allows for improved detail in BSM, with most electrodes placed on the left chest (Hoekema *et al.*, 1999, Taccardi *et al.*, 1998). The appropriateness of using Lomb as an individual method for producing reduced-lead BSM systems might therefore be insufficient. Similarly, however, current techniques (e.g. PCA) do not converge to an optimal BSM electrode positioning with a single setup (Finlay et al., 2006, Lux et al., 1978). Future research could focus on investigating the combination of Lomb analysis with alternative mathematical techniques that can evaluate optimal electrode positioning. One possibility could be structural similarity (SSIM), which is currently used in the comparison of images (Zhou *et al.*, 2004).

Lastly, the effect of reduced BSM systems on inverse solutions could be analysed further. Recent work has shown the possibility to reconstruct epicardial/pericardial signals from 12-lead ECG systems in cases with simple ventricular malfunctions such as premature ventricular contractions (PVCs) (van Dam *et al.*, 2013) and induced bundle branch blocks (BBBs) (van Dam *et al.*, 2014). An interesting point would be to further determine optimal lead number and position for inverse solution of other cardiac arrhythmias, as was shortly mentioned in a works by Messinger-Rapport, Barr and Cuffin (Barr *et al.*, 1970, Cuffin and Geselowitz, 1977, Messinger-Rapport and Rudy, 1990)

3.6 Study Limitations

Data were obtained from a limited number of healthy, young, male volunteers. This study group cannot be regarded as representative for the general

population. Other research projects in the field have had the advantage of larger study sizes (Barr et al., 1971, Finlay et al., 2006, Lux et al., 1978). Further investigation should also take into account various disease types, which could lead to a general or disease-specific BSM setup. However, as this research only desired to understand behaviour of the cardiac activity on the body surface using a body surface map, rigorous investigation of lead reduction was not considered.

3.7 Clinical Relevance of Findings

Optimisation of reduced-lead body surface maps is of major relevance to the clinical implementation of body surface mapping. By focussing on relevant components of the cardiac signal, improved diagnostic accuracy can be obtained compared to standard ECG analysis (Taccardi *et al.*, 1998). Reduced-lead systems allow these components to be analysed with minimal processing memory and time, as well as minimal application time of the body surface mapping electrodes to the patient. Especially the latter is of major importance to allow frequent use of body surface mapping for fast, accurate diagnosis of cardiac diseases, e.g. in emergency situations (Punske, 2003).

Reduction in body surface mapping has been investigated using a variety of methodologies. Here, the Lomb-Scargle Spectral Analysis was used. Although suboptimal, the importance of finding a similar number of necessary electrodes during QRS intervals compared to more advanced analytical tools provides further confirmation about the need for about 30 electrodes. Previous suggestions of 64 electrodes to account for complex behaviour therefore seem relevant (Hoekema *et al.*, 1998). Future technological advancements could look into implementing optimal 64-lead systems (vests) for optimal implementation of BSM in clinic.

3.8 Conclusion

Body surface mapping systems might have a significant impact on the current strategies of cardiac disease diagnosis. They would allow for more detailed, and therefore more accurate, diagnosis compared to standard ECG systems. However, due to the significant increase in amount of data, and the time

consumption for applying the system to the subject have prevented BSM analysis from becoming routinely implemented. Reduced-lead BSM systems were developed, but no standardised system has been suggested. In this chapter, further insight in lead reduction was obtained via Lomb-Scargle spectral analysis of spatial data from a 128-electrode BSM system. Results showed that smaller numbers of electrodes would be sufficient for capturing most of the information kept in the body surface signals, as was indicated by previous research. Interestingly, it was found here that, in case one is interested in atrial activity, a higher number of electrodes would be needed than for ventricular activity. This is probably mainly due to the lower strength of the atrial signals on the BSMs. Future research could look in further investigating optimal lead positioning for analysing atrial activity on BSM, as well as for providing optimal inverse solutions.

4 Forward and Inverse Solutions on Spherical Models

4.1 Introduction

The following chapter can be considered an introduction to chapters 5 and 6 in which inverse problems will be analysed for the inside-out (invasive) and outside-in (non-invasive) variants, respectively. As these real-life inverse problems encounter many difficulties due to the complexity of the volume conductor shape, as well as the influence of noise on the data, a theoretical appreciation and validation of the inverse problem model used as well as the effects of noise will be detailed below.

As highlighted in chapter 1, the volume conductor will be analysed according to the Boundary Element Method (BEM). The BEM assumes a solution towards (electrical) sources, and can be used to derive the potential at any point within a volume conductor according to equation (1-15) repeated here:

$$\Phi(\vec{x'}) = \Phi_{\infty}(\vec{x'}) - \frac{1}{4\pi}\int \Phi(\vec{x}) d\omega(\vec{x'}, \vec{x}) - \frac{1}{4\pi\sigma}\int \frac{J_n}{R} dS \qquad (4\text{-}1)$$

For solving this forward solution, one has to consider the effect of sources represented as a virtual double layer (middle integral of equation (4-1)) and as a virtual monolayer (right integral) affecting the infinite medium potential (Plonsey and van Oosterom, 2012).

To solve the forward solution and find potential on the irregularly shaped torso surface, the surface is subdivided into smaller elements, mostly triangles. In early applications, a forward solution would be calculated for the centre of gravity of these individual triangles, which would lead to unwanted, unrealistic discontinuities across the edges of neighbouring triangles (van Oosterom, 2012a). Nowadays, field points are considered to be at the vertices of triangles. This has the advantages that the points can coincide directly with real measurement points, and discontinuities between neighbouring triangles can be avoided. The source strength of the triangle is generally taken as the average of the values at the vertices (Barr *et al.*, 1977).

Another important progress was the proof of closed-form analytical expressions for virtual double layers (De Munck, 1992) and monolayers (van Oosterom,

2012a). These expressions can be used in the BEM, avoiding the need of numerical approaches to the solutions of sources on a triangle, which would give rise to errors (Meijs *et al.*, 1989). Besides this, the analytical expressions appear to reduce processing time significantly (van Oosterom, 2012a).

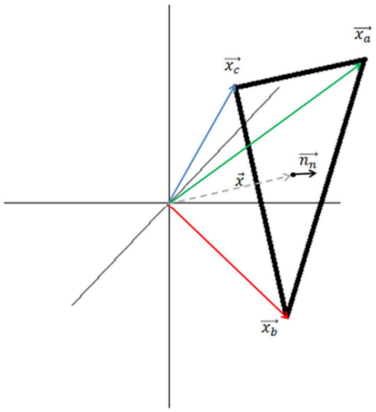

Figure 4-1: Setup for explanation of the monolayer source on a triangle (adapted from (van Oosterom, 2012b)).

For the monolayer source on a triangle, Figure 4-1 provides an overview of the setup, with the field point at the origin. In chapter 1 (equation (1-16)), the potential field from a monolayer source can be calculated as (van Oosterom, 2012a):

$$\Phi(o) = \frac{1}{4\pi\sigma}\int_{\Delta} \frac{J_{\Delta}(\vec{x})}{x} dS \tag{4-2}$$

Where o denotes the origin and x determines the distance of the triangle's centre of gravity from the origin.

For a linearly distributed monolayer, the monolayer strength can be written as:

$$J_{\Delta}(\vec{x}) = J(\overrightarrow{x_a})w_a(\vec{x}) + J(\overrightarrow{x_b})w_b(\vec{x}) + J(\overrightarrow{x_c})w_c(\vec{x}) \tag{4-3}$$

where w_a, w_b and w_c are linear shape functions with unit value at the indexed vertex of the triangle and zero at the others. This allows the integral of equation (4-3) to be broken up into 3 integrals such that:

$$\Phi(o) = \frac{1}{4\pi\sigma}\sum_{j=a,b,c} J(\overrightarrow{x_j})\int_{\Delta} \frac{w_j(\vec{x})}{x} dS \tag{4-4}$$

A numerical implementation for the integral is to be sought. By introducing the triple product $T = \overrightarrow{x_a} \times \overrightarrow{x_b} \cdot \overrightarrow{x_c}$ and $\overrightarrow{z_a} = \overrightarrow{x_b} \times \overrightarrow{x_c}$, each integral can be rewritten as:

$$\sum_{j=a,b,c} J(\overrightarrow{x_j}) \int_{\Delta} \frac{w_j(\vec{x})}{x} dS = \frac{1}{T} \overrightarrow{z_j} \cdot \int_{\Delta} \frac{\vec{x}}{x} dS \tag{4-5}$$

Recognising that addition of the individual integrals for each vertex would result in the integral for the entire triangle, and introducing an auxiliary function;

$$G = \overrightarrow{n_n} \times \sum_{j=a,b,c} \frac{\vec{r_j}}{T} \overrightarrow{z_j} \cdot \int_{\Delta} \frac{\vec{x}}{x} dS \tag{4-6}$$

van Oosterom could develop a matrix of linear systems:

$$\begin{bmatrix} N \\ u' \end{bmatrix} \Gamma = \begin{bmatrix} y \\ \Gamma_{\Delta} \end{bmatrix} \tag{4-7}$$

with N a $3x3$ matrix consisting of the vectors $\overrightarrow{n_n} \times \vec{r_j}$, u' a row vector of unit elements, $y = \sum_{j=a,b,c} \frac{\overrightarrow{e_j}}{e_j} I_{1,j}$ with $I_{1,j}$ denoting the line integral I_1 pertaining to edge j, and Γ_{Δ} integral (4-5) over the entire triangle (van Oosterom, 2012a). The least squares solution of this system then yields the numerical form for the integral in equation (4-4):

$$\Gamma = (Z' \boldsymbol{n}_n \Gamma_{\Delta} - E'_c E_n I_1)/n \tag{4-8}$$

With Z' the row vector of all z_j as defined above, E_c a matrix of edge coordinates for the source matrix, E_n a matrix of normalized edge vectors, n the norm of the triangle and $\boldsymbol{n}_n$ and I_1 the column vector of normalised norm and line integrals, respectively.

The potential field for a double layer was established as (equation (1-17)):

$$\Phi_{\infty}(\overrightarrow{x'}) = \frac{1}{4\pi\sigma} \int_S \frac{\vec{R} \cdot p(\vec{x})}{R^3} d\vec{S} \tag{4-9}$$

van Oosterom provided a rewritten formula of De Munck's (De Munck, 1992) formula for the analytical implementation of this source (van Oosterom, 2012a)**:**

$$\omega = (Z'\boldsymbol{n}_n\Omega_\Delta - E'_cE_n\gamma T)/n^2 \quad (4\text{-}10)$$

where ω is the weighted solid angles for the three vertices, similar to the value of Γ in equation (4-8). The calculation of these solid angles as the key factor in implementing double layers has been shown previously (Meijs *et al.*, 1989, Plonsey and Barr, 2007). The solid angle of the entire triangle is represented by Ω_Δ. The vector γ represents the line integrals.

Both equations (4-8) and (4-10) are needed to solve the forward solution as in equation (4-1). Before application of these formulas to complex shapes, a further intuition of these source distributions was developed.

4.1.1 Research Aims and Objectives

To further investigate the analytical expressions for solving the forward solution, a mathematical setup consisting of spherical shapes to represent the volume conductors was used to compare the forward solutions with analytical solutions for a dipole. These analytical solutions have been published previously (Cuffin and Cohen, 1979, Rudy *et al.*, 1979). This method was used to analyse both inside-out and outside-in forward solutions. Further intuition into the inverse solution was also established by using the forward models and applying various alterations to the signals on the balloon and torso sphere. The effect of variation in conductivity in the volume conductor was also investigated.

4.2 Methods

4.2.1 Source Triangle as seen from Different Observation Points

For further understanding of the double layer and monolayer fields obtained from a triangular source and observed from different field points, an arbitrary triangle was constructed with vertex 1 at [-1; 0.5; -0.5], vertex 2 at [1; 0.25; 0.2] and vertex 3 at [0.2; -0.25; -0.2] in Matlab. Two lines of field points crossing the triangle through the centre and third vertex where set up (Figure 4-2). This was achieved by plotting a line between the origin and the centre or vertical point, respectively. For this, the mean coordinates between the origin and the point on the triangle were calculated and subtracted from the original coordinates. The resulting coordinates were then assembled into a 2x3 matrix and the

covariance of the matrix was calculated. An eigenvector analysis was performed on the covariance matrix, and the eigenvector with the highest eigenvalue was used to fit an optimal line through the origin and the point on the triangle. Based on the eigenvector function, an interpolation was performed to obtain 200 field points on the line ranging from an x value between -1 and 1. The dipole layer and monolayer source strength were then measured for each field point according to the above equations.

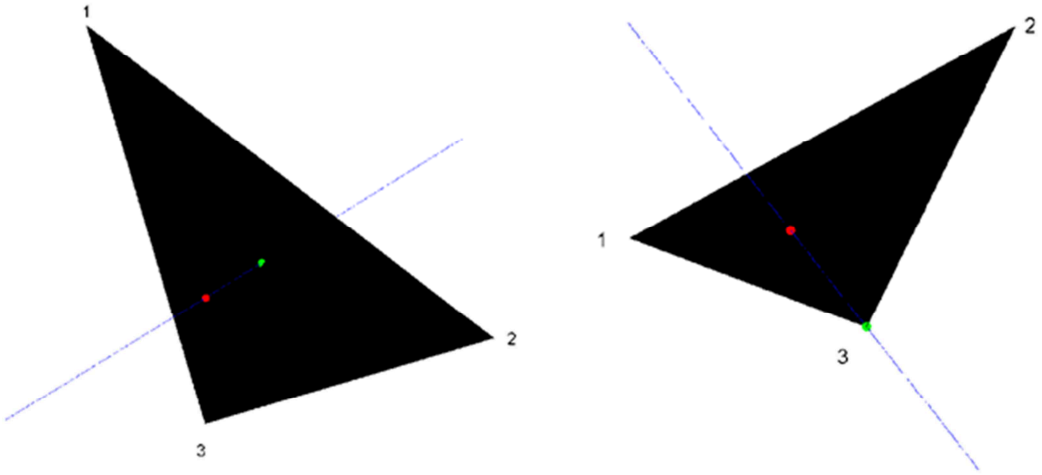

Figure 4-2: Setup of a source triangle with field points on a line passing through the centre (left) and third vertex (right) of the triangle. The point of crossing the triangle is indicated by a green dot. The red dot represents a second point used for orienting the line.

4.2.2 Inside-out Solutions on a Spherical Model

To study the implementation of the monolayer and double layer sources on the forward and inverse solution, homogeneous, spherical torso models were constructed including an eccentric endocardial and balloon sphere (Figure 4-3). Two models were constructed: one with a dense mesh for all spheres (642 nodes, 1280 triangles) and one with a scattered mesh (162 nodes, 320 triangles). A cardiac activity was simulated on a (pericardial) sphere concentric with and close to the endocardial sphere (radius = 0.4). Three dipoles with unit strength were positioned on each of the nodes of this sphere, directed parallel to the x-axis, y-axis and z-axis, respectively. The number of nodes on the pericardial sphere was equivalent to the other three spheres in the model

Analytical solutions for the torso, endocardial and balloon sphere were then calculated according to the formulas provided by Cuffin and Cohen (Cuffin and Cohen, 1979).

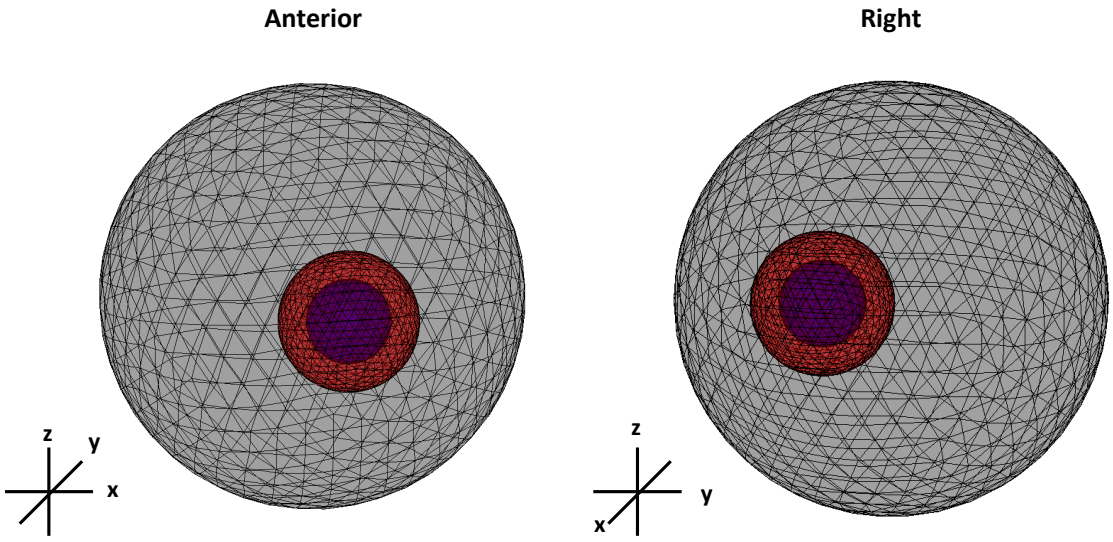

Figure 4-3: Setup of a homogeneous torso sphere with endocardial (red) and balloon (blue) sphere incorporated. All spheres consist of 642 nodes (1280 triangles). The torso sphere is centred around the origin (radius = 1), the cardiac sphere is centred around [1/3; 0; 0] (radius = 1/3). The balloon sphere is concentric with the heart (radius = 1/5).

4.2.2.1 Transfer matrix

For the inside-out problem, a forward solution was calculated from the pericardial data towards the balloon sphere according to equation (4-1). The transfer matrix included the infinite medium potential calculated for the double layer source on the pericardium. Each of the dipoles on the layer could successively be switched on and off for the analysis. During this procedure, the balloon was considered to be insulating (as expected from the EnSite Balloon Array), as well as conducting (as e.g. in contact basket catheters, conductivity equal to endocardial cavity). The pericardium was given unit conductivity. The equivalent sources taken into account were monolayer and double layer sources on the endocardium and a double layer source on the balloon in case the balloon was considered insulating.

Mathematically, the transfer matrix needs to be derived from the geometrical aspects and potentials on the endocardium to the balloon. For the geometrical transfer, the weights calculated in equation (4-8) for the monolayer and (4-10) for the double layer need to be included. The double layer weights are scaled by 4π as needed for the potential field computation (De Munck, 1992). For the potentials on the endocardium, a numerical form of (4-1) can be established as follows:

$$\Phi_E = \Omega_{EE}\Phi_E + \Gamma_{EE}J_E + \Omega_{EB}\Phi_B \tag{4-11}$$

where Ω_{jk} is the solid angle of a triangular element on the sphere related to node *j* seen from node *k*, $\Gamma_{j,k}$ is the distributed monolayer weight for element *j* as seen from node *k*, J_E is the monolayer strength, Φ_B is the infinite medium potential on the balloon and Φ_E the infinite medium potential on the endocardium, both calculated according to equation (1-18).

A similar equation can be set up for the potentials on the balloon:

$$\Phi_B = \Omega_{BE}\Phi_E + \Gamma_{BE}J_E + \Omega_{BB}\Phi_B \tag{4-12}$$

The forward transfer can then be derived as follows: assuming Φ_E is known from the analytical solution, the monolayer strength can be derived by rearranging (4-11):

$$\Gamma_{EE}J_E = \Phi_E - \Omega_{EE}\Phi_E + \Omega_{EB}\Phi_B \tag{4-13}$$

As Γ_{EE} is square and non-singular:

$$J_E = (\Gamma_{EE})^{-1}(\Phi_E - \Omega_{EE}\Phi_E + \Omega_{EB}\Phi_B) \tag{4-14}$$

Inserting (4-14) into (4-12) gives:

$$\Phi_B = \Omega_{BE}\Phi_E + \Gamma_{BE}(\Gamma_{EE})^{-1}(\Phi_E - \Omega_{EE}\Phi_E + \Omega_{EB}\Phi_B) + \Omega_{BB}\Phi_B \tag{4-15}$$

By stating that $\Gamma\Gamma_{BE} = \Gamma_{BE}(\Gamma_{EE})^{-1}$ and rearranging the formula to collect all terms related to the individual infinite medium potentials:

$$\Phi_B = [\Omega_{BE} + \Gamma\Gamma_{BE}(I - \Omega_{EE})]\Phi_E + (-\Gamma\Gamma_{BE}\Omega_{EB} + \Omega_{BB})\,\Phi_B \tag{4-16}$$

Here, I is an identity matrix of the appropriate dimensions. An auxiliary factor to the second term on the left of (4-16) was then used to distinguish between an insulating and conducting balloon:

$$\Phi_B = [\Omega_{BE} + \Gamma\Gamma_{BE}(I - \Omega_{EE})]\Phi_E + \delta(-\Gamma\Gamma_{BE}\Omega_{EB} + \Omega_{BB})\,\Phi_B \tag{4-17}$$

For a conducting balloon, δ equals 0 such that the non-existing double layer on the balloon can be dropped. For an insulating balloon, δ equals 1. This equation provides the numerical implementation of the forward solution. This could be rewritten as:

$$\Phi_B = [I - \delta(-\Gamma\Gamma_{BE}\Omega_{EB} + \Omega_{BB})]^{-1}[\Omega_{BE} + \Gamma\Gamma_{BE}(I - \Omega_{EE})]\Phi_E \tag{4-18}$$

This can be written in a matrix formulation:

$$\Phi_B = A\Phi_E \tag{4-19}$$

where A defines the weighted solid angles and distributed monolayer values for all nodes considered on the balloon and endocardium

Finally, rearranging (4-17) to solve the inverse solution would give:

$$\Phi_E = [\Omega_{BE} + \Gamma\Gamma_{BE}(I - \Omega_{EE})]^{-1}(I - \delta(-\Gamma\Gamma_{BE}\Omega_{EB} + \Omega_{BB}))\,\Phi_B \tag{4-20}$$

or, in matrix format

$$\Phi_E = A^{-1}\,\Phi_B \tag{4-21}$$

The accuracy of the forward solution was compared against the analytical solution for a variety of conductivity ratios between the balloon and the endocardial cavity, included in the transfer matrix for the infinite medium potentials (sigma value in (4-1)).

For each variation in conductivity, the transfer matrix was inverted and an inverse solution was calculated towards the endocardium. Two different regularisation functions were considered to understand their smoothing effect: a zero-order Tikhonov and second-order Tikhonov regularisation. Analytical balloon data were used for calculating the inverse solution. Different regularisation parameters were selected to determine the effect of the strength

of regularisation on the inverse solution. The Tikhonov regularisation can be written as:

$$\Phi_E = \min\|A\Phi_E - \Phi_B\|_F^2 + \lambda^2\|R\Phi_E\|_F^2 \tag{4-22}$$

with $R = I$ for zero-order Tikhonov and $R = L$, the surface Laplacian for second-order Tikhonov regularisation. Here, $\|...\|_F$ denotes the Frobenius norm.

For both forward and inverse solutions, differences between the numerical (Φ_N) and analytical (Φ_A) results were evaluated based on the residual error (RE):

$$RE = \frac{\|\Phi_N - \Phi_A\|_F}{\|\Phi_A\|_F} \tag{4-23}$$

4.2.3 Outside-in Solutions on a Spherical Model

To study the outside-in solutions, the same setup of Figure 4-3 was used for developing analytical solutions to the torso. For reasons that will be explained in the discussion, these solutions were only described for dipoles positioned at [0.5; 0; 0]. Again one dipole was oriented parallel to each of the axes. Forward and inverse solutions from the pericardium to the torso and endocardium, respectively, where analysed based on the source layer model described above. The transfer matrices were analysed similarly to equations (4-17) and (4-20) for the forward and inverse solution, respectively. In the formulae, the balloon potentials were exchanged for the torso potentials, and the endocardial for epicardial potentials. An additional step to aid the algorithm towards convergence was performed by applying the deflation technique as described by Lynn and Timlake (Lynn and Timlake, 1968a). The inverse solution was calculated for a zero-order and second-order Tikhonov regularisation.

To investigate the effect of reducing leads, a crude implementation was set up in which the analytical solutions for nodes under the x axis were replaced by an interpolation of the values at nodes above the x axis. The interpolation was performed using the surface Laplacian techniques as discussed in Chapter 2. Lastly, the effect of noise was investigated by adding Gaussian noise G with strength $\sigma = \{0; 0.15\}$ to the analytical solution using Matlab's *randn* function and following equation:

$$\Phi_G = \Phi_A + \sigma G \tag{4-24}$$

4.3 Results

4.3.1 Source Triangle as seen from Different Observation Points

Figure 4-4 shows the resulting monolayer and dipole layer strength as observed from different field points on a line through the centre (A and C) and the third vertex (B and D, third vertex as indicated in Figure 4-2) of a source triangle. The arrows indicate the point at which the line crosses the sources triangle. A strong discontinuity can be observed in the double layer 'potentials'. Besides this, the source behaviour of the triangle resembles strongly the source behaviour on the third vertex when the line passes through this point. For a line passing through the centre, the triangular source strength appears as a more equal contribution of the source strengths at all the vertices on the field points.

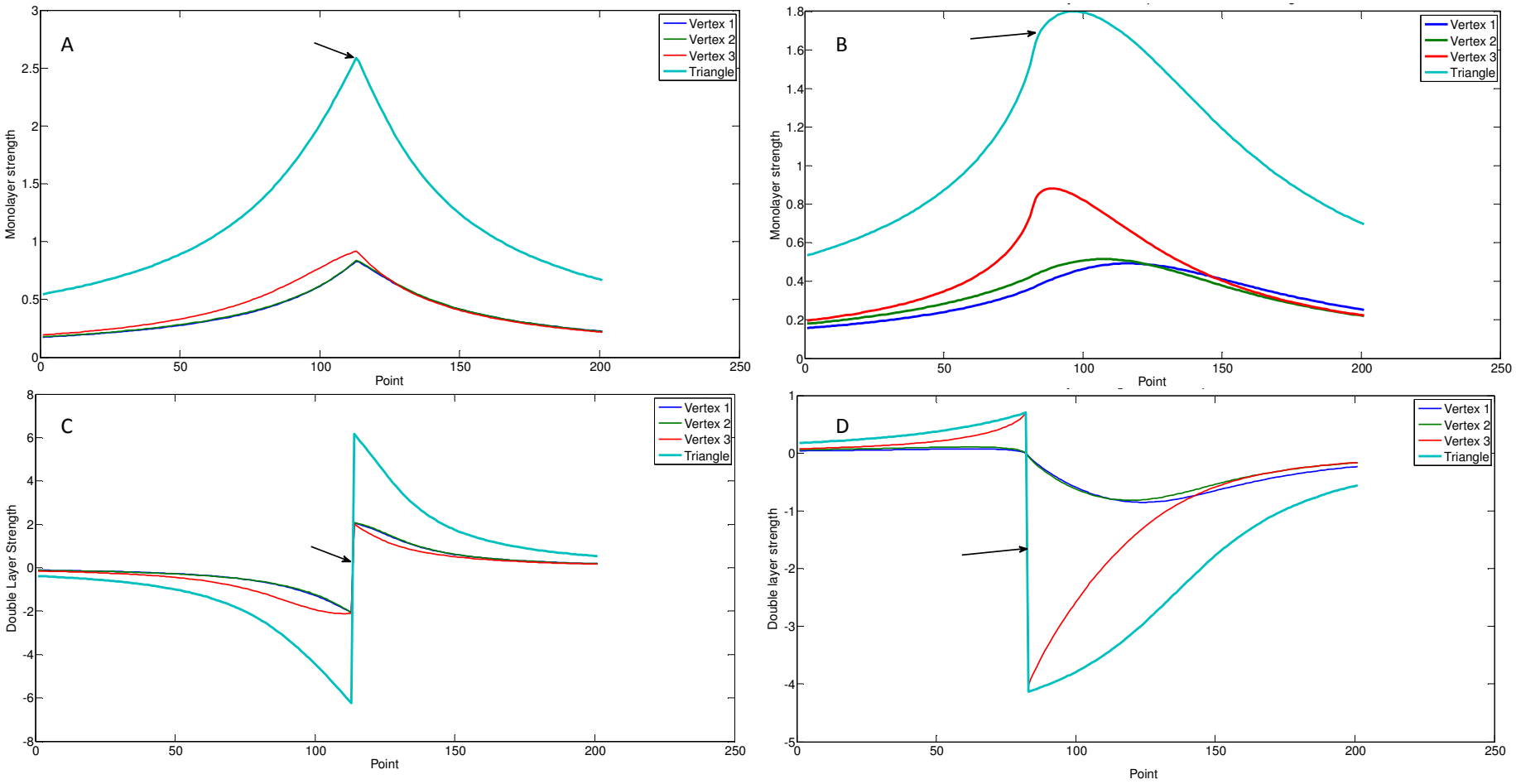

Figure 4-4: Top: Monolayer source as seen from different points on a line passing through the centre (A) or third vertex (B). Bottom: Double layer source for a line through the centre (C) and third vertex (D). Arrows indicate points at which the triangle is crossed.

4.3.2 Inside-out Solutions on a Spherical Model

A comparison between forward and analytical inside-out solution for the pericardial sphere toward the balloon sphere is shown in Figure 4-5. These results can be generalised to all other pericardial dipoles under investigation.

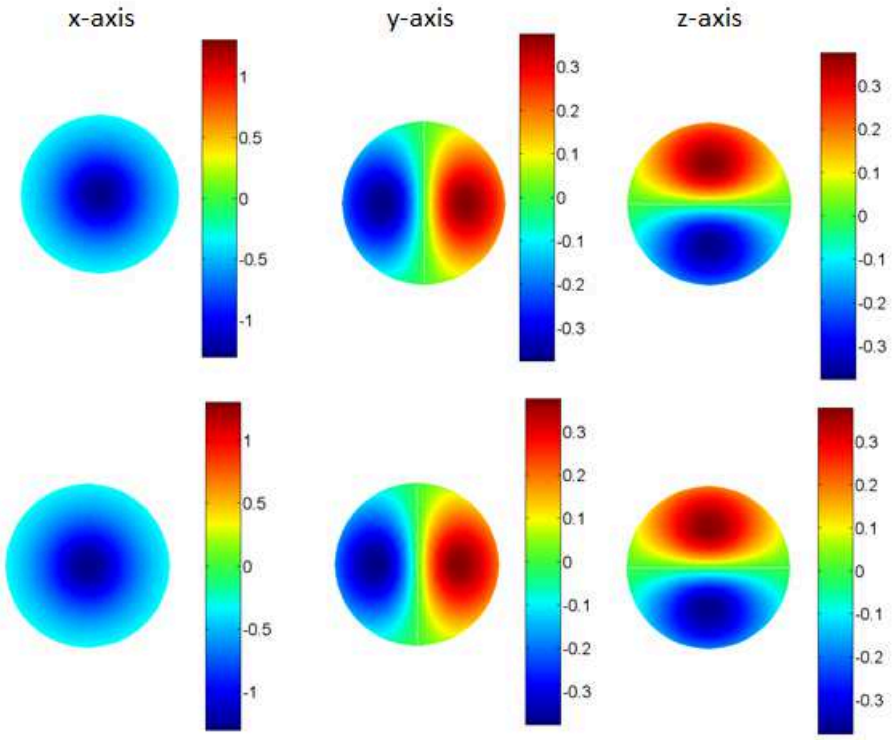

Figure 4-5: Comparison of the analytical (top) and forward (bottom) solutions on the balloon sphere for a dipole positioned at [0.73; -4.67e^{-17}; 0]. The axis labels indicate to which axis the dipole is parallel. The conductivity ratio was 1-5-0 (Torso-Endocardium-Balloon).

As seen in Figure 4-6, an almost perfect correlation could be obtained between the 'potentials' measured from the forward and analytical solution. The figure shows the examples for a model where the endocardium has a conductivity 5 times higher than the pericardium and the balloon is considered to be insulating (RE = 0.001). The REs of other setups are given in Table 4-1 and Table 4-2 for dense and crude triangulations, respectively.

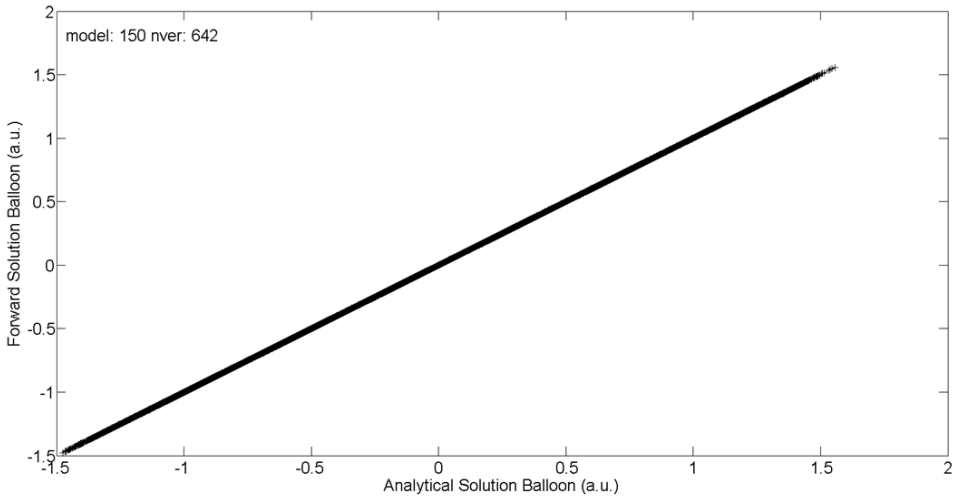

Figure 4-6: Regression analysis between the analytical and forward solution to the balloon sphere with 642 triangles. The conductivity of the endocardial volume was 5 times higher than the pericardium. The balloon was considered insulating.

Figure 4-7 shows the results of an inverse solution using second-order Tikhonov regularisation with a regularisation factor equal to 0.46. A good correlation can be observed. However, the inverse solution shows some small errors, especially in the bordering of the positive and negative sides of the dipole parallel to the z-axis (RE = 0.055).

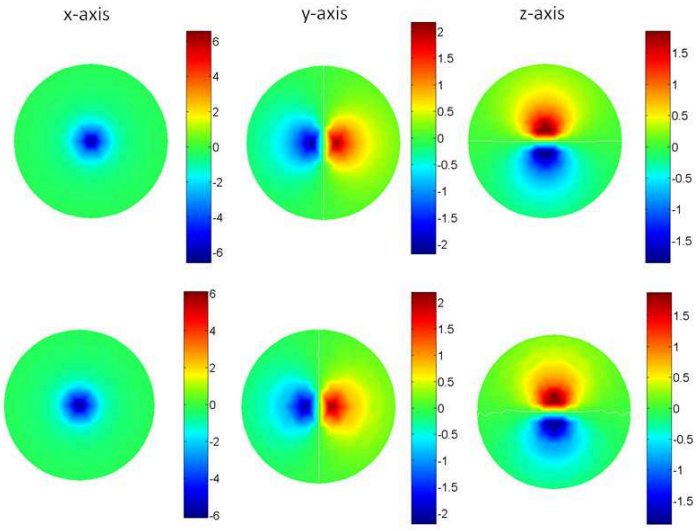

Figure 4-7: Comparison of analytical (top) and inverse (bottom) solutions on the endocardial sphere. Dipole specifications are the same as in Figure 4-5. A regularisation factor of $\lambda = 0.46$ was used.

The increase in RE for the inverse compared to the forward solution can be easily observed in Figure 4-8. This graph shows the relation between the analytical and inverse solution on the endocardium for the same setup as in Figure 4-6. From the graph, it appears that two different linear relations exist between the analytical and inverse solution.

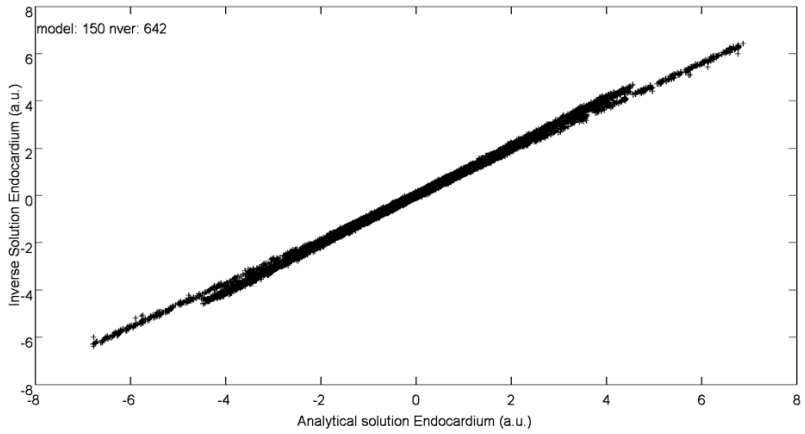

Figure 4-8: Regression analysis between the analytical and inverse solution to the endocardial sphere. The setup was identical to the one in Figure 4-6.

The effect of regularisation on the inside-out inverse solution was also studied. From Figure 4-9, it can be observed that very low regularisation leads to high errors between the analytical and inverse solution. However, for regularisation parameters as low as 0.1, relatively accurate inverse solutions can be obtained (RE < 0.1).

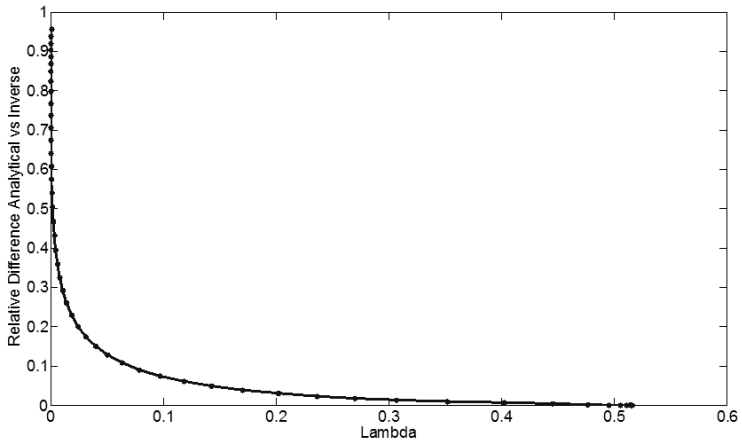

Figure 4-9: Comparison of the relative differences between the analytical and inverse inside-out solution for different regularisation parameters (lambda). Conductivity ratios were used as per Figure 4-5

Table 4-1: Relative errors for forward and inverse solutions under different conductivity ratios for spheres of 642 triangles.

Conductivity (Torso-Endocardium-Balloon)	Zero-order Tikhonov		Second-order Tikhonov	
	Relative Error Forward	Relative Error Inverse	Relative Error Forward	Relative Error Inverse
1-5-0	0.001	0.059	0.001	0.055
1-4-0	0.001	0.067	0.001	0.063
1-5-5	0.001	0.067	0.001	0.064
1-4-4	0.001	0.073	0.001	0.070
1-3-0	0.001	0.078	0.001	0.074
1-3-3	0.001	0.082	0.001	0.079
1-2-0	0.002	0.095	0.002	0.090
1-2-2	0.001	0.098	0.001	0.093
1-1-0	0.003	0.125	0.003	0.119
1-1-1	0.003	0.128	0.003	0.122

Table 4-2: Relative errors for forward and inverse solutions under different conductivity ratios for spheres of 162 triangles.

Conductivity (Torso-Endocardium-Balloon)	Zero-order Tikhonov		Second-order Tikhonov	
	Relative Error Forward	Relative Error Inverse	Relative Error Forward	Relative Error Inverse
1-5-0	0.021	0.099	0.021	0.099
1-4-0	0.021	0.099	0.021	0.099
1-5-5	0.017	0.102	0.017	0.102
1-4-4	0.020	0.114	0.020	0.114
1-3-0	0.031	0.124	0.031	0.124
1-3-3	0.026	0.129	0.026	0.129
1-2-0	0.041	0.148	0.041	0.148
1-2-2	0.036	0.153	0.036	0.153
1-1-0	0.067	0.210	0.067	0.210
1-1-1	0.062	0.214	0.062	0.214

4.3.3 Outside-in Solutions

A comparison between the analytical and forward solution for a homogeneous torso sphere is shown in Figure 4-10. The results for a pericardial dipole source at [0.5; 0; 0] are considered. A good correlation could be found between both solutions, however, the forward solution seems to be a diluted (blurred) representation of the analytical solution (RE=0.037).

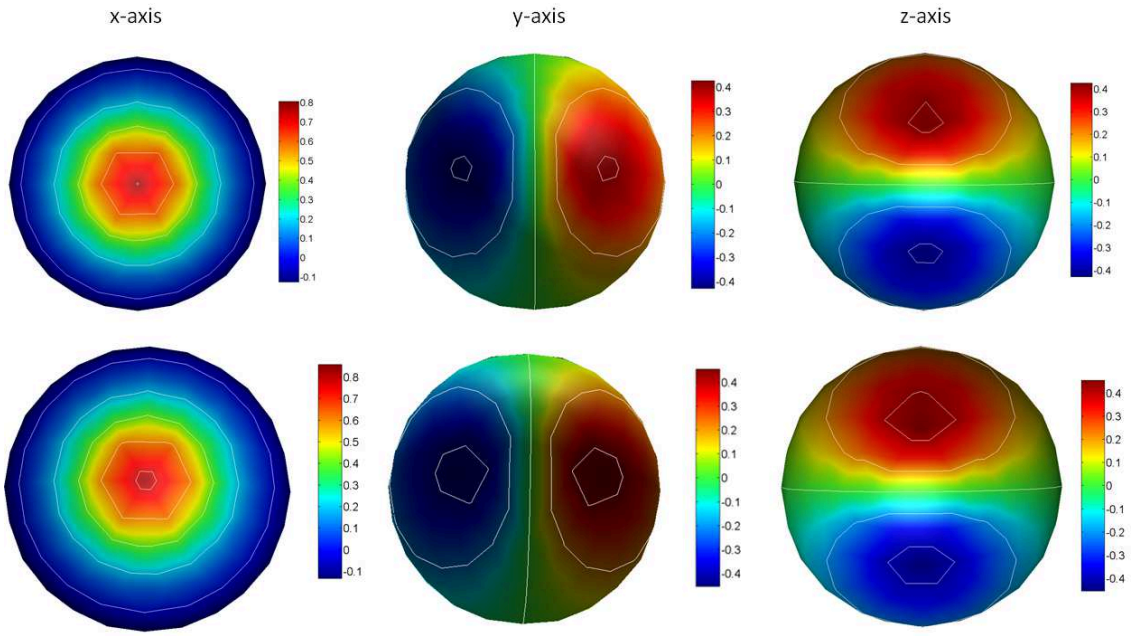

Figure 4-10: Comparison of the analytical (top) and forward (bottom) solution for the torso sphere. Measurements are in arbitrary units. The dipole is positioned at [0.5; 0; 0].

The results for an inverse solution from the analytical torso data towards the endocardium are compared with the analytical solution on the endocardium in Figure 4-11. Without regularisation, a relatively accurate (RE=0.113) could be obtained. However, the inverse solution appears to underestimate the 'potentials'. It further shows a difference in the position of the isopotential lines, making the centre of the dipole smaller in the inverse compared to the analytical solution.

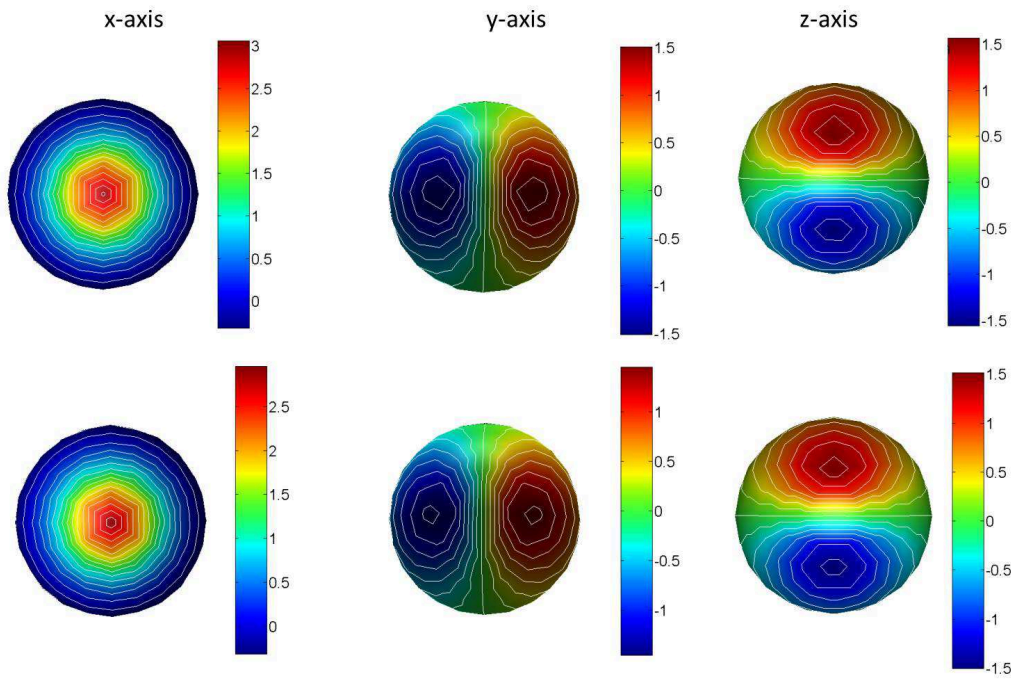

Figure 4-11: Comparison of analytical (top) and inverse (bottom) outside-in inverse solutions without regularisation.

Further tests on the outside-in inverse solution focussed on the effect of removing and interpolating data from half of the nodes. Figure 4-12 shows the results of the inverse solution when the bottom half of torso data is interpolated. Without regularisation, a significant effect on the inverse solution occurs, leaving high errors compared to the analytical solution (RE=0.691). These errors could be reduced with a second-order Tikhonov regularisation (RE=0.486).

Similarly, the effect of noise on the torso data was briefly investigated. Figure 4-13 and Figure 4-14 show the results for a Gaussian noise with a strength 5% and 15% compared to the analytical values, respectively. Without regularisation, the correlation between the inverse and analytical solution on the endocardium is completely lost. A regularisation parameter of 0.5 allows for a reconstruction of the basic morphology of the dipole behaviour, but strong errors continue to exist (RE=0.772). Stronger noise effects do not allow for any accurate reconstruction, irrespective of smoothing.

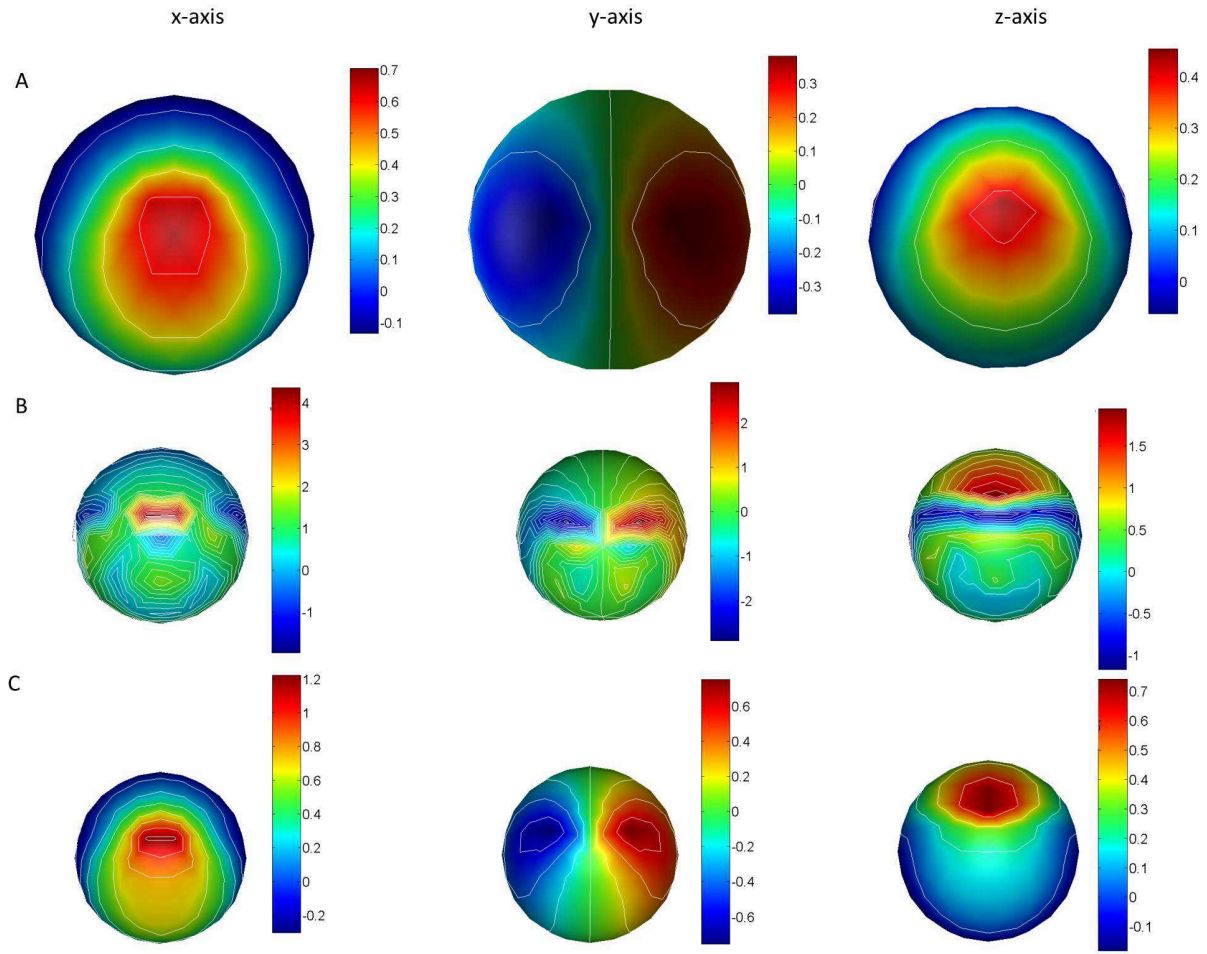

Figure 4-12: A) Analytical solution on torso with bottom nodes interpolated. B) Inverse solution without regularisation. C) Inverse solution with second-order Tlkhonov regularisation ($\lambda = 0.5$).

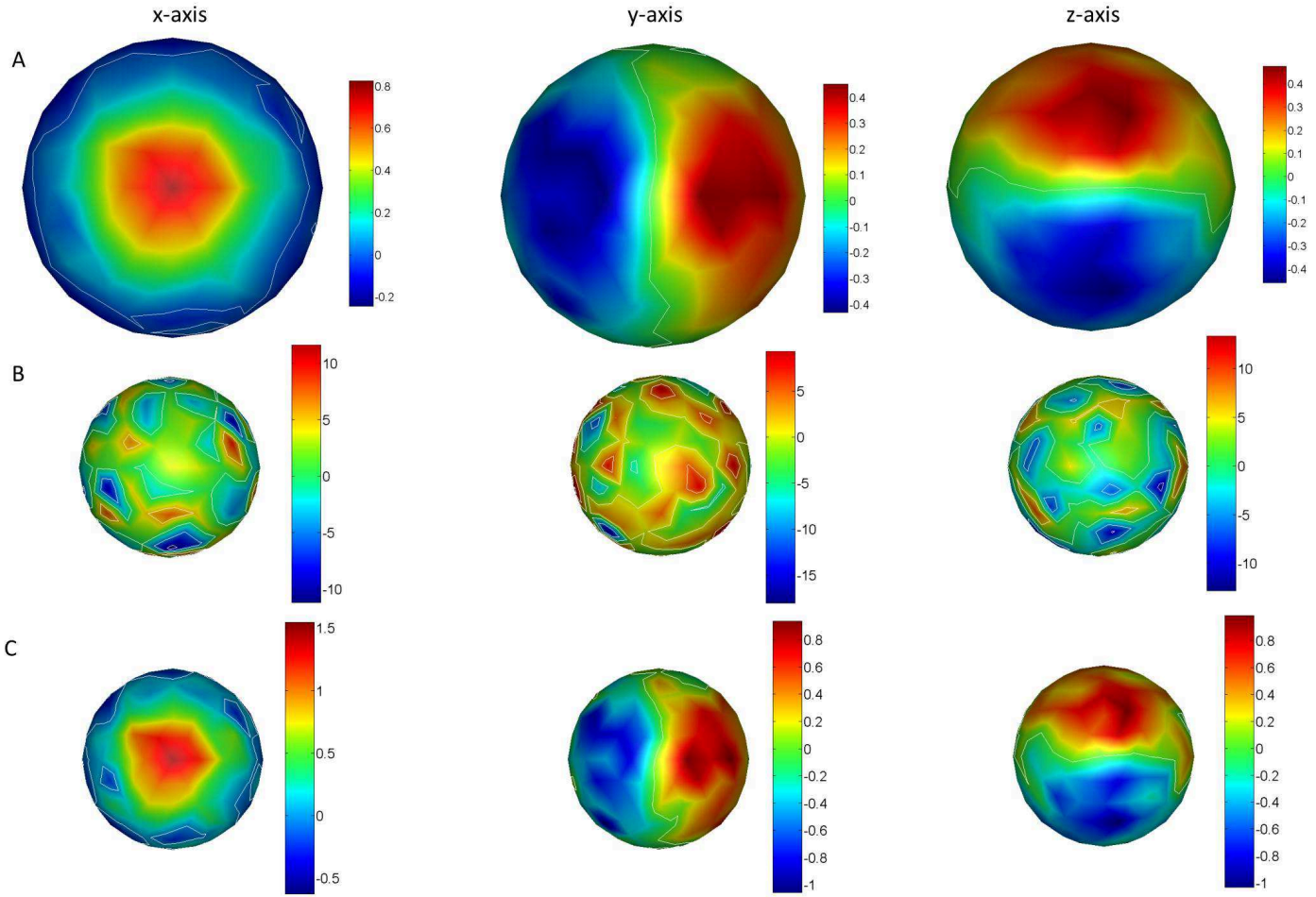

Figure 4-13: A) Analytical solution on torso with noise ($\sigma = 0.05$). B) Inverse solution with no regularisation. C) Inverse solution with second-order Tikhonov regularisation ($\lambda = 0.5$).

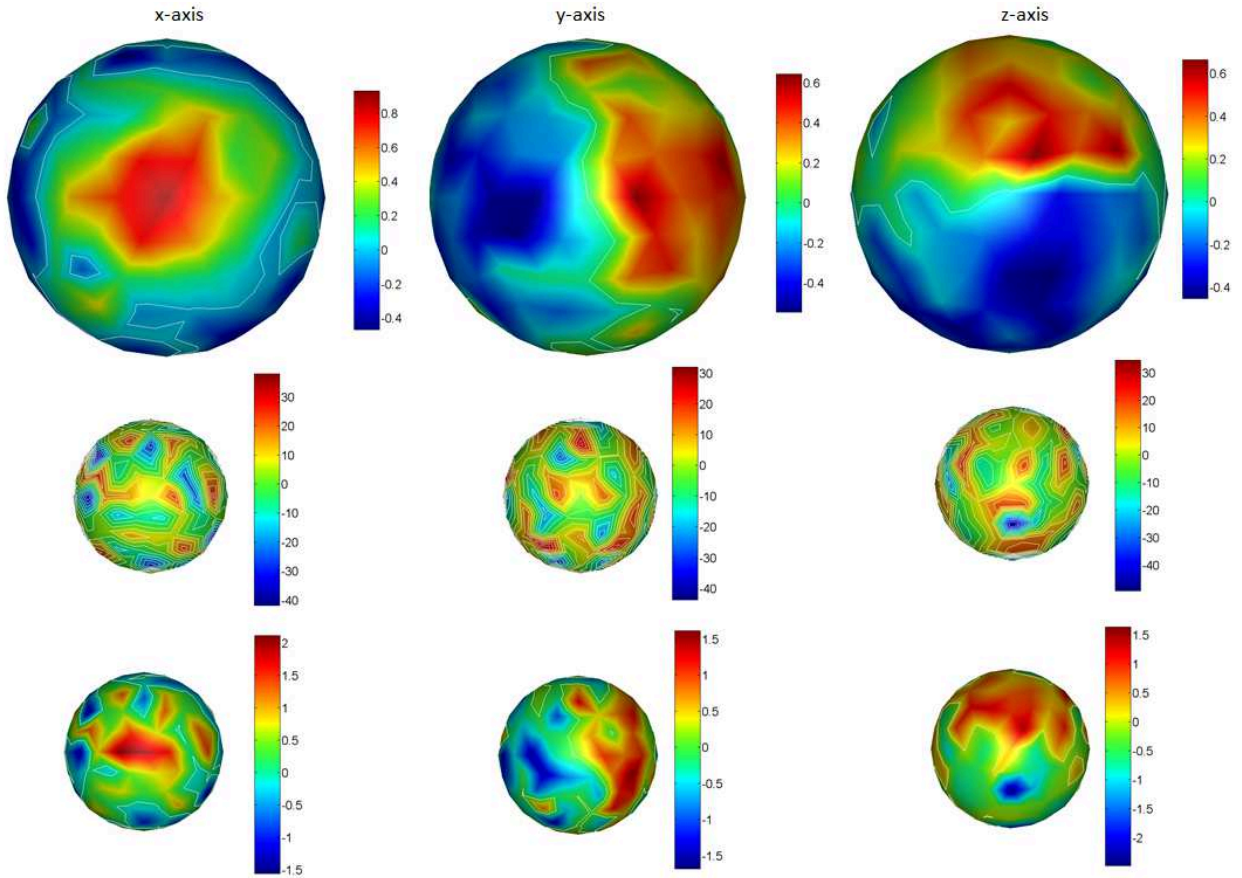

Figure 4-14: A) Analytical solution on torso with noise ($\sigma = 0.15$). B) Inverse solution with no regularisation. C) Inverse solution with second-order Tikhonov regularisation ($\lambda = 0.5$).

4.4 Discussion

4.4.1 Source Triangle as seen from Different Observation Points

The reason for attempting to represent the active and passive sources of the heart and volume conductor as monolayer and dipole layer sources is derived from a biological perspective. A moving double layer, in the sense that at each sample taken during the cardiac cycle the double layer moves, appears to resemble activation and repolarisation wave fronts (Plonsey and van Oosterom, 2012). For the activation wave front, the double layer represents the border before which cardiac cells have depolarised. The cells to which the double layer has to migrate are still in a resting phase. A similar analogy can be set up for the repolarisation phase. Monolayers can be of interest to represent charge layers, which include areas within the volume conductor that differ in conductivity (e.g. blood cavity) (Panofsky and Phillips, 2005).

The left graphs of Figure 4-4 show the classical examples of a monolayer and double layer triangular source as seen from different field points on the line passing through the centre of that triangle, as e.g. in Panofsky and Phillips (Panofsky and Phillips, 2005). The double layer is characterised by a discontinuity when the field point crosses the triangle. The monolayer on the other hand shows a discontinuity in the slope when crossing the triangle. Comparing these observations with previous literature (Panofsky and Phillips, 2005, van Oosterom, 2012a), it could be assumed that the implementation of the source model layers was accurate.

It can also be observed that the source fields are appreciated differently when the field point is positioned at different locations. When the field points are situated on a line crossing the triangle through a vertex, this vertex gives a more significant contribution to the observation of the total triangular source. From this, it can thus be understood that changes in the position of the cardiac source affect ECG signals over time and space.

4.4.2 Inside-out Solutions on a Spherical Model

The forward and inverse solution methodology for the inside-out model (balloon to endocardium) was tested on a spherical model before implementation on patient-specific models. The reason for this was to understand better the inherent errors that might occur when solving inverse problems for which no gold standard is available. On spheres, the forward and inverse algorithms can be tested against analytical solutions for dipoles and therefore can be used as a simulation study to test the accuracy of inverse problem algorithms. As the analysis provided in this thesis can only estimate equivalent sources (van Oosterom and Oostendorp, 1992b), the models were set up such that the endocardial sphere was close to but not on the source layer.

Figure 4-5 provides a comparison between the analytical and forward solution for one of the dipole sources on the pericardium towards the balloon sphere. From the relative error, it could be shown that an almost exact reproduction of the analytical solution is possible. This accuracy could be obtained for each of the individual dipole sources, which avoided the need of reproducing all data for the outside-in forward solution.

A relative error of 5.5% was obtained for the inverse solution from the analytical balloon data to the endocardial sphere. This result is similar to other simulation studies investigating the inside-out inverse problem (Khoury *et al.*, 1995). It shows that even under perfect conditions, small errors will occur in the inverse solution, even after regularisation. Regularisation is, however, effective in diminishing the error, as can be observed from Figure 4-9. In this work, zero- and second-order Tikhonov regularisations were tested. Results showed that second-order Tikhonov allowed a marginally better reconstruction of the analytical data on the dense triangulation model. From previous work, it appears that the best form of regularisation might depend on which source model is used to represent cardiac activity (Messinger-Rapport and Rudy, 1988, Cheng *et al.*, 2003a). Although not included in this study, the method for choosing the optimal regularisation parameter might also affect the choice of the optimal regularisation function.

From the regression analysis shown in Figure 4-8, two linear behaviours appeared to occur in the relationship between analytical and inverse endocardial solutions. The exact reason for this is unknown, but might be due to numerical rounding or small errors in the auto-solid angle measurement (Meijs *et al.*, 1989). Higher density of the triangular mesh also seems to reduce this behaviour, and therefore the relative error with the analytical solution.

From Table 4-1 and Table 4-2, it can be observed that, assuming a dipole source, it is of importance to include heterogeneity for obtaining more accurate forward and inverse solutions. A higher blood cavity-to-torso conductivity ratio appeared to improve the solutions significantly. Here, conductivity ratios up to 5:1 were tested, as this was sufficient to keep all the inverse solutions under a relative error of 10%. Furthermore, assuming a non-conductive balloon appeared to provide marginally better results than a conducting basket.

Previous work has suggested including the Brody effect in the calculations (Khoury *et al.*, 1995). Also, for the outside-in inverse solution the need for including inhomogeneities to optimise source estimation has been shown (Klepfer *et al.*, 1997, van Dam and van Oosterom, 2005). Ramanathan and co-workers however suggested that torso homogeneity may be assumed in case one is interested specifically in estimating global behaviour of the cardiac activity (Ramanathan and Rudy, 2001). Much debate is still ongoing on the use of heterogeneities, regularisation techniques and regularisation parameter choice. As this discussion is beyond the scope of the current thesis, no deeper analysis was performed for these issues. In the later chapters, the EnSite balloon inverse solution was considered a gold standard to which the regularisation was standardised.

4.4.3 Outside-In Solutions

To study the forward and inverse solutions for monolayer and dipole layer equivalent sources, an analytical solution for a dipole source was set up in a homogeneous torso. Figure 4-10 and Figure 4-11 show the comparison between the forward and analytical solution and inverse and analytical solution, respectively. Small variations in morphology and ‘potentials’ can be observed for both cases, possibly due to small numerical errors in the algorithms as

discussed for the inside-out solution. No heterogeneities were investigated, but previous work has shown that the inclusion of heterogeneities can have significant influence on both the forward and inverse solution (Messinger-Rapport and Rudy, 1988, Messinger-Rapport and Rudy, 1986). Again, as the analysis was performed on simple, regular shapes, the fact that errors do occur, even after regularisation, means that any outside-in forward and especially inverse solution has to be treated with care.

This is especially evident in the small tests that were performed including the interpolation of signals as well as the addition of Gaussian noise. For the interpolation data, a relatively satisfying reproduction of the endocardial analytical solution can be obtained after regularisation, however the relative error increased significantly. In the study by Messinger-Rapport, some attention was given on inverse solutions with reduced lead systems on a sphere. Even with careful selection of the position of the leads in the reduced system, higher errors would occur compared to a complete lead (Messinger-Rapport and Rudy, 1990). Studies by Barr and Cuffin found a possibility to optimally reduce the number of leads for a uniform double layer source, without losing much accuracy in the inverse solution (Barr *et al.*, 1970, Cuffin and Geselowitz, 1977). Further research into this might be of interest, as recent works have suggested that at least cardiac activity of simple disorders can be reconstructed with reduced lead systems (van Dam *et al.*, 2013).

As for the noise tests, and due to the ill-posedness of the inverse solution, it can be observed that Gaussian noise of strengths of 15% compared to the original signal can make a reconstruction of the equivalent sources extremely challenging, such that only a grasp of the morphology of the source behaviour can be reconstructed. The quality of the recorded data is therefore of high importance (van Oosterom, 2012c). For the reconstruction from noisy data, signal processing such as filtering and baseline correction can be of aid, taking into account that these processes might affect signal morphology and therefore can decrease the accuracy of the inverse solution.

4.5 Conclusion

To obtain an improved understanding of the concepts behind the forward and inverse problems in electrocardiology, inside-out and outside-in algorithms were compared with analytical solutions for spherical volume conductors. The results show that, even under strongly controlled environments, small errors will occur in the inverse solutions. These errors can be reduced by including more measurement points. Inclusion of heterogeneities can also improve the accuracy of forward and inverse solution. Besides this, one has to take into account the significant errors that can be induced due to noise and removal of measurement points. Regularisation can only improve the inverse solution to a certain extent. The results of these experiments were taken into account for the inside-out and outside-in solutions towards patient-specific models.

5 The Inside-Out Inverse solution: A Comparison of Two Source Models

5.1 Introduction

Over the last two decades, interest in clinical applications of the inverse problem of electrocardiology has risen significantly. This is mostly due to the enormous progress that has been made in solving this problem (van Oosterom, 2012c). Most applications have been based on solving the inside-out inverse problem, in which a balloon catheter is placed inside the cardiac cavity of interest, and endocardial signals are estimated (Jarman *et al.*, 2012, Lemery *et al.*, 2004, Salinet Jr *et al.*, 2010, Schilling *et al.*, 2000). The array that is mostly used for this purpose is the EnSite Balloon Array (St Jude Medical), which consists of 64 electrodes. The EnSite system solves the inverse problem based on an equivalent potential source: it uses the voltages measured on the balloon to estimate the voltages on a layer close to the endocardial surface (Khoury *et al.*, 1995). This inverse problem is solved to 64 nodes on the endocardial surface, from which a further interpolation to 2048 electrodes can be obtained (Salinet Jr *et al.*, 2010).

Some issues have been found while using this system, however. As the source model is potential-based, no reflection of the exact cardiac source is possible, making the electrophysiological relevance of the solution harder to understand (van Oosterom, 2012c). Besides this, correlations between the estimated endocardial electrograms and contact data are generally only reasonable. Jarman *et al.* showed a correlation of 0.7±0.15 for 62 random locations in the left atrium (Jarman *et al.*, 2012). Schilling *et al.* found a correlation of 0.74±0.19 for 3600 electrograms tested in the right atrium (Schilling *et al.*, 2000). For ventricular data, better cross-correlations were found up to 0.87±0.12. In the same work it was shown that correlation decreased with increasing distance between the endocardial node and the balloon (Schilling *et al.*, 1998). The loss of 100% correlation could be due to effects of noise on the data, the issue of dealing with a closed commercial system makes it hard to test the system and develop possible improvements in the source setup, meshing and regularisation.

Some clear improvements can be made, as shown e.g. in Figure 5-1. Here, a left atrial mesh is shown as exported from the EnSite Velocity system. The mesh appears to converge into 2 poles, and different sizes of the elemental triangles can be observed. Converging of many triangles into a single point should be avoided, as it distorts the inverse solution and interpolation. This might give rise to misinterpretations of the data. Besides this, it is known that for best results, the elemental shapes of a complex geometry should be similar in area (Brebbia and Dominguez, 1996, Haueisen *et al.*, 2002), which is not the case for the EnSite mesh. An improved method for meshing the cardiac cavity from the EnSite system, based on the 64 points to which an inverse solution is directly calculated will be provided in this chapter.

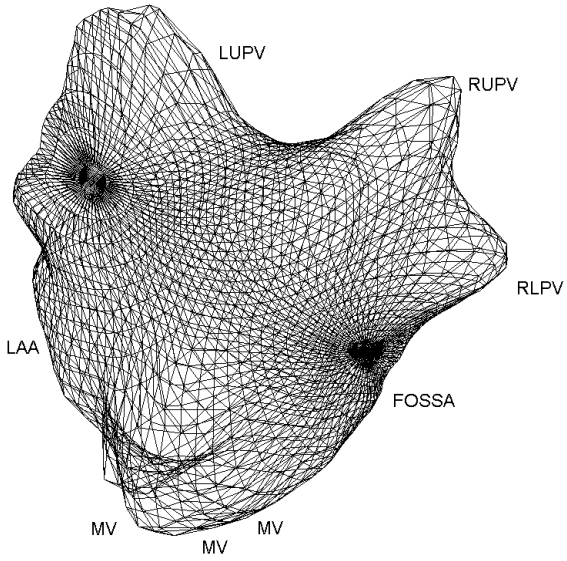

Figure 5-1: Example of a triangulated mesh as exported from the EnSite Velocity system. A convergence to two poles can be observed, as well as a strong variation in the area of the triangles.

Besides this, as the outside-in inverse solution in Chapter 6 will be based on a current density source, the EnSite inside-out inverse solution (referred to as EnS) will be reformulated towards a similar source, represented as a combination of dipole layers and monolayers (referred to as the UoL inside-out solution). Regularisation will be adjusted towards the inverse solution as provided by the EnSite system, which can be considered a clinical gold standard for inside-out inverse problems. The inside-out inverse solution can

then be better compared to its outside-in counterpart, as a similar equivalent source representation will be considered.

As it has been shown in previous literature, a good agreement between dominant frequencies (DFs) can be obtained between inverse solutions from the EnSite Array and contact electrograms (Jarman *et al.*, 2012). The main focus in this thesis will be on comparing DFs between the inside-out solutions, body surface maps and the outside-in solution.

5.1.1 Research Aims and Objectives

To allow a direct comparison between inside-out and outside-in inverse solutions, the EnS inverse solution was reformulated to equivalent current-density sources based on double layer and monolayer models. This reformulation took into account a remeshing of the atrial cavity. Only data of the left atrium were considered, as balloon data were available for this atrium only. The results of the new inverse solution are compared to the EnS solution. In chapter 6, the results will be compared to outside-in inverse solutions to provide further understanding of cardiac activity during AF. Most attention will be focussed on dominant frequency analysis. Here, the effect of an alteration of the equivalent source on the DF value will be considered.

5.2 Methods

As no torso models were available for the last 4 volunteers of the cohort at the time of writing this thesis, only data for the first 5 volunteers as discussed in Chapter 2 will be provided.

For each subject, left atrial geometry and balloon signals were exported from the EnSite Velocity system. Besides this, the LA virtual electrograms and ECG data were made available (see Table 2-2 for details). Labels for orientation and lesions representing ablated areas were also provided. Signals were exported as raw data and filtered. The same filtering setups were used as provided in section 2.2.5. Resampling and alignment of the signals was also performed similarly to the method described in section 2.2.6.2.

5.2.1 Remeshing the Left Atrium

The EnSite Velocity system allows exporting the Balloon Array wave forms together with the coordinates of the 64 nodes on the left atrial mesh to which the inverse problem is directly solved.

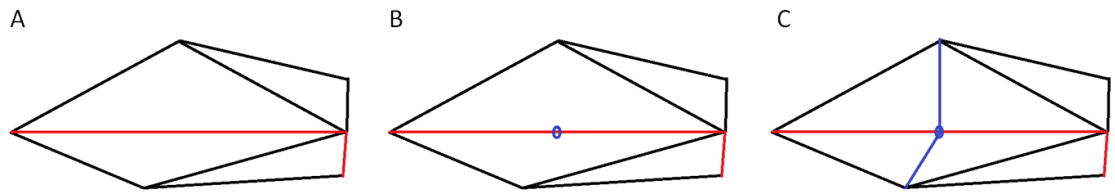

Figure 5-2: Example for mesh redefinition. A) The longest edge of the mesh and the triangles sharing this mesh are found (red). B) The central point of this mesh is defined (blue circle). C) A line is drawn between the central point and the vertex of each sharing triangle not coinciding with the longest edge.

To remesh the left atrium, first a crude triangulation between these 64 nodes was established. This mesh was then refined to 800 nodes by an iterative process in which the edge with longest length was split by adding an additional node at the centre of this edge and redefining the triangulation by including this node. This refinement was achieved by identifying the triangles sharing the edge. A line between the vertex of the triangles which was not on the edge and the new node on the edge was then added to define the new triangulation. A schematic 2D representation of the refinement is given in Figure 5-2. An example of the implementation of this method to remesh the left atrium is given in Figure 5-3.

A transfer matrix for the inverse solution was then developed as per equation (4-20) in section 4.2.2.1. Here, the measured balloon potentials were used to estimate directly an inverse solution to all 800 nodes on the endocardium.

5.2.2 UoL Inverse Solution

The optimal UoL inverse solution was found by applying a second-order Tikhonov regularisation as in equation (4-22). The strength of the regularisation was adapted such that the 2D correlation coefficient between the EnS and UoL inverse solution was as high as possible. This coefficient was calculated based

on the signals before QRST segmentation. The 2D correlation coefficient was calculated as follows:

$$r = \frac{\sum_m \sum_n (EnS_{mn} - \overline{EnS})(UoL_{mn} - \overline{UoL})}{\sqrt{(\sum_m \sum_n (EnS_{mn} - \overline{EnS})^2)(\sum_m \sum_n (UoL_{mn} - \overline{UoL})^2)}} \quad (5\text{-}1)$$

where m and n represent the dimensions of the estimated potential matrices at the nodes and $\bar{x}$ represents the mean. Only the 64 points to which the EnS inverse solution is calculated directly are taken into account as these "measurement points" can also be found on the UoL mesh, and therefore a direct comparison can be made. Besides this, a signal-by-signal conventional 1D correlation coefficient was calculated between the EnS and UoL nodes.

The EnSite inverse solution was used as a gold standard as insufficient contact mapping data were available, and the EnSite system is a clinically approved tool for diagnosis and treatment of cardiac diseases based on the inside-out inverse solution.

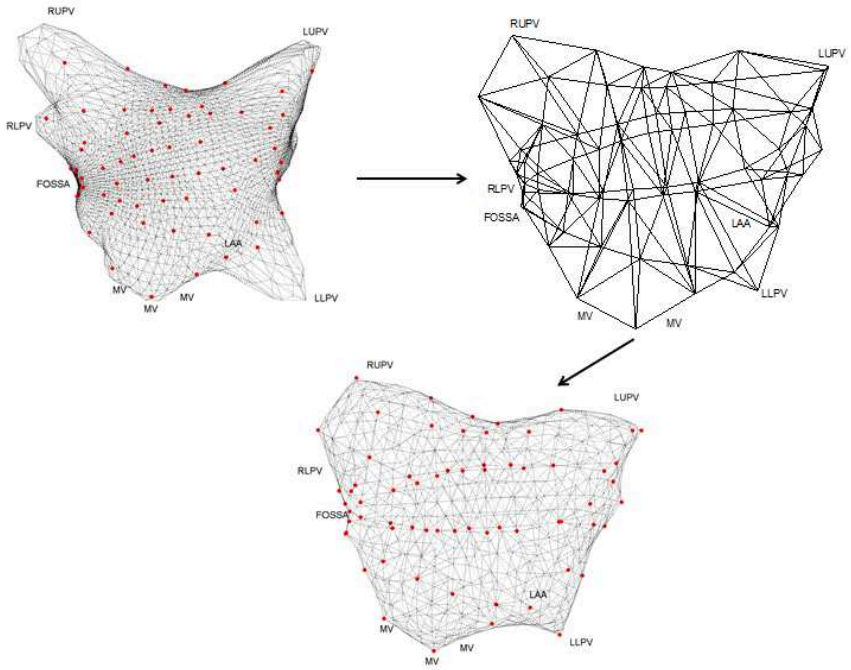

Figure 5-3: Example of remeshing the left atrium. First, the 64 nodes (red dots) to which an inverse problem is directly solved are identified from the EnSite Velocity system (left top). A crude mesh is developed from these 64 nodes (right top). This mesh is then refined to an 800 node mesh which still included the original 64 EnSite nodes.

5.2.3 AF Dominant Frequency

The DF behaviour for remeshed left atrium using the UoL inverse solution was analysed and compared to the original DF results with the EnS inverse solution as described in chapter 2. Only the left atrium was further analysed as the UoL inverse solution could only be made available for this atrium.

For the original data extracted from the EnSite system, QRST segmentation was performed on the 64 inversely solved virtual electrograms. To ensure the best possible similarity in methodology, QRST segmentation was also performed on the UoL virtual electrograms after inversely solving. QRST segmentation and DF analysis were performed as described in sections 1.1.1 and 2.2.7. Attention was focussed on the DF distribution for the 64 individual nodes only. Besides this, the highest dominant frequency (HDF) for the UoL and EnS solutions were compared for these nodes only. Both comparisons were performed using a Wilcoxon matched-pairs signed-rank test. Representation on a 3D map for the DF was performed by performing a surface Laplacian. The HDF 3D map was derived from this interpolated map, as this procedure is similar to the HDF derivation applied in chapter 2, where the HDF site is derived from the 2048 interpolated virtual electrograms.

5.3 Results

5.3.1 UoL Inverse Solution

A comparison for a 3D voltage map between the EnS and UoL inverse solution is given in Figure 5-4. The voltage maps were taken during atrial activity as indicated by the electrograms. The electrograms are taken from the same node on both meshes. This node was one of the 64 nodes to which the EnS inverse solution was calculated directly. For the EnSite mesh, an interpolation was performed from the 64 nodes to the total 2048 nodes using the surface Laplacian. An inverse solution was calculated directly to all 800 nodes of the UoL mesh.

The spatiotemporal (2D) correlation between the EnS and UoL solution for all subjects is provided in Figure 5-5 for data before and after ablation. For all the data inspected, a 2D correlation higher than 0.5 could be established. An

overview of the distribution of the temporal correlation for the individual 64 nodes is provided in Figure 5-6. It can be observed that there is a strong variation in the distribution for all volunteers. This is further exemplified in Figure 5-7, which shows the average temporal correlation for the individual nodes over all volunteers before and after ablation. A pattern seems to appear for each combination of 8 nodes.

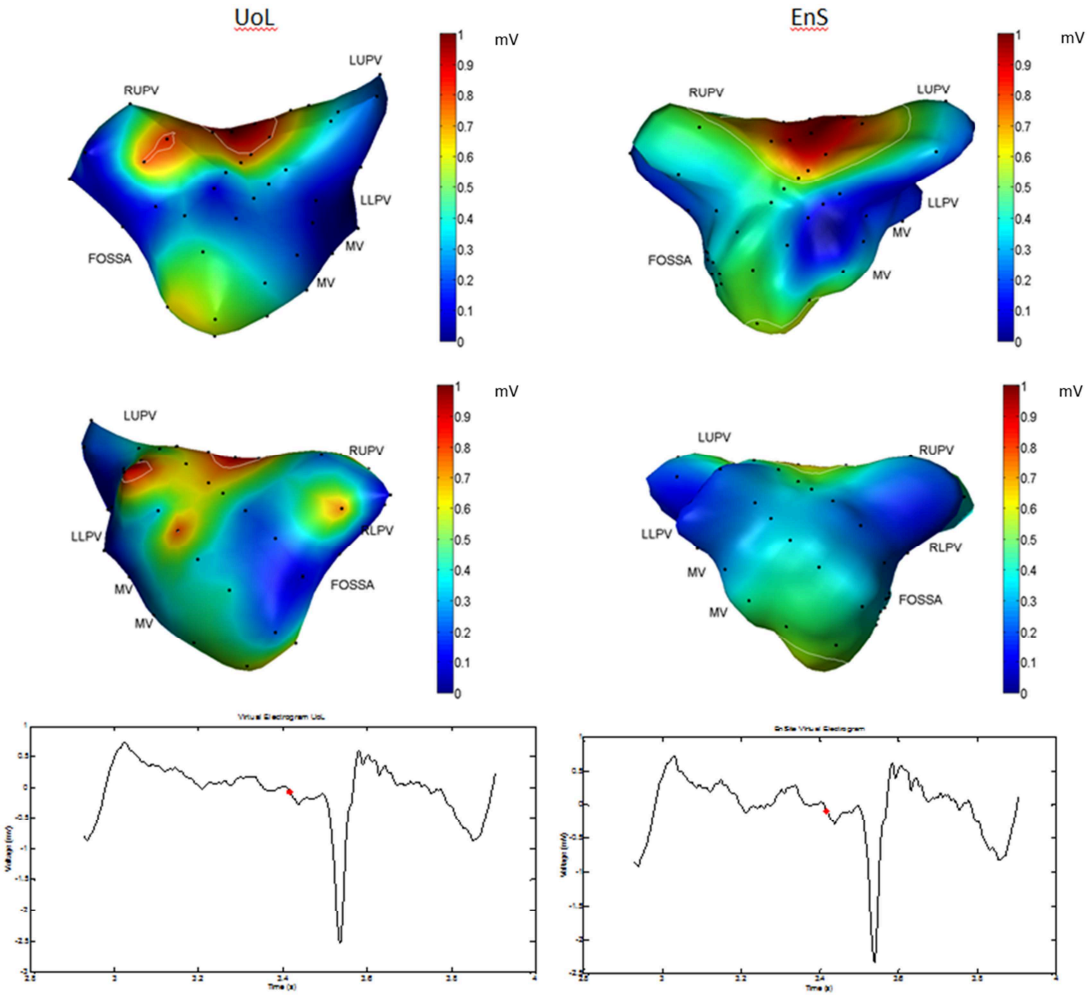

Figure 5-4: Comparison of normalised voltage maps of the UoL and EnS inside-out inverse solution. The virtual electrogram of one of the 64 nodes (black dots) directly estimated by the EnSite system is shown and compared to its UoL counterpart. Top: anterior; Middle: posterior left atrium.

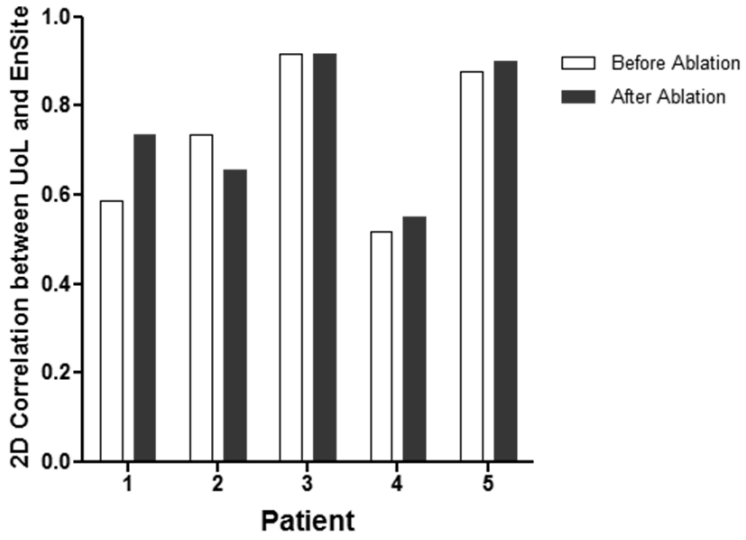

Figure 5-5: Spatiotemporal (2D) correlation between the EnSite and UoL inside-out inverse solution.

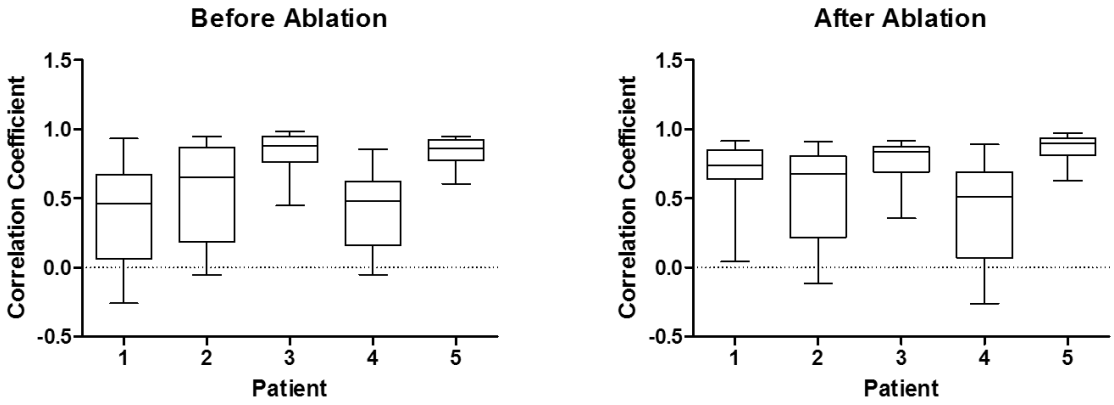

Figure 5-6: Distribution of the temporal correlation between the EnSite and UoI inverse solution as observed from 64 nodes.

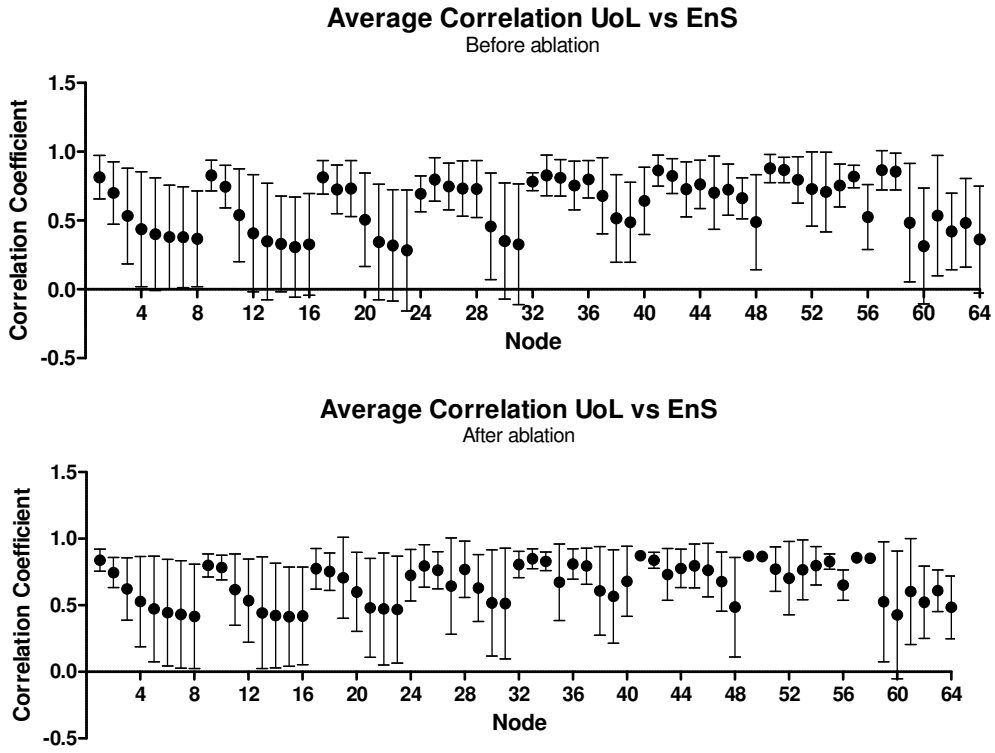

Figure 5-7: Average 1D temporal correlation between the 64 individual nodes on the UoL and EnSite meshes.

5.3.2 AF Dominant Frequency

Figure 5-8 shows the frequency spectra for all 64 nodes considered during 1 window for subject 3 before and subject 5 after ablation. It appears that both inverse solutions show similar morphologies, but the power is reduced in the UoL solution, as shown by the colour map on the images.

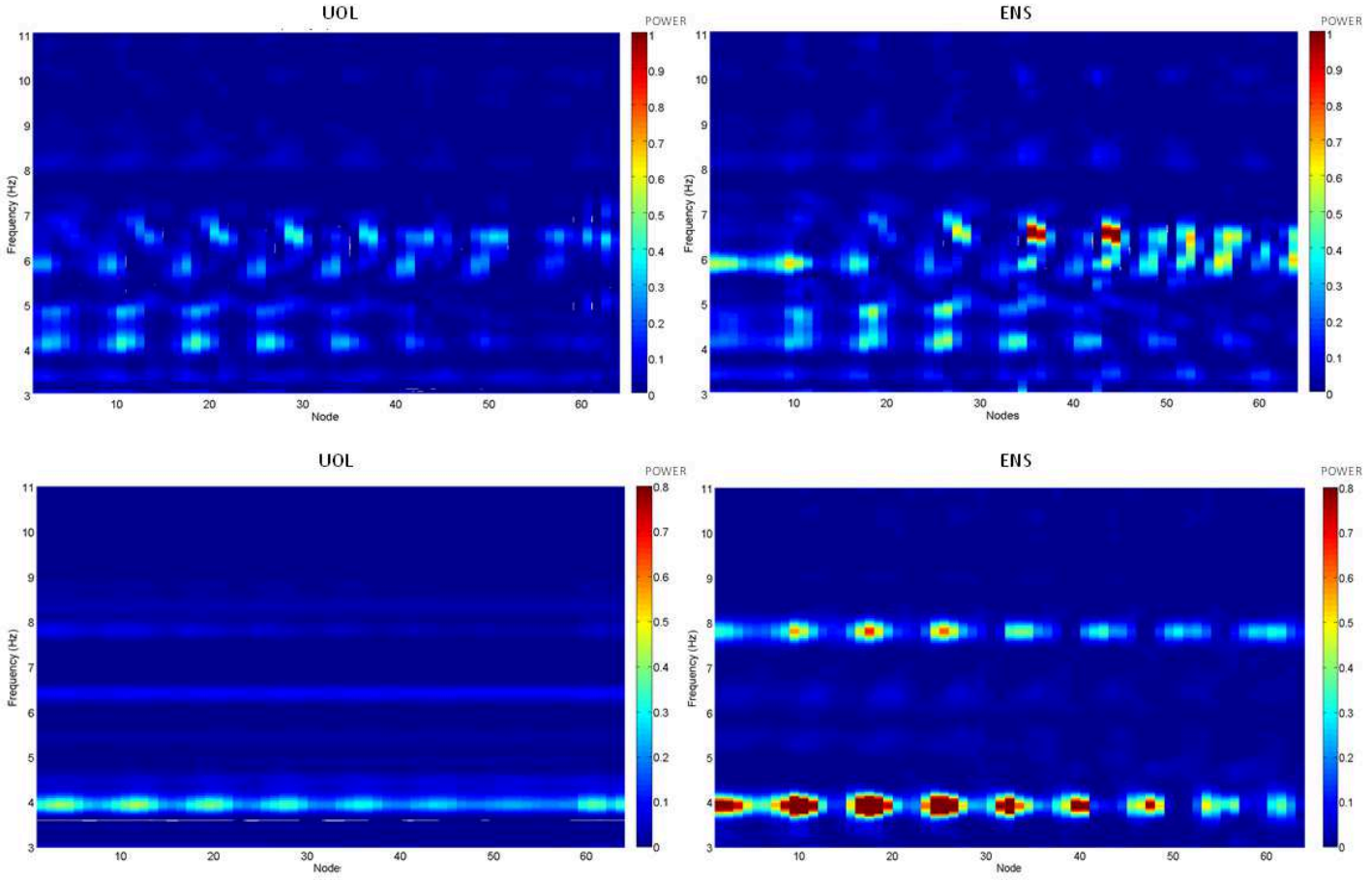

Figure 5-8: Comparison of the frequency spectra for 1 window for subject 3 before ablation (top) and 5 after ablation (bottom). Frequencies are shown for all nodes which could be directly compared between the UoL and EnS inverse solution. Colours represent the power of each frequency peak in the spectrum.

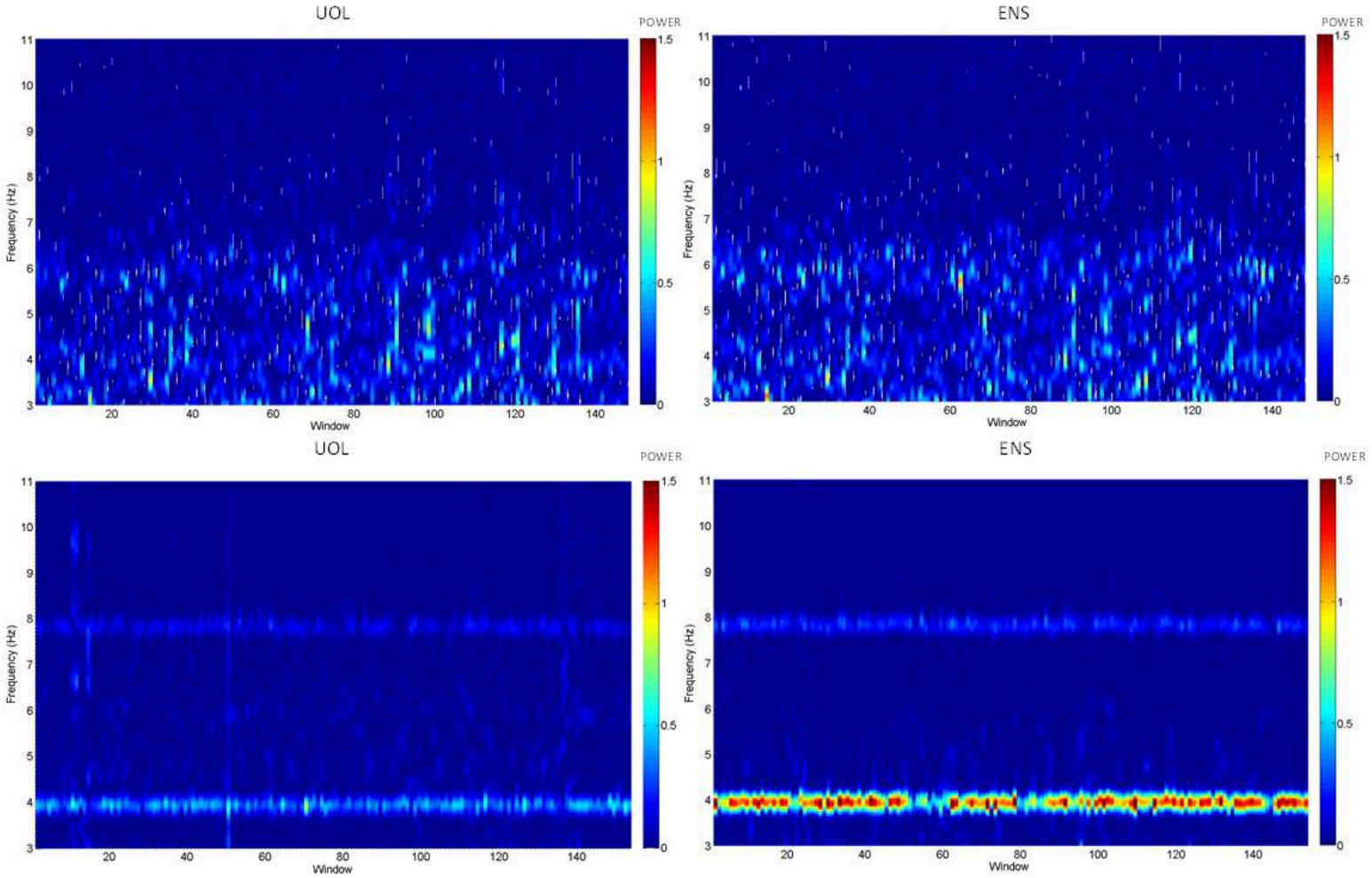

Figure 5-9: Comparison of the frequency spectra for node 1 for subject 3 before ablation (top) and 5 after ablation (bottom) over all windows.

Similarly, Figure 5-9 compares the frequency spectra for one of the 64 nodes over all windows for the same volunteers. Here, again the power for the UoL inverse solution appears to be reduced. Although for subject 5, the morphology of the spectra is reasonably similar between both inverse solutions, more variation exists for subject 3.

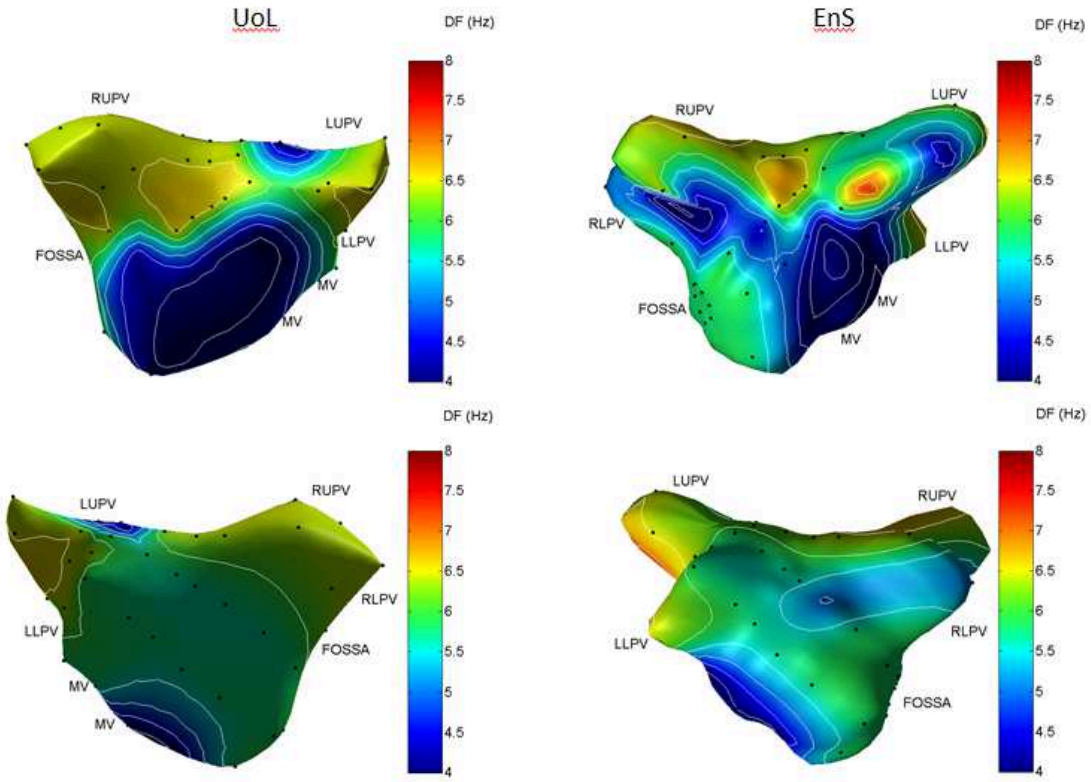

Figure 5-10: Comparison of UoL and EnS DF maps for one window. Top: anterior; Bottom: posterior left atrium. Dots indicate the nodes to which the EnS solution is directly calculated.

Figure 5-10 shows an example of an atrial fibrillation DF map for the same window of subject 3 as in Figure 5-8. Both the UoL and EnS inverse solution are displayed. The DF map was calculated by applying the Fourier analysis after QRST cancellation on the 64 known signals for the UoL and EnS inverse. The DF was selected as described in chapter 2. An interpolation of this DF was then performed on both meshes to determine the DF at the remaining nodes.

A direct comparison for 3 subject datasets is given in Figure 5-11. A choice was made to represent one dataset with low (top), reasonable (middle) and high

(bottom) spatiotemporal signal correlation between the UoL and EnS inverse solution. It can be observed that, for all cases, the interquartile range of the DF values appears similar for all nodes, independent on the signal correlation. However, with lower correlation, the full range of DF values between the UoL and EnS solution appears more varying.

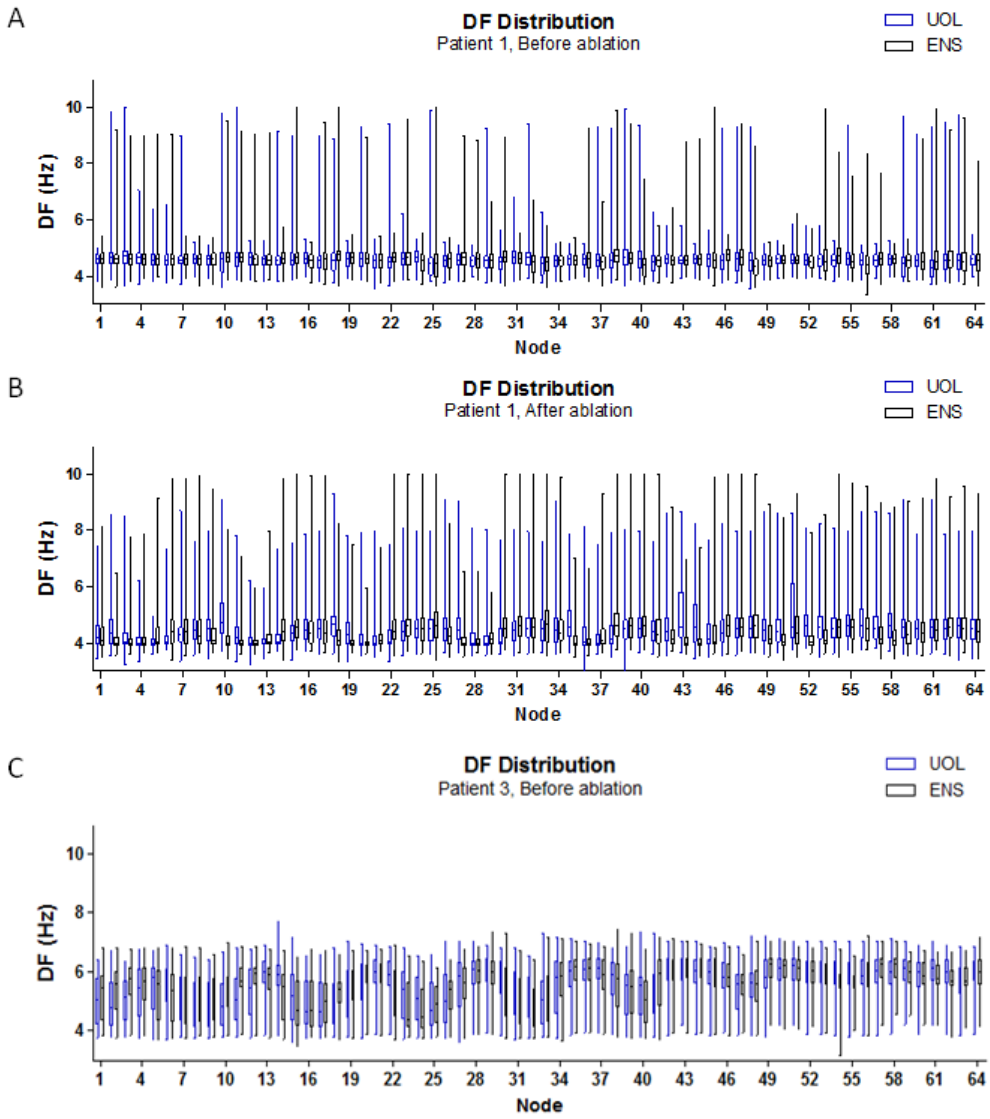

Figure 5-11: Comparison of DF distribution for 64 nodes of the UoL and EnS inverse solution for signals with low spatiotemporal correlation (A, $r = 0.59$), reasonable correlation (B, $r = 0.74$) and high correlation (C, $r = 0.92$).

Figure 5-12 shows the distribution of the DF median compared between the UoL and EnS inverse solution for the individual datasets. No DF data for subject 4 after ablation were available, as this subject was not in AF after ablation. In some cases, a significant variation in the DF median distribution

could be found after a window-by-window statistical comparison. The occurrence of these variations was not subject-specific.

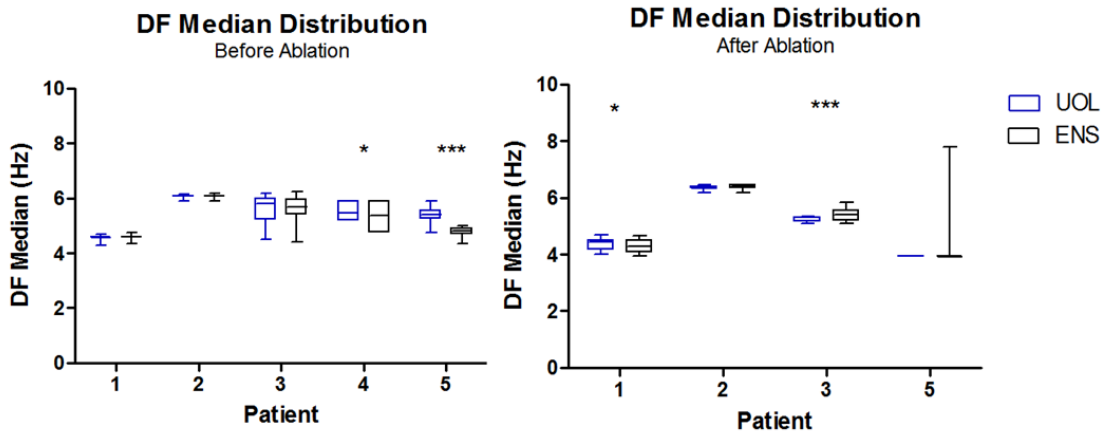

Figure 5-12: Distribution of DF median for the UoL and EnS inverse solution for all volunteers. Asterisks indicate statistical significance at *p* values equal to 0.05 (*), 0.01 (**) and 0.001(***).

Figure 5-13 shows the results of a paired window-by-window comparison between the UoL and EnS inverse solutions. For all subjects, significant variation in the HDF value could be found between both solutions for individual windows. In some cases, these variations were due to harmonics. Mostly, however, the effect was caused by other reasons discussed later.

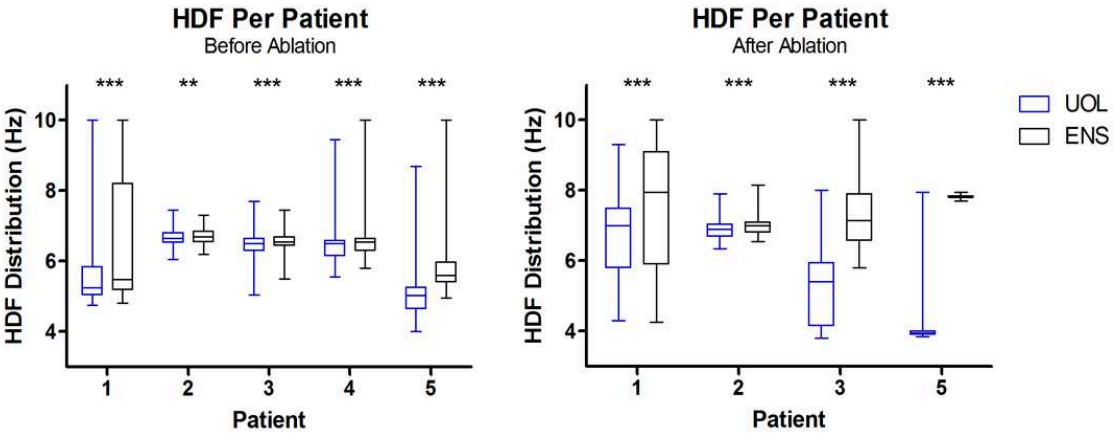

Figure 5-13: Comparison of the highest DF (HDF) distribution for all volunteers for both inside-out inverse solutions. Asterisks indicate statistical significance at *p* values equal to 0.05 (*), 0.01 (**) and 0.001(***).

As the values and distribution of the HDF values was significantly variable, no good correlation was expected between the HDF sites for both inverse solutions for individual windows. Figure 5-14 shows the location of the HDF for a particular window of the subject 5 data after ablation. The HDF appears on the right pulmonary vein area. The location for both inverse solutions is reasonably similar, and a large variation in the HDF value due to harmonics has to be considered as a possible cause of variation.

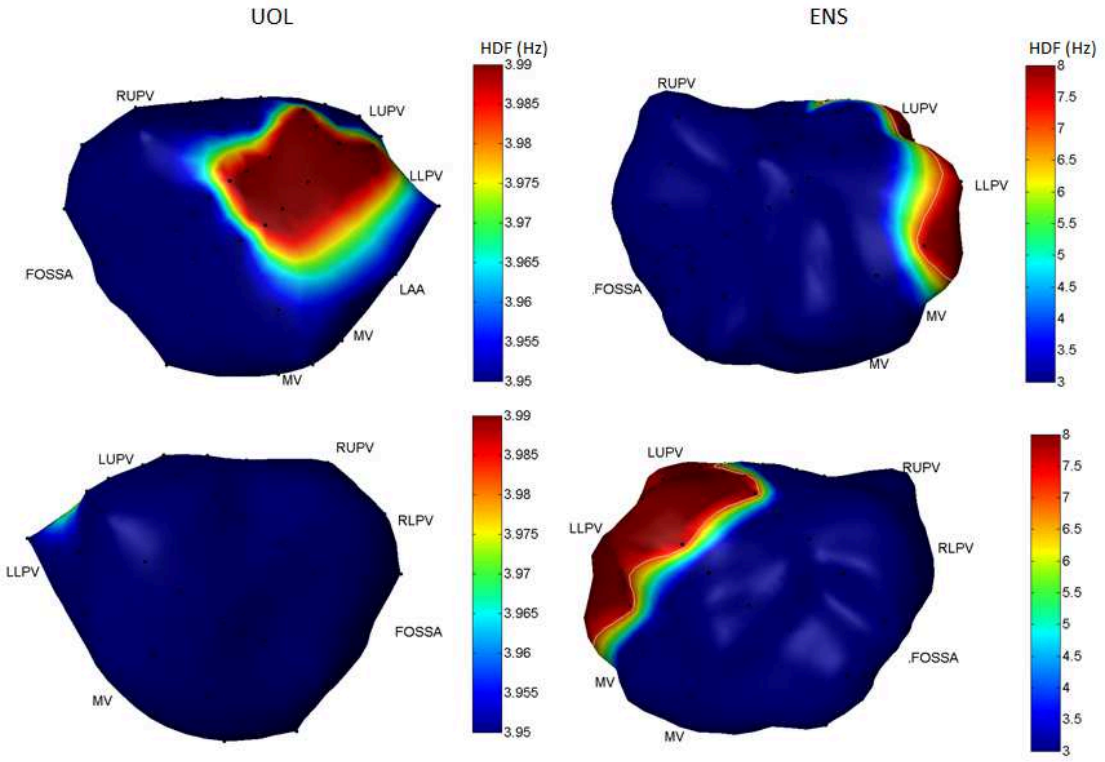

Figure 5-14: Comparison of the highest DF (HDF) site for one window of subject 5 after ablation on both inverse solutions.

In Figure 5-15, the HDF sites for one window of subject 3 before ablation are compared. Here, a strong variation in the position and value of the HDF is observed, which cannot be allocated directly to the effect of harmonics. In this image, The UoL inverse appears to find distinct HDF areas in both the left and right pulmonary veins. The EnS solutions seems to only locate a HDF area at the right pulmonary veins. For many windows, similar behaviour could be observed, leaving further (statistical) analysis of the HDF location seemingly irrelevant.

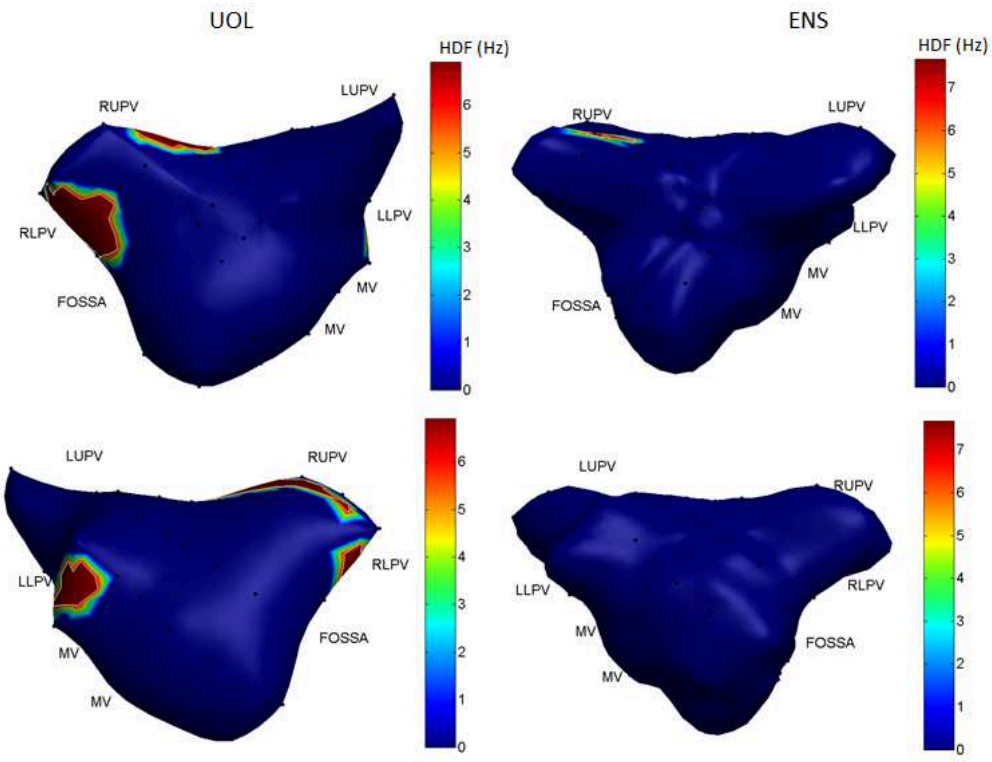

Figure 5-15: Comparison of the highest DF (HDF) site for one window of subject 3 before ablation on both inverse solutions.

5.4 Discussion

Much variation exists in the applied models for solving the inverse problem of electrocardiography (Cheng *et al.*, 2003a, van Oosterom, 2012c). Unfortunately, this has led to some confusion and difficulties in comparing results from previous work, and also explains in part the strong variation that has been found in the accuracy of the models (Barr *et al.*, 1970, Brooks and Ahmad, 1999, Cheng *et al.*, 2003a, Colli-Franzone *et al.*, 1985b, Cuppen and van Oosterom, 1984, Huiskamp and Greensite, 1997, Rudy and Burnes, 1999, Tilg *et al.*, 2003) as well as the appropriate choice of regularisation function and choice of regularisation parameter (Cheng *et al.*, 2003a, Zhang *et al.*, 2005). According to the current knowledge of the author, only one research group has attempted comparing several inverse solutions on the same data (Cheng *et al.*, 2003a).

The use of the mono- and double layer model could be considered an evolution from the inverse solutions based on dipoles or multipoles (Barr *et al.*, 1966,

Frank, 1956, Geselowitz, 1964), which were based on the original works of Einthoven (Einthoven, 1913, Einthoven *et al.*, 1913). The idea of considering layers of dipoles was first suggested by Wilson and co-workers (Wilson *et al.*, 1933). This Uniform Double Layer (UDL) model suggested the reconstruction of cardiac sources based on activation wave fronts. Afterwards, the development of a multiple dipole source model by Miller and Geselowitz (Miller III and Geselowitz, 1978) allowed reproduction of the activation wave front during ventricular depolarisation. Using this model, the ventricular activation sequence for a healthy heart as described by Durrer *et al.* (Durrer *et al.*, 1970) could be reconstructed. The development of the Equivalent Double Layer model by Cuppen and van Oosterom (Cuppen and van Oosterom, 1984) as suggested theoretically by Salu (Salu, 1978) allowed for an improved reconstruction of repolarisation wave fronts. These methodologies have been improved over the years and allow accurate reconstruction of atrial depolarisation and repolarisation in healthy circumstances (van Dam and van Oosterom, 2003). The major limitation for these types of models is that a direct comparison of the source estimation with real cardiac sources is impossible, meaning that these types of sources should be considered equivalent sources (van Oosterom, 2012a). The major advantage is that these equivalent sources can closely resemble the exact behaviour of the cardiac activation wave front, whereas potential-based models cannot always be straightforwardly linked to the electrophysiological background of a cardiac disease (van Oosterom, 2012c). However, different inverse solutions should be able to reconstruct almost identical isopotential maps, if the correct approximations are used and under ideal circumstances (e.g. no geometric errors, no noise on data).

The current study provides an opportunity to compare an inverse solution based on current density sources to a commercially available inverse solution based on potential sources. Although this commercial system is not necessarily the “best” inverse solution available, its use in clinical practise can be deemed sufficient to be considered the current gold standard.

5.4.1 UoL Inverse Solution

Figure 5-5 shows the most optimal spatiotemporal correlation that could be achieved between the EnS and UoL inverse solution. A spatiotemporal correlation was considered, as it does not only provide an indication of the temporal agreement between the inverse solutions, but also takes into account spatial variation. In this way, variations in activation wave fronts over space can be accounted for. Of major concern in the comparison was the high amount of smoothing that had to be applied to the UoL inverse solution to achieve these correlations (median $\lambda = 45.555$, $IQR\ \lambda = \{45.555; 64.4245\}$). This leads generally to a smoother endocardial inverse solution for the UoL solution isopotential maps (e.g. Figure 5-4). Apart from the knowledge that the EnS solution might not be the gold standard, and therefore differ from the real (endocardial contact-mapping) signals, other reasons might be the difference in regularisation. The EnSite system allows application of a spatial filter, which was disabled during the extraction of the balloon and virtual data. This spatial filter might work as a low-pass spatial filter and would therefore induce smoothing on the EnS inverse solution isopotential maps. The EnSite system also appears to only allow exporting temporally filtered virtual electrograms. The type of filtering used is unknown, which makes further exploitation of reasons behind the difference in UoL and the EnS inverse solution challenging. Geometrical aspects do not provide a reason for the difference, as the coordinates of the points which were correlated were the same for both solutions. Besides this, their position with respect to the balloon was identical.

From the temporal correlation distribution of Figure 5-6, it can be further observed that for subjects with low spatiotemporal correlation, a higher spread in the temporal correlation between the individual nodes can be observed. This variation might be partially related to the strong smoothing in the UoL inverse solution, from which the effects can be seen on the electrograms of Figure 5-4. Although the general shape of the electrograms is the same, the UoL inverse solution has lost the capacity to identify small fluctuation in the signal. The loss of these fluctuations will not only affect the temporal correlation, but also the spatiotemporal correlation. There was however no direct link between the reduction of the correlation and higher regularisation of the UoL inverse

solution, suggesting that other aspects related to the inverse solution model can impact this relationship.

Figure 5-7 shows the average correlation between the UoL and EnS inverse solution for each node over all volunteers before and after ablation. A pattern can be observed for each 8 nodes. This is due to the allocation of the node positions onto the endocardial wall. The nodes could be considered a representation of the EnSite elliptical balloon Array on the endocardium. For this reason, some of the nodes are at a large distance from the balloon, which leads to the well-known reduction of accuracy of the inverse solution (Schilling *et al.*, 1998). These results should always be taken into account when analysing data obtained from inside-out inverse solutions, even more so as it seems that different inverse problem algorithms appear to deal differently with this distance effect.

As the temporal data show variation, it was considered to perform a further comparison of the UoL and EnS inverse solution based on frequency analysis. As frequency analysis works with longer time intervals (4 second windows in this project), it can be considered as a means to summarise cardiac behaviour over these intervals. Previous work looking at atrial fibrillation frequency analysis has shown that the correlation between the dominant frequency of inversely solved and direct contact mapping electrograms is higher than the temporal comparison (Jarman *et al.*, 2012).

5.4.2 AF Dominant Frequency

A comparison between the frequency spectra for two subject datasets is provided in Figure 5-8 and Figure 5-9 over all nodes and for a single node over all windows, respectively. These subjects were chosen as the first (top images) shows a general behaviour found for most subjects and the second (lower images) showed a particular result for well-organised AF. As was stated in chapter 2, a stable AF activity could be observed for subject 5 after ablation, with a main frequency of 3.95 Hz. The UoL inverse solution seems to be able to reconstruct this behaviour very similarly to the EnS solution. The only difference appears in the power of this dominant frequency, possibly due to the strong smoothing applied to the UoL solution. For the other subjects, some of

the morphology of the EnS spectra remained visible with the UoL solution. This can be observed for subject 3 on Figure 5-10, where slight variations in the dominant frequency can be found on the nodes to which the EnS solution is directly calculated (i.e. variation not due to the interpolation). Furthermore, it could be observed that when higher spatiotemporal correlation existed between the EnS and UoL solution, a better relation between the DF distribution could be observed (see Figure 5-11). Although most of the spectral variation could be allocated to the high smoothing, additional noise artefacts from the signal or possibly induced by QRST cancellation might have influenced these DF distributions.

The variation in the frequency spectra between both solutions also gives rise to variations in dominant frequency median and highest DF values. Figure 5-12 shows the variation in DF median between the inverse solutions for all datasets. For some cases, significant variation in the DF median distribution could be found. This was not related to the strength of the temporal correlation between the solutions. From Figure 5-13, significant variations in the highest DF (HDF) values can be observed for all subjects. As in most cases the HDF values of the UoL inverse solution appear lower in overall distribution than those of the EnS solution, the strong smoothing seems to be causing this effect, as this would set up a low-pass filtering effect to avoid the influence of high-frequency noise component on the final solutions (Hansen, 2010). Higher UoL HDF values can probably be caused by the differences in inverse solution algorithms for both solutions, e.g. in dealing with auto solid angles (Meijs *et al.*, 1989). These influences together with the effect of interpolation also lead to a different position of the HDF areas on the left atrium as shown in Figure 5-14 and Figure 5-15. Although part of the variation in HDF area could be due to the differences in the mesh setup, the variation in smoothing and inverse solution algorithm, as well as the general accuracy of the inverse solution, can have major influences on the temporal and frequency-based analysis of AF, and therefore on the success of ablation procedures based on these analyses. More robust understanding of the differences in the inverse solutions algorithms, as well as a comparison to a true gold standard (e.g. contact electrograms) should be considered. Future studies might also look at

achieving a better correlation based on frequency analysis between the EnS and other inside-out solutions.

5.5 Study Limitations

The two major limitations of this work are the small size of the study group and the lack of a gold standard to compare both inverse solutions. This latter limitation is partly solved by the results from other studies comparing the inverse solution of the EnSite system to contact mapping data, and the fact that the simulations studies for the UoL inverse solution as discussed in chapter 4 showed the possibility to accurately reconstruct dipole sources on a spherical volume conductor. Future studies could however provide a better gold standard and allow measurements for additional subjects to improve the quality and significance of the current data. The studies should also have the possibility to export inverse solutions from raw data from the EnSite system.

5.6 Clinical Relevance of Findings

As the EnSite technology has been verified and widely accepted as a tool for estimating endocardial signals from non-contact electrodes, one could find the clinical relevance of this chapter doubtful. The main argument presented is that the EnSite system provides one possible inverse solution out of a pool of many alternatives. One of these alternatives is the suggested current-layer based model described in this and the previous chapter (UoL model).

The most important reason why the current-layer based inverse algorithms are of interest is that a direct relationship can be achieved the theoretical model and electrophysiology, which is not the case for the potential-based solution of the EnSite system (van Oosterom, 2012c). In their most advanced status of the equivalent double layer model, current-based source models can be constrained by including aspects of local cardiac transmembrane potentials, which reflect local action potential behaviour (van Oosterom, 2014a). Alterations in action potential duration and depression in the action potential plateau have been suggested as major contributors to AF and ventricular fibrillation (Allessie *et al.*, 2001, Riccio *et al.*, 1999). An accurate implementation of current source models could therefore provide clinicians

directly with relevant information regarding the complexity and underlying phenomena of (atrial) fibrillation, rather than having to derive this information from a “closer look” of cardiac activity as provided by potential-based solutions.

Combined with the previous chapter, it is also shown that further attention needs to be given towards optimisation of inverse algorithms in clinical environments. This can be deduced from the strong regularisation that had to be used to reach maximal correlation between the potential- and current-based solutions. Although part of this could be partly explained by the difference in source model, artefacts such as high ventricular far-field signals, suboptimal atrial meshes as well as technical aspects such as the EnSite filter settings could have influenced this relationship. To minimise far-field signal artefacts, technological considerations could be investigated to optimise non-catheter mapping arrays towards atrial signal detection. One suggestion could be to reduce the distance between the measurement location and atrial muscle wall. Another alternative could be to implement software for QRST cancellation within the system. A protocol for optimisation of the mesh has been provided in this chapter. Lastly, the effect of pre-processing signals on the accuracy of the inverse solution could be established. For the moment, clinicians should be made aware of these issues and the fact that the inverse solution remains an estimation of the cardiac signal. Both previous and current chapters attempt to provide this information such that clinicians can shape their interpretation of the data taking into account these technical aspects.

5.7 Conclusion

This study investigated the effect of two different inverse problem algorithms for estimating endocardial data from a non-contact balloon Array. The EnSite (EnS) inverse solution is a commercially available tool providing a potential-based source estimation, whereas the University of Leicester (UoL) solution provides an inverse solution from current density equivalent sources, based on equations (4-1), (1-17) and (1-19). The EnS solution was considered to be the gold standard.

Results suggest that a high regularisation (smoothing) parameter needed to be included to allow good spatiotemporal correlation between the EnS and UoL

solution based on isopotential maps. This is mainly due to the unknown effect of the EnS filtering and regularisation of the virtual electrograms. In most subjects, the spatiotemporal correlation was only considered good to reasonable (0.73±0.17 before, 0.75±0.15 after ablation, represented as mean±SD). Besides this, temporal correlation was affected by the distance between the measurement point and balloon. In cases of larger distance between the balloon Array electrodes and the endocardial surface, a lower correlation existed between both inverse solutions. This further proves the effect of geometrical error as shown in previous literature. It also shows that different inverse solutions will treat this error differently.

The spatiotemporal effects were of major influence on the differences in (dominant) frequency analysis between both inverse solutions. Alternative inverse problem algorithms can thus have significant impact on the temporal and frequency aspects of cardiac signals. This should be taken into account for comparing different studies and during clinical practise.

6 The Outside-In Inverse Problem: a Path towards Investigating Atrial Transmurality

6.1 Introduction

One of the main interests of this project is to further understand the mechanisms behind atrial fibrillation by combining outside-in and inside-out solutions. Although both types of solutions have their limitations in accurately reproducing endocardial and epicardial signals, it is believed that the study of certain characteristics of the atrial electrograms, such as (highest) dominant frequency behaviour, could lead to a better understanding of the behaviour of both muscle layers during advanced atrial fibrillation. The main objective is to provide further knowledge regarding the possible transmural behaviour during atrial fibrillation.

6.1.1 Experimental Evidence of Atrial Transmurality

One major study in AF subjects has been conducted to provide evidence of atrial transmural dyssynchrony as a possible driver of fibrillation. In 2010, de Groot *et al.* found that transmurality, and especially endo-epicardial decoupling could be a relevant trigger for persistent AF (persAF) (de Groot *et al.*, 2010). Comparing 24 AF subjects with structural heart disease to 25 Wolff-Parkinson-White syndrome subjects with induced AF, they showed that a higher number of epicardial breakthroughs occurred in persAF. These breakthroughs were not repetitive in space. The authors argued that this behaviour could be related to multiple wavelet re-entry circuits where the wave would rotate throughout the myocardium, with one limb in the endocardium and one in the epicardium. This would provide an understanding for the failure of catheter ablation in some of the persAF subjects. In these subjects, the AF trigger would not be localised ectopic foci or a single re-entry wave, as suggested by different works (Haïssaguerre *et al.*, 1998, Narayan *et al.*, 2012), but many wandering wavelets. The burning of small sections in the atrium would be insufficient to remove all wavelets and therefore terminate AF (de Groot *et al.*, 2010).

The underlying aspect of transmurality as a possible trigger of AF could be an increase in endo-epicardial electrical dissociation. Eckstein *et al.* (Eckstein *et*

al., 2011) confirmed the existence of this dissociation in goat hearts by comparing goats that were exposed to acute AF, persAF for 3 weeks and persAF for 6 months. Measurements were taken from the epicardium and endocardium. They showed that endo-epicardial decoupling (EED) is a prerequisite for breakthroughs to occur. Due to the structural and electrical remodelling of AF with longer AF exposure, they showed a significant increase in the dissociation. Due to this progressive increase, fibrillation becomes a more three-dimensional process within the heart, giving rise to complex 3D multiple wavelet re-entries.

One study by Everett *et al.* has looked at the variation of DF and highest DF in a canine model on epicardial and endocardial data (Everett *et al.*, 2007). Here, 4 different cardiac disease models were compared to controls to determine the effect of atrial remodelling. LA endocardial data were mapped with the EnSite 3000 system, whereas epicardial data were collected with a contact electrode sock for both atria. Signals were first band-pass filtered between 40 to 250 Hz (2nd order Butterworth) after which the absolute value of the signals were low-pass filtered at 20 Hz. Frequency analysis was performed on 2 s windows (50% overlap, Hamming window). Their work showed that for most cases, the highest DF occurred on the endocardium. A good correlation could be established between the type of atrial remodelling (i.e. structural or electrical) and the AF characteristics or mechanism. With electrical remodelling, AF appeared as multiple wavelets and showed high disorganisation. For structural remodelling, ectopic foci with stable DFs were found. A major issue with the methodology is the allowance of DF values up to 20 Hz. Not only is any relevant atrial behaviour at these rates highly unlikely for humans, as the low-pass filtering was set at 20 Hz, a filtering effect could occur at the higher end of the DF spectrum, thereby significantly altering the temporal and frequency behaviour of the signal. This would make the correct interpretation of these high frequency peaks challenging. Other studies measuring epicardial and endocardial data simultaneously on the extracted right atrium have shown that the activation of both layers can be dyssynchronous due to the heterogeneity of the RA architecture, leading to complex activation sequences (Schuessler *et al.*, 1993).

6.1.1.1 Atrial Transmurality in Simulations

Gharaviri *et al.* found atrial transmural behaviour in a 3D dual-layer model (Gharaviri *et al.*, 2012). Here, a combination of two layers was used to represent the atrial membrane (endocardium and epicardium). AF electrophysiological behaviour was modelled using an adapted Courtemanche Model to describe atrial fibrillation action potentials and a Monodomain model to describe atrial signal propagation. Results showed that transmural activity could significantly enhance the stability of the AF signal. Due to induced stimulations, dyssynchrony occurred between the epicardial and endocardial method, inducing breakthroughs. A good correlation could be found between the amount of dyssynchrony and breakthroughs. Interestingly, breakthroughs tended to reduce dyssynchrony.

Some studies have further showed an effect of anisotropy on atrial conduction. They also showed that atrial wall thickness heterogeneity significantly increased AF stability (Harrild and Henriquez, 2000, Yamazaki *et al.*, 2012). However, further investigations are needed to confirm the existence of transmural drivers in AF. As the direct mapping of epicardial and endocardial data in humans is challenging, an alternative is to make use of inverse estimations.

6.1.2 Current Standards of Outside-In Inverse Solutions

As this study focussed on the detection of atrial epicardial and endocardial dyssynchrony using inverse problems, a short summary of the clinical implementations of outside-in (OI) inverse solutions is provided.

A current commercially available OI inverse solution is based on a potential-source. This type of source is the most known form of inverse problems in electrocardiology, and is sometimes referred to as electrocardiographic imaging (ECGI). This technology can indeed be seen as an imaging technology as it attempts to estimate the potentials at a circumference enclosing the heart from body surface measurements. It therefore can be seen as providing a closer look at the heart (van Dam *et al.*, 2009). As the potentials on the body surface can be considered a blurred version of the potentials on this circumference, the

methodology becomes a sort of deblurring technique to reveal cardiac activation (van Oosterom, 2012c).

The possibility of reconstructing these "epicardial" potentials from body surface maps was suggested by Zablow (Zablow, 1966) and theoretically described by Martin and Pilkington (Martin and Pilkington, 1972). The methodology is valid on the theory that a unique relationship exists between the potentials around the heart and those on the torso, assuming noise-free circumstances (van Dam *et al.*, 2009). A first complete worked-out methodology in torso tank models can be found in the work of Colli-Franzone and co-workers (Colli-Franzone *et al.*, 1985b). An implementation on spherical and realistic torso models can be found in the works of Messinger-Rapport and Rudy (Messinger-Rapport and Rudy, 1990, Messinger-Rapport and Rudy, 1985, Messinger-Rapport and Rudy, 1988). These models simulate the various effects of the volume conductor and possible measurement and geometrical errors on the inverse solution.

First experiments on volunteers were performed to estimate cardiac activity under healthy and pathological conditions on small-sized groups. Ramanathan and co-workers communicated the possibility to reconstruct activation and repolarisation sequences for a healthy volunteer as well as during right bundle branch block, ventricular pacing and chronic atrial flutter (Ramanathan *et al.*, 2004). In a later study they showed the reproducibility of reconstructing cardiac activation and repolarisation in 7 healthy volunteers, showing the possibility to accurately identify epicardial breakthroughs (Ramanathan *et al.*, 2006). A first study on reconstructing atrial activity during AF was conducted by Cuculich *et al.* (Cuculich *et al.*, 2010). After showing the possibility of reconstructing the location of pacing sites with high accuracy, they showed the possibility to estimate the location of possible AF triggers. Multiple wavelets were found in most of the 26 subjects. Besides this, more than half of the subjects showed signs of ectopic foci. Rotor activity was only found in a low number of cases.

Haïssaguerre *et al.* showed the possibility to use ECGI as a tool to guide AF catheter ablation based on re-entry circuit (rotor) detection (Haïssaguerre *et al.*, 2013). A more elaborate study was performed on 103 subjects with persAF.

Using specific algorithms for rotor detection, a high number of re-entry circuits and foci could be detected using non-invasive imaging. It was also shown that the number of driver regions increased with the AF severity. These rotors were mostly unstable, but would occur repetitively in the same area (Haïssaguerre *et al.*, 2014).

Other clinical studies have also used potential-based inverse problem techniques for detection of ventricular activity. Using a standard torso model, Navarro *et al*. were successful in improving the detection of acute myocardial infarct with an inverse model compared to standard 12-lead ECG or BSM mapping (Navarro *et al.,* 2003), albeit with a reduced specificity. In a further study, McClelland *et al.* showed the possibility to reconstruct epicardial activity after ventricular pacing (McClelland *et al.*, 2006).

Alternatively to the ECGI methods, activation time imaging has emerged as a possible means to estimate cardiac potentials. This imaging modality is based on current density layer sources which, in most cases, represent the border between depolarised (repolarised) cell and cells in rest (active) (Cuppen and van Oosterom, 1984). As these activation time models are non-linearly related to the body surface potentials, an initial estimate has to be provided. For atrial activity, good reproducibility could be achieved by a propagation wave based on the Huygens principle (van Dam *et al.*, 2009).

The method was first theoretically described by Wilson (Wilson *et al.*, 1933), assuming a uniform double layer model. As this model only allows accurate estimation of ventricular activation (Plonsey and van Oosterom, 2012), an equivalent double layer was suggested theoretically by Salu (Salu, 1978) and later implemented in model studies by Cuppen and van Oosterom (Cuppen and van Oosterom, 1984). This EDL model allows an accurate reconstruction of cardiac activation and repolarisation times (van Oosterom, 2001), which can be converted into isopotential maps (van Oosterom, 2012b).

A first implementation of the activation-based UDL model on healthy volunteers was performed by Huiskamp and van Oosterom (Huiskamp and Van Oosterom, 1988). Here, ventricular activation was estimated from a 64-lead body surface map for 3 healthy volunteers. Results showed that, with appropriate Surface

Laplacian regularisation, activation patterns similar to those measured by Durrer *et al.* (Durrer *et al.*, 1970) could be obtained. With the forward solution from these activation patterns, 12-lead standard ECGs could be reproduced with high accuracy. A later study on a healthy volunteer and a volunteer with Wolff-Parkinson-White syndrome using a higher advanced model and regularisation technique based on the critical point theorem reproduced these results (Huiskamp and Greensite, 1997).

In a series of studies, the EDL model was further assessed for its performance in clinical data. Tilg *et al.* (Tilg *et al.*, 2002) showed the possibility to estimate initial endocardial breakthrough points within $15\,mm$ accuracy for right ventricular signals. In this work, the activation-time based inverse solution was compared with contact mapping data. In a later study by the same group on 4 volunteers, it was shown that atrial activation-based imaging using the EDL model was feasible, albeit the inverse solution being more ill-conditioned than for ventricular activity due to the smaller signals provoked by atrial activity on the body surface map (Modre *et al.*, 2003). Good correlation between measured ECG data and forward solutions was also found in a study on a healthy volunteer, and two individual with Wolff-Parkinson-White and Brugada syndrome respectively (van Dam *et al.*, 2009). However, large cohort studies implementing these activation-based imaging modalities are currently lacking.

6.1.3 Inverse Algorithm: Current Study

The methodology applied for the OI inverse solution in this thesis is based on a representation as suggested in chapter 5, where the endocardial activity to be estimated is replaced by the epicardial activity, and the balloon signals by the body surface signals. The volume conductor model will take into account the variation in conductivity by the lungs. Results will be compared with the EnSite solutions only, as only for these a full interpretation of the right and left atrial activity were provided. With this methodology, it is expected that variations in atrial epicardial and endocardial activity can be explored, possibly leading to a better understanding of the transmural behaviour of atrial fibrillation.

6.1.3.1 Combining Inside-Out and Outside-In Inverse Problems

As far as the author's knowledge, the only study attempting to compare non-contact balloon array data with epicardial potentials reconstructed from body surface signals was conducted by Shannon and co-workers (Shannon *et al.*, 2007). Here, left ventricular isochrones and isopotential maps were qualitatively and semi-quantitatively compared for 3 volunteers undergoing LV pacing. Results showed correlation between the endocardial data reconstructed with an EnSite 3000 system and the epicardial potentials. An exception to this was found when pacing was performed in the septal area of the left ventricle. Both inverse solutions were based on potential sources, with the EnSite system reconstructing the volume conductor using boundary element methods. The epicardial potential was reconstructed using finite element methods. Agreement in pacing spike localisation was performed by fitting the centroid of the endocardial 3D mesh onto the centroid of the mesh obtained from a male torso model. A line was then created between this centroid and the point of earliest epicardial activation. The distance between the intersection of this line with the endocardium and the endocardial site of earliest activation was then used to measure agreement. Besides the low number of recordings, the study was limited by the use of non-specific torso models, as acknowledged by the authors, and the lack of invasive right ventricular data, which could have aided in further understanding the activation propagation.

6.1.4 Research Aims and Objectives

This chapter aims at comparing the inverse solution from body surface maps (outside-in inverse solution) with the EnSite inside-out inverse solution. The EnSite solution was used as it provided details of the virtual endocardium of both atria, whereas only left atrial data are provided for the UoL solution. By comparing the virtual epicardial data from the outside-in (OI) inverse solution and the virtual endocardial data, a first attempt to better understand the possible transmurality of the atria is provided based on frequency analysis. This type of research could share new lights on AF pathology and might help in diagnosis and setting up treatment strategies (e.g. assessing the chance of ablation success). Focus will be on the dominant frequency (DF) and highest

DF (HDF) behaviour between the inside-out and outside-in solution. Further research is underway in our research lab to investigate transmurality based on temporal (isopotential and isochronal) analysis.

6.2 Methods

For reasons mentioned in chapter 5, the data of the first five volunteers described in chapter 2 were used only to set up the OI inverse solution. Data from these solutions could only be compared directly to the EnSite inside-out inverse solution due to the lack of right atrial data for the home-made inside-out solution. However, the variations in the analysis between the EnS and UoL inside-out inverse solution were taken into account in the discussion below.

6.2.1 MRI Acquisition and Processing

MRIs were taken for each subject prior to their ablation procedure. Landmark positions were indicated with Vitamin A capsules attached to the front and back of the torso prior to the MRI study. A photograph was taken to further aid in locating the correct position of the BSM electrodes. Transverse torso MR images ranging from the lower neck to the umbilicus (30-45 slides per subject) were obtained according to the HASTE (Half Fourier Acquisition Single Shot Turbo Spin Echo) protocol on a 1.5 T scanner with a 6 channel phased array cardiac coil (Avanto, Siemens, Erlangen, Germany). Images were extracted as DICOM (Digital Images and Communication in Medicine) files and converted using the Matlab image processing toolbox (Version 8.3, The Mathworks Inc) into uint16 (16-bit unsigned integer) greyscale images. This file type allows separation of greyscale intensities into 65536 values (16-bit precision) (Yates, 2009). Images were further processed using a 2D median filter (5x5 matrix) to remove noise. For individual images, an upscaling to the full uint16 range of intensities was performed by calculating the factor between the maximum intensity value for uint16 file types and the highest intensity found in the original image and multiplying each image pixel in the image by this factor. Image stacks were then exported from Matlab as DICOM files. Manual segmentation and 3D modelling was performed in ITK-SNAP (Version 2.4.0) (Yushkevich *et al.*, 2006). A 3D surface mesh was developed for the lungs, atrial muscle and torso. Meshes were exported as .vtk files and imported into Matlab for

developing the transfer matrix. Prior to this, the torso model was remeshed to reduce the number of nodes and ensure co-localisation of nodes with the electrode positions. For this, the position of each image in the 3D torso model was identified. Per image, a transverse torso circumference consisting of 200 nodes was constructed using a continuous 2D Fourier interpolation technique (van Oosterom, 1978). For each reconstructed circumference, 20 nodes were selected, which were allocated to an electrode position were necessary. In total, each torso model consisted of maximally 450 nodes. Lung meshes would consist of up to 200 nodes, whereas atrial muscle meshes would consist up to 1400 nodes.

6.2.2 Transfer Matrix Setup

For the OI inverse solution, an inhomogeneous volume conductor containing the lungs was considered. The conductivity of the lungs was set at one third of the conductivity of the atrial muscle. A monolayer and double layer were used to represent the sources on the lungs, atrial muscle and torso. According to the superposition theorem, inhomogeneities can be included as follows (van Oosterom and Oostendorp, 1992a):

$$\Phi(\overrightarrow{x'}) = \Phi_{\infty}(\overrightarrow{x'}) - \frac{1}{4\pi}\sum_{m=1}^{M}\frac{\sigma_m^- - \sigma_m^+}{\sigma_{x'}^-}\int_{S_m}\Phi(\vec{x})d\omega(\overrightarrow{x'},\vec{x}) - \frac{1}{4\pi\sigma_{x'}^-}\int_{S_{x'}}\frac{J_n}{R}dS \qquad (6\text{-}1)$$

Here, σ_m^- represents the conductivity just inside the surface S_m and σ_m^+ the conductivity just outside the surface. The value of $\sigma_{x'}^-$ is the conductivity of the surface in which x' resides.

Following a similar methodology as in chapter 4, a numerical variation from this formula can be obtained:

$$\Phi_{x'} = \Omega_{x'x'}\Phi_{x'} + \frac{1}{\sigma_{x'}^-}\sum_{m=1}^{M}\Gamma_{mx'}J_{x'} + \sum_{m=1}^{M}\frac{\sigma_m^- - \sigma_m^+}{\sigma_{x'}^-}\Omega_{x'm}\Phi_m \qquad (6\text{-}2)$$

From this, a forward inverse solution can be set up after defining matrices B and G accordingly:

$$b_{ij} = \frac{\sigma_m^- - \sigma_m^+}{\sigma_{x'}^- - \sigma_{x'}^+}\Omega_{ij}$$
$$g_{ij} = \frac{1}{\sigma_{x'}^- - \sigma_{x'}^+}\Gamma_{ij} \quad (6\text{-}3)$$

Here, Ω_{ij} represents the solid angle related to node j as seen from node i and Γ_{ij} is the distributed monolayer weight for element j as seen from node i. This leads to the matrix formulation (van Oosterom and Oostendorp, 1992a):

$$\Phi_{x'} = B\Phi + GJ \quad (6\text{-}4)$$

This provides the relationship between equivalent atrial muscle potentials and the potentials on the different interfaces considered in the torso volume conductor. The formulation is therefore the basis of the OI inverse solution considered here. Equation (6-2) can be used in numerical implementations.

The OI inverse solution was calculated from the 131 measurement points on the torso (128 BSM and 3 limb leads) to all nodes on the atrial muscle after applying a zero-mean reference. As the second-order Tikhonov regularisation showed improved reconstruction of analytical solutions in chapter 4, this type of regularisation was chosen to smooth the data. As no direct comparison with epicardial atrial contact mapping data was possible, the strength of the regularisation parameter was fixed between 0 and 3. The optimal inverse solution (Φ_{opt}) was chosen to minimise the normalised relative difference between the forward solution ($A\Phi_{est}$) and the observed data (Φ_{obs}):

$$\Phi_{opt} = \min\left(\frac{\|A\Phi_{est} - \Phi_{obs}\|_F}{\|\Phi_{obs}\|_F}\right) \quad (6\text{-}5)$$

6.2.3 Outside-In vs Inside-Out Inverse Solution: Frequency Analysis

As most interest during this PhD project was focussed on the frequency analysis of atrial fibrillation, atrial signals were estimated BSM signals aligned with the EnSite data. The inverse algorithm was applied before QRST subtraction as this would maintain the chronological order of the procedure similar to AF frequency analysis on the EnSite data. After subtraction, AF

frequency spectra were generated as described in chapter 2. Further analysis focussed on comparing the dominant frequency (DF) and highest DF (HDF) behaviour between the EnSite inside-out inverse solution (4096 nodes), the BSM data and the OI inverse solution. For this purpose, a Friedman Analysis of Variance (ANOVA) test with Dunn's correction for multiple comparisons was used to allow for an overall analysis as well as a paired comparison between the three systems (EnSite vs. OI, EnSite vs. BSM and BSM vs. OI).

6.3 Results

An example of the isopotential maps on the body surface and atrial muscle after applying the inverse solution is given in Figure 6-1. An atrial electrogram before QRST subtraction shows the moment at which the isopotential maps were taken (red dot). For this particular subject, the regularisation strength was 1.35, giving a normalised relative difference of 9.46%. Over all volunteers, the average regularisation used was 1.53±0.43 (mean±SD), with an average relative difference of 13.2%±11.1% between the BSM data and the forward solution.

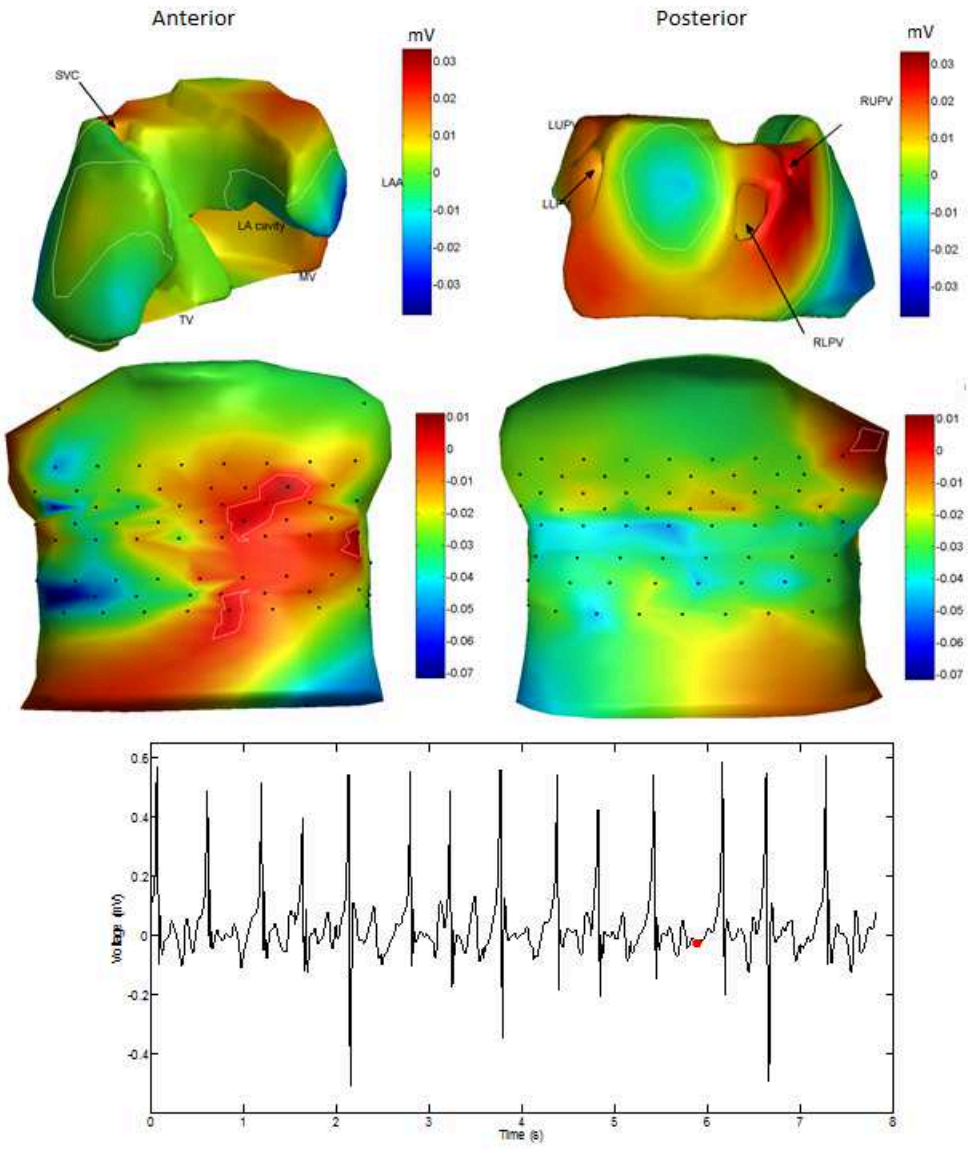

Figure 6-1: Example of an outside-in isopotential map on the atria. Top: atrial activity. Middle: body surface map taken at the time of the atrial isopotential map; dots indicate electrode positions. Bottom: atrial electrogram; the red dot indicates the moment at which the isopotential map was given.

6.3.1 Outside-In vs Inside-Out Inverse Solution: Frequency Analysis

Figure 6-2 and Figure 6-3 show a top view of the frequency spectra for subject 3 before ablation and 5 after ablation. The spectra are shown for all atrial nodes during one 4s window and for all windows on 1 node, respectively. For the EnSite data per window, the left 2048 nodes represent the left atrium. Nodes 2049 to 4096 represent the right atrium.

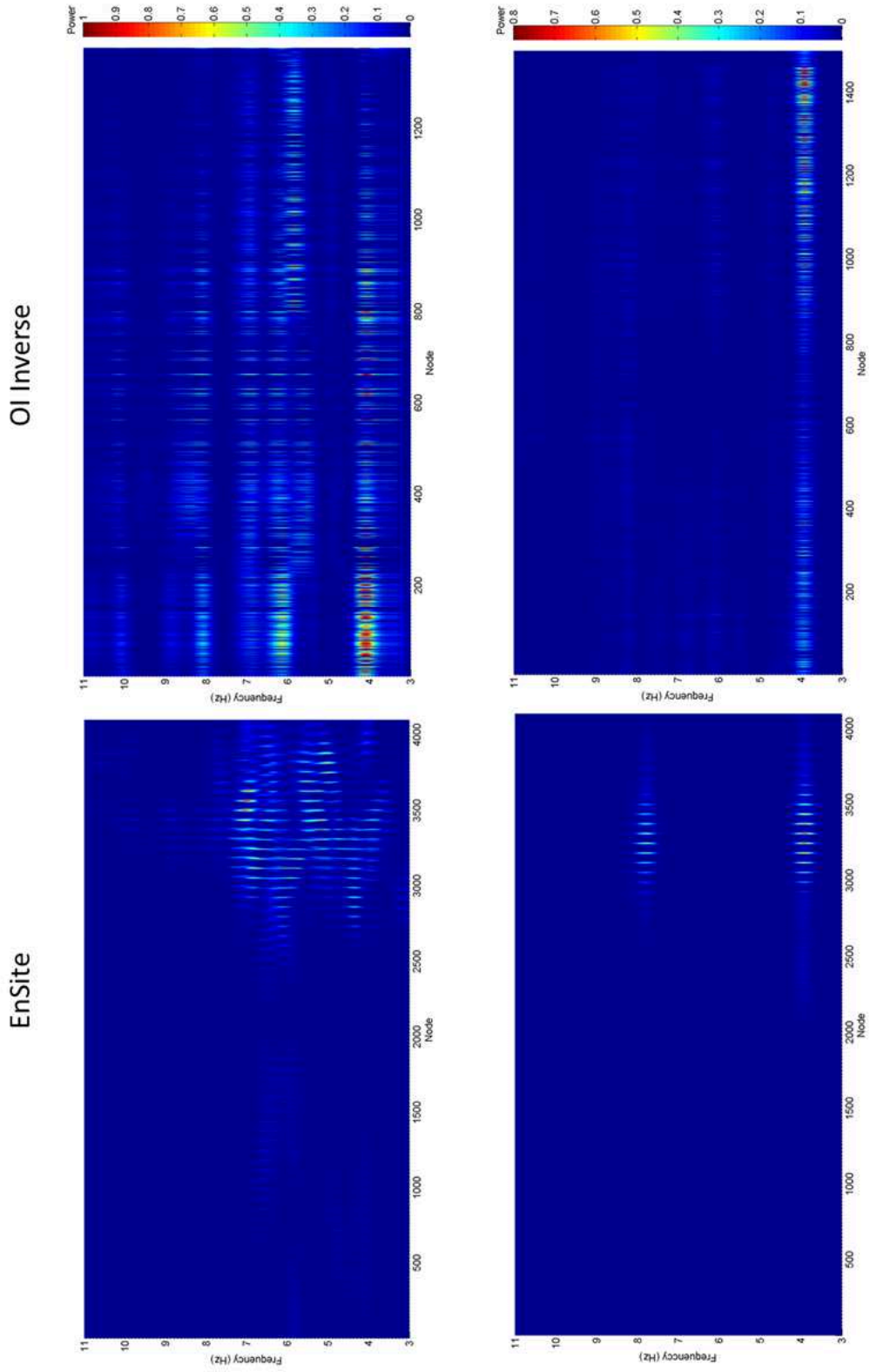

Figure 6-2: Comparison of the frequency spectra for 1 window for subject 3 (top, before ablation) and 5 (bottom, after ablation).

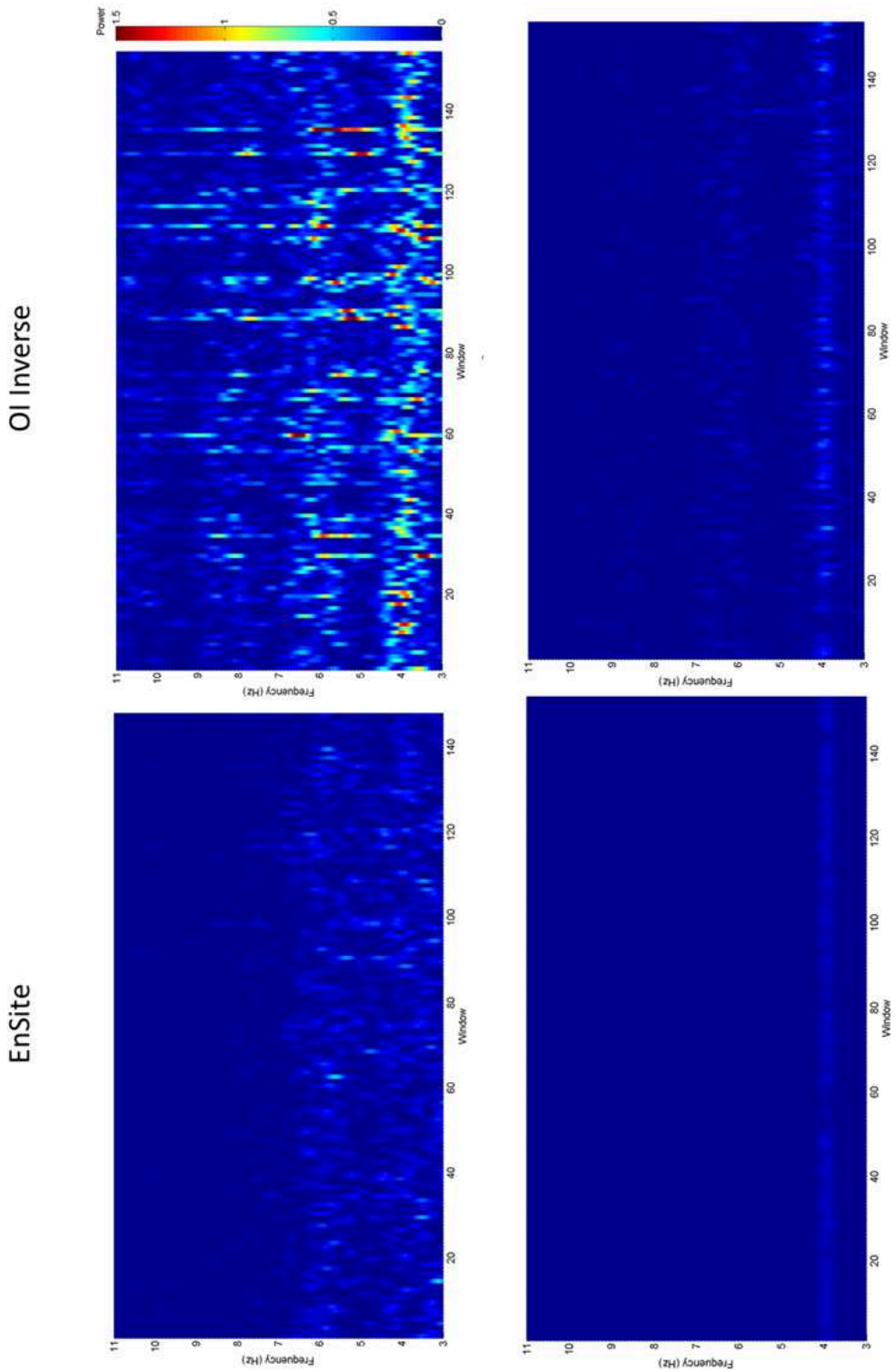

Figure 6-3: Comparison of the frequency spectra for node 1 for subject 3 (top, before ablation) and 5 (bottom, after ablation) over all windows.

Figure 6-4 compares the 3D dominant frequency map for one window of subject 3 before ablation. It shows the EnSite right atrial (left) and left atrial (middle) virtual electrogram representation as well as the OI inverse solution (right). The accompanying body surface DF map is shown in Figure 6-5.

As significant difference could be observed between the EnSite and OI inverse solution, statistical analysis was performed to describe these differences. Results for the ANOVA test are represented in Figure 6-6. It could be shown that for all volunteers, significant variance existed between the BSM, OI inverse and EnSite inverse solution ($p < 0.001$). The results for the individual comparisons between groups is represented in Table 6-1. In most cases, significant to very significant differences could be found between the three modalities

Table 6-1: Results of the multiple comparison tests (p values) between DF values of the three different modalities. >0.05 represents not significant, <0.05 borderline significant, <0.01 significant and <0.001 very significant differences.

Subject		Multiple Comparison Results (p values)		
		EnSite vs. BSM	EnSite vs. OI	BSM vs. OI
1	Pre	<0.001	<0.001	>0.05
	Post	<0.001	<0.001	>0.05
2	Pre	<0.001	<0.001	<0.001
	Post	<0.001	<0.001	<0.001
3	Pre	<0.001	<0.001	<0.001
	Post	<0.001	<0.001	<0.001
4	Pre	<0.05	<0.001	<0.001
5	Pre	<0.001	<0.001	<0.001
	Post	<0.01	<0.001	<0.001

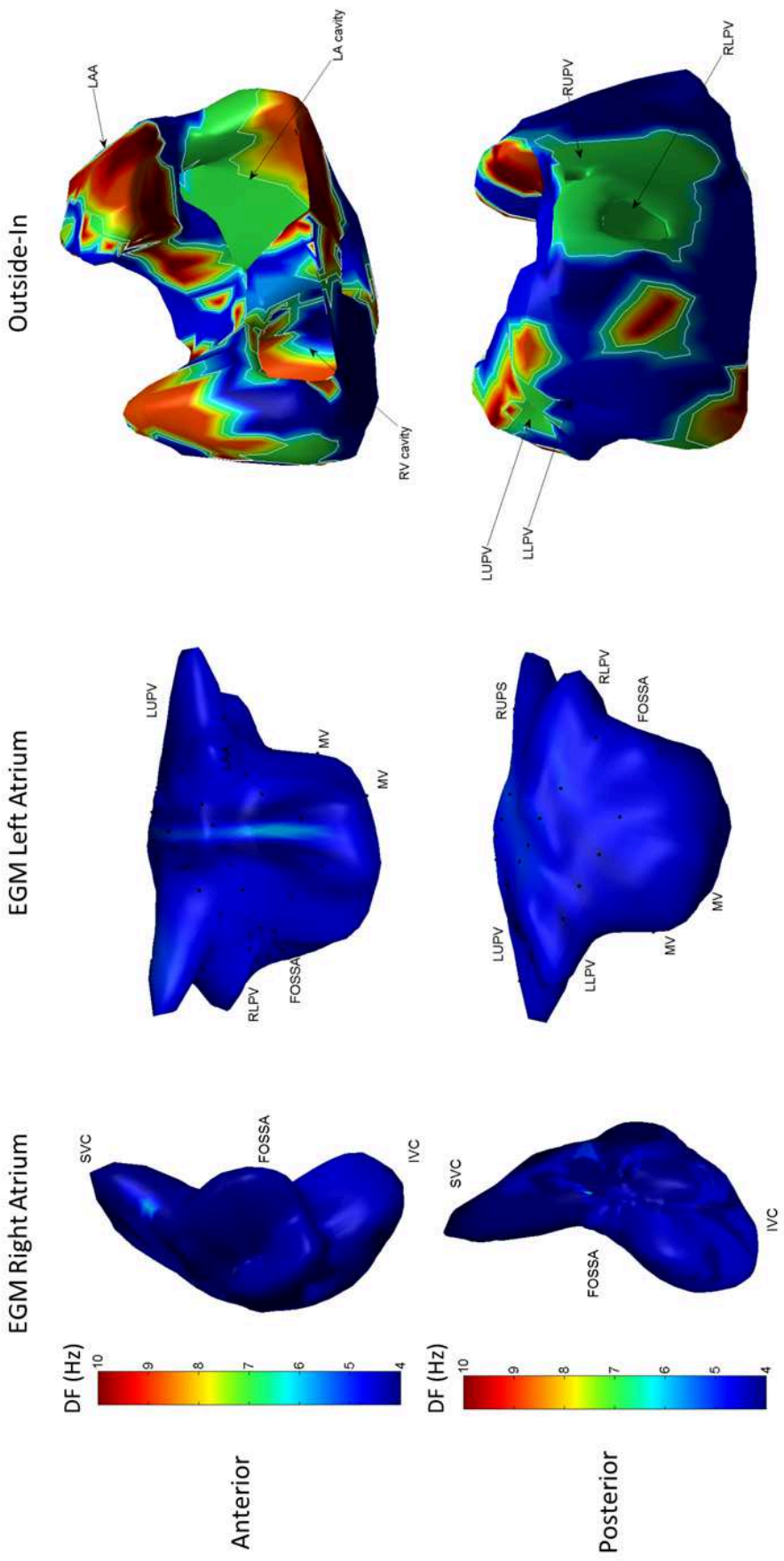

Figure 6-4: Comparison of the DF map for the EnSite right (left) and left (middle) atrium and Outside-In inverse solution (right) for one window.

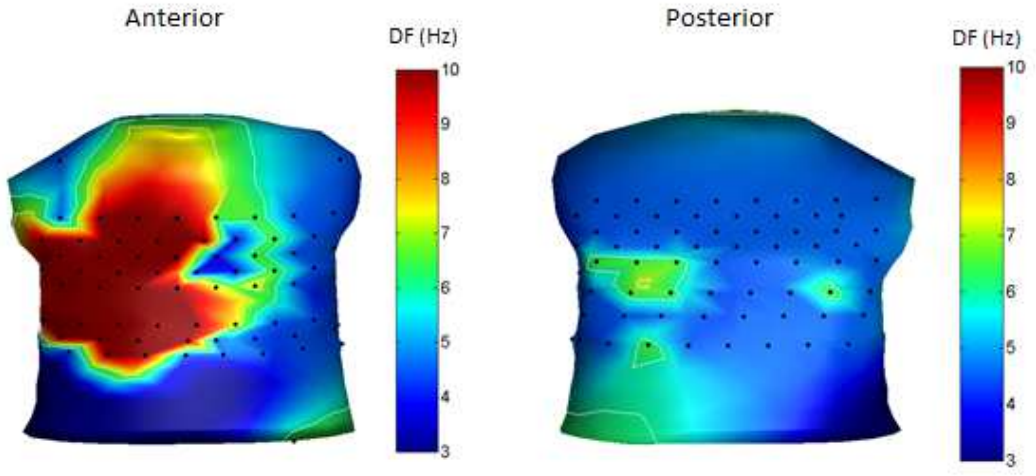

Figure 6-5: Body surface DF map for the same window as the atrial DF maps shown in Figure 6-4.

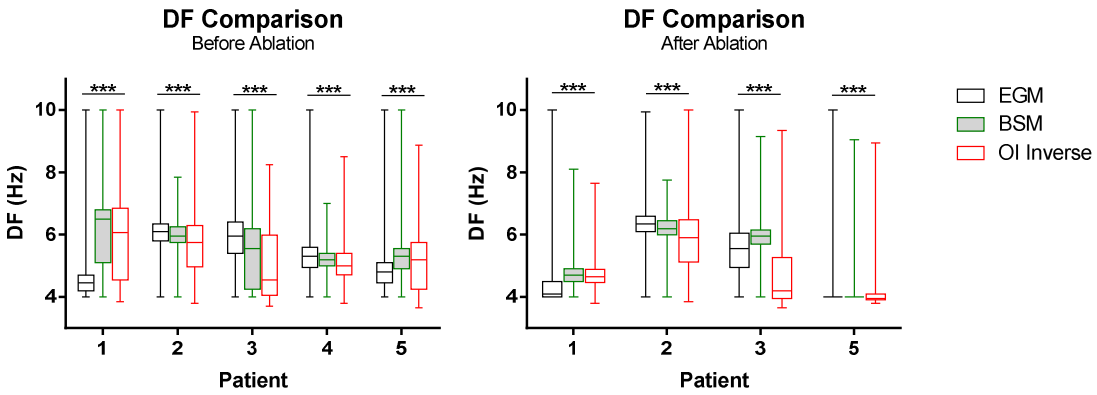

Figure 6-6: Comparison of the DF behaviour between the BSM, EGM and outside-in inverse solutions for all subjects before and after ablation. Asterisks indicate statistical significance at *p* values equal to 0.05 (*), 0.01 (**) and 0.001(***).

Similarly, comparisons were made for the highest DF (HDF) behaviour between both inverse solutions and the BSM data. One example for subject 3 after ablation is given in Figure 6-7. The HDF area on the body surface appears to the left side of the torso. On the OI inverse, the HDF seems to reside around the septum. The EnSite data show a small HDF area in the right atrium, and a left atrial HDF in the right pulmonary veins. The left atrial HDF has a lower value than the right atrial HDF.

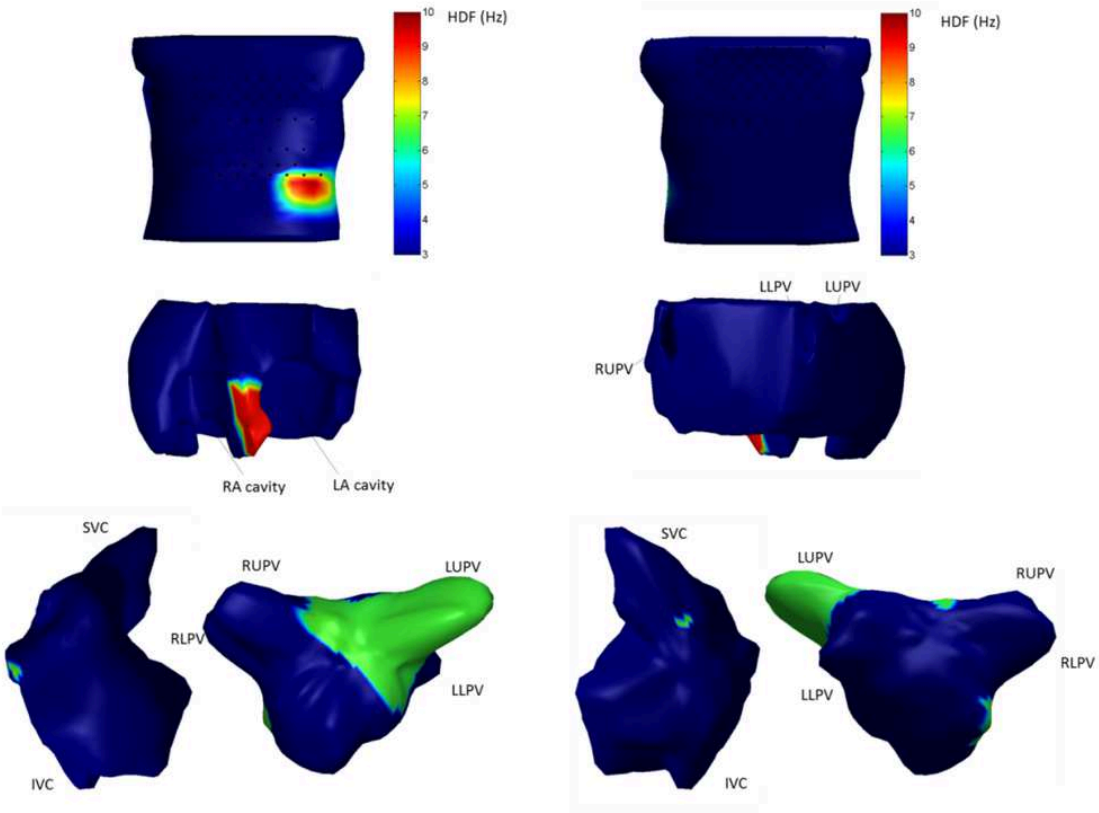

Figure 6-7: Comparison of HDF areas on the body surface (top), OI inverse solution (middle) and EnSite meshes (bottom).

A comparison of the HDF behaviour per subject was performed between the inverse solutions and the body surface maps. Results of the Friedman ANOVA test are given in Figure 6-8. It can be observed that the OI inverse solution HDF values appear higher than those found on the body surface maps. The variance between the three modalities is considered very significant ($p < 0.001$).

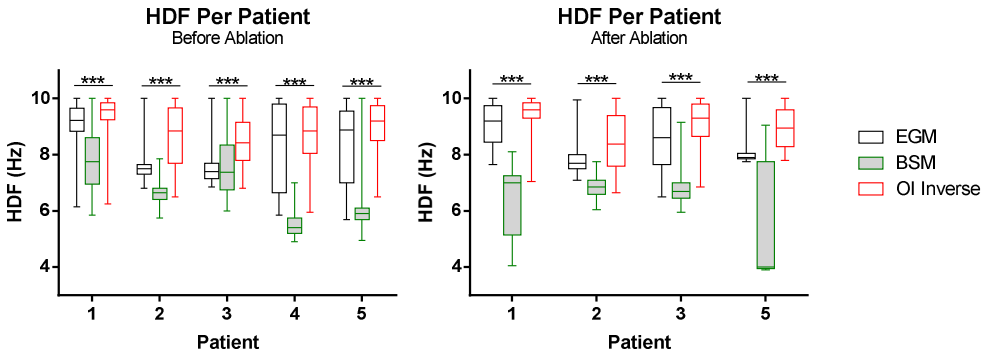

Figure 6-8: Comparison of the HDF behaviour per subject for the three modalities. Asterisks indicate statistical significance at *p* values equal to 0.05 (*), 0.01 (**) and 0.001(***).

Table 6-2 represents the results of the individual comparisons between the three modalities. For most cases, the results between the inverse solutions and the body surface data appear very significant, whereas the difference is less significant between both OI and EnSite inverse solutions.

Table 6-2: Results of the multiple comparison tests (p values) between the HDF values of the three different modalities. >0.05 represents not significant, <0.05 borderline significant, <0.01 significant and <0.001 very significant differences.

Subject		Multiple Comparison Results (p values)		
		EnSite vs. BSM	EnSite vs. OI	BSM vs. OI
1	Pre	<0.001	<0.001	<0.001
	Post	<0.001	<0.05	<0.001
2	Pre	<0.001	<0.001	<0.001
	Post	<0.001	<0.01	<0.001
3	Pre	>0.05	<0.001	<0.001
	Post	<0.001	<0.05	<0.001
4	Pre	<0.05	>0.05	<0.001
5	Pre	<0.001	<0.05	<0.001
	Post	<0.01	<0.001	<0.001

6.4 Discussion

The work presented here offers an alternative inverse solution compared to the well-known potential-based inverse solution and the activation-time based imaging. It can be considered as an advanced version of the dipole and double layer models suggested in early literature (Barr *et al.*, 1966, Geselowitz, 1964). Its benefit, compared to the potential-based inverse solution, is that it takes into account equivalent sources for the cardiac activity, rather than giving a closer look to pericardial potential. The advantage compared to activation-time based

algorithms is that easier validation can be performed, as the solution results in a potential field which can be compared with direct contact mapping data. Besides this, there is no need for an initial estimate of the activation propagation. Its disadvantages are that the equivalent source model might not be sufficiently accurate to represent cardiac behaviour, a problem that is avoided with potential-based transfers. A disadvantage compared to activation-time based imaging is that this methodology needs the inclusion of regularisation which might not be directly related to cardiac electrophysiology.

6.4.1 Inverse Algorithm

Figure 6-1 provides an example of an isopotential map on the atrial muscle after inversely solving from the body surface. From these observations, it proved difficult to qualitatively or quantitatively assess the accuracy of the inverse solution. From the average relative difference between the forward solution and body surface map, it can be considered that additional steps have to take into account to further improve the inverse solution. Most improvements can possibly be made in avoiding measurement and geometrical noise. The manual segmentation of the atrial muscle proved rather challenging, as well as correctly allocating body surface nodes to electrode positions.

Some possibilities to improve 3D tissue segmentation can be considered. One possibility is the use of computed tomography (CT) images rather than MR images. This would allow the images to be taken whilst the subject is wearing the BSM electrodes, thereby providing an exact location of the BSM measurement positions (Ramanathan *et al.*, 2004). The use of CT was avoided in this work due to radiation exposure. Alternatively, a standard model could be set up to which the subject's geometry is morphed. Jamison *et al.* showed the possibility to use a standard female torso for acquiring accurate inverse solutions of different volunteers. This standardisation did not provide sufficient accuracy for subjects with a torso varying strongly to the standard model, however (Jamison *et al.*, 2011). Other groups have also indicated the significant effect of geometric error in the cardiac position on the inverse problem (Hoekema *et al.*, 1996, Messinger-Rapport and Rudy, 1986).

However, a similar morphing technique for the heart in a standard torso might be sufficient to provide accurate results.

Besides this, the inclusion of other torso tissues and organs besides the lungs might improve the current inverse solution. Studies have focussed on the inclusion of various tissues in the volume conductor model, showing that some tissues have significant effect on the forward and inverse solution (Klepfer *et al.*, 1997, Messinger-Rapport and Rudy, 1990). Further investigations are needed in this field however, especially regarding what conductivity should be allocated to the various tissues, and if anisotropy of muscle layers should be taken into account.

Further to this, a comparison between the EnSite inside-out and the current OI solution was challenging. One source of variation would be the variation in the approach to the source of the cardiac potentials. The use of a potential-based transfer model compared to the double layer and monolayer equivalent source model will induce variation in the inverse solution which, as far as the author knows, has not been investigated in clinical trials. However, the evidence from the previous chapter shows that remarkable difference exists, as it took strong regularisation to make a double layer inverse solution appear similar to the EnSite solution for the left atrium. This effect could not be further investigated here due to the lack of a potential-based OI inverse solution. The lack of a double-layer based inverse solution for the right atrium made a comparison of the outside-in with the home-made inside-out inverse solution difficult. Further studies are underway to tackle both issues.

As it was difficult to assess this variation, evidence of transmurality could not be provided with certainty based on isopotential maps. Possible further evidence was therefore sought from frequency analysis.

6.4.2 Outside-In Frequency Analysis

From Figure 6-2 and Figure 6-3, it can be observed that, in cases of organised AF (bottom figures) the current inverse solution was able to correctly determine the dominant frequency of the AF cycle. With more complex AF behaviour, the relationship between the EnSite endocardial and the outside-in inverse solution

was less pronounced. One problem that did arrive with the outside-in inverse solution was a difficulty in appropriately removing the QRST interval. This could be the reason why in most cases, a significant variation existed between the EnSite and OI inverse solution DF distribution. The influence of ventricular activity can also provide some explanation for the similarity between body surface maps and the OI inverse solution DF distributions. Future work might therefore opt to perform QRST subtraction prior to the inverse solution. Other reasons might be an effect of atrial transmurality, and the fact that frequency measurements were taken from different locations. The effect of transmurality can only be assessed after ensuring a proper QRST subtraction has been performed, and when the node locations on the endocardial site of the atrial muscle are aligned with the atrial cavity nodes as accurately as possible. Research has been performed to link electro-anatomical mapping system meshes (such as the EnSite mesh) with MR images with relatively good success (Knowles *et al.*, 2010). Further research is ongoing in the group to merge meshes of different modalities.

As for the HDF behaviour, the results show that the OI HDF results are significantly different from the BSM data, but in some cases show similarity with the EnSite data. Taking into account the issues with QRST subtraction, these results do seem to indicate that the OI inverse solution can take into account the filtering effects of the volume conductor, and reproduce high frequency signals from smoothed, blurred images. Reasons for the variation in HDF behaviour between the OI and EnSite inverse solution are similar as those discussed for the DF behaviour. Reasons for similarity could mean that both systems indeed show the same behaviour, or could be due to the fact that the HDF values are close to the physiological range of 10 Hz for relevant AF signals, as suggested in this work. The 3D visualisation of the HDF areas seems to relate more to the latter, as no direct correlation between the EnSite HDF location and OI HDF location could be observed in many cases. However, as the effect of transmurality could not be clearly assessed in this work, further research might indicate that this effect is an important cause of the lack of co-localisation of HDF areas.

6.5 Study Limitations

One of the major limitations in the study is the small study size. Current research is underway in the group to increase the number of subjects for which endocardial maps and body surface maps are available. For these subjects, also balloon data for the right atrium will be available, which will make it possible to not only perform the home-made inside-out inverse solution on the right atrium but also to compare the results of this inside-out inverse solution with the outside-in inverse solution presented in this chapter. This would allow a direct comparison of inverse solutions that assume the same source model.

Besides this, no direct epicardial contact mapping data were available to compare the inverse solution with. Although our inverse solution was validated using a simple model, a further validation in torso-tank models could be beneficial to assess the quality of the inverse solution and provide better understanding of the effects of noise on the inverse solution. Lastly, further optimisation of the 3D models should be considered. It would be of interest to work on an automated segmentation modality that can develop patient-specific models accurately, reducing image processing time compared to the current, manual approach.

6.6 Clinical Relevance of Findings

As discussed in the previous chapter, current-based source models provide an alternative view on the inverse estimation of cardiac signals compared to potential-based solutions. Optimised versions of current-based algorithms can be set up to take into account local effect of transmembrane potential distributions. Equivalent double layer models would provide means to estimate atrial cell depolarisation (and repolarisation) sequences, which could provide clinicians with information to directly interpret the relevance of local atrial activation phenomena with possible AF drivers. Previous work has shown the successful use of the EDL model estimating cardiac activity (van Oosterom, 2014a), also with specific focus toward atrial activity (van Dam and van Oosterom, 2005). The suggested inverse solution algorithm would be able to provide more electrophysiologically relevant information compared to potential-based source models that have started to emerge as clinical tools (Cuculich *et*

al., 2010, Haïssaguerre *et al.*, 2014), once further optimisation is provided in segmenting the volume conductor as well as the process of collecting and processing cardiac signals.

As inverse problems are an estimation of cardiac behaviour, the combination of inside-out and outside-in inverse solutions for relevant interpretation of atrial transmurality might remain challenging. The relation between this estimation and true cardiac behaviour will be dependent on the accuracy of the source model. Besides this, effects of volume conductor, geometrical errors and signal artefacts will further complicate this interpretation. Verification of the inverse solutions with measured data would help in determining the clinical relevance of the transmurality analysis, but complete clinical evaluation of this phenomenon based solely on the inverse solution will remain cumbersome.

6.7 Conclusion

This chapter attempted in combining the EnSite inside-out inverse solution with a home-made OI inverse solution based on a double layer model to assess the possible transmural behaviour of the atrial muscle during atrial fibrillation. From isopotential maps, no evidence of this transmurality could be concluded due to difficulty in comparing the inverse solutions. This comparison was hampered by the difference in source models from which both solutions originate, as well as possible geometrical errors from suboptimal MRI segmentation. Similarly, it was difficult to make any strong conclusions on the variation in DF behaviour and the effect of atrial transmural dyssynchrony on this behaviour. On the positive side, the OI inverse solution seems to be able to reconstruct simple AF behaviour in the frequency spectrum, and is able to reproduce high-frequency behaviour on the atrial muscle which might have been smoothed on the body surface. Further investigation in optimising the OI inverse solution and linking the results with endocardial data is however required.

7 Project Summary and Future Perspectives

Atrial fibrillation (AF) is the most occurring cardiac arrhythmia in the world. Although not lethal, it increases the risk of stroke by fivefold and has been linked to increased risks of myocardial infarct. These consequences can be lethal, or inflict serious reductions in quality of life. As the susceptibility for AF increases with age, current data suggest a significant increase of AF patients over the coming decades. Current treatment methods are based on drugs, cardioversion or catheter ablation. Although well-developed, these treatment techniques are not always successful, and AF relapse occurs frequently. Further understanding of the triggers and maintainers of AF is therefore sought.

An interesting approach to investigate AF behaviour in clinic is by the use of body surface mapping and electrophysiological studies (contact or non-contact endocardial mapping). Electrophysiological studies are invasive and therefore carry risk to the patient. This risk can be avoided using body surface mapping, but the data from these torso surface measurements are relatively distant from the cardiac source, and therefore only provide blurred images of AF behaviour. By combining BSM signals with a volume conductor model representing the torso, atrial signals can be estimated taking into account variations in conductivity for different torso organs. The location of these organs can be obtained from medical images (e.g. MRI scans). This estimation of cardiac potentials can be called the outside-in inverse problem of electrocardiography. Similarly, the estimation of endocardial electrograms from non-contact mapping catheters can be called the inside-out inverse problem of electrocardiography.

In this work, AF analysis was performed on body surface signals, virtual endocardial signals from a non-contact mapping system and virtual atrial muscle wall signals from an outside-in inverse solution. As data for both inverse solutions were taken simultaneously, an analysis of the possible transmural dyssynchrony between the endocardial and epicardial wall of the atria was investigated. Most attention was paid on the frequency analysis of the AF signal, and how variations in the frequency results could be deduced from the different measurement modalities.

7.1 Project Novelties

The main novelties of the current work are:

- The simultaneous frequency analysis of bi-atrial non-contact mapping and body surface data, showing a spatiotemporal filtering effect of the volume conductor on the BSM highest dominant frequency value under clinical condition, similar to simulation studies described in previous literature.
- The development of inverse algorithms by using the analytical formulas for double layer and monolayer sources. This avoids the use of numerical implementations for the boundary element model, and can therefore reduce errors.
- A representation of the effect of different source models on non-contact inside-out inverse solutions in a clinical situation. Previous work has shown some of these effects in simulation studies only. A further implementation of this work could be of high significance in improving inverse solution algorithms.
- The comparison of an inside-out and outside-in inverse solution for atrial fibrillation as a starting point to further understand the drivers behind AF. Although further investigations are needed for this, first results indicate that simple AF behaviour can be traceable with an outside-in inverse solution based on frequency analysis.

7.2 Main findings

From chapter 2, the most striking results could be found in the variation of the highest dominant frequency (HDF) distribution between the body surface signals and virtual electrograms on the endocardium obtained from non-contact mapping data (EnSite Balloon Array). HDF values appear to be lower on the body surface map then on the endocardium. An exponential curve could be fitted between the difference of the HDF value on the body surface and on the endocardium versus the endocardial HDF value. This behaviour shows strong similarity to previous simulation studies assessing the effect of the volume conductor as a spatio-temporal filter. Our results suggest that this filtering effect can be seen on clinical data for cardiac measurements, and should be taken into account in case body surface signals are used for assessing AF behaviour and treatment strategies.

In chapter 3, an indication of the effect of reduced lead systems on body surface maps was investigated using Lomb Spatial Spectral analysis. Although this methodology does not allow developing accurate reduced-lead systems, it can provide an idea of the number of electrodes needed to represent a body surface map assuming the electrodes are uniformly positioned over the body surface. The results indicated that our current 131 lead system is sufficient to represent full body surface maps in healthy volunteers, and therefore could be considered appropriate and useful in estimating cardiac sources from inverse solutions.

The feasibility of using inverse solutions based on monolayer and double layer sources was investigated in chapter 4. The forward and inverse solution for a cardiac source surrounding the heart was compared to the analytical solution for both an inside-out and outside-in inverse solution. Results suggest that the forward and inverse solutions could accurately reproduce the analytical solutions on the spherical model. For endocardial inverse solution, the volume conductor effect was investigated, and it appeared that better solutions could be obtained when including heterogeneities in this volume conductor model. For the outside-in inverse solution, the effect of reduced leads and measurement noise was assessed. Noise levels of low amplitude appear to be

allowable for accurate reproduction of signals, with the necessary smoothing. Generally, however, care must be taken to avoid noise. Also, reduced-lead inverse solutions should be carefully assessed.

A comparison between a commercially available potential-based inverse solution and a home-made double layer-based inside-out inverse solution was investigated in chapter 5. It could be observed that different source models in the inverse problem provide different solutions for the virtual electrocardiograms, which could be of importance for the correct clinical interpretation of these inverse solutions. Other aspects that could affect the final electrograms are different ways of filtering the original balloon signals, the type of regularisation used (as shown in chapter 4) and geometrical variation (3D meshes). For this particular comparison, a high regularisation parameter had to be used on the double-layer based inverse solution to obtain high similarity with the potential-based solution. This high smoothing affected the frequency analysis of the former inverse solution drastically, indicated by the significant differences in DF and HDF behaviour between both inverse solutions.

Chapter 6 provided an analysis of the DF and HDF behaviour from an outside-in inverse solution based on a double layer model. Results were compared with an inside-out inverse solution based on a potential source. This chapter provided a first step towards analysing possible dyssynchrony between atrial epicardium and endocardium during atrial fibrillation. As both inverse solutions were based on different source models, it remained difficult to provide any conclusions regarding the existence of this transmurality. Besides this, possible errors in QRST subtraction and cardiac position will have affected the outside-in inverse solution. Bearing these issues in mind, it could still be shown that simple AF behaviour could be reproduced accurately in the frequency domain.

7.3 Future perspectives

Several ways forward can be seen from the current thesis project. On one hand, the further identification of DF and HDF as possible representations of AF drivers can be further explored. Future research could consider including the effect of harmonics and dominant frequency organisation on the

identification of HDF sites. This could provide a more true analysis of the highest dominant frequency, and it might provide further indications of the strength of the filtering effect of the volume conductor. This latter could be assessed by comparing the amplitude (or power) of a frequency peak in the spectrum of atrial data, be it with contact or non-contact mapping, endocardial or epicardial, with those on the body surface map.

For the inside-out inverse problem, further analysis could be performed by comparing the virtual electrograms of both the EnSite as the home-made inverse solution with contact mapping data, preferably taken at sites to which the EnSite system performs a direct inverse solution. This could indicate better how different inverse solutions affect the clinical interpretation, and how realistic these interpretations are to the signals seen immediately on the endocardial wall. For the home-made inverse solution, balloon data of both the right and left atrium could be made available to test a more complete inverse solution, which could also be further investigated in clinic as well as using experimental simulations, such as torso tank models. A potential-source based inverse solution could also be created for comparison with the EnSite system, as it would provide further understanding of how this system interprets data and estimates endocardial signals.

For the outside-in inverse solution, a further optimisation of setting up the volume conductor model needs to be investigated, as the current methodology appears prone in errors and is highly time-expensive. Further analysis on the effect of filtering and other signal processing steps could be performed. One interesting approach would be to first subtract QRST segments from the body surface maps and use these atrial signals to perform the inverse solution towards the atria. Once a double-layer based inverse solution for the right atrial endocardium becomes available, research can pay attention to merge the endocardial cavities onto the MRI or CT derived torso model for a more feasible assessment of the correlation between epicardial and endocardial data. As with the inside-out inverse solution, new algorithms based on a potential source or activation-based imaging could be set up to compare the differences in inverse solutions and assess their performance. Lastly, performing outside-in inverse solutions with reduced-lead systems and comparing their accuracy to a full

electrode set could prove useful not only in reducing computational time and memory but especially in setting up body surface maps and outside-in inverse algorithms in clinical environments.

REFERENCES

AFA, A. F. A. 2011. *What is Atrial Fibrillation ?* [Online]. Available: http://www.atrialfibrillation.org.uk/patient-information/atrial-fibrillation.html [Accessed 04/07/2014.

AGUR, A. M. R. & DALLEY, A. F. 2005. *Grant's Atlas of Anatomy,* Philadelphia, PA, USA, Lippincott Williams & Wilkins.

ALIOT, E. & RUSKIN, J. N. 2008. Controversies in ablation of atrial fibrillation. *European Heart Journal Supplements,* 10**,** H32-H54.

ALLESSIE, M., AUSMA, J. & SCHOTTEN, U. 2002. Electrical, contractile and structural remodeling during atrial fibrillation. *Cardiovascular Research,* 54**,** 230-246.

ALLESSIE, M. A. 1985. Experimental evaluation of Moe's multiple wavelet hypothesis of atrial fibrillation. *Cardiac arrhythmias***,** 265-276.

ALLESSIE, M. A., BONKE, F. I. M. & SCHOPMAN, F. J. G. 1977. Circus movement in rabbit atrial muscle as a mechanism of tachycardia. III. The 'leading circle' concept: a new model of circus movement in cardiac tissue without the involvement of an anatomical obstacle. *Circulation Research,* 41**,** 9-18.

ALLESSIE, M. A., BOYDEN, P. A., CAMM, A. J., KLÉBER, A. G., LEGATO, M. J., ROSEN, M. R., SCHWARTZ, P. J., SPOONER, P. M., VAN WAGONER, D. R. & WALDO, A. L. 2001. Pathophysiology and prevention of atrial fibrillation. *Circulation,* 103**,** 769-777.

ARTHUR, R. M., GESELOWITZ, D. B., BRILLER, S. A. & TROST, R. F. 1972. Quadrupole components of the human surface electrocardiogram. *American Heart Journal,* 83**,** 663-677.

ATIENZA, F., ALMENDRAL, J., JALIFE, J., ZLOCHIVER, S., PLOUTZ-SNYDER, R., TORRECILLA, E. G., ARENAL, Á., KALIFA, J., FERNÁNDEZ-AVILÉS, F. & BERENFELD, O. 2009. Real-time dominant frequency mapping and ablation of dominant frequency sites in atrial fibrillation with left-to-right frequency gradients predicts long-term maintenance of sinus rhythm. *Heart Rhythm,* 6**,** 33-40.

AYDIN, U. & DOGRUSOZ, Y. S. 2011. A Kalman filter-based approach to reduce the effects of geometric errors and the

measurement noise in the inverse ECG problem. *Medical and Biological Engineering and Computing,* 49**,** 1003-1013.

BARR, R. C., PILKINGTON, T. C., BOINEAU, J. P. & ROGERS, C. L. 1970. An Inverse Electrocardiographic Solution with an ON-OFF Model. *Biomedical Engineering, IEEE Transactions on,* BME-17**,** 49-57.

BARR, R. C., PILKINGTON, T. C., BOINEAU, J. P. & SPACH, M. S. 1966. Determining surface potentials from current dipoles, with application to electrocardiography. *IEEE Transactions on Biomedical Engineering,* 13**,** 88-92.

BARR, R. C., RAMSEY, M. & SPACH, M. S. 1977. Relating Epicardial to Body Surface Potential Distributions by Means of Transfer Coefficients Based on Geometry Measurements. *Biomedical Engineering, IEEE Transactions on,* BME-24**,** 1-11.

BARR, R. C., SPACH, M. S. & HERMAN-GIDDENS, G. S. 1971. Selection of the Number and Positions of Measuring Locations for Electrocardiography. *Biomedical Engineering, IEEE Transactions on,* BME-18**,** 125-138.

BEATTY, G. E., BUDD, J. R. & KAGAN, J. 2010. Endocardial mapping system. Google Patents.

BECK, J. V. & ARNOLD, K. J. 1977. *Parameter estimation in engineering and science*, James Beck.

BEN-HAIM, S. A., OSADCHY, D., SCHUSTER, I., GEPSTEIN, L., HAYAM, G. & JOSEPHSON, M. E. 1996. Nonfluoroscopic, in vivo navigation and mapping technology. *Nature Medicine,* 2**,** 1393-1395.

BENARROCH, E. E. 1993. The central autonomic network: Functional organization, dysfunction, and perspective. *Mayo Clinic Proceedings,* 68**,** 988-1001.

BOJARNEJAD, M., BLAKE, J., BOURKE, J. P., MURRAY, A. & LANGLEY, P. Comparison of body surface and intracardiac ECG recordings in patients with atrial fibrillation during electrophysiological studies. IFMBE Proceedings, 2013. 612-615.

BOND, R. R., FINLAY, D. D., NUGENT, C. D. & MOORE, G. 2010a. A Web-based tool for processing and visualizing body

surface potential maps. *Journal of Electrocardiology,* 43**,** 560-565.

BOND, R. R., FINLAY, D. D., NUGENT, C. D. & MOORE, G. 2010b. XML-BSPM: An XML format for storing Body Surface Potential Map recordings. *BMC Medical Informatics and Decision Making,* 10.

BORON, W. F. & BOULPAEP, E. L. 2012. *Medical Physiology*, Elsevier Health Sciences.

BREBBIA, C. A. & DOMINGUEZ, J. 1996. *Boundary elements: an introductory course*, WIT press.

BRODY, D. A. 1956. A theoretical analysis of intracavitary blood mass influence on the heart-lead relationship. *Circulation research,* 4**,** 731-738.

BROOKS, D. H. & AHMAD, G. F. 1999. Inverse electrocardiography by simultaneous imposition of multiple constraints. *IEEE Transactions on Biomedical Engineering,* 46**,** 3-18.

BRUDER, H., SCHOLZ, B. & ABRAHAM-FUCHS, K. 1994. The influence of inhomogeneous volume conductor models on the ECG and the MCG. *Physics in Medicine and Biology,* 39**,** 1949-1968.

BRUTSAERT, D. L. 2003. Cardiac endothelial-myocardial signaling: Its role in cardiac growth, contractile performance, and rhythmicity. *Physiological Reviews,* 83**,** 59-115.

BUDD, J. R., HAUCK, J. A. & BEATTY, G. E. 1996. Endocardial measurement method. Google Patents.

BURKHOFF, D., MIRSKY, I. & SUGA, H. 2005. Assessment of systolic and diastolic ventricular properties via pressure-volume analysis: a guide for clinical, translational, and basic researchers. *American Journal of Physiology-Heart and Circulatory Physiology,* 289**,** H501-H512.

CALVETTI, D., LEWIS, B. & REICHEL, L. Restoration of images with spatially variant blur by the GMRES method. Proceedings of SPIE - The International Society for Optical Engineering, 2000. 364-374.

CAMM, A. J., KIRCHHOF, P., LIP, G. Y. H., SCHOTTEN, U., SAVELIEVA, I., ERNST, S., VAN GELDER, I. C., AL-ATTAR,

N., HINDRICKS, G., PRENDERGAST, B., HEIDBUCHEL, H., ALFIERI, O., ANGELINI, A., ATAR, D., COLONNA, P., DE CATERINA, R., DE SUTTER, J., GOETTE, A., GORENEK, B., HELDAL, M., HOHLOSER, S. H., KOLH, P., LE HEUZEY, J. Y., PONIKOWSKI, P., RUTTEN, F. H., VAHANIAN, A., AURICCHIO, A., BAX, J., CECONI, C., DEAN, V., FILIPPATOS, G., FUNCK-BRENTANO, C., HOBBS, R., KEARNEY, P., MCDONAGH, T., POPESCU, B. A., REINER, Z., SECHTEM, U., SIRNES, P. A., TENDERA, M., VARDAS, P. E., WIDIMSKY, P., AGLADZE, V., ALIOT, E., BALABANSKI, T., BLOMSTROM-LUNDQVIST, C., CAPUCCI, A., CRIJNS, H., DAHLÖF, B., FOLLIGUET, T., GLIKSON, M., GOETHALS, M., GULBA, D. C., HO, S. Y., KLAUTZ, R. J. M., KOSE, S., MCMURRAY, J., PERRONE FILARDI, P., RAATIKAINEN, P., SALVADOR, M. J., SCHALIJ, M. J., SHPEKTOR, A., SOUSA, J., STEPINSKA, J., UUETOA, H., ZAMORANO, J. L. & ZUPAN, I. 2010. Guidelines for the management of atrial fibrillation. *European Heart Journal,* 31**,** 2369-2429.

CAPPATO, R., CALKINS, H., CHEN, S. A., DAVIES, W., IESAKA, Y., KALMAN, J., KIM, Y. H., KLEIN, G., PACKER, D. & SKANES, A. 2005. Worldwide survey on the methods, efficacy, and safety of catheter ablation for human atrial fibrillation. *Circulation,* 111**,** 1100-1105.

CASTELLS, F., MORA, C., RIETA, J. J., MORATAL-PÉREZ, D. & MILLET, J. 2005. Estimation of atrial fibrillatory wave from single-lead atrial fibrillation electrocardiograms using principal component analysis concepts. *Medical and Biological Engineering and Computing,* 43**,** 557-560.

CHENG, L. K., BODLEY, J. M. & PULLAN, A. J. 2003a. Comparison of potential- and activation-based formulations for the inverse problem of electrocardiology. *IEEE Transactions on Biomedical Engineering,* 50**,** 11-22.

CHENG, L. K., BODLEY, J. M. & PULLAN, A. J. 2003b. Effects of experimental and modeling errors on electrocardiographic inverse formulations. *IEEE Transactions on Biomedical Engineering,* 50**,** 23-32.

CLELAND, J. G. F., SWEDBERG, K., FOLLATH, F., KOMAJDA, M., COHEN-SOLAL, A., AGUILAR, J. C., DIETZ, R., GAVAZZI, A., HOBBS, R., KOREWICKI, J., MADEIRA, H. C.,

MOISEYEV, V. S., PREDA, I., VAN GILST, W. H., WIDIMSKY, J., FREEMANTLE, N., EASTAUGH, J. & MASON, J. 2003. The EuroHeart Failure survey programme - A survey on the quality of care among patients with heart failure in Europe. Part 1: Patient characteristics and diagnosis. *European Heart Journal,* 24**,** 442-463.

CLERC, L. 1976. Directional differences of impulse spread in trabecular muscle from mammalian heart. *Journal of Physiology,* 255**,** 335-346.

COLLI-FRANZONE, P., GUERRI, L., TACCARDI, B. & VIGANOTTI, C. 1985a. Finite element approximation of regularized solutions of the inverse potential problem of electrocardiography and applications to experimental data. *Calcolo,* 22**,** 91-186.

COLLI-FRANZONE, P., GUERRI, L., TENTONI, S., VIGANOTTI, C., BARUFFI, S., SPAGGIARI, S. & TACCARDI, B. 1985b. A mathematical procedure for solving the inverse potential problem of electrocardiography. analysis of the time-space accuracy from in vitro experimental data. *Mathematical Biosciences,* 77**,** 353-396.

COLLI-FRANZONE, P., GUERRI, L., VIGANOTTI, C., MACCHI, E., BARUFFI, S., SPAGGIARI, S. & TACCARDI, B. 1982. Potential fields generated by oblique dipole layers modeling excitation wavefronts in the anisotropic myocardium. Comparison with potential fields elicited by paced dog hearts in a volume conductor. *Circulation Research,* 51**,** 330-346.

COMTOIS, P., KNELLER, J. & NATTEL, S. 2005. Of circles and spirals: Bridging the gap between the leading circle and spiral wave concepts of cardiac reentry. *Europace,* 7**,** S10-S20.

CONNOLLY, S. J., EZEKOWITZ, M. D., YUSUF, S., EIKELBOOM, J., OLDGREN, J., PAREKH, A., POGUE, J., REILLY, P. A., THEMELES, E., VARRONE, J., WANG, S., ALINGS, M., XAVIER, D., ZHU, J., DIAZ, R., LEWIS, B. S., DARIUS, H., DIENER, H. C., JOYNER, C. D., WALLENTIN, L., ALINGS, A. M. W., AMERENA, J. V., AVEZUM, A., BAUMGARTNER, I., BRUGADA, J., BUDAJ, A., CAICEDO, V., CEREMUZYNSKI, L., CHEN, J. H., COMMERFORD, P. J., CONNOLLY, S. J., DANS, A. L., DARIUS, H., DI PASQUALE, G., DIAZ, R., EROL, C., EZEKOWITZ, M. D., FERREIRA, J., FLAKER, G.

C., FLATHER, M. D., FRANZOSI, M. G., GAMBOA, R., GOLITSYN, S. P., GONZALEZ HERMOSILLO, J. A., HALON, D., HEIDBUCHEL, H., HOHNLOSER, S. H., HORI, M., HUBER, K., JANSKY, P., KAMENSKY, G., KELTAI, M., KIM, S., LAU, C. P., LE HEUZEY, J. Y. F., LEWIS, B. S., LIU, L. S., NANAS, J., OLDGREN, J., PAIS, P. S., PARKHOMENKO, A. N., PEDERSEN, K. E., PIEGAS, L. S., RAEV, D., RAZALI, O., SIMMERS, T. A., SMITH, P. J., TALAJIC, M., TAN, R. S., TANOMSUP, S., TOIVONEN, L., VINEREANU, D., WALLENTIN, L., XAVIER, D., YUSUF, S. & ZHU, J. 2009. Dabigatran versus warfarin in patients with atrial fibrillation. *New England Journal of Medicine,* 361**,** 1139-1151.

CORBIN II, L. V. & SCHER, A. M. 1977. The canine heart as an electrocardiographic generator. Dependence on cardiac cell orientation. *Circulation Research,* 41**,** 58-67.

CORREA DE SA, D. D., THOMPSON, N., STINNETT-DONNELLY, J., ZNOJKIEWICZ, P., HABEL, N., MÜLLER, J. G., BATES, J. H. T., BUZAS, J. S. & SPECTOR, P. S. 2011. Electrogram Fractionation: The Relationship Between Spatiotemporal Variation of Tissue Excitation and Electrode Spatial Resolution. *Circulation: Arrhythmia and Electrophysiology,* 4**,** 909-916.

COURTEMANCHE, M., RAMIREZ, R. J. & NATTEL, S. 1998. Ionic mechanisms underlying human atrial action potential properties: Insights from a mathematical model. *American Journal of Physiology - Heart and Circulatory Physiology,* 275**,** H301-H321.

COX, J. L., SCHUESSLER, R. B., CAIN, M. E., CORR, P. B., STONE, C. M., D'AGOSTINO JR, H. J., HARADA, A., CHANG, B. C., SMITH, P. K. & BOINEAU, J. P. 1989. Surgery for atrial fibrillation. *Seminars in Thoracic and Cardiovascular Surgery,* 1**,** 67-73.

COX, J. L., SCHUESSLER, R. B., D'AGOSTINO JR, H. J., STONE, C. M., CHANG, B. C., CAIN, M. E., CORR, P. B. & BOINEAU, J. P. 1991. The surgical treatment of atrial fibrillation: III. Development of a definitive surgical procedure. *Journal of Thoracic and Cardiovascular Surgery,* 101**,** 569-583.

CRANEFIELD, P. F. 1977. Action potentials, afterpotentials, and arrhythmias. *Circulation Research,* 41**,** 415-423.

CUCULICH, P. S., WANG, Y., LINDSAY, B. D., FADDIS, M. N., SCHUESSLER, R. B., DAMIANO, R. J., LI, L. & RUDY, Y. 2010. Noninvasive characterization of epicardial activation in humans with diverse atrial fibrillation patterns. *Circulation,* 122**,** 1364-1372.

CUFFIN, B. N. & COHEN, D. 1979. Comparison of the magnetoencephalogram and electroencephalogram. *Electroencephalography and Clinical Neurophysiology,* 47**,** 132-146.

CUFFIN, B. N. & GESELOWITZ, D. B. 1977. Studies of the electrocardiogram using realistic cardiac and torso models. *IEEE Transactions on Biomedical Engineering,* 24**,** 242-252.

CUPPEN, J. J. M. & VAN OOSTEROM, A. 1984. Model studies with the inversely calculated isochrones of ventricular depolarization. *IEEE Transactions on Biomedical Engineering,* 31**,** 652-659.

D' ALCHÉ, P., DUCIMETIERE, P. & LACOMBE, J. 1974. Computer model of cardiac potential distribution in an infinite medium and on the human torso during ventricular activation. *Circulation Research,* 34**,** 719-729.

DAMEN, A. A. & VAN DER KAM, J. 1982. The use of the singular value decomposition in electrocardiography. *Medical and Biological Engineering and Computing,* 20**,** 473-482.

DE GROOT, N., HOUBEN, R. P. M., SMEETS, J. L., BOERSMA, E., SCHOTTEN, U., SCHALIJ, M. J., CRIJNS, H. & ALLESSIE, M. A. 2010. Electropathological substrate of longstanding persistent atrial fibrillation in patients with structural heart disease: Epicardial breakthrough. *Circulation,* 122**,** 1674-1682.

DE MUNCK, J. C. 1990. The estimation of time varying dipoles on the basis of evoked potentials. *Electroencephalography and Clinical Neurophysiology,* 77**,** 156-160.

DE MUNCK, J. C. 1992. A linear discretization of the volume conductor boundary integral equation using analytically integrated elements. *IEEE Transactions on Biomedical Engineering,* 39**,** 986-990.

DELORME, A. & MAKEIG, S. 2004. EEGLAB: An open source toolbox for analysis of single-trial EEG dynamics including

independent component analysis. *Journal of Neuroscience Methods,* 134**,** 9-21.

DI MARCO, L. Y., RAINE, D., BOURKE, J. P. & LANGLEY, P. 2014. Recurring patterns of atrial fibrillation in surface ECG predict restoration of sinus rhythm by catheter ablation. *Computers in Biology and Medicine,* 54**,** 172-179.

DIERCKX, H., BERNUS, O. & VERSCHELDE, H. 2011. Accurate eikonal-curvature relation for wave fronts in locally anisotropic reaction-diffusion systems. *Physical Review Letters,* 107.

DÖSSEL, O., KRUEGER, M. W., WEBER, F. M., WILHELMS, M. & SEEMANN, G. 2012. Computational modeling of the human atrial anatomy and electrophysiology. *Medical and Biological Engineering and Computing,* 50**,** 773-799.

DURRER, D., VAN DAM, R. T., FREUD, G. E., JANSE, M. J., MEIJLER, F. L. & ARZBAECHER, R. C. 1970. Total excitation of the isolated human heart. *Circulation,* 41**,** 899-912.

EBASHI, S. 1991. Excitation-contraction coupling and the mechanism of muscle contraction. *Annual Review of Physiology,* 53**,** 1-16.

ECKSTEIN, J., MAESEN, B., LINZ, D., ZEEMERING, S., VAN HUNNIK, A., VERHEULE, S., ALLESSIE, M. & SCHOTTEN, U. 2011. Time course and mechanisms of endo-epicardial electrical dissociation during atrial fibrillation in the goat. *Cardiovascular Research,* 89**,** 816-824.

EINTHOVEN, W. 1913. Über die Deutung des Elektrokardiogramms. *Pflüger's Archiv für die Gesamte Physiologie des Menschen und der Tiere,* 149**,** 65-86.

EINTHOVEN, W., FAHR, G. & DE WAART, A. 1913. Über die Richtung und die manifeste Grösse der Potentialschwankungen im menschlichen Herzen und über den Einfluss der Herzlage auf die Form des Elektrokardiogramms. *Pflüger's Archiv für die Gesamte Physiologie des Menschen und der Tiere,* 150**,** 275-315.

ELVAN, A., LINNENBANK, A. C., VAN BEMMEL, M. W., MISIER, A. R. R., DELNOY, P. P. H. M., BEUKEMA, W. P. & DE BAKKER, J. M. T. 2009. Dominant frequency of atrial fibrillation correlates poorly with atrial fibrillation cycle length. *Circulation: Arrhythmia and Electrophysiology,* 2**,** 634-644.

EPSTEIN, A. E. 2004. Relationships between Sinus Rhythm, Treatment, and Survival in the Atrial Fibrillation Follow-Up Investigation of Rhythm Management (AFFIRM) Study. *Circulation,* 109**,** 1509-1513.

EVANS, D. H., SCHLINDWEIN, F. S. & LEVENE, M. I. 1989. An automatic system for capturing and processing ultrasonic Doppler signals and blood pressure signals. *Clinical Physics and Physiological Measurement,* 10**,** 241-251.

EVERETT, T. H. I. V., WILSON, E. E., HULLEY, G. S. & OLGIN, J. E. 2007. Transmural characteristics of atrial fibrillation in canine models of structural and electrical atrial remodeling assessed by simultaneous epicardial and endocardial mapping. *Heart Rhythm,* 7**,** 506-517.

FARINA, D. & MERLETTI, R. 2001. A novel approach for precise simulation of the EMG signal detected by surface electrodes. *Biomedical Engineering, IEEE Transactions on,* 48**,** 637-646.

FINLAY, D. D., NUGENT, C. D., DONNELLY, M. P., LUX, R. L., MCCULLAGH, P. J. & BLACK, N. D. 2006. Selection of optimal recording sites for limited lead body surface potential mapping: A sequential selection based approach. *BMC Medical Informatics and Decision Making,* 6.

FOZZARD, H. A., LIPKIND, G., GOTSMAN, M. S., MORAD, M., BASSINGTHWAIGHTE, J., MARBAN, E., LAB, M. & KESSLER-ICEKSON, G. 1995. Ion channels and pumps in cardiac function. *Advances in Experimental Medicine and Biology,* 382**,** 3-10.

FRANK, E. 1956. An accurate, clinically practical system for spatial vectorcardiography. *Circulation,* 13**,** 737-749.

FRY, C. H. & JABR, R. I. 2010. The action potential and nervous conduction. *Surgery,* 28**,** 49-54.

FUSTER, V., RYDÉN, L. E., CANNOM, D. S., CRIJNS, H. J., CURTIS, A. B., ELLENBOGEN, K. A., HALPERIN, J. L., LE HEUZEY, J. Y., KAY, G. N., LOWE, J. E., OLSSON, S. B., PRYSTOWSKY, E. N., TAMARGO, J. L., WANN, S., SMITH JR, S. C., JACOBS, A. K., ADAMS, C. D., ANDERSON, J. L., ANTMAN, E. M., HALPERIN, J. L., HUNT, S. A., NISHIMURA, R., ORNATO, J. P., PAGE, R. L., RIEGEL, B., PRIORI, S. G., BLANC, J. J., BUDAJ, A., CAMM, A. J.,

DEAN, V., DECKERS, J. W., DESPRES, C., DICKSTEIN, K., LEKAKIS, J., MCGREGOR, K., METRA, M., MORAIS, J., OSTERSPEY, A., TAMARGO, J. L. & ZAMORANO, J. L. 2006. ACC/AHA/ESC 2006 guidelines for the management of patients with atrial fibrillation: A report of the American College of Cardiology/American Heart Association Task Force on practice guidelines and the European Society of Cardiology Committee for practice guidelines (Writing committee to revise the 2001 guidelines for the management of patients with atrial fibrillation). *Circulation,* 114**,** e257-e354.

GABOR, D. & NELSON, C. V. 1954. Determination of the resultant dipole of the heart from measurements on the body surface. *Journal of Applied Physics,* 25**,** 413-416.

GABRIEL, S., LAU, R. W. & GABRIEL, C. 1996. The dielectric properties of biological tissues: II. Measurements in the frequency range 10 Hz to 20 GHz. *Physics in Medicine and Biology,* 41**,** 2251-2269.

GARREY, W. E. 1924. *Auricullar Fibrillation*.

GELERNTER, H. L. & SWIHART, J. C. 1964. A Mathematical-Physical Model of the Genesis of the Electrocardiogram. *Biophysical journal,* 4**,** 285-301.

GERSTENFELD, E. P., SIPPENSGROENEWEGEN, A., LUX, R. L. & LESH, M. D. 2000. Derivation of an optimal lead set for measuring ectopic atrial activation from the pulmonary veins by using body surface mapping. *Journal of Electrocardiology,* 33**,** 179-185.

GESELOWITZ, D. B. 1964. Dipole theory in electrocardiography. *The American Journal of Cardiology,* 14**,** 301-306.

GESELOWITZ, D. B. 1965. Two theorems concerning the quadrupole applicable to electrocardiography. *IEEE Transactions on Biomedical Engineering,* 12**,** 164-168.

GESELOWITZ, D. B. 1989. On the theory of the electrocardiogram. *Proceedings of the IEEE,* 77**,** 857-876.

GESELOWITZ, D. B. 1992. Description of cardiac sources in anisotropic cardiac muscle: Application of bidomain model. *Journal of Electrocardiology,* 25**,** 65-67.

GESELOWITZ, D. B. & MILLER III, W. T. 1983. A bidomain model for anisotropic cardiac muscle. *Annals of Biomedical Engineering,* 11**,** 191-206.

GHARAVIRI, A., VERHEULE, S., KUIJPERS, N. & SCHOTTEN, U. Mutual influence between dyssynchrony and transmural conduction maintains atrial fibrillation. 39th Computing in Cardiology Conference, CinC 2012, 2012 Krakow. 897-900.

GORDON, A. M., HOMSHER, E. & REGNIER, M. 2000. Regulation of contraction in striated muscle. *Physiological Reviews,* 80**,** 853-924.

GRAY, R. A., PERTSOV, A. M. & JALIFE, J. 1998. Spatial and temporal organization during cardiac fibrillation. *Nature,* 392**,** 75-78.

GREENSITE, F. 1994. Well-posed formulation of the inverse problem of electrocardiography. *Annals of Biomedical Engineering,* 22**,** 172-183.

GREENSITE, F. & HUISKAMP, G. 1998. An improved method for estimating epicardial potentials from the body surface. *IEEE Transactions on Biomedical Engineering,* 45**,** 98-104.

GUILLEM, M. S., CLIMENT, A. M., MILLET, J., ARENAL, Á., FERNÁNDEZ-AVILÉS, F., JALIFE, J., ATIENZA, F. & BERENFELD, O. 2013. Noninvasive localization of maximal frequency sites of atrial fibrillation by body surface potential mapping. *Circulation: Arrhythmia and Electrophysiology,* 6**,** 294-301.

GUILLEM, M. S., CLIMENT, A. M., MILLET, J., HUSSER, D., BOLLMANN, A. & CASTELLS, F. Non invasive mapping of human atrial fibrillation. IFMBE Proceedings, 2009. 575-578.

GULRAJANI, R. M. & MAILLOUX, G. E. 1983. A simulation study of the effects of torso inhomogeneities on electrocardiographic potentials, using realistic heart and torso models. *Circulation Research,* 52**,** 45-56.

HADAMARD, J. 1902. Sur les problèmes aux dérivées partielles et leur signification physique. *Princeton university bulletin,* 13**,** 28.

HAÏSSAGUERRE, M., HOCINI, M., DENIS, A., SHAH, A. J., KOMATSU, Y., YAMASHITA, S., DALY, M., AMRAOUI, S.,

ZELLERHOFF, S., PICAT, M. Q., QUOTB, A., JESEL, L., LIM, H., PLOUX, S., BORDACHAR, P., ATTUEL, G., MEILLET, V., RITTER, P., DERVAL, N., SACHER, F., BERNUS, O., COCHET, H., JAIS, P. & DUBOIS, R. 2014. Driver domains in persistent atrial fibrillation. *Circulation,* 130**,** 530-538.

HAÏSSAGUERRE, M., HOCINI, M., SHAH, A. J., DERVAL, N., SACHER, F., JAIS, P. & DUBOIS, R. 2013. Noninvasive panoramic mapping of human atrial fibrillation mechanisms: A feasibility report. *Journal of Cardiovascular Electrophysiology,* 24**,** 711-717.

HAÏSSAGUERRE, M., JAÏS, P., SHAH, D. C., TAKAHASHI, A., HOCINI, M., QUINIOU, G., GARRIGUE, S., LE MOUROUX, A., LE MÉTAYER, P. & CLÉMENTY, J. 1998. Spontaneous initiation of atrial fibrillation by ectopic beats originating in the pulmonary veins. *New England Journal of Medicine,* 339**,** 659-666.

HANSEN, P. C. 1994. Regularization Tools: A Matlab package for analysis and solution of discrete ill-posed problems. *Numerical Algorithms,* 6**,** 1-35.

HANSEN, P. C. 2010. *Discrete Inverse Problems,* Philadelphia, PA, USA, Society for Industrial and Applied Mathematics.

HARRILD, D. & HENRIQUEZ, C. 2000. A computer model of normal conduction in the human atria. *Circulation research,* 87**,** E25-36.

HARRIS, F. J. 1978. On the use of windows for harmonic analysis with the discrete Fourier transform. *Proceedings of the IEEE,* 66**,** 51-83.

HAUEISEN, J., SCHREIBER, J., BRAUER, H. & KNOSCHE, T. R. 2002. Dependence of the inverse solution accuracy in magnetocardiography on the boundary-element discretization. *Magnetics, IEEE Transactions on,* 38**,** 1045-1048.

HELMHOLTZ, H. 1853. Ueber einige Gesetze der Vertheilung elektrischer Ströme in körperlichen Leitern mit Anwendung auf die thierisch-elektrischen Versuche. *Annalen der Physik,* 165**,** 211-233.

HENRIQUEZ, C. S. 1993. Simulating the electrical behavior of cardiac tissue using the bidomain model. *Critical Reviews in Biomedical Engineering,* 21**,** 1-77.

HOBBS, F. R., FITZMAURICE, D., MANT, J., MURRAY, E., JOWETT, S., BRYAN, S., RAFTERY, J., DAVIES, M. & LIP, G. 2005. A randomised controlled trial and cost-effectiveness study of systematic screening (targeted and total population screening) versus routine practice for the detection of atrial fibrillation in people aged 65 and over. The SAFE study. *Health Technology Assessment,* 9**,** 93pp.

HOEKEMA, R., UIJEN, G. J. H., STILLI, D. & VAN OOSTEROM, A. 1998. Lead system transformation of body surface map data. *Journal of Electrocardiology,* 31**,** 71-82.

HOEKEMA, R., UIJEN, G. J. H. & VAN OOSTEROM, A. 1996. Normalization of the electrocardiogram by standardization of heart position and orientation. *Computers in Cardiology,* 0**,** 717-720.

HOEKEMA, R., UIJEN, G. J. H. & VAN OOSTEROM, A. 1999. On selecting a body surface mapping procedure. *Journal of Electrocardiology,* 32**,** 93-101.

HOLLAND, R. P. & ARNSDORF, M. F. 1977. Solid angle theory and the electrocardiogram: physiologic and quantitative interpretations. *Progress in Cardiovascular Diseases,* 19**,** 431-457.

HORAN, L. G., FLOWERS, N. C. & BRODY, D. A. 1964. The limits of information in the vectorcardiogram: Comparative resynthesis of body surface potentials with different lead systems. *American Heart Journal,* 68**,** 362-369.

HSU, L. F., JAÏS, P., SANDERS, P., GARRIGUE, S., HOCINI, M., SACHER, F., TAKAHASHI, Y., ROTTER, M., PASQUIÉ, J. L., SCAVÉE, C., BORDACHAR, P., CLÉMENTY, J. & HAÏSSAGUERRE, M. 2004. Catheter ablation for atrial fibrillation in congestive heart failure. *New England Journal of Medicine,* 351**,** 2373-2383.

HUISKAMP, G. 1991. Difference formulas for the surface Laplacian on a triangulated surface. *Journal of Computational Physics,* 95**,** 477-496.

HUISKAMP, G. & GREENSITE, F. 1997. A new method for myocardial activation imaging. *IEEE Transactions on Biomedical Engineering,* 44**,** 433-446.

HUISKAMP, G. & VAN OOSTEROM, A. 1988. The depolarization sequence of the human heart surface computed from measured body surface potentials. *IEEE Transactions on Biomedical Engineering,* 35**,** 1047-1058.

IHARA, Z., VAN OOSTEROM, A., JACQUEMET, V. & HOEKEMA, R. 2007. Adaptation of the standard 12-lead electrocardiogram system dedicated to the analysis of atrial fibrillation. *Journal of Electrocardiology,* 40**,** 68.e1-68.e8.

ISRAEL, C. W., GRÖNEFELD, G., EHRLICH, J. R., LI, Y. G. & HOHNLOSER, S. H. 2004. Long-Term Risk of Recurrent Atrial Fibrillation as Documented by an Implantable Monitoring Device: Implications for Optimal Patient Care. *Journal of the American College of Cardiology,* 43**,** 47-52.

JAMISON, C., NAVARRO, C., TURNER, C., SHANNON, J., ANDERSON, J. & ADGEY, J. 2011. The inverse problem utilizing the boundary element method for a nonstandard female torso. *IEEE Transactions on Biomedical Engineering,* 58**,** 876-883.

JARMAN, J. W. E., WONG, T., KOJODJOJO, P., SPOHR, H., DAVIES, J. E., ROUGHTON, M., FRANCIS, D. P., KANAGARATNAM, P., MARKIDES, V., DAVIES, D. W. & PETERS, N. S. 2012. Spatiotemporal behavior of high dominant frequency during paroxysmal and persistent atrial fibrillation in the human left atrium. *Circulation: Arrhythmia and Electrophysiology,* 5**,** 650-658.

JONGSMA, H. J. & WILDERS, R. 2000. Gap junctions in cardiovascular disease. *Circulation Research,* 86**,** 1193-1197.

KADISH, A., HAUCK, J., PEDERSON, B., BEATTY, G. & GORNICK, C. 1999. Mapping of atrial activation with a noncontact, multielectrode catheter in dogs. *Circulation,* 99**,** 1906-1913.

KAGAN, J., BEATTY, G. E. & BUDD, J. R. 1994. Heart mapping catheter. Google Patents.

KALLERGIS, E. M., MANIOS, E. G., KANOUPAKIS, E. M., MAVRAKIS, H. E., GOUDIS, C. A., MALIARAKI, N. E.,

SALOUSTROS, I. G., MILATHIANAKI, M. E., CHLOUVERAKIS, G. I. & VARDAS, P. E. 2010. Effect of Sinus Rhythm Restoration After Electrical Cardioversion on Apelin and Brain Natriuretic Peptide Prohormone Levels in Patients With Persistent Atrial Fibrillation. *American Journal of Cardiology,* 105**,** 90-94.

KANNEL, W. B., WOLF, P. A., BENJAMIN, E. J., LEVY, D., PRITCHETT, E., REIFFEL, J. A., OLSHANSKY, B., LUDERITZ, B., REITER, M., FALK, R. H. & CAMM, J. 1998. Prevalence, incidence, prognosis, and predisposing conditions for atrial fibrillation: Population-based estimates. *American Journal of Cardiology,* 82**,** 2N-9N.

KEATING, M. T. & SANGUINETTI, M. C. 2001. Molecular and cellular mechanisms of cardiac arrhythmias. *Cell,* 104**,** 569-580.

KEETON, P., SCHLINDWEIN, F. & EVANS, D. 1997. A study of the spectral broadening of simulated Doppler signals using FFT and AR modelling. *Ultrasound in medicine & biology,* 23**,** 1033-1045.

KERR, C. R., HUMPHRIES, K. H., TALAJIC, M., KLEIN, G. J., CONNOLLY, S. J., GREEN, M., BOONE, J., SHELDON, R., DORIAN, P. & NEWMAN, D. 2005. Progression to chronic atrial fibrillation after the initial diagnosis of paroxysmal atrial fibrillation: Results from the Canadian Registry of Atrial Fibrillation. *American Heart Journal,* 149**,** 489-496.

KHOURY, D. S., TACCARDI, B., LUX, R. L., ERSHLER, P. R. & RUDY, Y. 1995. Reconstruction of endocardial potentials and activation sequences from intracavitary probe measurements: Localization of pacing sites and effects of myocardial structure. *Circulation,* 91**,** 845-863.

KLEPFER, R. N., JOHNSON, C. R. & MACLEOD, R. S. 1997. The effects of inhomogeneities and anisotropies on electrocardiographic fields: A 3-D finite-element study. *IEEE Transactions on Biomedical Engineering,* 44**,** 706-719.

KNOWLES, B. R., CAULFIELD, D., COOKLIN, M., RINALDI, C. A., GILL, J., BOSTOCK, J., RAZAVI, R., SCHAEFFTER, T. & RHODE, K. S. 2010. 3-D Visualization of Acute RF Ablation Lesions Using MRI for the Simultaneous Determination of the

Patterns of Necrosis and Edema. *Biomedical Engineering, IEEE Transactions on,* 57**,** 1467-1475.

KONINGS, K. T. S., KIRCHHOF, C. J. H. J., SMEETS, J. R. L. M., WELLENS, H. J. J., PENN, O. C. & ALLESSIE, M. A. 1994. High-density mapping of electrically induced atrial fibrillation in humans. *Circulation,* 89**,** 1665-1680.

KORNREICH, F., MONTAGUE, T. J., RAUTAHARJU, P. M., BLOCK, P., WARREN, J. W. & HORACEK, M. B. 1986. Identification of best electrocardiographic leads for diagnosing anterior and inferior myocardial infarction by statistical analysis of body surface potential maps. *The American Journal of Cardiology,* 58**,** 863-871.

KORNREICH, F., RAUTAHARJU, P. M., WARREN, J., MONTAGUE, T. J. & HORACEK, B. M. 1985. Identification of best electrocardiographic leads for diagnosing myocardial infarction by statistical analysis of body surface potential maps. *The American Journal of Cardiology,* 56**,** 852-856.

KUMAGAI, K., SAKAMOTO, T., NAKAMURA, K., NISHIUCHI, S., HAYANO, M., HAYASHI, T., SASAKI, T., AONUMA, K. & OSHIMA, S. 2013. Combined dominant frequency and complex fractionated atrial electrogram ablation after circumferential pulmonary vein isolation of atrial fibrillation. *Journal of Cardiovascular Electrophysiology,* 24**,** 975-983.

LANGLEY, P., MACGOWAN, G. A. & MURRAY, A. 2009. Spatial and temporal organization of the dominant frequencies in the fibrillating heart: Body surface potential mapping in a rare case of sustained human ventricular fibrillation. *Europace,* 11**,** 324-327.

LAWSON, C. L. & HANSON, R. J. 1974. *Solving least squares problems*, SIAM.

LEMAY, M., JACQUEMET, V., JOUSSET, F., VESIN, J.-M. & VAN OOSTEROM, A. The mean firing rate of atrial fibrillation as estimated from the ecg evaluation using a biophysical model. Computers in Cardiology, 2007, 2007. IEEE, 37-40.

LEMERY, R., SOUCIE, L., MARTIN, B., TANG, A. S. L., GREEN, M. & HEALEY, J. 2004. Human study of biatrial electrical coupling: Determinants of endocardial septal activation and

conduction over interatrial connections. *Circulation,* 110**,** 2083-2089.

LEMOLA, K., TING, M., GUPTA, P., ANKER, J. N., CHUGH, A., GOOD, E., REICH, S., TSCHOPP, D., IGIC, P., ELMOUCHI, D., JONGNARANGSIN, K., BOGUN, F., PELOSI JR, F., MORADY, F. & ORAL, H. 2006. Effects of Two Different Catheter Ablation Techniques on Spectral Characteristics of Atrial Fibrillation. *Journal of the American College of Cardiology,* 48**,** 340-348.

LEVINE, D. M., STEPHAN, D. F., KREHBIEL, T. C. & BERENSON, M. L. 2005. *Statistics for managers using Microsoft Excel*, Pearson Prentice Hall Upper Saddle Creek, NJ.

LIN, W. S., TAI, C. T., HSIEH, M. H., TSAI, C. F., LIN, Y. K., TSAO, H. M., HUANG, J. L., YU, W. C., YANG, S. P., DING, Y. A., CHANG, M. S. & CHEN, S. A. 2003. Catheter ablation of paroxysmal atrial fibrillation initiated by non-pulmonary vein ectopy. *Circulation,* 107**,** 3176-3183.

LINDSTROM, L. H. & MAGNUSSON, R. I. 1977. Interpretation of myoelectric power spectra: A model and its applications. *Proceedings of the IEEE,* 65**,** 653-662.

LOMB, N. R. 1976. Least-squares frequency analysis of unequally spaced data. *Astrophysics and Space Science,* 39**,** 447-462.

LUX, R. L., SMITH, C. R., WYATT, R. F. & ABILDSKOV, J. A. 1978. Limited Lead Selection for Estimation of Body Surface Potential Maps in Electrocardiography. *Biomedical Engineering, IEEE Transactions on,* BME-25**,** 270-276.

LYNN, M. & TIMLAKE, W. 1968a. The Use of Multiple Deflations in the Numerical Solution of Singular Systems of Equations, with Applications to Potential Theory. *SIAM Journal on Numerical Analysis,* 5**,** 303-322.

LYNN, M. S. & TIMLAKE, W. P. 1968b. The numerical solution of singular integral equations of potential theory. *Numerische Mathematik,* 11**,** 77-98.

MADEIRO, J. P. V., CORTEZ, P. C., MARQUES, J. A. L., SEISDEDOS, C. R. V. & SOBRINHO, C. R. M. R. 2012. An innovative approach of QRS segmentation based on first-derivative, Hilbert and Wavelet Transforms. *Medical Engineering and Physics,* 34**,** 1236-1246.

MARASCUILO, L. A. 1966. Large-sample multiple comparisons. *Psychological Bulletin,* 65**,** 280.

MARQUARDT, D. W. 1963. An algorithm for least-squares estimation of nonlinear parameters. *Journal of the Society for Industrial & Applied Mathematics,* 11**,** 431-441.

MARTIN, R. O. & PILKINGTON, T. C. 1972. Unconstrained Inverse Electrocardiography: Epicardial Potentials. *Biomedical Engineering, IEEE Transactions on,* BME-19**,** 276-285.

MCCLELLAND, A. J. J., OWENS, C. G., NAVARRO, C., SMITH, B., ROBERTS, M. J. D., ANDERSON, J. & ADGEY, A. A. J. 2006. Usefulness of Body Surface Maps to Demonstrate Ventricular Activation Patterns During Left Ventricular Pacing and Reentrant Activation During Ventricular Tachycardia in Men With Coronary Heart Disease and Left Ventricular Dysfunction. *American Journal of Cardiology,* 98**,** 591-596.

MEDVEGY, M., DURAY, G., PINTÉR, A. & PRÉDA, I. 2002. Body surface potential mapping: Historical background, present possibilities, diagnostic challenges. *Annals of Noninvasive Electrocardiology,* 7**,** 139-151.

MEIJS, J. W. H., WEIER, O. W., PETERS, M. J. & VAN OOSTEROM, A. 1989. On the numerical accuracy of the boundary element method. *IEEE Transactions on Biomedical Engineering,* 36**,** 1038-1049.

MENG, S., ZHAO, J., BURTON, B. M., LEVER, N. A., LEGRICE, I. J. & SMAILL, B. H. Accurate endocardial activation representation of atria by noncontact mapping. Computing in Cardiology, 2012. 709-712.

MEO, M., ZARZOSO, V., MESTE, O., LATCU, D. G. & SAOUDI, N. 2013. Catheter ablation outcome prediction in persistent atrial fibrillation using weighted principal component analysis. *Biomedical Signal Processing and Control,* 8**,** 958-968.

MESSINGER-RAPPORT, B. & RUDY, Y. 1990. Noninvasive recovery of epicardial potentials in a realistic heart-torso geometry. Normal sinus rhythm. *Circulation research,* 66**,** 1023-1039.

MESSINGER-RAPPORT, B. J. & RUDY, Y. 1985. Effects of the torso boundary and internal conductivity interfaces in

electrocardiography: An evaluation of the 'Infinite medium' approximation. *Bulletin of Mathematical Biology,* 47**,** 685-694.

MESSINGER-RAPPORT, B. J. & RUDY, Y. 1986. Inverse Problem in Electrocardiography: A Model Study of the Effects of Geometry And Conductivity Parameters on the Reconstruction of Epicardial Potentials. *IEEE Transactions on Biomedical Engineering,* BME-33**,** 667-676.

MESSINGER-RAPPORT, B. J. & RUDY, Y. 1988. Regularization of the inverse problem in electrocardiography: A model study. *Mathematical Biosciences,* 89**,** 79-118.

MILLER III, W. T. & GESELOWITZ, D. B. 1978. Simulation studies of the electrocardiogram. I. The normal heart. *Circulation Research,* 43**,** 301-315.

MINES, G. R. 1913. On dynamic equilibrium in the heart. *Journal of Physiology,* 46**,** 349-383.

MIYASAKA, Y., BARNES, M. E., GERSH, B. J., CHA, S. S., SEWARD, J. B., BAILEY, K. R., IWASAKA, T. & TSANG, T. S. M. 2005. Time trends of ischemic stroke incidence and mortality in patients diagnosed with first atrial fibrillation in 1980 to 2000: Report of a community-based study. *Stroke,* 36**,** 2362-2366.

MODRE, R., TILG, B., FISCHER, G., HANSER, F., MESSNARZ, B., SEGER, M., SCHOCKE, M. F. H., BERGER, T., HINTRINGER, F. & ROITHINGER, F. X. 2003. Atrial noninvasive activation mapping of paced rhythm data. *Journal of Cardiovascular Electrophysiology,* 14**,** 712-719.

MODRE, R., TILG, B., FISCHER, G. & WACH, P. 2002. Noninvasive myocardial activation time imaging: A novel inverse algorithm applied to clinical ECG mapping data. *IEEE Transactions on Biomedical Engineering,* 49**,** 1153-1161.

MOE, G. K., RHEINBOLDT, W. C. & ABILDSKOV, J. A. 1964. A computer model of atrial fibrillation. *American Heart Journal,* 67**,** 200-220.

MONRO, D. M., GUARDO, R. A. L., BOURDILLON, P. J. & TINKER, J. 1974. A Fourier technique for simultaneous electrocardiographic surface mapping. *Cardiovascular Research,* 8**,** 688-700.

MOORE JR, J. E. & MAITLAND, D. J. 2013. *Biomedical Technology and Devices*, CRC press.

NABAUER, M., GERTH, A., LIMBOURG, T., SCHNEIDER, S., OEFF, M., KIRCHHOF, P., GOETTE, A., LEWALTER, T., RAVENS, U., MEINERTZ, T., BREITHARDT, G. & STEINBECK, G. 2009. The Registry of the German Competence NETwork on Atrial Fibrillation: Patient characteristics and initial management. *Europace,* 11**,** 423-434.

NADEMANEE, K., MCKENZIE, J., KOSAR, E., SCHWAB, M., SUNSANEEWITAYAKUL, B., VASAVAKUL, T., KHUNNAWAT, C. & NGARMUKOS, T. 2004. A new approach for catheter ablation of atrial fibrillation: Mapping of the electrophysiologic substrate. *Journal of the American College of Cardiology,* 43**,** 2044-2053.

NARAYAN, S. M., KRUMMEN, D. E. & RAPPEL, W. J. 2012. Clinical mapping approach to diagnose electrical rotors and focal impulse sources for human atrial fibrillation. *Journal of Cardiovascular Electrophysiology,* 23**,** 447-454.

NASH, M. P. & PULLAN, A. J. 2005. Challenges facing validation of noninvasive electrical imaging of the heart. *Annals of Noninvasive Electrocardiology,* 10**,** 73-82.

NATTEL, S. 2002. New ideas about atrial fibrillation 50 years on. *Nature,* 415**,** 219-226.

NAVARRO, C., OWENS, C., RIDDELL, J., MCCLELLAND, A., ANDERSON, J. M., ESCALONA, O., TURNER, C. & ADGEY, J. 2003. The Use of Calculated Epicardial Potentials Improves Significantly the Sensitivity of a Diagnostic Algorithm in the Detection of Acute Myocardial Infarction. *Journal of Electrocardiology,* 36**,** 127-132.

NERBONNE, J. M. & KASS, R. S. 2005. Molecular physiology of cardiac repolarization. *Physiological Reviews,* 85**,** 1205-1253.

NEUMANN, T., VOGT, J., SCHUMACHER, B., DORSZEWSKI, A., KUNISS, M., NEUSER, H., KURZIDIM, K., BERKOWITSCH, A., KOLLER, M., HEINTZE, J., SCHOLZ, U., WETZEL, U., SCHNEIDER, M. A. E., HORSTKOTTE, D., HAMM, C. W. & PITSCHNER, H. F. 2008. Circumferential Pulmonary Vein Isolation With the Cryoballoon Technique. Results From a

Prospective 3-Center Study. *Journal of the American College of Cardiology,* 52**,** 273-278.

NG, J. & GOLDBERGER, J. J. 2007. Understanding and interpreting dominant frequency analysis of AF electrograms. *Journal of cardiovascular electrophysiology,* 18**,** 680-685.

NG, J., KADISH, A. H. & GOLDBERGER, J. J. 2006. Effect of electrogram characteristics on the relationship of dominant frequency to atrial activation rate in atrial fibrillation. *Heart Rhythm,* 3**,** 1295-1305.

NIEUWLAAT, R., CAPUCCI, A., CAMM, A. J., OLSSON, S. B., ANDRESEN, D., DAVIES, D. W., COBBE, S., BREITHARDT, G., LE HEUZEY, J. Y., PRINS, M. H., LÉVY, S. & CRIJNS, H. J. G. M. 2005. Atrial fibrillation management: A prospective survey in ESC Member Countries - The Euro Heart Survey on atrial fibrillation. *European Heart Journal,* 26**,** 2422-2434.

NOWAK, C. N., FISCHER, G., WIESER, L., TILG, B., NEURAUTER, A. & STROHMENGER, H. U. 2008. Spatial-temporal filter effect in a computer model study of ventricular fibrillation. *Biomedizinische Technik,* 53**,** 163-173.

OAKES, R. S., BADGER, T. J., KHOLMOVSKI, E. G., AKOUM, N., BURGON, N. S., FISH, E. N., BLAUER, J. J., RAO, S. N., DIBELLA, E. V. & SEGERSON, N. M. 2009. Detection and quantification of left atrial structural remodeling with delayed-enhancement magnetic resonance imaging in patients with atrial fibrillation. *Circulation,* 119**,** 1758-1767.

OOSTENDORP, T. F. & VAN OOSTEROM, A. 1989. Source parameter estimation in inhomogeneous volume conductors of arbitrary shape. *IEEE Transactions on Biomedical Engineering,* 36**,** 382-391.

OOSTENDORP, T. F., VAN OOSTEROM, A. & HUISKAMP, G. 1989. Interpolation on a triangulated 3D surface. *Journal of Computational Physics,* 80**,** 331-343.

OSTER, H. S. & RUDY, Y. 1992. The use of temporal information in the regularization of the inverse problem of electrocardiography. *IEEE Transactions on Biomedical Engineering,* 39**,** 65-75.

OSTER, H. S., TACCARDI, B., LUX, R. L., ERSHLER, P. R. & RUDY, Y. 1997. Noninvasive electrocardiographic imaging:

Reconstruction of epicardial potentials, electrograms, and isochrones and localization of single and multiple electrocardiac events. *Circulation,* 96**,** 1012-1024.

OSTER, H. S., TACCARDI, B., LUX, R. L., ERSHLER, P. R. & RUDY, Y. 1998. Electrocardiographic imaging: Noninvasive characterization of intramural myocardial activation from inverse-reconstructed epicardial potentials and electrograms. *Circulation,* 97**,** 1496-1507.

PANFILOV, A. & HOGEWEG, P. 1993. Spiral breakup in a modified FitzHugh-Nagumo model. *Physics Letters A,* 176**,** 295-299.

PANOFSKY, W. K. & PHILLIPS, M. 2005. *Classical electricity and magnetism*, Courier Dover Publications.

PLONSEY, R. & BARR, R. C. 2007. *Bioelectricity: A Quantitative Approach,* New York, NY, USA, Springer.

PLONSEY, R. & VAN OOSTEROM, A. 2012. Introductory Physics and Mathematics. *In:* MACFARLANE, P. W., VAN OOSTEROM, A., PAHLM, O., KLIGFIELD, P., JANSE, M. J. & CAMM, A. J. (eds.) *Comprehensive Electrophysiology.* 2 ed. London, UK: Springer.

PRESS, W. H., TEUKOLSKY, S. A., VETTERLING, W. T. & FLANNERY, B. P. 2002. Numerical Recipes in C+.

PULLAN, A. J., BUIST, M. L., SANDS, G. B., CHENG, L. K. & SMITH, N. P. 2003. Cardiac Electrical Activity - From Heart to Body Surface and Back Again. *Journal of Electrocardiology,* 36**,** 63-67.

PUNSKE, B. B. 2003. Noninvasive electrical imaging: Is it ready for clinical application? *Journal of Cardiovascular Electrophysiology,* 14**,** 720-721.

RAJAPPAN, K. & SCHILLING, R. J. 2009. Principles of Noncontact Endocardial Cardiac Mapping. *Cardiac Mapping, Third Edition.*

RAMANATHAN, C., GHANEM, R. N., JIA, P., RYU, K. & RUDY, Y. 2004. Noninvasive electrocardiographic imaging for cardiac electrophysiology and arrhythmia. *Nature Medicine,* 10**,** 422-428.

RAMANATHAN, C., JIA, P., GHANEM, R., CALVETTI, D. & RUDY, Y. 2003. Noninvasive electrocardiographic imaging (ECGI): Application of the generalized minimal residual (GMRes) method. *Annals of Biomedical Engineering,* 31**,** 981-994.

RAMANATHAN, C., JIA, P., GHANEM, R., RYU, K. & RUDY, Y. 2006. Activation and repolarization of the normal human heart under complete physiological conditions. *Proceedings of the National Academy of Sciences of the United States of America,* 103**,** 6309-6314.

RAMANATHAN, C. & RUDY, Y. 2001. Electrocardiographic imaging: II. Effect of torso inhomogeneities on noninvasive reconstruction of epicardial potentials, electrograms, and isochrones. *Journal of Cardiovascular Electrophysiology,* 12**,** 241-252.

REUMANN, M., FITCH, B. G., RAYSHUBSKIY, A., KELLER, D. U. J., WEISS, D. L., SEEMANN, G., DÖSSEL, O., PITMAN, M. C. & RICE, J. J. Comparison of computational load of a simple and complex electrophysiological cell models in large anatomical data-sets on the Blue Gene/L supercomputer. WMSCI 2008 - The 12th World Multi-Conference on Systemics, Cybernetics and Informatics, Jointly with the 14th International Conference on Information Systems Analysis and Synthesis, ISAS 2008 - Proc., 2008. 139-141.

RICCIO, M. L., KOLLER, M. L. & GILMOUR, R. F. 1999. Electrical restitution and spatiotemporal organization during ventricular fibrillation. *Circulation Research,* 84**,** 955-963.

RODRIGO, M., CLIMENT, A. M., LIBEROS, A., PEDRON-TORRECILLA, J., MILLET, J., FERNANDEZ-AVILES, F., ATIENZA, F., BERENFELD, O. & GUILLEM, M. S. Non-invasive location of re-entrant propagation patterns during atrial fibrillation. Computing in Cardiology, 2013. 1235-1238.

RODRIGO, M., GUILLEM, M. S., CLIMENT, A. M., PEDRÓN-TORRECILLA, J., LIBEROS, A., MILLET, J., FERNÁNDEZ-AVILÉS, F., ATIENZA, F. & BERENFELD, O. 2014. Body surface localization of left and right atrial high-frequency rotors in atrial fibrillation patients: A clinical-computational study. *Heart Rhythm,* 11**,** 1584-1591.

ROOS, T., MYLLYMAKI, P. & TIRRI, H. 2002. A statistical modeling approach to location estimation. *Mobile Computing, IEEE Transactions on,* 1**,** 59-69.

ROSNER, B. 2010. *Fundamentals of biostatistics*, Cengage Learning.

RUDY, Y. & BURNES, J. E. 1999. Noninvasive electrocardiographic imaging. *Annals of Noninvasive Electrocardiology,* 4**,** 340-359.

RUDY, Y. & MESSINGER-RAPPORT, B. J. 1988. The inverse problem in electrocardiography: solutions in terms of epicardial potentials. *Critical reviews in biomedical engineering,* 16**,** 215-268.

RUDY, Y. & PLONSEY, R. 1980. A comparison of volume conductor and source geometry effects on body surface and epicardial potentials. *Circulation Research,* 46**,** 283-291.

RUDY, Y., PLONSEY, R. & LIEBMAN, J. 1979. The effects of variations in conductivity and geometrical parameters on the electrocardiogram, using an eccentric spheres model. *Circulation Research,* 44**,** 104-111.

RUDY, Y., WOOD, R., PLONSEY, R. & LIEBMAN, J. 1982. The effect of high lung conductivity on electrocardiographic potentials. Results from human subjects undergoing bronchopulmonary lavage. *Circulation,* 65**,** 440-445.

SAAD, Y. & SCHULTZ, M. H. 1986. GMRES: A generalized minimal residual algorithm for solving nonsymmetric linear systems. *SIAM Journal on scientific and statistical computing,* 7**,** 856-869.

SABOURI, S., MATENE, E., VINET, A., RICHER, L. P., CARDINAL, R., ARMOUR, J. A., PAGÉ, P., KUS, T. & JACQUEMET, V. 2014. Simultaneous epicardial and noncontact endocardial mapping of the canine right atrium: Simulation and experiment. *PLoS ONE,* 9.

SALINET, J. L., TUAN, J. H., SANDILANDS, A. J., STAFFORD, P. J., SCHLINDWEIN, F. S. & ANDRÉ NG, G. 2014. Distinctive patterns of dominant frequency trajectory behavior in drug-refractory persistent atrial fibrillation: Preliminary characterization of spatiotemporal instability. *Journal of Cardiovascular Electrophysiology,* 25**,** 371-379.

SALINET JR, J. L., AHMAD, A., BROWN, P. D., STAFFORD, P., ANDRE NG, G. & SCHLINDWEIN, F. S. Three-dimensional frequency mapping from the noncontact unipolar electrograms in atrial fibrillation. Computing in Cardiology, 2010. 745-748.

SALINET JR, J. L., MADEIRO, J. P. V., CORTEZ, P. C., STAFFORD, P. J., ANDRÉ NG, G. & SCHLINDWEIN, F. S. 2013. Analysis of QRS-T subtraction in unipolar atrial fibrillation electrograms. *Medical and Biological Engineering and Computing,* 51**,** 1381-1391.

SALU, Y. 1978. Relating the multipole moments of the heart to activated parts of the epicardium and endocardium. *Annals of Biomedical Engineering,* 6**,** 492-505.

SANDERS, P., BERENFELD, O., HOCINI, M., JAÏS, P., VAIDYANATHAN, R., HSU, L. F., GARRIGUE, S., TAKAHASHI, Y., ROTTER, M., SACHER, F., SCAVÉE, C., PLOUTZ-SNYDER, R., JALIFE, J. & HAÏSSAGUERRE, M. 2005. Spectral analysis identifies sites of high-frequency activity maintaining atrial fibrillation in humans. *Circulation,* 112**,** 789-797.

SCARGLE, J. D. 1982. Studies in astronomical time series analysis. II-Statistical aspects of spectral analysis of unevenly spaced data. *The Astrophysical Journal,* 263**,** 835-853.

SCHILLING, R. J., KADISH, A. H., PETERS, N. S., GOLDBERGER, J. & DAVIES WYN, D. 2000. Endocardial mapping of atrial fibrillation in the human right atrium using a non-contact catheter. *European Heart Journal,* 21**,** 550-564.

SCHILLING, R. J., PETERS, N. S. & DAVIES, D. W. 1998. Simultaneous endocardial mapping in the human left ventricle using a noncontact catheter: Comparison of contact and reconstructed electrograms during sinus rhythm. *Circulation,* 98**,** 887-898.

SCHLINDWEIN, F. S., YI, A. C., EDWARDS, T. & BIEN, I. C. H. Optimal frequency and bandwidth for FIR bandpass filter for QRS detection. IET 3rd International Conference MEDSIP 2006: Advances in Medical, Signal and Information Processing, 2006 Glasgow. 61.

SCHOTTEN, U., VERHEULE, S., KIRCHHOF, P. & GOETTE, A. 2011. Pathophysiological mechanisms of atrial fibrillation: A translational appraisal. *Physiological Reviews,* 91**,** 265-325.

SCHUESSLER, R. B., KAWAMOTO, T., HAND, D. E., MITSUNO, M., BROMBERG, B. I., COX, J. L. & BOINEAU, J. P. 1993. Simultaneous epicardial and endocardial activation sequence mapping in the isolated canine right atrium. *Circulation,* 88**,** 250-263.

SCHUESSLER, R. B., KAY, M. W., MELBY, S. J., BRANHAM, B. H., BOINEAU, J. P. & DAMIANO JR, R. J. 2006. Spatial and temporal stability of the dominant frequency of activation in human atrial fibrillation. *Journal of Electrocardiology,* 39**,** S7-S12.

SEIFTER, J., SLOANE, D. & RATNER, A. 2005. *Concepts in medical physiology*, Lippincott Williams & Wilkins.

SHANNON, H. J., NAVARRO, C. O., SMITH, B. A., MCCLELLAND, A. J., LAU, E. W., ROBERTS, M. J. D., ANDERSON, J. M. C. & ADGEY, J. A. 2007. Activation patterns during selective pacing of the left ventricle can be characterized using noninvasive electrocardiographic imaging. *Journal of Electrocardiology,* 40**,** S111-S117.

SHOR, R., WAINSTEIN, J., OZ, D., BOAZ, M., MATAS, Z., FUX, A. & HALABE, A. 2008. Low HDL levels and the risk of death, sepsis and malignancy. *Clinical Research in Cardiology,* 97**,** 227-233.

SHOUCRI, R. M. 1991. Theoretical study of pressure-volume relation in left ventricle. *American Journal of Physiology - Heart and Circulatory Physiology,* 260**,** H282-H291.

SHOUCRI, R. M. 1993. Pressure-volume relation in the right ventricle. *Journal of Biomedical Engineering,* 15**,** 167-169.

SIPPENSGROENEWEGEN, A., LESH, M. D., ROITHINGER, F. X., ELLIS, W. S., STEINER, P. R., SAXON, L. A., LEE, R. J. & SCHEINMAN, M. M. 2000. Body surface mapping of counterclockwise and clockwise typical atrial flutter: A comparative analysis with endocardial activation sequence mapping. *Journal of the American College of Cardiology,* 35**,** 1276-1287.

SIPPENSGROENEWEGEN, A., PEETERS, H. A. P., JESSURUN, E. R., LINNENBANK, A. C., ROBLES DE MEDINA, E. O., LESH, M. D. & VAN HEMEL, N. M. 1998. Body Surface Mapping During Pacing at Multiple Sites in the Human Atrium : P-Wave Morphology of Ectopic Right Atrial Activation. *Circulation,* 97**,** 369-380.

SLOCUM, J., BYROM, E., MCCARTHY, L., SAHAKIAN, A. & SWIRYN, S. 1985. Computer detection of atrioventricular dissociation from surface electrocardiograms during wide QRS complex tachycardias. *Circulation,* 72**,** 1028-1036.

STEGEMAN, D. F., BLOK, J. H., HERMENS, H. J. & ROELEVELD, K. 2000. Surface EMG models: Properties and applications. *Journal of Electromyography and Kinesiology,* 10**,** 313-326.

STINSTRA, J. G. & PETERS, M. J. 1998. The volume conductor may act as a temporal filter on the ECG and EEG. *Medical and Biological Engineering and Computing,* 36**,** 711-716.

TACCARDI, B. 1963. Distribution of Heart Potentials on the Thoracic Surface of Normal Human Subjects. *Circulation Research,* 12**,** 341-352.

TACCARDI, B., ARISI, G., MACCHI, E., BARUFFI, S. & SPAGGIARI, S. 1987. A new intracavitary probe for detecting the site of origin of ectopic ventricular beats during one cardiac cycle. *Circulation,* 75**,** 272-281.

TACCARDI, B., PUNSKE, B. B., LUX, R. L., MACLEOD, R. S., ERSHLER, P. R., DUSTMAN, T. J. & VYHMEISTER, Y. 1998. Useful lessons from body surface mapping. *Journal of Cardiovascular Electrophysiology,* 9**,** 773-786.

TILG, B., FISCHER, G., MODRE, R., HANSER, F., MESSNARZ, B. & ROITHINGER, F. X. 2003. Electrocardiographic imaging of atrial and ventricular electrical activation. *Medical Image Analysis,* 7**,** 391-398.

TILG, B., FISCHER, G., MODRE, R., HANSER, F., MESSNARZ, B., SCHOCKE, M., KREMSER, C., BERGER, T., HINTRINGER, F. & ROITHINGER, F. X. 2002. Model-based imaging of cardiac electrical excitation in humans. *Medical Imaging, IEEE Transactions on,* 21**,** 1031-1039.

TROST, R. F., ARTHUR, R. M., GESELOWITZ, D. B. & BRILLER, S. A. 1977. A dipole plus quadrupole lead system for human electrocardiography. *Journal of Electrocardiology,* 10**,** 27-38.

TUAN, J., JEILAN, M., KUNDU, S., NICOLSON, W., CHUNG, I., STAFFORD, P. J. & NG, G. A. 2011. Regional fractionation and dominant frequency in persistent atrial fibrillation: Effects of left atrial ablation and evidence of spatial relationship. *Europace,* 13**,** 1550-1556.

TWOMEY, S. 1965. The application of numerical filtering to the solution of integral equations encountered in indirect sensing measurements. *Journal of the Franklin Institute,* 279**,** 95-109.

UIJEN, G. J. H. & VAN OOSTEROM, A. 1992. On the detection of the number of signals in multilead ECGs. *Methods of Information in Medicine,* 31**,** 247-255.

VAN DAM, P. M., OOSTENDORP, T. F., LINNENBANK, A. C. & VAN OOSTEROM, A. 2009. Non-invasive imaging of cardiac activation and recovery. *Annals of Biomedical Engineering,* 37**,** 1739-1756.

VAN DAM, P. M., PRONIEWSKA, K., MAUGENEST, A. M., VAN MIEGHEM, N. M., MAAN, A. C., DE JAEGERE, P. P. T. & BRUINING, N. 2014. Electrocardiographic imaging-based recognition of possible induced bundle branch blocks during transcatheter aortic valve implantations. *Europace,* 16**,** 750-757.

VAN DAM, P. M., TUNG, R., SHIVKUMAR, K. & LAKS, M. 2013. Quantitative localization of premature ventricular contractions using myocardial activation ECGI from the standard 12-lead electrocardiogram. *Journal of Electrocardiology,* 46**,** 574-579.

VAN DAM, P. M. & VAN OOSTEROM, A. 2003. Atrial Excitation Assuming Uniform Propagation. *Journal of Cardiovascular Electrophysiology,* 14**,** S166-S171.

VAN DAM, P. M. & VAN OOSTEROM, A. 2005. Volume conductor effects involved in the genesis of the P wave. *Europace,* 7**,** S30-S38.

VAN DER GRAAF, A. W. M., BHAGIRATH, P., RAMANNA, H., VAN DRIEL, V. J. H. M., DE HOOGE, J., DE GROOT, N. M. S. & GÖTTE, M. J. W. 2014. Noninvasive imaging of cardiac

excitation: Current status and future perspective. *Annals of Noninvasive Electrocardiology,* 19**,** 105-113.

VAN OOSTEROM, A. 1978. Triangulating the human torso. *The Computer Journal,* 21**,** 253-258.

VAN OOSTEROM, A. 2001. Genesis of the T wave as based on an equivalent surface source model. *Journal of Electrocardiology,* 34**,** 217-227.

VAN OOSTEROM, A. 2012a. Closed-form analytical expressions for the potential fields generated by triangular monolayers with linearly distributed source strength. *Medical and Biological Engineering and Computing,* 50**,** 1-9.

VAN OOSTEROM, A. 2012b. The Equivalent Double Layer: Source Models for Repolarization. *In:* MACFARLANE, P. W., VAN OOSTEROM, A., PAHLM, O., KLIGFIELD, P., JANSE, M. J. & CAMM, A. J. (eds.) *Comprehensive Electrophysiology.* 2 ed. London, UK: Springer.

VAN OOSTEROM, A. 2012c. The inverse problem of bioelectricity: An evaluation. *Medical and Biological Engineering and Computing,* 50**,** 891-902.

VAN OOSTEROM, A. 2014a. A comparison of electrocardiographic imaging based on two source types. *Europace,* 16**,** iv120-iv128.

VAN OOSTEROM, A. 2014b. Electric Volume Conduction in Biomedicine. Nijmegen, Netherlands: Radboud University.

VAN OOSTEROM, A. & HUISKAMP, G. J. M. 1992. Implicit and explicit constraints in inverse electrocardiography. *Journal of Electrocardiology,* 25**,** 87-92.

VAN OOSTEROM, A., IHARA, Z., JACQUEMET, V. & HOEKEMA, R. 2007. Vectorcardiographic lead systems for the characterization of atrial fibrillation. *Journal of Electrocardiology,* 40**,** 343.e1-343.e11.

VAN OOSTEROM, A. & OOSTENDORP, T. 1992a. On computing pericardial potentials and current densities in inverse electrocardiography. *Journal of electrocardiology,* 25**,** 102-106.

VAN OOSTEROM, A. & OOSTENDORP, T. F. 1992b. On computing pericardial potentials and current densities in inverse electrocardiography. *Journal of Electrocardiology,* 25**,** 102-106.

VAN OOSTEROM, A. & OOSTENDORP, T. F. 2004. ECGSIM: An interactive tool for studying the genesis of QRST waveforms. *Heart,* 90**,** 165-168.

VAN OOSTEROM, A., OOSTENDORP, T. F. & VAN DAM, P. M. 2011. Potential applications of the new ECGSIM. *Journal of Electrocardiology,* 44**,** 577-583.

VARAH, J. 1979. A Practical Examination of Some Numerical Methods for Linear Discrete Ill-Posed Problems. *SIAM Review,* 21**,** 100-111.

VERMA, A., LAKKIREDDY, D., WULFFHART, Z., PILLARISETTI, J., FARINA, D., BEARDSALL, M., WHALEY, B., GIEWERCER, D., TSANG, B. & KHAYKIN, Y. 2011. Relationship between complex fractionated electrograms (CFE) and dominant frequency (DF) sites and prospective assessment of adding DF-guided ablation to pulmonary vein isolation in persistent atrial fibrillation (AF). *Journal of Cardiovascular Electrophysiology,* 22**,** 1309-1316.

WALLER, A. D. 1888. On the electromotive variations which accompany the beat of the human heart. *Nature,* 38**,** 619-621.

WIJFFELS, M. C. E. F., KIRCHHOF, C. J. H. J., DORLAND, R. & ALLESSIE, M. A. 1995. Atrial fibrillation begets atrial fibrillation: A study in awake chronically instrumented goats. *Circulation,* 92**,** 1954-1968.

WILSON, F. N., MACLEOD, A. G. & BARKER, P. S. 1933. The distribution of the action currents produced by heart muscle and other excitable tissues immersed in extensive conducting media. *The Journal of General Physiology,* 16**,** 423-456.

YAMAZAKI, M., MIRONOV, S., TARAVANT, C., BREC, J., VAQUERO, L. M., BANDARU, K., AVULA, U. M. R., HONJO, H., KODAMA, I., BERENFELD, O. & KALIFA, J. 2012. Heterogeneous atrial wall thickness and stretch promote scroll waves anchoring during atrial fibrillation. *Cardiovascular Research,* 94**,** 48-57.

YATES, R. 2009. Fixed-point arithmetic: An introduction. *Digital Signal Labs,* 81**,** 198.

YOSHIDA, K., CHUGH, A., ULFARSSON, M., GOOD, E., KUHNE, M., CRAWFORD, T., SARRAZIN, J. F., CHALFOUN, N., WELLS, D., BOONYAPISIT, W., VEERAREDDY, S., BILLAKANTY, S., WONG, W. S., JONGNARANGSIN, K., PELOSI JR, F., BOGUN, F., MORADY, F. & ORAL, H. 2009. Relationship between the spectral characteristics of atrial fibrillation and atrial tachycardias that occur after catheter ablation of atrial fibrillation. *Heart Rhythm,* 6**,** 11-17.

YUSHKEVICH, P. A., PIVEN, J., HAZLETT, H. C., SMITH, R. G., HO, S., GEE, J. C. & GERIG, G. 2006. User-guided 3D active contour segmentation of anatomical structures: Significantly improved efficiency and reliability. *NeuroImage,* 31**,** 1116-1128.

ZABLOW, L. 1966. An equivalent cardiac generator which preserves topography. *Biophys J,* 6**,** 535-6.

ZAZA, A., WILDERS, R. & OPTHOF, T. 2012. Cellular Electrophysiology. *In:* MACFARLANE, P. W., VAN OOSTEROM, A., PAHLM, O., KLIGFIELD, P., JANSE, M. J. & CAMM, A. J. (eds.) *Comprehensive Electrocardiology.* 2 ed. London, UK: Springer.

ZHANG, Y., GHODRATI, A. & BROOKS, D. H. 2005. An analytical comparison of three spatio-temporal regularization methods for dynamic linear inverse problems in a common statistical framework. *Inverse Problems,* 21**,** 357.

ZHOU, W., BOVIK, A. C., SHEIKH, H. R. & SIMONCELLI, E. P. 2004. Image quality assessment: from error visibility to structural similarity. *Image Processing, IEEE Transactions on,* 13**,** 600-612.